Fluid-Dynamic Fluctuations and Flow Structures in Centrifugal Pumps due to Rotor-Stator Interaction

Jens Keller

Universidad de Oviedo

Doctoral Thesis presented in the
Doctoral Programme of Energy Engineering

April 2014

Fluid-Dynamic Fluctuations and Flow Structures in Centrifugal Pumps due to Rotor-Stator Interaction

Jens Keller

Universidad de Oviedo

Supervisors: Prof. Dr. Jorge Luis Parrondo Gayo
Dr. Raúl Barrio Perotti
Dr. Eduardo Blanco Marigorta

Doctoral Thesis presented in the
Doctoral Programme of Energy Engineering

Gijón, April 2014

To my beloved wife and our wonderful child

Zwei Dinge sind zu unserer Arbeit nötig:
Unermüdliche Ausdauer und die Bereitschaft, etwas,
in das man viel Zeit und Arbeit gesteckt hat,
wieder wegzuwerfen.
Albert Einstein

Abstract

This thesis deals with flow structures and pressure fluctuations due to rotor-stator interaction in centrifugal pumps with volute casing. The magnitude of pressure fluctuations generated is dependent on the internal geometry of the pump and its operating point, as well as on the acoustic response of the hydraulic system. To investigate the flow phenomena by particle image velocimetry (PIV) a transparent pump with a 2D-shaped impeller with backward-curved blades was built. The flow in the centerplane perpendicular to the pump axis was captured using fluorescent seeding particles. Phase-averaged velocity fields in the volute tongue region and other fluid-dynamic variables are presented for three flow-rates, different magnifications, and various blade positions, covering one blade passage period. PIV measurements include stereo PIV to obtain the three velocity components in the measurement plane. Spatial distribution of the spectral components at the blade-passing frequency (BPF) and harmonics reveal that at 40 % of nominal flow-rate and at nominal flow-rate (Q_N) the highest spectral content is concentrated at BPF. For 150 % Q_N the second harmonic is dominant in the narrow region of the volute at the tongue tip. The impeller-tongue interaction is dominated by intense vorticity sheets shed from the impeller channels, especially from the blade trailing edges. Turbulence production is mainly concentrated in the wake regions of the blade leading and trailing edges and of the tongue tip. For 40 % Q_N turbulent kinetic energy (TKE) production is maximum in the tongue region before the blade pressure side arrives at the tongue tip, in accordance with vorticity development in the tongue wake. For 150 % Q_N TKE production reaches its maximum behind the blade trailing edge when the blade aligns with the tongue tip.
The effect of the acoustic coupling of a centrifugal pump with its hydraulic circuit was investigated using two different experimental facilities: an industrial pump facility with double-curved impeller blades and the transparent pump facility also used for the PIV measurements. Unsteady pressure measurements at the volute and at the hydraulic circuit were conducted to quantify experimentally the influence of the acoustic characteristics of the hydraulic circuit on the pressure fluctuations. A 2-port acoustic model, including a transfer matrix analysis, was applied to describe the acoustic behaviour and predict resonance frequencies. The acoustic impedance was changed by varying the pump rotational speed and by activating a dead-end branch connected to the circuit. At a certain resonance frequency, the amplitude of the pressure fluctuations at the pump could be reduced by up to 36 % by activating the dead-end branch without changing the pump speed. With these models, reduction of the pressure fluctuations directly at the pump and at the hydraulic circuit can be predicted.

Resumen

Esta tesis trata sobre las estructuras del flujo y fluctuaciones de presión debidas a la interacción rotor-estator en bombas centrífugas con voluta. La magnitud de las fluctuaciones de presión depende de la geometría interna de la bomba, de su punto de operación y de la respuesta acústica del sistema hidráulico. Para investigar los fenómenos del flujo mediante PIV (velocimetría por imágenes de partículas) se construyó una bomba transparente 2D con álabes curvados hacia atrás. Se investigó el flujo en el plano medio perpendicular al eje de la bomba mediante el uso de partículas fluorescentes. Se han obtenido los campos de velocidad promediados en fase en la zona de la lengüeta y otras variables fluidodinámicas para tres caudales, distintas ampliaciones y diferentes posiciones del álabe. Las medidas PIV incluyen PIV estéreo que permitió obtener las tres componentes de la velocidad en el plano de medida. La distribución espacial de las componentes espectrales a la frecuencia de paso de álabe (BPF) y sus armónicos muestran que al 40 % del caudal nominal y al caudal nominal (Q_N) el contenido espectral más alto se concentra en BPF. Para 150 % Q_N el segundo armónico es dominante en la zona estrecha de la voluta próxima a la lengüeta. La interacción entre rodete y lengüeta está muy influenciada por intensas capas de vorticidad que se desprenden desde los canales del rodete, especialmente desde los bordes de salida de los álabes. La producción de turbulencia se concentra en las zonas de estela de los bordes de ataque y de salida de los álabes y de la punta de la lengüeta. Para 40 % Q_N la producción de energía cinética turbulenta (TKE) es máxima en la zona de la lengüeta antes de que la cara de presión del álabe llegue a la punta de la misma, en concordancia con el desarrollo de la vorticidad en la estela de la lengüeta. Para 150 % Q_N la producción de TKE alcanza su máximo detrás del borde de salida del álabe, cuando este se alinea con la punta de la lengüeta.

Se estudió el efecto del acoplamiento acústico de una bomba con su circuito hidráulico utilizando dos bancos de laboratorio: un banco con una bomba industrial de álabes con doble curvatura, y el banco con la bomba transparente que se utilizó para las medidas PIV. Se midió la presión fluctuante en la voluta y en el circuito para cuantificar experimentalmente la influencia de las características acústicas del circuito en las fluctuaciones de presión. Se utilizó un modelo de dos puertos, que incluía un análisis matricial de transferencia, para describir el comportamiento acústico y predecir frecuencias de resonancia. La impedancia acústica se modificó mediante la variación de la velocidad de rotación de la bomba y mediante la apertura de una rama lateral ciega. A una determinada frecuencia de resonancia la amplitud de las fluctuaciones de presión se redujo hasta en un 36 % mediante la activación de dicha rama, sin haber modificado la velocidad de la bomba. Mediante estos modelos se puede predecir la reducción de las fluctuaciones de presión directamente en la bomba y en el circuito.

Acknowledgements

I would like to thank my supervisors for all their support and inspiration, Jorge Parrondo for his continuous help and motivation, Raúl Barrio for all his motivation and support and Eduardo Blanco for all the great ideas that facilitated especially the PIV measurements.

My thanks go also to all the other professors at the Department of Energy and my colleagues for their discussions and motivation. They were a great help and supported me during my years at this department. Many thanks to Carlos Suárez for helping with the fabrication of the pump.
I would like to acknowledge the financial support of the Spanish Ministry of Science and Innovation for the grant *FPI* (BES-2010-037565).
I thank also Prof. Dr. Gérard Bois and Dr. Giorgio Pavesi, acting as reviewer of this thesis, for their reports.

Furthermore, I would like to acknowledge all the people who made possible my research stays at Johns-Hopkins-University (JHU) in Baltimore, USA, and at the Swiss Federal Institute of Technology (ETH) Zurich, Switzerland. At JHU I would like to thank in particular Prof. Joseph Katz for inviting me to the Laboratory for Experimental Fluid Dynamics and PhD Rinaldo Miorini, David Tan and PhD Pranav Joshi who shared their knowledge about PIV (particle image velocimetry) and turbomachinery. At ETH Zurich I thank especially Prof. Robert Boes and Dr. Georg Möller for inviting me to VAW (Laboratory of Hydraulics, Hydrology and Glaciology) and for giving me the possibility to work at such a unique laboratory.

I would like to thank my family, especially my parents Helga and Bernd, for all their continuous support over all these years. Without them I would never be where I am now.

My special thanks go to my lovely and amazing wife Constanze for all her support and love and to our beloved child.

Contents

List of Figures

List of Tables

Nomenclature

Latin symbols

A	cross-sectional area [m^2]
c	speed of sound [m/s]
c_w	speed of sound in water [m/s]
D	impeller diameter [m]
D_a	aperture diameter of camera [m]
d_p	particle diameter [m]
d_s	diffraction-limited minimum image diameter [m]
d_τ	particle diameter recorded on image [m]
E	Young's modulus [Pa]
f	frequency [Hz]
f_{BP}	blade-passing frequency [Hz]
f_L	focal length [m]
$f_\#$	f-number of camera [-]
f_R	rotation frequency [Hz]
f_{ref}	reference frequency [Hz]
f_s	sampling frequency [Hz]
H	head [m]
K	bulk modulus of water [Pa]
k_{2D}	in-plane turbulent kinetic energy (TKE) [m^2/s^2]
L	length [m]
M	magnification factor [-]
Ma	Mach number [-]
N	number of data points [-]; interrogation area length [px]
n_s	dimensionless specific speed [-]
p	pressure amplitude [Pa]
P	pressure (amplitude and phase) [Pa,°]
P_{ij}	production rate tensor of TKE [m^2/s^3]
P_{2D}	in-plane production rate of TKE [m^2/s^3]
P_s	shaft power [W]
P_u	useful power [W]
Q	flow-rate [m^3/s]
Re	Reynolds number [-]
r_{tip}	blade tip radius [m]
S_{ij}	rate-of-strain tensor [1/s]

s	distance between sensors [m]
t	time [s]
U	velocity magnitude [m/s]
$\vec{U}$	phase-averaged absolute velocity vector [m/s]
u	velocity component in x-direction [m/s]
$\vec{u}$	instantaneous velocity vector [m/s]
U_p	particle velocity [m/s]
u_r	velocity component in radial direction [m/s]
U_s	velocity slip [m/s]
u_θ	velocity component in tangential direction [m/s]
U_tip	blade tip speed [m/s]
V	acoustic mass flow [kg/s]
v	velocity component in y-direction [m/s]
w	axial velocity component [m/s]
$\vec{W}$	phase-averaged relative velocity vector [m/s]
z	specific acoustic impedance [N/m^3]
Z	acoustic impedance [m^2/s^2]

Greek symbols

α	attenuation factor [rad/m]
β	blade angle [°]
δ	Dirac delta
δ_z	depth of field [m]
Δ	delay
ε_res	residual error
η	efficiency [-]
ζ	acoustic impedance for a plane wave [1/(ms)]
λ	wavelength [m]
τ_{ij}	Reynolds stress tensor [m^2/s^2]
ρ	density [kg/m^3]
ϕ, φ	phase with respect to tongue tip [°]
Φ	flow coefficient, non-dimensional = $Q/(\Omega D^3)$ [-]
Ψ	head coefficient, non-dimensional = $gH/(\Omega D)^2$ [-]
ω_z	out-of-plane vorticity [1/s]
Ω	pump rotational speed (=2 πf_R) [rad/s]
Ω_{ij}	rate-of-rotation tensor [1/s]

Superscripts

$'$	fluctuating component
$*, \hat{}$	normalized value
$+$	radiated component
$-$	returning component

Subscripts

a	air
BP	blade-passing
N	nominal value
th	theoretical value
w	water
1	at impeller inlet
2	at impeller outlet
2D	in-plane component

Acronyms

BEP	best efficiency point
BPF	blade-passing frequency
CCD	charge coupled device
CFD	computational fluid dynamics
DFT	discrete Fourier transform
FFT	fast Fourier transform
FOV	field of view
IA	interrogation area
LDV	laser Doppler velocimetry
PIV	particle image velocimetry
PTV	particle tracking velocimetry
RSI	rotor-stator interaction
SNR	signal to noise ratio
TKE	turbulent kinetic energy
TMA	transfer matrix analysis

Part I

Introduction

1 Introduction and fundamentals

1.1 Background

Centrifugal pumps are one of the most used machines and their range of application is widely spread. They are used in a variety of industrial processes and civil engineering applications. These machines force the circulation of the fluid, while supplying energy to it, by means of a bladed rotor, usually denominated impeller. The magnitude of the energy transferred to the fluid is usually expressed in terms of work per unit weight of fluid, which is usually referred to as the pump head. In comparison with axial pumps, centrifugal pumps have typically a lower specific speed and are employed for lower flow-rates and higher pressure rises.

Besides its prime energy transfer purpose between machine and fluid, centrifugal pumps also have to fulfil mechanical, economical and even ecological requirements. In particular, they have to be robust, reliable and have to operate with low vibration levels even at off-design conditions. Otherwise, they might provoke the failure of the hydraulic circuit and the coupled systems.

Different types of centrifugal pumps exist. On one hand, their rotor can be shrouded, unshrouded or open. On the other hand, the stator may have a vaned or a vaneless diffuser, as well as a single or double volute. In spite of this variety the basic working principle is the same for all centrifugal pumps: the impeller increases the angular momentum of the fluid, so that work is being transferred to the fluid, which results in an increase of pressure. The fluid enters the impeller in the axial direction and leaves it in the radial direction towards the diffuser. Subsequently, the fluid can either be collected by a volute and conducted to the pump exit or, in the case of multistage pumps, the fluid can proceed to the next stage.

The design and kinematics of the pump elements to produce the energy exchange between machine and fluid provoke that the internal flow is non-uniform and unsteady. In fact, the flow inside pumps is considerably complex, as it is characterized by high temporal and spatial velocity gradients and secondary flow structures. At off-design conditions the unsteady flow phenomena are stronger. In particular, the flow exiting the impeller, which exhibits a non-uniform pattern modulated by the impeller channels, is perceived at the stator as unsteady flow. Hence, this rotor-stator interaction (RSI) creates an internal

dynamic load. This fluid-dynamic excitation leads to pressure pulsations resulting in acoustic waves radiated towards the suction and discharge pipe of the hydraulic circuit. Furthermore, the radiated waves can be reflected at different elements of the hydraulic circuit. Combination of the radiated and reflected waves can lead in certain cases either to mechanical or acoustical resonance inducing excessively high noise and vibration levels.

The pressure fluctuation amplitudes are very dependent on the pump geometry, especially the tongue region and the operating point. They also depend on the acoustic coupling of the hydraulic circuit with the pump.
To ensure stable operation under a broad range of conditions, pumps have to satisfy certain limits of vibration levels, as vibration of mechanical elements may lead to failure due to fatigue. Especially for pumps with high output power, operating over a wide range of rotational speeds and flow conditions, it is essential to understand the flow field inside in order to predict possible fluid-dynamic phenomena which can lead to excessive vibration levels.

To consider these aspects already in the design process many pump manufacturers use computational fluid dynamics (CFD) to study different pump geometries and their fluid-dynamic behaviour. CFD codes aim at simulating these flow phenomena numerically. They are suitable for predicting the general characteristics of a pump, such as the flow-rate and the head. However, their capability to precisely describe complex flow phenomena, e.g. due to rotor-stator interaction or other secondary flow structures, is more limited. Indeed, to validate the CFD models and to choose appropriate boundary conditions and other calculation parameters, such as the correct turbulence model, experimental results are still needed to provide benchmark data.

1.2 Fundamentals of centrifugal pumps

Some fundamentals of centrifugal pumps are described in this section. Further detailed information can be found in books about centrifugal pumps, such as Karassik et al. (1986), Brennen (1994) and Guelich (2010).
The flow inside centrifugal pumps can be described in a stationary reference frame, i.e. fixed on a stationary element, or in a relative reference frame, i.e. moving with the rotation of the impeller. The velocities in a stationary coordinate system are denominated absolute velocities $\vec{U}$, whereas the velocities observed from the reference frame on the impeller are called relative velocities $\vec{W}$. The absolute velocity vector $\vec{U}$ can be described by adding the relative velocity vector $\vec{W}$ to the velocity of the impeller due to its rotation:

$$\vec{U} = \vec{W} + \vec{\Omega} \times \vec{r}, \tag{1.1}$$

being $\vec{\Omega}$ the pump rotational speed and $\vec{r}$ the position vector.

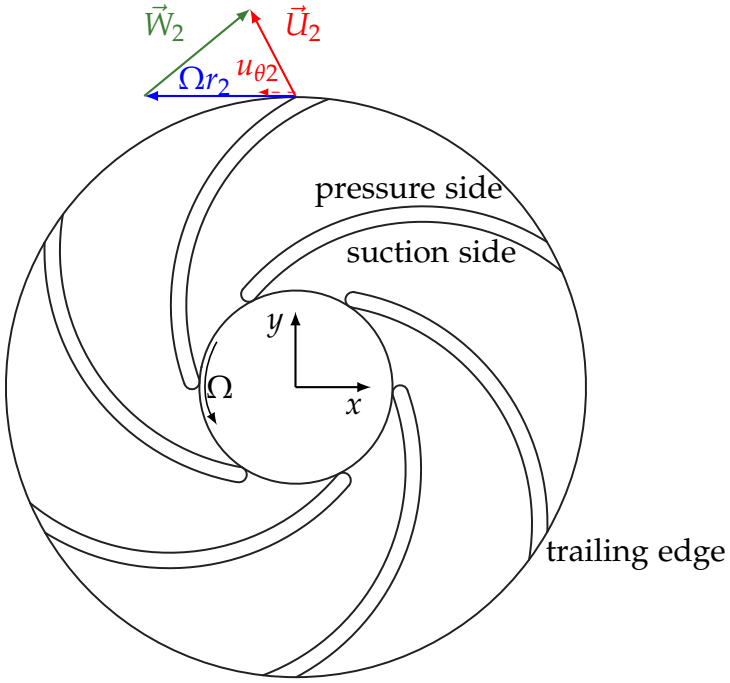

Figure 1.1: Velocity triangle at impeller outlet

Euler's turbomachine equation can be used to obtain the theoretical head:

$$H_{\text{th}} = \frac{1}{g}(\Omega r_2 u_{\theta 2} - \Omega r_1 u_{\theta 1}), \tag{1.2}$$

being r_1 and r_2 the impeller radius and $u_{\theta 1}$ and $u_{\theta 2}$ the tangential velocity component at the impeller inlet and outlet, respectively. In this equation the variables correspond to values averaged with the mass flow in the circumferential direction. However, the actually obtained head is lower due to viscous hydraulic losses, associated to high velocity gradients, flow separation and turbulence which lead finally to dissipation of vortices and transformation into heat. Further losses are of mechanical kind, mainly due to friction at internal parts (discs) or external parts (bearings or seals).
The actual head H is obtained as the energy difference of the fluid between pump exit (e) and inlet (i):

$$H = \frac{p_e - p_i}{\rho g} + \frac{u_e^2 - u_i^2}{2g} + h_e - h_i, \tag{1.3}$$

being p the static pressure, ρ the fluid density, u the mean velocity and h the geometric height.
The useful power of a pump is obtained by

$$P_u = \rho g Q H, \tag{1.4}$$

being Q the flow-rate. The efficiency is obtained by the ratio of the useful power P_u to the shaft power P_s

$$\eta = \frac{P_u}{P_s}. \tag{1.5}$$

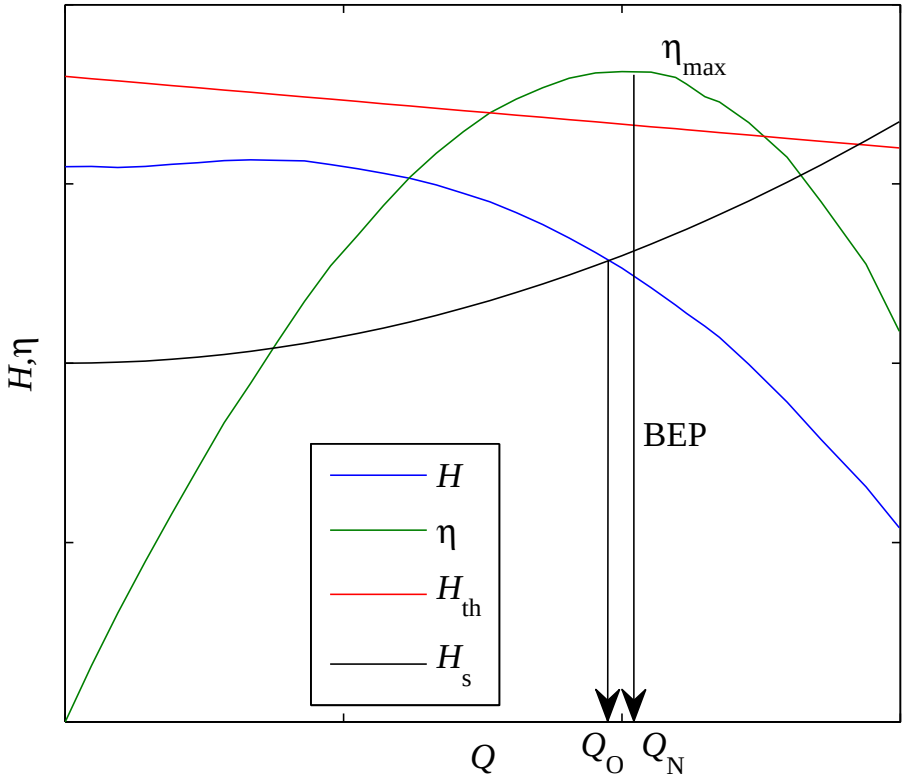

Figure 1.2: Characteristic curves: theoretical head H_{th}, actual head H, system curve H_s and efficiency η as a function of the flow-rate Q

When changing the flow-rate, the corresponding head, power consumption and thereby the efficiency change. Representing these values as a function of the flow-rate lead to the pump characteristic curves (see Fig. 1.2). The operating point Q_O is obtained by the intersection of the $H - Q$ curve with the system curve of the hydraulic circuit H_s. The point with the maximum efficiency η_{max} is denominated the best efficiency point (BEP). The flow-rate at this point is called nominal flow-rate Q_N. The installation should be designed so that the pump can be operated most of the time near or close to the BEP.
The design of the volute is only optimal for one flow-rate (Q_N). For part load (below Q_N) the flow and therefore the velocities coming from the impeller are smaller than they are designed to be. This leads to increasing pressure for increasing circumferential angle of the volute. For flow-rates above the nominal flow-rate the contrary is the case. Higher velocities lead to decreasing pressure

along the volute. Therefore, the head delivered by the pump is decreasing for increasing flow-rates (Lorett and Gopalakrishnan, 1986).

To compare the performance of pumps with different geometries the main parameters are made dimensionless. The results of a dimensional analysis of the flow through hydraulic machines are the affinity laws, which relate variables of geometrically similar machines that operate at homologous points. In particular, it relates the density of the fluid ρ, pump rotational speed Ω and the impeller diameter D with the flow-rate Q, the head rise by the pump H and the shaft power P_s.

The dimensionless flow coefficient is

$$\Phi = \frac{Q}{\Omega D^3}. \tag{1.6}$$

The dimensionless head coefficient is

$$\Psi = \frac{gH}{(\Omega D)^2}. \tag{1.7}$$

The dimensionless power coefficient is

$$C_\mathrm{p} = \frac{P_\mathrm{s}}{\rho \Omega^3 D^5}. \tag{1.8}$$

A pump should be chosen depending on the desired flow-rate Q_N and head H_N which is achieved at a certain pump rotational speed Ω. These parameters are used to calculate the dimensionless specific speed n_s, which is used to classify pumps (Karassik et al., 1986):

$$n_\mathrm{s} = \frac{\Phi^{1/2}}{\Psi^{3/4}} = \frac{\Omega Q_\mathrm{N}^{1/2}}{(gH_\mathrm{N})^{3/4}}. \tag{1.9}$$

1.3 Unsteady flow

The energy transfer of the impeller to the fluid by rotation in form of angular momentum leads inherently to non-uniform and unsteady flow. The interaction of the flow structures exiting the impeller with stationary elements, such as the volute, is called rotor-stator interaction. This leads to unsteady flow phenomena which are stronger at off-design conditions. The main phenomena and other important unsteady flow structures are described in this section.

The flow in the impeller of a centrifugal pump is composed of two main flow structures (Brennen, 1994). The first one is the throughflow related to the pumped flow-rate. The second flow structure is a counterrotating flow due to the trend of the flow to maintain its angular momentum. The flow before entering the

impeller has in general no or low vorticity. The impeller channel has a vorticity due to its solid rotation of two times the pump rotational speed (2Ω). As the fluid enters the impeller channel it tries to maintain its angular momentum and counterrotates with a vorticity of -2Ω, according to the Helmholtz theorem. This is valid for inviscid flows and leads to a non-uniform flow (see Fig. 1.3). It is concentrated towards the blade pressure side and leads to a reduced tangential velocity component and therefore to a lower head. This phenomenon is described by the slip factor.

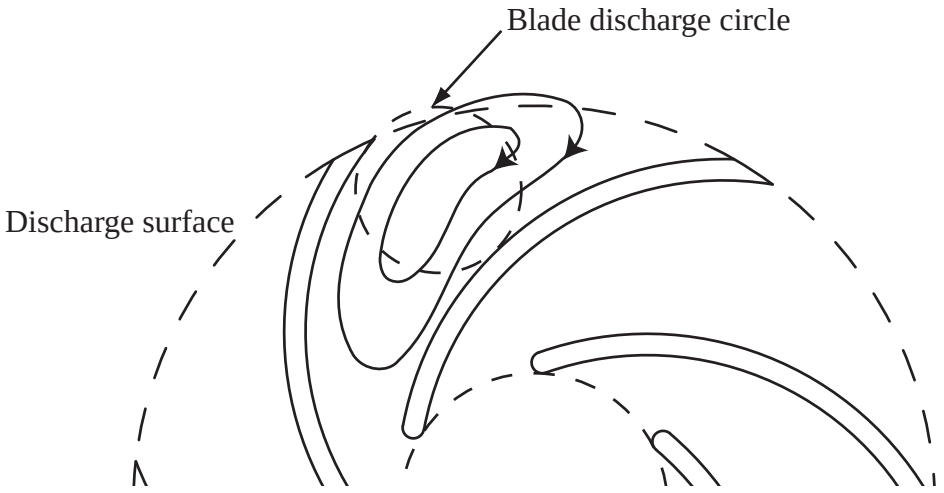

Figure 1.3: Flow pattern in an impeller for inviscid flow (adapted from Brennen (1994))

The viscous effects of the fluid lead to a boundary layer growth along the impeller blades. Adverse pressure gradients, i.e. rising pressure from impeller inlet to outlet, facilitate flow separation and recirculation. Furthermore, flow detachment can take place at the blade leading edge at partial flow-rate from the suction side of the blade and for high flow-rates from the pressure side, due to the mismatch between the angle of attack of the flow and the blade inlet angle.

Flow detachment can occur from the blade suction side, even at nominal flow-rate (Q_N). This leads to lower velocities in this zone, normally extending to the impeller outlet. Therefore, the flow at the outlet consists of a wake at the suction and of a jet at the blade pressure side (Brennen, 1994). However, this flow structure counteracts the rotational effect described for inviscid flow.

The phenomena described lead to a non-uniform flow called jet-wake phenomenon with alternating zones of high and low velocities. In the boundary layer of the rotating impeller blades relative velocities are close to zero due to the no-slip condition for viscous flow. Therefore, absolute velocities in this region are about the blade tip speed, as shown in Fig. 1.4. This means that a wake with low relative velocities results in high absolute velocities.

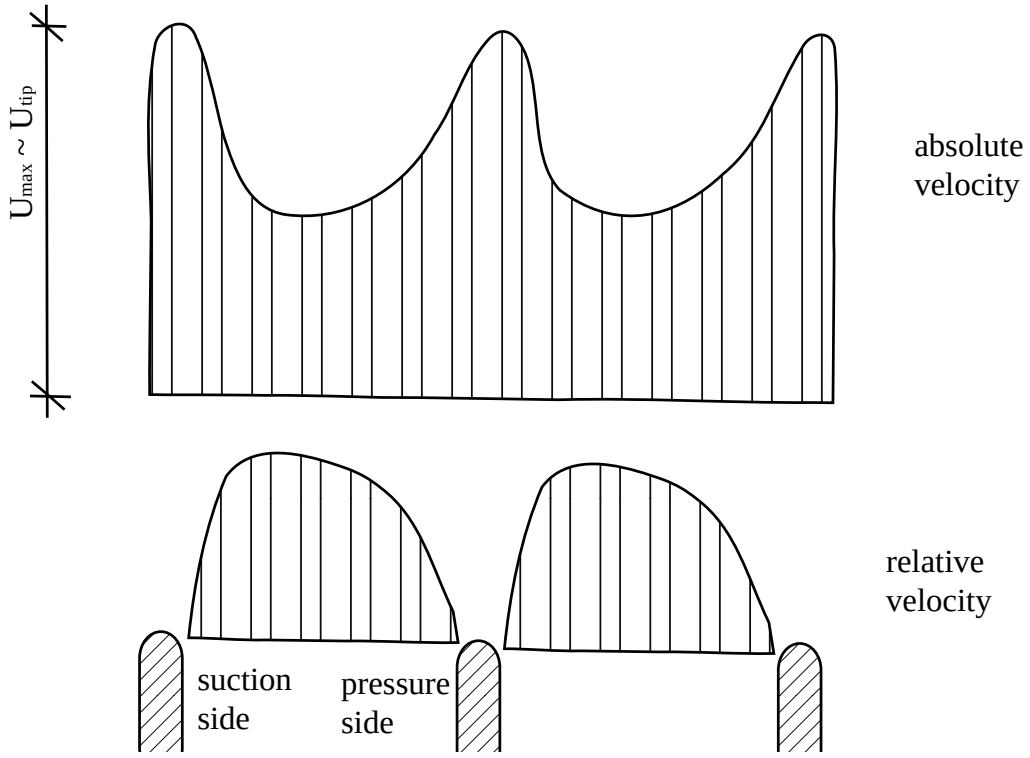

Figure 1.4: Representation of the wake in a relative and absolute reference frame (adapted from Guelich and Bolleter (1992))

The flow structures exiting the impeller, e.g. in form of wakes with high vorticity, interact with the stationary elements, such as the tongue or diffuser blades for vaned diffusers (RSI). They create new flow structures, such as flow separation with high vorticity and turbulence production. Afterwards, they are convected with the stream and decay. In an absolute reference frame, i.e. seen from stationary elements, this is perceived as non-uniform and unsteady flow, repeating mainly at f_{BP} and harmonics.

Other secondary flow structures exist in the impeller and volute which are complex and lead to hydraulic losses:

- Flow separation leads to areas with stalled fluid and can cause recirculation. This blockage involves higher velocities in the vicinity, as the effective cross-section area is reduced. The momentum exchange between high and low velocities causes high hydraulic losses. In some cases this can lead to rotating stall. At part load, due to the high angle of attack at the blade leading edge, the blockage in a certain channel causes a higher flow-rate in the next channel. This phenomenon propagates in general at a frequency different than the blade-passing frequency (BPF) or harmonics.

- As the boundary layer flow on the hub or shroud encounters the impeller leading edge the deceleration moves the flow away from the blade into the channels. A *horseshoe* vortex can be formed which leads to blockage and non-uniform flow (Guelich, 2010). This phenomenon can also facilitate cavitation.
- In zones of high velocities and low pressure, with a local drop in the pressure below the saturated vapour pressure, cavitation appears. This can lead to damage of mechanical surfaces such as impeller blades due to erosion.
- Leakage flow, i.e. recirculation from the impeller outlet to the inlet through the gap between the impeller shroud and the casing, is related to the pressure difference at the seal. This flow can lead to a higher non-uniform velocity distribution at the impeller inlet.
- Turbulence can be produced due to vortex structures and the flow structures described. Especially high turbulence production occurs in boundary layers and flow separation zones from the blade leading and trailing edges or tongue tip.
- Asymmetric mounting or small defects of the impeller with respect to the volute lead to fluctuations at the pump rotation frequency or harmonics.

At nominal flow-rate Q_N the flow exiting the impellers is supposed to be collected by the volute with a uniform circumferential pressure distribution and sent to the pump exit. The tongue tip of the volute separates the narrow region of the volute from the pump exit. At Q_N the stagnation point is situated at the centre of the tongue tip. However, at off-design conditions the flow hits the tongue tip with an oblique angle of attack. For partial flow-rates part of the flow recirculates into the volute and the stagnation point shifts towards the pump exit duct (Miner et al., 1989). This leads to a flow separation zone with high vorticity and turbulence in the narrow region of the volute. For flow-rates above Q_N the stagnation point shifts along the tongue towards the narrow region of the volute. The consequence is a flow separation zone with a wake extending into the pump exit duct.

1.4 Measurement techniques

Different measurement techniques exist for obtaining the velocities in a centrifugal pump. Optical measurement techniques have the advantage of being non-intrusive, this means that the flow is not disturbed by a probe and it is, under certain conditions, even possible to measure velocities inside the impeller. Hot-wire or Acoustic Doppler Velocimetry measurement techniques have the disadvantage of needing to introduce a probe into the pump which can disturb

the flow field. Optical techniques, which use a laser, can be divided into point measurement techniques such as laser Doppler velocimetry (LDV) and whole field measurement techniques like PIV and particle tracking velocimetry (PTV). LDV may give a high temporal resolution at a specific point but to obtain a spatial resolution the LDV system needs to be moved. This means it does not give an instantaneous velocity field as PIV or PTV do. PTV has an unstructured grid as the trajectories of individual particles are tracked.
Classic PIV consists of a laser and a camera to obtain the two in-plane velocity components in a measurement plane (2D2C PIV). A detailed description of PIV is given in section 4.1.1. PIV can be further classified into time-resolved PIV, employing a high-speed camera and a high-speed laser, stereo PIV (2D3C PIV), to obtain also the out-of-plane velocity component by using two cameras, and tomographic PIV measuring all three velocity components in a volume with several cameras.

1.5 Pressure fluctuations

The described unsteady fluid-dynamic phenomena lead to pressure fluctuations and fluid-borne sound. Due to rotor-stator interaction (RSI) pressure fluctuations occur mainly at BPF and harmonics. Acoustic waves are radiated from the pump towards the suction and discharge pipe of the hydraulic circuit.

The assumption of incompressibility for water, i.e. constant density, is only valid in terms of hydrodynamic considerations. In terms of hydroacoustics, e.g. radiation and propagation of acoustic waves, the density cannot be considered constant.
The water as compressible fluid experiences sudden variations in local pressure and velocity which results in a radiated pressure wave travelling at the speed of sound. Two zones can be distinguished. The first zone is the so-called *hydrodynamic near field* (Guelich and Bolleter, 1992), which is a relatively small zone around the perturbation zone. In the second zone, the *far field*, only a small portion of the initial energy is received in form of pressure pulsations. Objects, like the diffuser vanes or volute tongue, act in combination with the flow structures as secondary noise sources. These are stronger noise sources than the primary noise sources from the flow structures directly. The frequency spectrum of the pressure has pronounced peaks at the BPF and harmonics, with the first and second harmonic being especially strong.

The distribution of the pressure fluctuation amplitude along the volute of a centrifugal pump at BPF is shown in Fig. 1.5 (Parrondo et al., 2002). Highest pressure fluctuations take place in the narrow region of the volute, close to the tongue edge. Furthermore, this figure shows that when operating close to the nominal flow-rate, the amplitude of the pressure fluctuations is small and rather uniform along the volute. However, for part and overload the pressure fluctu-

ation amplitude increases, particularly in the narrow zone of the volute. This indicates a progressive reinforcement of the blade–tongue interaction when deviating from nominal operating conditions. For each flow-rate this figure shows a succession of minima and maxima. They are the result of the positive or the negative combination of the hydraulic fluctuations in the volute that follow the rotation of the impeller blades with the acoustic emission from the tongue region. Hereby the effect of the hydraulic fluctuations only has a localized influence. The acoustic waves propagate at the speed of sound and can affect significantly a large part of the pump. The speed of sound is about two orders of magnitude higher than the impeller velocity. The seven impeller blades for this pump lead to seven minima and maxima. Along the volute, both pressure fluctuations combine with a relative phase that is dependent on the angular position φ, so that the resulting fluctuations can be either reinforced or reduced.

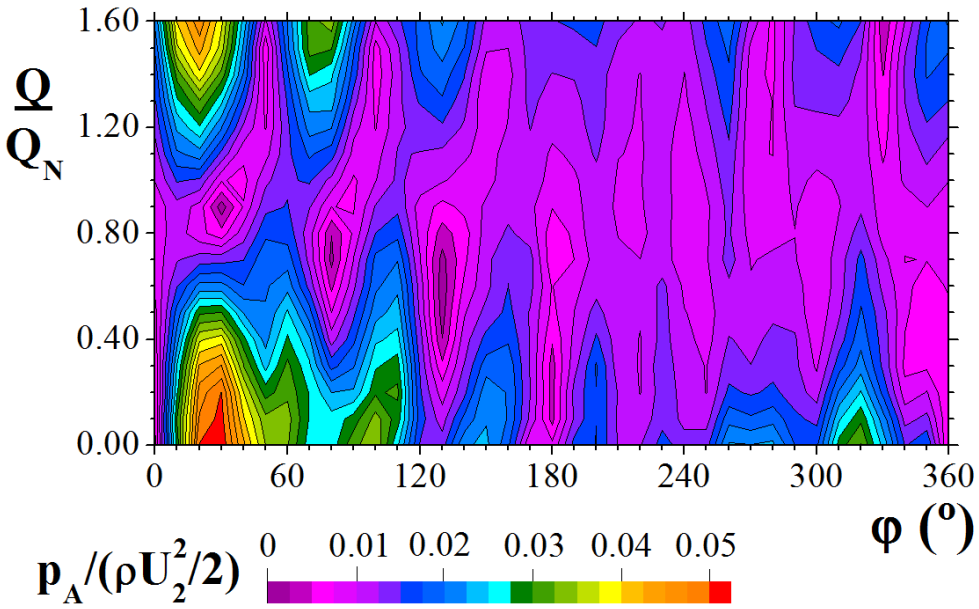

Figure 1.5: Pressure fluctuation amplitude at f_{BP} as a function of the flow-rate (Parrondo et al., 2002)

The noise generation can be described by ideal sound sources. A monopole (Howe, 2003) radiates equally in all directions with the same amplitude and phase, i.e. it behaves like a pulsating sphere. In a monopole the acoustic power ($\sim$ to square of pressure pulsation) increases with the fourth power of the speed. It is used to describe the noise generation by volume displacement of the fluid due to the rotating impeller blades (Neise, 1992). In pumps these noise sources are normally weak due to the low Mach number.
For unsteady forces on solid surfaces, due to the unsteady flow and its pressure fluctuations, a dipole is used (Curle, 1955). It radiates like two monopoles lo-

cated very close to each other, which radiate with the same amplitude, but with a phase shift of 180°. This results in zero amplitude perpendicular to the two monopoles and maximum amplitude in the direction of the two monopoles. A dipole describes the noise generation at BPF and harmonics due to RSI, which is normally the strongest noise source in centrifugal pumps. Another noise generation source is the interaction of vortices with the volute tongue and the blade trailing edges (Howe, 1991), due to *chopping* of the vortices. However, the associated frequency is higher than BPF or harmonics. In a dipole the acoustic power increases with the sixth power of the speed and in a quadrupole with the eighth power. Quadrupoles are used to describe noise generation in turbulent flows due to shear stresses, but their magnitude is small in pumps with low Mach number (Neise, 1992).
Large-scale turbulence and vortices, especially at part load, cause broad band frequency pressure pulsations (Guelich and Bolleter, 1992). Higher Reynolds numbers lead to thinner boundary layers which can reduce pressure fluctuations when no separation takes place.

The radiated acoustic waves are reflected in the hydraulic circuit, e.g. at valves, bifurcations or at a water tank. This wave reflection, which can lead to standing waves and resonance, can influence the acoustic waves. This means that in a hydraulic system the amplitude and phase of the pressure fluctuations can be influenced by the acoustic characteristics of the hydraulic circuit. Furthermore, other elements like valves or orifices in the system can also act as noise sources. Acoustic resonance can result in excessive vibration and even in failure of mechanical elements due to fatigue.

The wave equation of linear acoustics, with density being independent of the position and without noise sources, is (Rossing, 2007):

$$\nabla^2 p = \frac{1}{c^2}\frac{\partial^2 p}{\partial t^2}, \tag{1.10}$$

with c being the speed of sound.
If the pipe diameter is very small compared to the wavelength λ, plane (1D) waves can be assumed propagating in x-direction (Davies and Holland, 2004):

$$\frac{\partial^2 p}{\partial x^2} = \frac{1}{c^2}\frac{\partial^2 p}{\partial t^2}. \tag{1.11}$$

This differential equation is solved after d'Alembert by the type of $p(x,t) = p(x \pm ct)$.
The radiated pressure fluctuations from the pump travel along the pipes as plane pressure waves P^+ with amplitude p^+, frequency f, wavenumber k^+ and phase φ^+:

$$P^+(x,t) = p^+ \mathrm{e}^{\mathrm{i}(2\pi f t - k^+ x + \varphi^+)}. \tag{1.12}$$

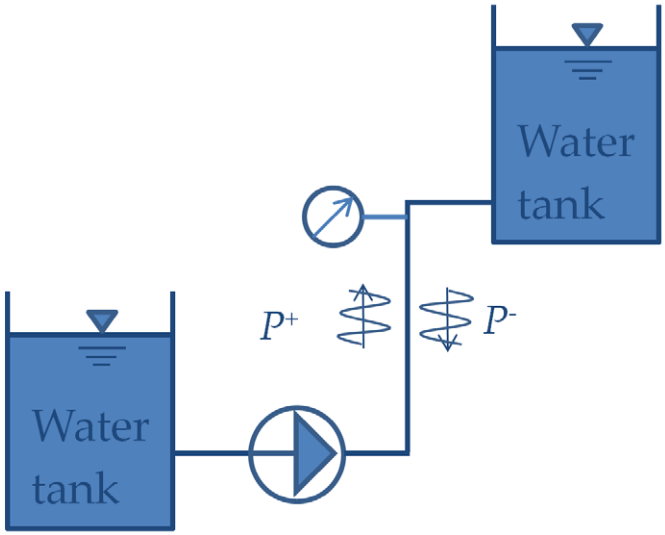

Figure 1.6: Representation of radiated and reflected pressure waves in hydraulic system

Reflections in the circuit lead to returning waves P^- (see Fig. 1.6). Therefore, the pressure P at a certain point x in the pipes is the sum of the radiated pressure wave P^+ and the reflected pressure wave P^-, that travel in opposite directions:

$$P(x,t) = P^+ + P^- = p^+ \mathrm{e}^{\mathrm{i}(2\pi f t - k^+ x + \varphi^+)} + p^- \mathrm{e}^{\mathrm{i}(2\pi f t + k^- x + \varphi^-)}, \tag{1.13}$$

with k^- being the wavenumber of the reflected wave.
For small acoustic pressure variations of the radiated and reflected waves the wave equation can be linearised, so that the relationship to the acoustic particle velocity U_p is

$$P^+ = \rho c U_\mathrm{p}^+, \tag{1.14}$$

$$P^- = -\rho c U_\mathrm{p}^-. \tag{1.15}$$

The specific acoustic impedance z_u is the ratio of the acoustic pressure fluctuations to the acoustic particle velocity

$$z_u = \frac{P}{U_\mathrm{p}}. \tag{1.16}$$

For a plane wave propagation and small acoustic pressure variations the specific acoustic impedance is (Lucas et al., 1997):

$$z = \rho c. \tag{1.17}$$

In pipes with varying cross-sections A the acoustic particle velocity U_p changes, but the acoustic mass flow $\rho A U_\mathrm{p}$ is constant. Therefore, it is convenient to work with the impedance based on acoustic mass flow. Using the relationship from

Eq. (1.17) the acoustic impedance based on acoustic mass flow for a plane wave is:

$$\zeta = \frac{P}{\rho A U_\mathrm{p}} = \frac{c}{A}. \tag{1.18}$$

The speed of sound c in a fluid with no effects of the surrounding walls, i.e. for a fluid in an infinitely large tank, equals

$$c = \sqrt{\frac{K}{\rho}}, \tag{1.19}$$

with K being the bulk modulus of the fluid.
However, the speed of sound in pipes c_w is influenced by the surrounding wall material and geometry, leading to

$$c_\mathrm{w} = \frac{1}{\sqrt{\rho_\mathrm{w}\left(\frac{1}{K} + \frac{d}{tE}\right)}}, \tag{1.20}$$

with d being the pipe diameter, t the pipe wall thickness and E the Young's modulus.

1.6 Literature review

In this section a review of studies of centrifugal pumps with an emphasis on experimental studies with rotor-stator interaction is given.

1.6.1 Studies of unsteady flow

Miner et al. (1989) applied laser velocimeter measurements in the impeller and volute of a centrifugal pump for flow-rates from 40 to 112 % Q_N. At Q_N for $r/r_\mathrm{tip} \geq 1.2$ they observed no visible influence on the velocities due to the impeller blade position. The flow behaved like a free vortex flow, with $u_\theta r$ being constant. For 40 % Q_N a recirculating flow was found in the impeller with backflow near the blade suction side and outflow near the pressure side.
Ubaldi et al. (1998) used LDV to measure velocities in the impeller and in the vaneless diffuser at design flow-rate. Phase-averaging allowed them to distinguish between periodic and turbulent fluctuations.

PIV measurements in centrifugal pumps were the subject of study of various authors.
Paone et al. (1989) were one of the first authors to perform PIV measurements in a centrifugal pump with a vaneless diffuser. They compared the results with LDV measurements and calculated the slip factor.
The most relevant informations on the unsteady flow field due to rotor-stator interaction in centrifugal pumps with vaneless volute were obtained in the 1990's

by J. Katz and his team. They (Dong et al., 1992a) carried out a detailed PIV investigation in the volute of a 2D-shaped centrifugal pump to study the phase-averaged unsteady flow, including blade-tongue interaction effects. Dong et al. (1992b) described and presented results of PIV measurements for flow-rates below ($\approx 50\,\%\,Q_N$), near and above ($\approx 135\,\%\,Q_N$) the design flow-rate. They used autocorrelation to obtain the velocity fields. Below design conditions backflow into the impeller near the tongue was observed. For flow-rate above design conditions they observed vortex trains exiting the impeller, attributed to u_θ gradients and the associated high shear stresses. Chu et al. (1995a,b) explained how to compute the pressure field from PIV data and presented the pressure field in the tongue region of the volute for a flow-rate of 135 % of the design flow-rate. Dong et al. (1997) extended the PIV tests to different tongue tip geometries and impeller-tongue gaps. They deduced that for a narrow impeller-volute gap the primary noise source is the impingement of the wakes shed by the blades on the tongue tip.

Akin and Rockwell (1994) used PIV to obtain the instantaneous pressure source in the wake of an impeller blade ($\frac{\partial u}{\partial x}\frac{\partial v}{\partial y} - \frac{\partial u}{\partial y}\frac{\partial v}{\partial x}$). However, this expression is only valid away from solid boundaries.

Sinha and Katz (2000) performed PIV measurements at a centrifugal pump with a vaned diffuser close to design conditions. 100 instantaneous velocity fields were taken to obtain converged phase-averaged velocity fields at five different impeller blade positions. Isotropic turbulence was assumed to calculate an approximation of the turbulent kinetic energy. Sinha et al. (2000) represented passage averaged velocities in the stator reference frame and also in the rotor reference frame. Deterministic stresses were obtained by the difference between the phase-averaged velocity fields and the passage averaged velocity field.

Sinha et al. (2001) combined PIV with pressure fluctuation measurements to investigate rotating stall below design flow-rate. They used low-pass filtered pressure signals to synchronize the pressure signals with the PIV measurements.

Wuibaut et al. (2002) performed PIV measurements at the SHF impeller with a vaneless diffuser in air. Close to design conditions the flow in the impeller channels was steady in the relative frame. The jet-wake pattern was described. At low partial flow-rates large instabilities were found.

Stickland et al. (2002) used a high-speed camera with a rotating mirror to obtain directly the relative velocity field inside an impeller of a centrifugal pump at two different field of views (FOVs). The relative velocity fields were compared to CFD simulations and a good agreement was found. Stickland et al. (2003) used the same system to present the relative velocity field inside the impeller near the tongue with the blade lining up with the tongue tip. A large vortex in the centre of the blade passage was observed, counterrotating to the rotation direction of the impeller.

Friedrichs and Kosyna (2003) investigated the unsteady flow by PIV measurements. A vaneless diffuser instead of a volute was used to have a uniform

circumferential pressure distribution at the impeller outlet. Different impellers were tested under rotating cavitation.

Pedersen et al. (2003) did PIV and LDV measurements at a shrouded centrifugal pump impeller with six blades, which discharged into a cylindrical tank. They presented instantaneous and ensemble averaged PIV velocity fields in the centerplane of the impeller using fluorescent seeding particles. Flow-rates at Q_N and 25 % Q_N were investigated. For Q_N no significant separation was observed, but near the pressure blade side a low velocity zone was found. Closer to the impeller exit the Coriolis force had more influence so that the flow moved towards the blade pressure side. For 25 % Q_N neighbouring blade passages showed different flow behaviour in contrast to Q_N. It is called a *two-channel* flow pattern with alternately stalled and unstalled passages. For one passage a recirculation zone near the blade leading edge was observed and a strong vortex was found at the outlet in the blade pressure zone.

Bachert et al. (2005) used PIV combined with LIF (Laser Induced Fluorescence) to measure the velocity fields inside and outside cavitation zones in the volute tongue region. Time-averaged velocity fields using 50 double images were presented. For 80 % Q_N and Q_N no flow separation from the tongue tip was observed. However, for 117 % Q_N flow separation and cavitation occurred at the tongue tip on the discharge nozzle side.

Dupont et al. (2005) used PIV measurements in a vaned diffuser pump to investigate the rotor-stator interaction. Phase-averaged velocities and associated fluctuations at different flow-rates showed the unsteady flow field at the impeller outlet and the interaction with the diffuser vane.

Krause et al. (2005, 2006) performed time-resolved PIV at partial flow-rate and at Q_N to investigate rotating stall. Stall cells started to appear at a flow-rate of 50 % Q_N and rotating stall was observed to begin at 41 % Q_N.

Wuibaut et al. (2006) compared PIV and LDV results of the flow in the SHF impeller. They presented phase-averaged velocities and velocity fluctuations at Q_N. Differences of the velocity fluctuations between the two measurement techniques were contributed mainly to the vaneless diffuser present for the PIV measurements in air and to the vaned diffuser for the LDV measurements in water. With both techniques they were able to detect the jet-wake pattern, with the LDV technique capturing a higher wake growth.

Feng et al. (2009a) compared LDV and PIV measurements with CFD simulations in a radial diffuser pump for design flow. They described the jet-wake flow structure near the impeller outlet. Feng et al. (2009b) used PIV measurements to validate CFD simulations for a radial diffuser pump below design conditions. They presented phase-averaged velocity fields and turbulence intensity fields. For 75 % Q_N no flow separation occurred, whereas for 50 % Q_N separation took place at the blade impeller suction side.

Kearney et al. (2009) did PIV measurements at two miniature-scale centrifugal pumps to investigate scaling effects on performance.

Wu et al. (2011b) investigated the global flow pattern in a pump with an unshrouded impeller by PIV. Fluorescent particles and another facility with index-matched fluid were used to obtain velocity fields and Reynolds stresses.
Cavazzini et al. (2011) compared numerical calculations with PIV measurements of the unsteady flow in a centrifugal pump with vaned diffuser. The results presented at three impeller positions and radial locations coincided reasonably well, especially for the unsteady numerical calculations.
Dazin et al. (2011) measured rotating instabilities at an impeller with vaneless diffuser by high-speed stereoscopic PIV. They described the *unforced unsteadiness* (Oro et al., 2009), which are coherent flow structures that are non-deterministic, i.e. not periodic with the BPF or harmonics. They obtained the velocity field at three heights (hub to shroud direction) at design flow-rate and partial flow-rates. Fourier analysis was used to characterize the developing instabilities and a rotating three cell structure was found.

1.6.2 Studies of pressure fluctuations

Schwartz and Nelson (1984) described the hydraulic fluctuations generated at BPF due to the interaction of the impeller blade with the tongue tip. They focused on acoustic resonance phenomena occurring in multistage pumps when the BPF or a harmonic coincides with an acoustic resonance frequency. An analytical model was used to predict acoustic resonance cases. The analytical model agreed well with pressure measurement data.
Rotor-stator interaction was investigated in diffuser pumps by Arndt et al. (1988). Pressure measurements showed that fluctuations occur mainly at BPF. The pressure decreased significantly for increasing radial gap between impeller and diffuser.
Guelich and Bolleter (1992) described the pressure fluctuations created in centrifugal pumps by the wake behind the blade trailing edge at certain frequencies. The negative effects of excessive pressure fluctuations were treated. Fracture of mechanical parts like diffuser or impeller vanes due to fatigue can occur, whereas the dynamic loading on the diffuser vanes is high due to the impingement of the wakes from the impeller on the diffuser vanes. The gap between impeller and diffuser vanes or volute tongue is the most important factor to reduce pressure fluctuations at the BPF. Unsteady stagnation pressure, pressure fluctuations and unsteady stresses decrease on average with the power of -0.77 of this gap. They point out the strong dependence of the location of the pressure transducers on the pressure fluctuations. To reduce uncertainties due to standing waves and resonance the pump speed should be varied and pressure fluctuations should be measured at different locations along the pipe and should be averaged afterwards.
Bolleter (1993) modelled the pump within the hydraulic circuit using transfer matrices. The pump was split into a system element matrix and a matrix which described the pressure fluctuations generated by the pump. The radiated and

reflected waves superpose to standing waves, so that the amplitude of pressure fluctuations is a function of the location along the pipe. He pointed out that the difficulties are the modelling of the damping, excitation source and appropriate boundary conditions.

Kaupert and Staubli (1999) described the unsteady pressure field in the impeller of a centrifugal pump with double spiral volute. They placed pressure sensors on the volute casing and on the impeller. The unsteady pressure field was investigated at different flow-rates (from 40 % Q_N to 120 % Q_N). The pressure fluctuation amplitude increased with decreasing flow-rate at part-load conditions and achieved up to 35 % of the pump head at 40 % Q_N.

Morgenroth and Weaver (1998) investigated the pressure fluctuations produced by a centrifugal volute pump. They distinguished between acoustic and hydraulic pressure fluctuations at BPF. The amplification of the pressure fluctuations due to acoustic resonance in a connected piping system was described. Therefore, pressure fluctuations at different pump speeds and flow-rates were measured. They deduced that the pump may act as an acoustic pressure or velocity source. Resonance occurred when a node in the standing pressure wave was situated at the pump location. Flow visualization by means of a tracer injected at the tongue tip allowed them to notice that flow separation at the tongue tip is directly related to noise generation. Rounding the tongue tip reduced the noise generation, apparently as it permits the movement of the stagnation point, which reduced the generated vorticity.

Rzentkowski and Zbroja (2000) described the acoustic characteristics of a double volute centrifugal pump at BPF. Resonance effects were investigated and the pressure signals were decomposed into the part associated with the pump action and the other part due to the circuit acoustics. They used a 2-port model to account for the coupling of the centrifugal pump with the hydraulic circuit. They concluded that the pressure wave radiated towards the discharge is a good measure to describe the pump pulsation level.

Timouchev and Tourret (2002) simulated the flow and interaction in a centrifugal pump numerically and focused on pressure fluctuations at BPF and harmonics. The pressure pulsation field can be divided into a *vortex mode* which decays rapidly and an *acoustic mode* with acoustic waves radiated into the hydraulic circuit (acoustic-vortex method).

Talha et al. (2002) compared the pressure fluctuations in two centrifugal turbomachines, a fan operated with air and a pump operated with water. They described the effect of different speeds of sound and different densities. As the speed of sound in water is several times higher than in air, the local signal and the signals from other sources are received nearly simultaneously. They concluded that the noise generation in the fan can be described by a dipole type, as the main noise source is the passing of the blade tips in front of the volute tongue. For the pump two noise sources were found. First, a dipole located in the tongue region is associated with the passing of the blade tip in front of the tongue. Second, a monopole type is a mass flow-rate oscillation due to the

blade-to-blade obstruction of the channels by the tongue. They found that for the pump employed the monopole is the dominant noise source.
Choi et al. (2003) performed experiments in a centrifugal water pump operating with air. The unsteady flow field and the noise generation in an impeller, without volute or diffuser, was investigated.
An important parameter in pump design is the radial gap between blade tip and volute tongue. Srivastav et al. (2003) investigated the influence of the radial gap between impeller and diffuser. Noise and vibration decreased for increasing gap, with the efficiency also decreasing. They observed that the vibration spectra have the dominant peak either at the impeller or diffuser vane passing frequency, depending on the radial gap.
Langthjem and Olhoff (2004a) simulated the flow in a 2D shaped centrifugal pump to calculate the flow-induced noise. For the inlet a point source was used. Vortex elements covered the impeller blades, whereas the casing was covered with source panels. To fulfil Kelvin's theorem vortices were shed from the blade trailing edges and convected with the flow. The unsteady Bernoulli equation was used to obtain the unsteady fluid forces from the velocity field.
The same authors (Langthjem and Olhoff, 2004b) described the hydroacoustic part of the centrifugal pump. The acoustic pressure field was determined, with the main noise source being the unsteady impeller blade surface forces. The dominant acoustic sources could be described as moving dipoles.
Berten et al. (2007) predicted the hydroacoustic pressure fluctuations in a multistage centrifugal pump. Therefore, CFD was used to obtain the pressure fluctuations due to rotor-stator interaction. Afterwards, the acoustic eigen-frequencies and standing waves were predicted by hydroacoustic simulations.
Pavesi et al. (2008) performed pressure fluctuation measurements at the inlet duct and impeller discharge of a centrifugal pump with a vaneless diffuser. They investigated the flow field instabilities and detected a low frequency pulsating phenomenon, associated with the water level fluctuations in the tank. A rotating structure at the impeller outlet, not associated with BPF, was found which generated non-linear components in the frequency spectra in interaction with fluctuations at BPF and of the system.
Barrio et al. (2008) conducted experimental measurements and numerical simulations (CFD) with different impeller diameters to study the effect of the radial gap between impeller and volute on fluid-dynamic fluctuations and forces.
Braun (2009) investigated flow phenomena in centrifugal pumps operating at part-load using numerical methods. Transient pressure and LDV measurements were taken to validate the three-dimensional flow field.
Berten (2010) studied hydrodynamic phenomena in a high speed pump with vaned diffuser. Pressure measurements revealed rotating pressure waves due to rotor-stator interaction.
Nicolet et al. (2010) applied a 1D hydroacoustical model to a Francis pump turbine. The pressure waves due to rotor-stator interaction were investigated with special emphasis on resonance cases.

Concluding the literature review, a deficit in understanding the flow structures in centrifugal pumps with vaneless volute was noticed. It was seen that the flow field in the tongue region, especially the behaviour of the flow structures in the narrow gap between impeller and volute tongue, the associated noise generation and the influence of the acoustic characteristics of the hydraulic circuit on the pressure fluctuations is not fully understood.

2 Outline

2.1 Objectives and methodologies

This thesis focuses on the fluctuations and flow structures in centrifugal pumps with vaneless volute due to the fluid-dynamic interaction between the flow structures originated by the impeller blades and the volute (rotor-stator interaction). These fluctuations generate pressure pulsations which are radiated in form of acoustic waves towards the pipes of the hydraulic circuit. The two main objectives established for this thesis are:

- The first objective is to experimentally achieve a detailed description and analysis of the fluid-dynamic fluctuations and the flow structures originated in the impeller channels and their interaction with the volute (rotor-stator interaction) in centrifugal pumps with vaneless volute. For this purpose, laboratory tests are planned to obtain the velocity fields and other fluid-dynamic variables in the pump by the use of PIV. As a first step a transparent pump and a special hydraulic circuit have to be designed and built. The study is focused on the flow structures associated with the BPF and harmonics and their interaction with the volute tongue at different flow-rates. In order to obtain an overview of the flow field in the impeller and volute, but also to resolve the flow fluctuations in the small impeller-tongue gap region with a high spatial resolution, different magnification factors are to be considered. The use of stereo PIV completes this study in order to obtain all three velocity components.

- The second objective is the characterization and quantification of the pressure fluctuations in centrifugal pumps due to rotor-stator interaction. In particular, the study is to be conducted at the laboratory pump used for the PIV tests and at an industrial pump facility. Of special interest for this study is the influence of the acoustic coupling between pump and hydraulic circuit. The aim is to explore the possible reduction of the generation of the pressure fluctuations in the pumps by changing the acoustic impedance of the circuit. For the experimental study the use of fast-response pressure transducers is planned. It is proposed to model the hydraulic system based on 2-port acoustic elements, each associated with a transfer matrix. The results of the transfer matrix analysis (TMA) are to be compared with the experimental results. Two possibilities are considered to change the acoustic impedance of the system at the pump excitation frequencies (BPF). The first possibility is to change the pump rotational speed.

The second possibility is to change the geometry of the hydraulic circuit by operating valves which lead to dead-end branches, with no mean flow through them.

2.2 Structure of this thesis

The present thesis is divided into five parts with a total of 8 chapters:

- In chapter 1 *Introduction and fundamentals* a short overview of centrifugal pumps and a literature review of the most important research studies related to this thesis are given.
- In chapter 2 *Outline* the objectives of this thesis and the applied methodologies are described.
- In chapter 3 *Experimental facilities* the industrial pump and the transparent pump with their hydraulic circuits, investigated in this thesis, are presented.
- In chapter 4 *Instrumentation and methodology* the employed PIV system is described. The working principle and the parameters chosen to obtain the velocity fields are given. Furthermore, the procedure of the unsteady pressure measurements to obtain the acoustic impedance is described. Afterwards, the acoustic models to obtain theoretically the acoustic characteristics, such as the impedance at the beginning of the discharge pipe, are explained.
- The results of the PIV measurements are detailed in chapter 5 *Flow field*. The relative and absolute velocities and other flow variables, such as vorticity and turbulent kinetic energy (TKE) together with its production, are shown for different blade positions. Results are presented below (40 % Q_N), at and above nominal flow-rate (150 % Q_N). Two different FOVs (one low and one high magnification) reveal the flow structures in the impeller, the volute and the rotor-stator interaction in the tongue region. Stereo PIV with another FOV is used to quantify the out-of-plane velocity component.
- In chapter 6 *Acoustic coupling with hydraulic circuit* the results of the influence of the acoustic coupling of the hydraulic circuits with the pumps are presented. The pressure fluctuations at the pumps are quantified and the influence of the acoustic impedance on the radiated pressure waves is determined experimentally and theoretically.
- In chapter 7 *Conclusions* the research work is summarized and the main conclusions are reported. Additionally, some recommendations for future investigations are given. The conclusions in Spanish are in chapter 8.

Part II

Experimental Setup and Methodology

3 Experimental facilities

3.1 Industrial pump facility

An industrial centrifugal pump available in the laboratory of the Chair of Fluid Mechanics of the Department of Energy at the University of Oviedo was used to investigate the influence of the acoustic impedance on pressure fluctuations. This pump has been studied in detail among others by Parrondo et al. (2002) experimentally to describe pressure pulsations in the volute and by Barrio et al. (2010) using numerical simulations to investigate the unsteady flow in the tongue region at different operating points.

3.1.1 Test pump

The investigated pump has an impeller with a diameter of 210 mm and seven double-curved blades, single suction and a vaneless volute. Further characteristics of this pump are described in Table 3.1. The impeller and the volute are shown in Fig. 3.1.

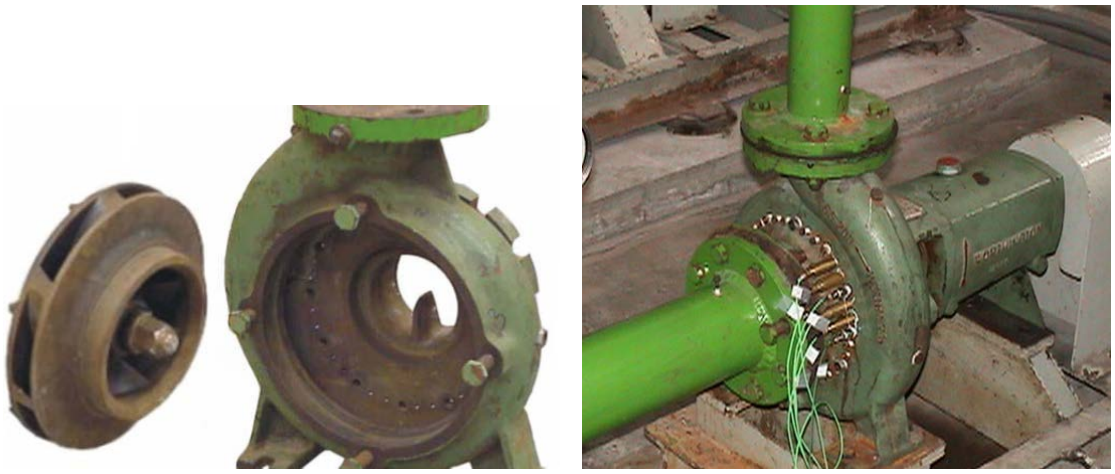

(a) Pump dismounted with volute casing and impeller (Barrio et al., 2010)

(b) Pressure transducers mounted at volute casing (Barrio et al., 2008)

Figure 3.1: Pictures of industrial pump

Table 3.1: Industrial pump characteristics

Impeller diameter at inlet [mm]	57
Impeller diameter at exit [mm]	210
Impeller outlet width [mm]	16
Number of blades	7
Inclination angle at outlet β_2 [°]	29
Cross-section at tongue A_{tip} [cm^2]	11.3
Gap referred to impeller radius [%]	11.4
Impeller-Volute-Gap (minimum) [mm]	24
Non-dimensional specific speed	0.46

3.1.2 Hydraulic circuit

The pump is located in a hydraulic circuit, which is depicted in Fig. 3.2. It has several auxiliary pipe deviations and butterfly valves to regulate and shut-off the flow. It is equipped with an electromagnetic flow meter installed in the horizontal part of the discharge pipe.

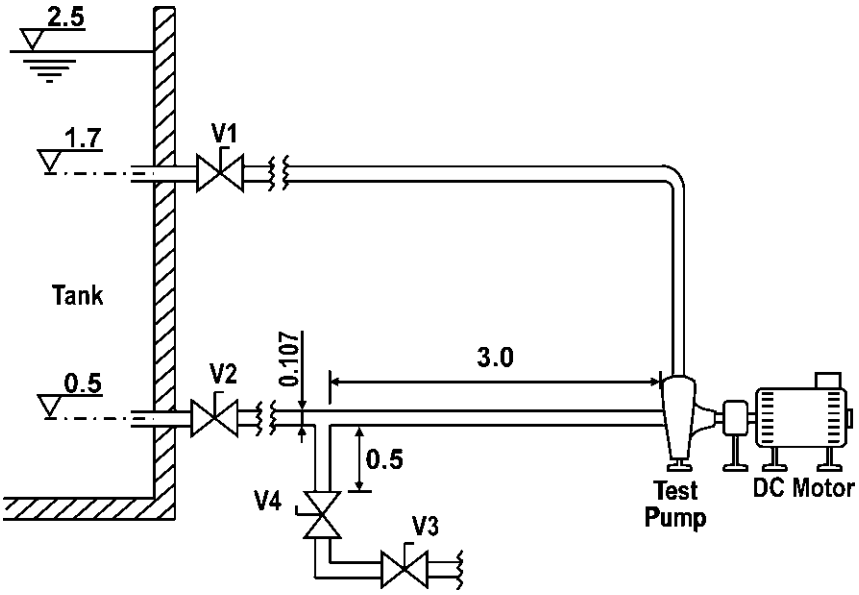

Figure 3.2: Hydraulic circuit of the industrial pump showing some details of the suction piping (units in m, not drawn to scale, adapted from Parrondo et al. (2002))

3.1.3 Characteristic curves

The data to determine the characteristic curves were already available at the Chair of Fluid Mechanics. They were obtained at a pump rotational speed of 1620 rpm. The normalized head Ψ and the efficiency η of the pump are presented in Fig. 3.3 as a function of the flow coefficient Φ. Maximum relative

uncertainty was ±1.5 % for the head and ±5.0 % for the efficiency. Uncertainty is ±2.5 % for flow-rates higher than 0.0085 m^3/s ($\Phi = 0.0054$), and less than ±4 % for lower flow-rates. Maximum efficiency occurs at a flow-rate of 55 m^3/h and a head of 16.8 m.

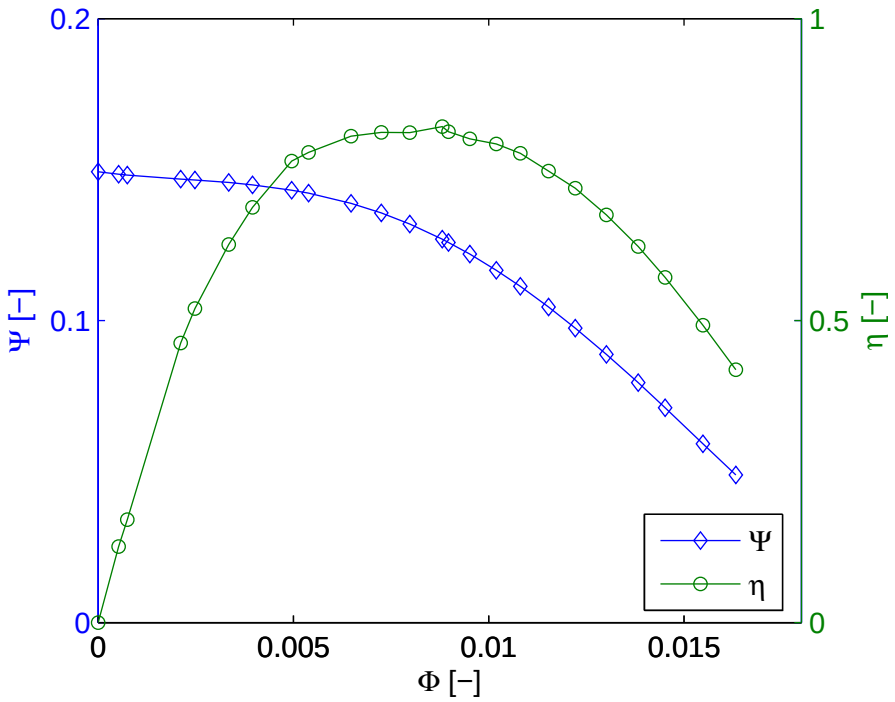

Figure 3.3: Characteristic pump curves of industrial pump: Head coefficient Ψ and efficiency η as a function of the flow coefficient Φ (unpublished data from Chair of Fluid Mechanics of University of Oviedo)

3.2 Transparent pump facility

The transparent pump used to study the internal flow structures in the impeller and volute, especially due to rotor-stator interaction, is described in this section. To obtain the velocity field and other fluid-mechanic variables derived thereof in the tongue region the PIV technique is used. As optical access from two sides is needed a pump with transparent impeller and volute was designed and built.

3.2.1 Test pump

A conventional centrifugal pump from Price Pump Co. (Model HP75-BN-600-06111-200-36-3T6) with a three-phase motor and a power of 1.5 kW was used, replacing the original volute and impeller by transparent ones. It has single suction and a vaneless volute. A front view of the transparent impeller is shown in Fig. 3.4 and a side view is given in Fig. 3.5.

Figure 3.4: Front view of impeller

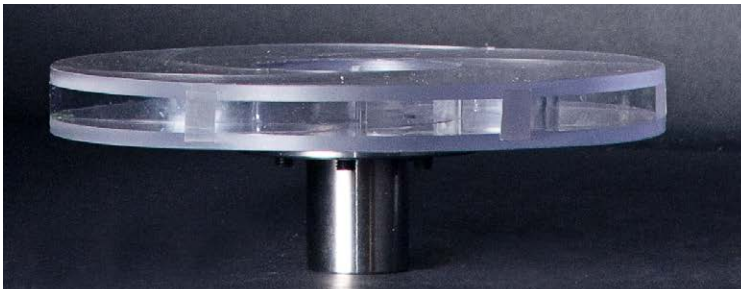

Figure 3.5: Side view of impeller

The blades and disks for hub and shroud were manufactured from polycarbonate (PC) plates with a nominal thickness of 4 mm. The impeller consists of six backward-curved blades with a constant curvature radius of 59 mm in the centreline. Each blade was heated to bend it into its desired shape. The blade width is 12 mm and a notch of 2 mm in each impeller disk allowed to put the blades in the correct place, so that the free space between disks is 8 mm. With hub and shroud disks being 4 mm thick, a space of 2 mm on each side of the front and rear shroud is left. A metal piece (Fig. A.1) with a curvature of 90° and a curvature radius of 5 mm placed at the impeller inlet facilitates the flow inlet without having a sharp edge to reduce flow separation. Another cylindrical metal piece connects the impeller to the motor axis (Fig. A.2). Impeller blades and volute have a 2D-shape, i.e. their shapes are constant in axial direction. The main pump characteristics are summarized in Table 3.2.

Table 3.2: Transparent pump characteristics

Impeller diameter at inlet [mm]	40
Impeller diameter at exit [mm]	150
Blade width [mm]	8
Number of blades	6
Inclination angle at inlet β_1 [°]	23
Inclination angle at exit β_2 [°]	28
Volute width [mm]	20
Curvature radius of tongue tip [mm]	1
Blade thickness [mm]	4
Curvature radius of blade (centreline) [mm]	59
Minimum volute radius (φ =0°) [mm]	78
Maximum volute radius (φ =345°) [mm]	120
Impeller-Volute-Gap (minimum) [mm]	3
Gap referred to impeller radius [%]	4
Non-dimensional specific speed	0.59

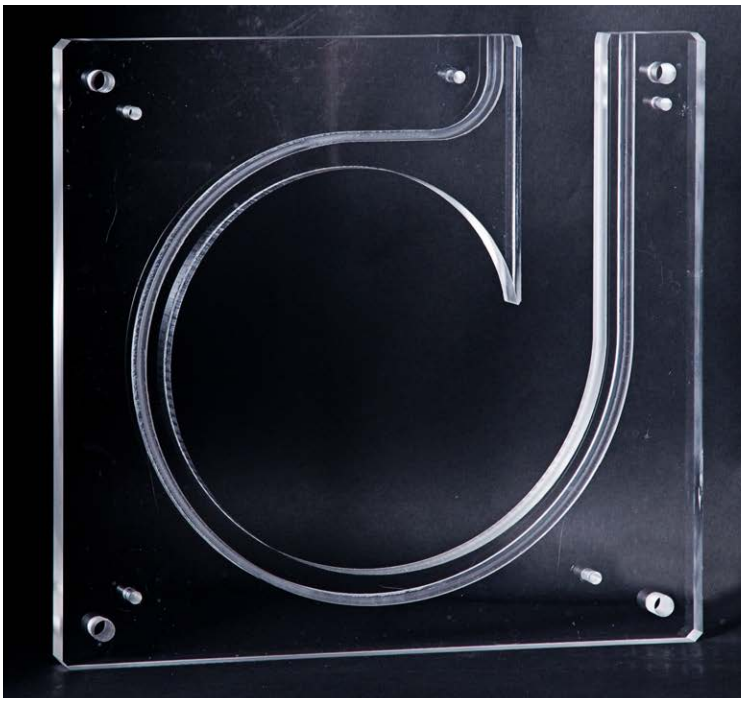

Figure 3.6: Volute shape

The casing with spiral volute was made out of three PMMA (polymethyl methacrylate) plates, also known as acrylic glass or Plexiglas®, each having a thickness of 20 mm. The geometry of the spiral is defined as:

$$r(\gamma) \;=\; r_{\mathrm{i}} + \frac{\gamma}{2\pi}(r_{\mathrm{f}} - r_{\mathrm{i}}) \;=\; 0.0755 + \frac{\gamma}{2\pi}(0.12 - 0.0755), \tag{3.1}$$

being r_{i} the radius at $r(\gamma = 0)$ and r_{f} the radius at $r(\gamma = 2\pi)$. The tongue tip is

situated at $\gamma = 15^\circ$ ($\varphi = 0^\circ$). It is rounded with a curvature radius of 1 mm. The minimum impeller-volute gap is 4 % of the impeller radius. The volute shape is shown in Fig. 3.6 and a detail of the tongue in Fig. 3.7.

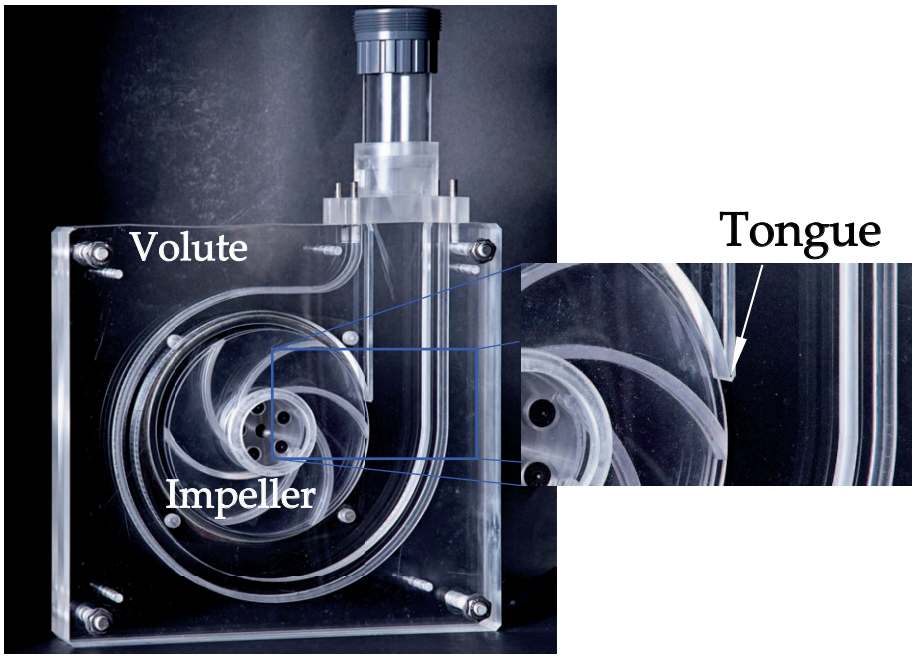

Figure 3.7: Impeller and volute with mounted diffuser and detail of the volute tongue

To make the pump impermeable a waterproof broad elastic band was fixed to the plates on top of the volute. Furthermore, a groove was made on both sides of the central part of the volute (see Fig. 3.6) and a waterproof elastic band was placed in this notch.

3.2.2 Hydraulic circuit

The pump was installed in a hydraulic circuit with regulation valves, pressure taps and an electromagnetic flow meter (see Figs. 3.8 and 3.9). A variable-frequency drive was mounted to control the pump speed. The suction and discharge pipes are transparent PC pipes with an inner diameter of 47 mm and a wall thickness of 1.5 mm. The connection from the volute outlet to the discharge pipe was established by a diffuser, with the rectangular cross-section of the volute changing gradually to the circular cross-section of the pipes. A vertical pipe was installed at the horizontal discharge pipe (see Fig. 3.8). Valve V3, situated at the beginning of this dead-end branch, allowed to be open or closed, so that the dead-end branch could be coupled to or shut-off from the hydraulic circuit. A very low water column of 8 cm remains when the valve is closed. The cavity could be partially filled with water up to a variable height, having air in the remaining upper part. At the top the dead-end branch was closed and regulation

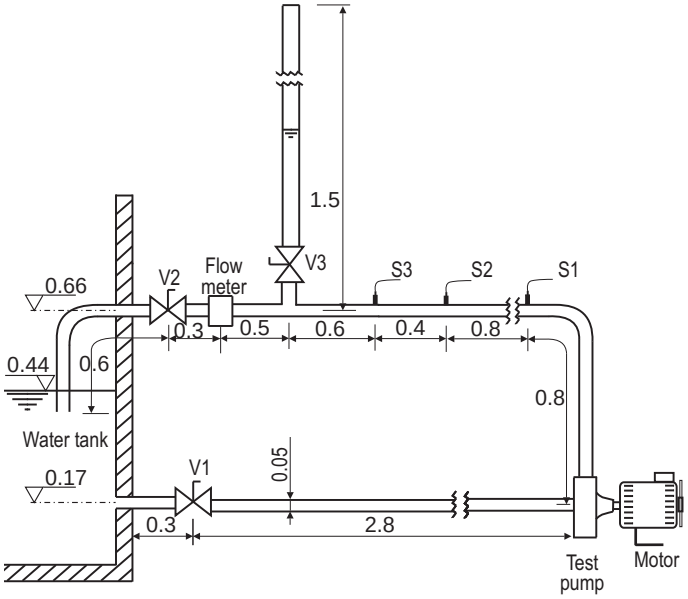

Figure 3.8: Hydraulic pump circuit (units in m, not drawn to scale)

of the desired water volume took place by opening or closing a small tap at the air section and by adjusting the pump rotation speed.

The water tank was fabricated for this hydraulic circuit (by Talleres Transglass S.L.) using PVC (polyvinyl chloride) plates with a thickness of 5 mm. A wall, 0.1 m lower than the outer walls, in the middle of the tank divides it into two volumes, so it can be used as a weir to measure the flow-rate (Fig. A.5). Furthermore, it allows to work only with one volume, needing less water to operate the pump.

Figure 3.9: Picture of pump facility

3.2.3 Characteristic curves

The characteristic curves of the pump were determined. The pump head was determined with a precision of $\pm 1\,\%$ by using a differential manometer connected to pressure taps at the inlet and outlet ports. Flow-rate was measured by means of an electromagnetic flow meter (Krohne 1300) with an uncertainty of less than $\pm 1\,\%$ for flow-rates higher than 2 m^3/h ($\Phi = 0.0024$). A diaphragm valve situated behind the flow meter was used to adjust the flow-rate precisely up to a flow-rate of $114\,\%\,Q_N$. To operate the pump at higher flow-rates the diaphragm valve was replaced with a butterfly valve with lower losses. The highest flow-rate was achieved by removing the valve behind the flow meter completely resulting in a flow-rate of $150\,\%\,Q_N$.
The power consumed by the motor and the pump was measured at the outlet of the variable-frequency drive. The results were obtained at a pump rotation speed of 660 rpm. The normalized head Ψ and the combined efficiency η of the motor-pump unit are presented in Fig. 3.10. The BEP is observed at a normalized flow-rate of $\Phi = 0.0068$ ($Q_N = 5.7$ m^3/h at 660 rpm). The pump in this hydraulic circuit can be operated in the range from $0\,\%\,Q_N$ to $150\,\%\,Q_N$. Below $30\,\%\,Q_N$ the behaviour of the pump can be unstable as the slope of the flow-head curve is positive. The non-dimensional specific speed at BEP is $2\pi f_R Q_N^{0.5}/(gH_N)^{0.75} = 0.59$.

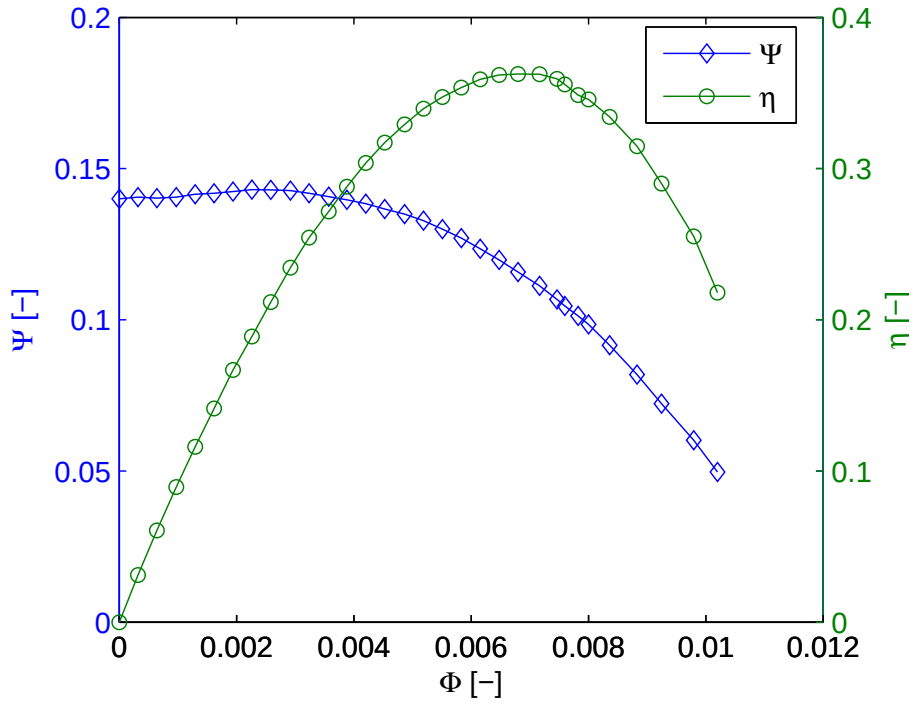

Figure 3.10: Characteristic pump curves for transparent pump: Head coefficient Ψ and efficiency η as a function of the flow coefficient Φ

4 Instrumentation and methodology

4.1 Particle image velocimetry

To obtain the velocity fields in the centrifugal pump a PIV system was used. PIV is an optical measurement technique where small seeding particles in the fluid, which follow the flow, are illuminated by laser pulses and the images of the particles are recorded by one or various cameras. Every image is divided into interrogation areas (IA), each containing several particle images, in order to obtain a structured mesh. The velocity for each IA is obtained by calculating the particle displacements between two subsequent images and dividing it by the time between the two laser pulses. Its main advantages are a high spatial resolution and that it is a non-intrusive measurement technique.

The main components of a PIV system are a laser, one or several cameras, the seeding particles and a PIV software for the control of the measurements and for the processing of the images. In this section the most important parameters and the chosen settings are explained. Among others the choice of the correct seeding particles, the camera settings and laser parameters are justified.

4.1.1 PIV setup

The PIV setup and the laser light sheet are shown in Figs. 4.1, 4.2 and 4.3. A PIV system from TSI Inc. was used to obtain the velocity fields in the zone around the tongue of the pump. Its main components are the laser, two cameras and the Insight 4G® software for controlling the PIV measurements and obtaining the velocity fields. This PIV system can be used as 2D2C PIV (two dimensions and two velocity components), employing only one camera, or as a stereo PIV system, using the two cameras. Stereo PIV is also denominated 2D3C PIV (two dimensions and three velocity components). Water was used as working fluid in the pump.

One requirement to obtain reliable in-plane velocity fields using only one camera is that the out-of-plane velocity component is small. The highest velocities occur in the plane with tangential and radial velocity components. Therefore, the measurements were taken in the centerplane of the impeller perpendicular to the pump rotation axis. The out-of-plane component corresponds to the axial velocity component.

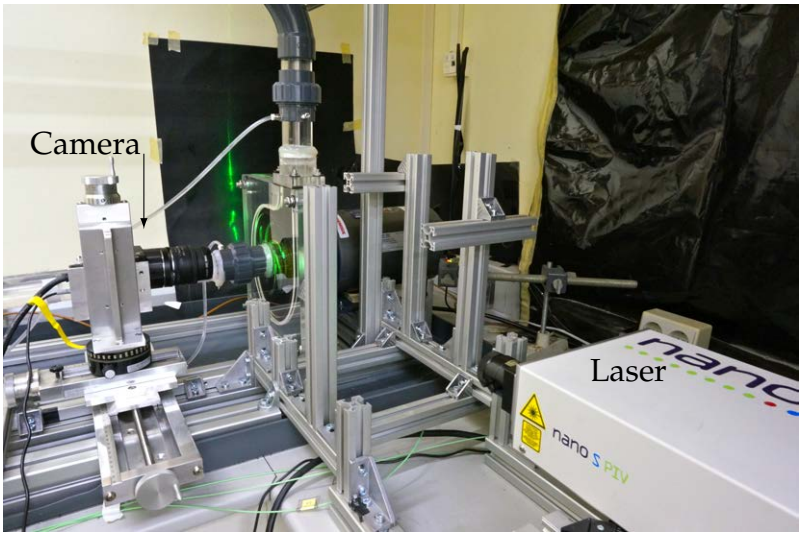

Figure 4.1: PIV setup with camera, pump and laser at low power

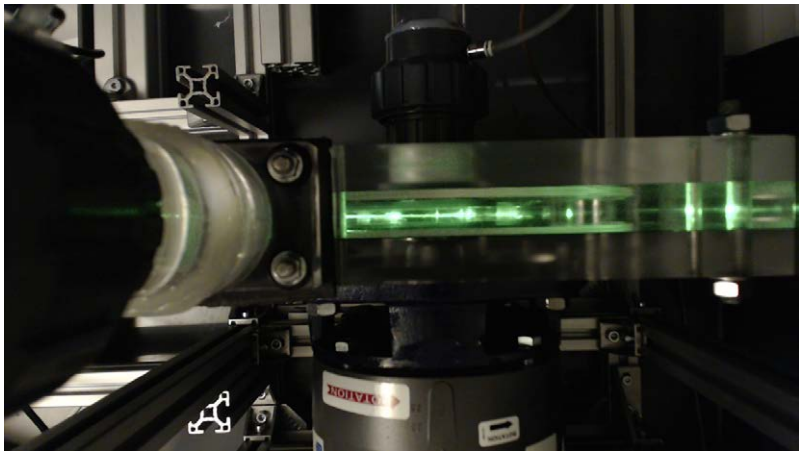

Figure 4.2: View from top with laser at low power

Seeding particles

The water needs to be seeded with many small particles that follow faithfully the flow. As not directly the fluid velocity, but the particle displacement is obtained, the particle slip needs to be negligibly small (Raffel et al., 2007). Using Stokes' drag law valid for very small Reynolds numbers Re, the velocity slip U_s can be derived as

$$\vec{U}_s = \vec{U}_p - \vec{U} = d_p^2 \cdot \frac{\rho_p - \rho_w}{18\mu}\vec{a}, \tag{4.1}$$

with μ being the dynamic viscosity, $\vec{a}$ the acceleration of the fluid and d_p the particle diameter. ρ_p is the particle density and ρ_w the water density. To have a negligible velocity slip the particle size should be as small as possible and

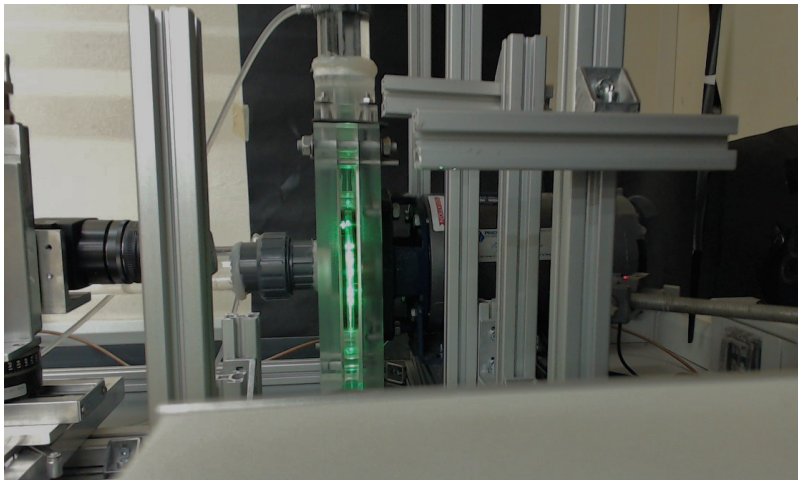

Figure 4.3: Setup seen from laser head

the density should be close to the fluid density, as can be seen from Eq. (4.1). However, particles cannot be too small as they still need to be detectable by the camera sensor and too small particles lead to aliasing effects and peak-locking which reduces the measurement accuracy considerably. For recorded particle image diameters smaller than one pixel the displacement values are biased towards integer values. This phenomenon is called peak-locking. To avoid this, each particle should occupy two to five pixels on the sensor. Furthermore, the particles should have a uniform diameter and homogeneous distribution in the whole FOV. The density of the particles needs to be high enough so that five to ten particles are visible in an interrogation area.
In this study two different types of solid seeding particles were used. The first ones are hollow-glass spheres and the second ones are fluorescent particles.

Table 4.1: Characteristics of seeding particles

TSI Inc. N°	Particle type	Mean diameter (μm)	ρ (g/cm^3)
10089	Hollow-glass spheres	8 - 12	1.05 - 1.15
10070-4	Fluorescent microspheres	30	1.05 - 1.19

Comparative measurements showed that the fluorescent ones gave better and less noisy results. With the fluorescent particles velocities can be obtained closer to surfaces and are more reliable, as the images are less corrupted, than with the hollow-glass spheres. Therefore, the results presented subsequently were obtained using fluorescent seeding particles.

Laser light sheet

The Nd:YAG double-pulsed Litron Nano S65-15 PIV laser emitted at a wavelength of λ = 532 nm using a wavelength doubler and a maximum output energy of 65 mJ per pulse. A cylindrical lens ($f_L = -15$ mm) was used to create

a laser sheet from the beam and a spherical lens ($f_L = 500$ mm) to control the light sheet thickness. The laser energy was set to 100 % to obtain an optimum and stable laser light sheet profile. The individual laser power per laser was set by adjusting the Q-switch delay of each laser, so that the first and second frames have similar intensity distributions. The time delay Δt between two laser pulses was set so that the maximum particle displacement due to the 1/4-rule (Keane and Adrian, 1990) was not exceeded. As maximum velocity the speed of the blade trailing edge was used. At high magnification a Δt of 33 µs, at low magnification 121 µs and for the stereo PIV measurements 86 µs were chosen, with a pump rotational speed of 625 rpm.

Image acquisition

The two cameras (PowerView™Plus 630057) with a charge coupled device (CCD) sensor have a spatial resolution of 2 Mpx (1600 px × 1200 px) and an intensity resolution of 12 bits (4096 different grayscale values). They have a progressive scan interline CCD with microlenses, so that each pixel captures more incoming light (Raffel et al., 2007). The maximum sample rate of one double image is 15 Hz. To capture only the light radiated from the fluorescent seeding particles at a wavelength of about 612 nm a 550 nm high pass filter was mounted on the camera lenses to block out the green laser light (532 nm).
The f-number is defined as:

$$f_\# = \frac{f_L}{D_a}, \tag{4.2}$$

being f_L the focal length of the lens and D_a the aperture diameter of the camera. The choice of the correct $f_\#$ is essential to obtain good images. It influences the depth of field, the amount of light collected which in excess can lead to saturation and the particle diameter on the sensor.
The lens Nikon AF Nikkor 50 mm f/1.8 was used. The focal length of the lens is f_L = 50 mm, so that the f-number $f_\#$ is a function of only the diameter of lens aperture D_a. The lens has a $f_\#$ range from 1.8 to 22 which allows to adjust the amount of light collected by the sensor, the depth of field and the particle diameter on the sensor. An extension ring (Nikon PK-12) was used for the high magnification measurements to obtain a higher spatial resolution with a smaller FOV. The advantage of a smaller $f_\#$ is that more particles are visible and they appear brighter on the CCD. However, this leads to a smaller depth of field, the CCD sensor can be saturated more easily and particle images on the sensor appear smaller.
The magnification factor M is the ratio between the size of the captured area in the object plane (laser light sheet) to the CCD sensor size (image plane):

$$M = L_{CCD}/L_{FOV}, \tag{4.3}$$

with L_{CCD} being the length of the CCD sensor and L_{FOV} the FOV length. The CCD sensor size is 0.0118 m × 0.0089 m with a pixel size of 7.4 µm × 7.4 µm.

Low magnification FOV To obtain a general view of the flow inside the pump, the rotor-stator interaction and the pump outlet a low magnification factor of the camera was chosen to have a relatively large FOV with 0.118 m $\times$ 0.088 m. This results in a magnification factor of $M = 0.10$ with a vector spacing of 1.2 mm. This FOV was used to detect flow structures in the impeller and the pump outlet duct.

High magnification FOV High magnification measurements with a magnification M of 0.37 were carried out to observe the flow especially in the small impeller-volute gap with high resolution and a FOV of 0.032 m $\times$ 0.024 m. The vector spacing is 0.3 mm, which results in a resolution four times higher than for the low magnification measurements.
The two different FOVs considered for low and high magnification measurements are represented in Fig. 4.4.

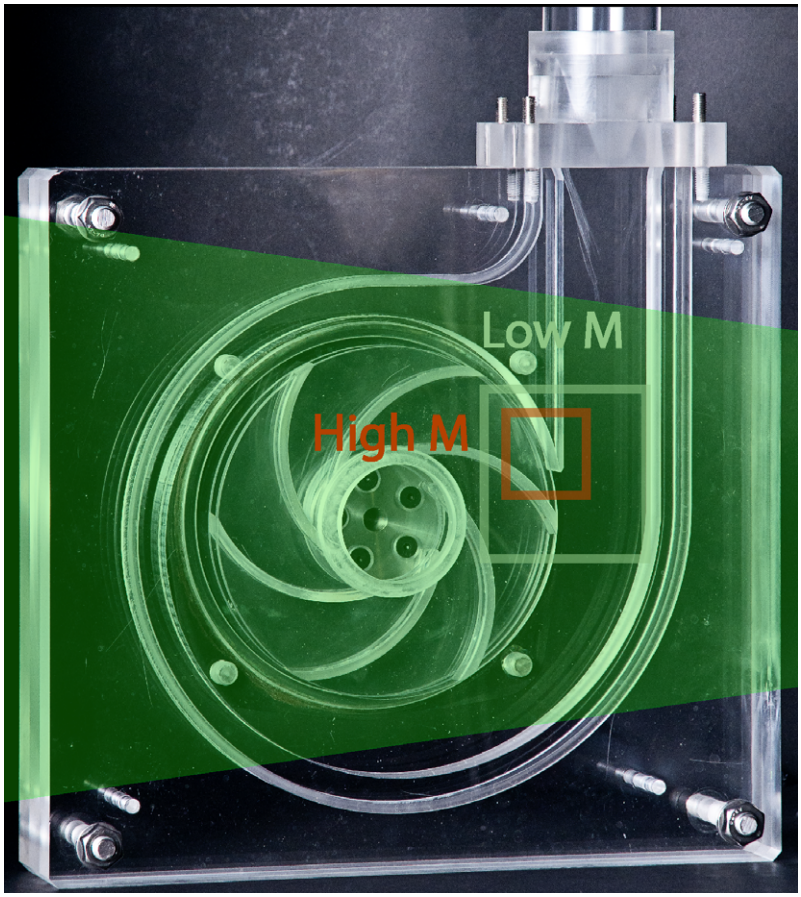

Figure 4.4: Volute and impeller of transparent pump. Green zone indicates laser sheet. Grey and red rectangles show the FOV used at low and high magnification PIV measurements

Stereo PIV FOV The medium magnification of $M = 0.14$ corresponds to the 2D3C measurements with a FOV of 0.085 m $\times$ 0.061 m and a vector spacing of 0.85 mm.

Depth of field The depth of field δ_z depends, for a constant magnification and a constant light wavelength λ, on the $f_\#$ (Raffel et al., 2007):

$$\delta_z = 2 f_\# d_s (M+1)/M^2, \tag{4.4}$$

where d_s is the diffraction-limited minimum image diameter (Adrian and Yao, 1985):

$$d_s \cong 2.44(1+M) f_\# \lambda. \tag{4.5}$$

The laser light sheet thickness is about 1 mm in the FOV. To ensure that all particles inside the laser light sheet are in focus a $f_\#$ of at least 5.6 needs to be chosen for the high magnification and at least 2.8 for the medium magnification, as shown in table 4.2. Only for the low magnification measurements it is possible to focus on all the particles inside the laser sheet independently of the $f_\#$.

Table 4.2: Depth of field as a function of M and $f_\#$

	$M = 0.10$	$M = 0.14$	$M = 0.37$
$f_\#$	δ_z [mm]	δ_z [mm]	δ_z [mm]
1.8	1.46	0.77	0.13
2.8	2.27	2.27	0.32
4	3.24	3.24	0.66
5.6	4.54	4.54	1.28
8	6.48	6.48	2.62
11	8.91	8.91	4.95
16	12.96	12.96	10.48
22	17.82	17.82	19.82

Particle image diameter The particle image diameter d_τ recorded on the CCD sensor of the camera depends on the $f_\#$. It is a composition of the diffraction-limited minimum image diameter d_s and the geometric imaging. The particle image diameter is (Adrian and Yao, 1985)

$$d_\tau \cong \sqrt{M^2 d_p^2 + d_s^2}. \tag{4.6}$$

A $f_\#$ of 11 was used in all PIV measurements to have all particles in focus and to avoid peak-locking effects. This $f_\#$ leads for the fluorescent seeding particles with a mean diameter of 30 µm to a particle image diameter on the CCD sensor of 2.5 px at $M = 0.10$, 2.6 px at $M = 0.14$ and 3.4 px at $M = 0.37$.

Synchronizer

The synchronizer 610035 was used to coordinate the PIV measurements and is controlled using the INSIGHT 4G® software. The laser, cameras, computer and trigger are all connected to it.

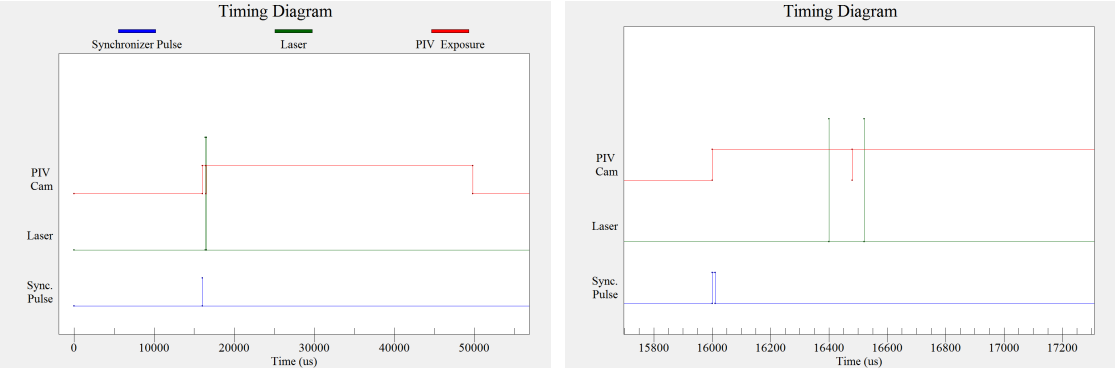

(a) Timing sequence (b) Zoom into timing sequence

Figure 4.5: Timing diagram of PIV system

An optical encoder was used as a trigger. It provides a TTL pulse each pump revolution due to an optical signal, which is reflected using a reflective strip on a blade of the pump motor cooling fan. The time between this signal and the start of a PIV sequence can be adjusted in order to achieve different rotor phases relative to the blade tongue (see synchronization pulse in Fig. 4.5a). At the start of a sequence the exposure of the CCD sensor begins to record the first image. A laser pulse from laser cavity one is fired just before the camera closes the shutter. The exposure for the second image starts and the laser cavity two is activated with a time delay Δt with respect to the first laser pulse (green lines in 4.5b). While the information of image one is read out the second exposure cannot be ended. As the measurements are done in a dark environment, only the light from the fluorescent seeding particles due to the laser pulses are visible on the images.

4.1.2 Image analysis

The software INSIGHT 4G® was also used to process the images. The analysis can be divided into the pre-processing, processing and post-processing steps.

Pre-processing

A calibration needs to be done in order to obtain the velocity in units of m/s. The displacements are transformed from pixels [px] to meters.
Special care was taken when setting up the PIV experiments. In PIV measurements undesired background noise can occur, which might be due to visible parts of the pump in the back of the laser sheet. To reduce this noise a thin

black foil was mounted on the rear volute plate. After having taken the PIV images the blade and tongue were masked out, so that in these regions no cross-correlation was done by INSIGHT 4G®, as any intent to obtain there a velocity vector would lead to wrong velocities. Each frame was normalized to account for variable light intensities using the minimum and maximum light intensity. The laser light sheet profile has approximately a Gaussian shape so that at the upper and lower edges light intensities may vary and as the laser used actually has two different laser cavities the intensity also varies slightly from laser pulse one to laser pulse two.

Processing

Each image is divided into interrogation areas (IA) using a rectangular grid. The highest peak in the cross-correlation map is the most likely displacement of the particles in each interrogation area. The cross-correlation function of two IAs is:

$$R_{II}(s) = \int I_1(x) I_2(x+s) dx, \tag{4.7}$$

being I_1 and I_2 the intensity values of the first and second IA, x is the interrogation location and s is the shift between the two images. A zoom of a RAW image is shown in Fig. 4.6, together with a valid velocity vector in an IA and its correspondent correlation map.

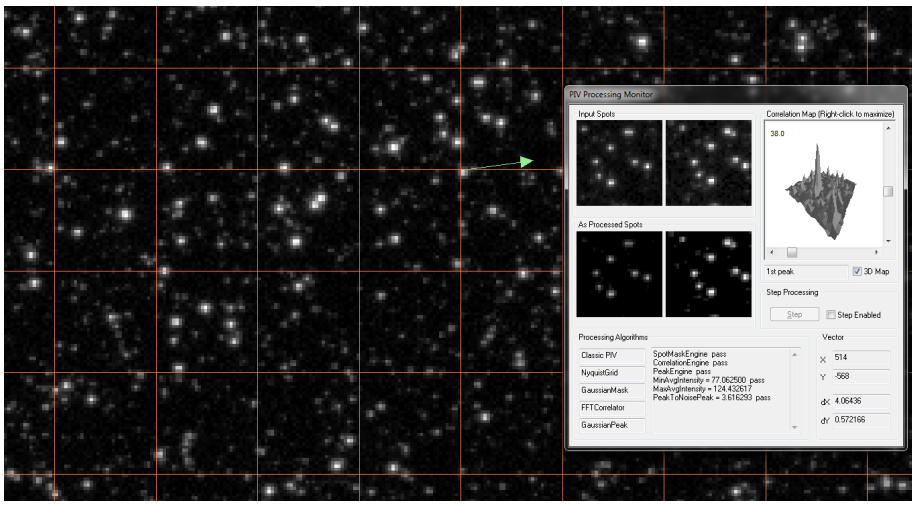

Figure 4.6: Zoom of raw image with interrogation areas and calculation of cross-correlation peak for one IA

The direct discrete cross-correlation function is (Raffel et al., 2007):

$$R_{II}(\Delta x, \Delta y) = \sum_{x=-N/2}^{N/2} \sum_{y=-N/2}^{N/2} I_1(x,y) I_2(x+\Delta x, y+\Delta y), \tag{4.8}$$

with N being the interrogation area length.

By dividing the position of the highest peak by the time between the two laser pulses Δt the in-plane velocity vector is obtained:

$$\vec{U} = \frac{\Delta\vec{X} \mid (R_{IImax})}{M\Delta t}. \tag{4.9}$$

This is done for all IAs, so that for each IA one velocity vector is obtained. Instead of the cross-correlation, a complex conjugate multiplication of the Fourier transforms of the two functions can be done to reduce computation time. Therefore, fast Fourier transform (FFT) is used. Computational cost is reduced compared with direct cross-correlation from $\mathcal{O}(N^4)$ operations to $\mathcal{O}(N^2 \log_2 N)$ operations (Roth and Katz, 2001). As the input data for FFT needs to be of a size of 2^m ($m \in \mathbb{N}$), 64 px $\times$ 64 px and 32 px $\times$ 32 px IA sizes were chosen.

An overlap of 50 % between the neighbouring interrogation areas was selected so that four times more velocity vectors were obtained than without using any overlap. A multi-pass algorithm was chosen, which started at 64 px $\times$ 64 px and ended at 32 px $\times$ 32 px, resulting in 99 x 73 velocity vectors. This results in a vector spacing of 1.2 mm for low magnification and 0.3 mm at high magnification. Advantages of this recursive method are a higher percentage of valid vectors. The loss of particles due to in-plane motion is avoided almost completely. When using only one pass, a bias error appears if velocity gradients inside one interrogation area are present, as then the measured velocities are prone to be lower than the actual velocities, as the faster particles may have left the interrogation area. This bias error is reduced by using in the first step a larger IA to estimate the mean particle displacements. In the second step each IA in frame B has already the offset determined in the first step.
To find the correct velocities with sub-pixel accuracy a Gaussian curve was fitted through the correlation peak. A signal to noise ratio (SNR) of 1.5 needs to be achieved in each interrogation area to keep a vector as a good one. Hereby, the ratio of the highest peak to the second highest peak in each correlation map is calculated. The second highest peak and all other peaks are supposed to be caused due to random pairing of different particles or due to noise. The higher the SNR the higher the possibility that the highest peak is the correct peak.

Post-processing

It is not always possible to have good vectors in all interrogation areas, often due to the lack of particles, loss of particles and high noise levels. In the post-processing step a validation of the vectors took place to detect bad vectors by using a global velocity range filter. Velocities which exceeded a displacement of 16 px in x- or in y-direction were set to invalid vectors. A second validation test was a local validation method which used a universal median test with a neighbourhood size of 5×5. Due to the high dynamic velocity range in the tongue region the universal median test improves the reliability compared to a normal median test. It compares the normalized median residual of each vector

to a normalized dimensionless value. The tolerance chosen was two in x- and in y-direction. Invalid vectors could be replaced by the second highest peak, if it was valid. Replacement was done by a recursive method using the local mean value of the neighbourhood with a 5×5 size.

After obtaining the instantaneous velocity fields MATLAB® was used to further process the velocity fields to calculate and to represent, among others, phase-averaged velocity and vorticity fields and turbulence results.

The instantaneous velocities were 3×3 median filtered for presentation purpose only. For the instantaneous vorticity fields another 3×3 median filter was applied to get rid of high frequency noise. However, for the phase-averaged velocity fields no smoothing was used. For visualization purpose the phase-averaged vorticity, TKE and TKE production were also median filtered with a filter size of 3×3.

Measurement uncertainty

As the velocity is obtained from the ratio of the particle displacement to the time separation between two laser pulses Δt, the estimation of the particle displacement contains some residual error ε_{res}. The velocity magnitude obtained is:

$$\left|\vec{U}\right| = \frac{|\Delta\vec{x}|}{M\Delta t} + \frac{\varepsilon_{\text{res}}}{M\Delta t}. \tag{4.10}$$

The first term is constant, i.e. that for increasing Δt the particle displacement augments linearly. Below a certain time separation Δt the residual error ε_{res} is not reduced, as the accuracy in estimating the correlation peak does not augment (Raffel et al., 2007). This means that the second term increases with decreasing Δt and therefore a high Δt should be chosen. Although, for higher Δt the noise level increases. This is due to the in-plane movement of particles, where particles leave the interrogation area and the out-of-plane movement, where particles are lost. Therefore, to adjust Δt the 1/4-rule was used (Keane and Adrian, 1990). The multi-pass algorithm described above and the two-dimensional shape of the impeller and volute helped to minimize the measurement error.

The measurement error can be divided into a random error and a bias error (Mulleners and Raffel, 2013). The bias error is mainly due to peak-locking. By assuring particle diameters larger than 2 px peak-locking effects could be avoided, which was confirmed by subpixel displacement histograms, so that the residual error ε_{res} is mainly composed of the random error. Typical measurement uncertainty values are of about 0.1 px (Wernet, 2000). This leads to an uncertainty for instantaneous velocities higher than 0.4 U_{tip} to 1-3 % of the measured velocity. After phase-averaging mean flow variables have reduced about an order of magnitude in uncertainty. For a detailed review about possible errors in PIV measurements see for example Huang et al. (1997) or Sciacchitano et al. (2013).

4.1.3 Stereo PIV

With one camera only the two in-plane velocity components u and v can be determined. To obtain the third velocity component w, which is the component leaving the laser light sheet plane (out-of-plane component), a second camera was added to the PIV setup for stereo measurements. It is also called 2D3C PIV, as three velocity components in two dimensions (measurement plane) are obtained. Both cameras were placed on the same side of the laser light sheet. The cameras were placed in a vertical arrangement. One camera was situated above the FOV and the second camera below the FOV (see Fig. 4.7a). A Scheimpflug mount was used for each camera (Prasad and Jensen, 1995). This allowed to tilt the CCD sensor with respect to the camera lens so that the image plane, lens plane and object plane intersect in a common line.

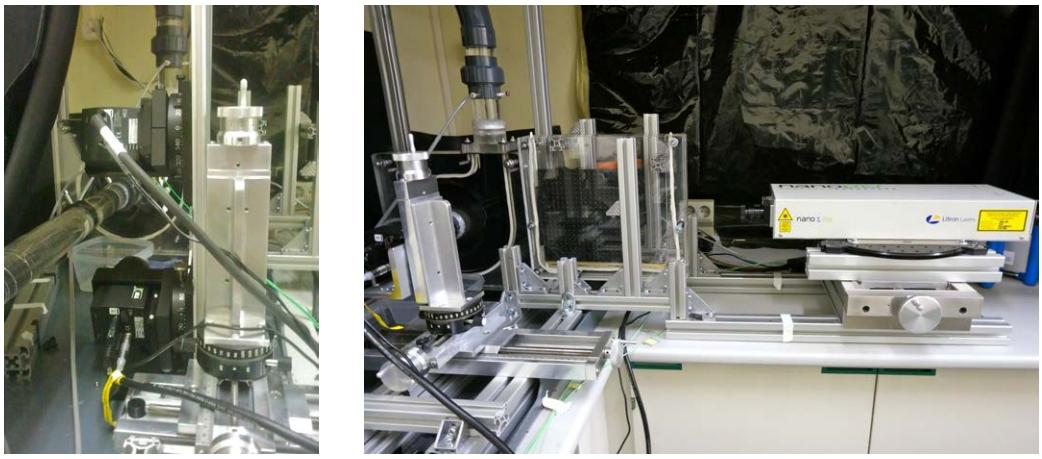

(a) Arrangement of the two cameras

(b) Calibration plate in volute casing placed next to pump

Figure 4.7: Stereo PIV setup. Note the positioning system to move the cameras in all three directions

The viewing angle in air was 30° between the two cameras. A small viewing angle was chosen due to geometric restrictions. The disadvantage is a higher measurement error of the out-of-plane velocity component w compared to the in-plane velocity components u and v (Lawson and Wu, 1997). The advantage is less distortion of the images and a larger overlapping of the FOVs.
Calibration of the stereo PIV system is not as straightforward as for the 2D2C system, where there is only a linear relationship between the pixels of the CCD sensor and the length in meters at the measurement plane. Due to the inclined viewing angle optical distortions appear which need to be accounted for. As a calibration plate could not be placed directly into the pump at the FOV, a second volute was built and filled with water, which has the same dimensions as the original volute, but without the spiral casing. This allowed to place a calibration plate from TSI Inc. in the laser light sheet plane between the pump and the laser. The camera was moved carefully by a linear translation system (UniSlide

from Velmex Inc.) to maintain the alignment of the cameras (see Fig. 4.7b). The calibration plate has a cross marked at the centre and dots spaced 10 mm on a black background and on two different planes with a distance of 1 mm. The INSIGHT 4G® software recognizes the dots and the cross which was used as origin for the coordinate system. Due to possible misalignment between the calibration plate and the laser sheet a *stereo automapping* was used to compensate for the alignment error (TSI, 2011).

4.2 Methodology for acoustic analysis

In this section the methodology employed to investigate the pressure fluctuations generated by a centrifugal pump and the effect of the acoustic coupling of the hydraulic circuit with the pump is described. For this investigation the industrial pump facility (described in section 3.1) and the transparent pump facility (described in section 3.2) were used. Experiments consist of unsteady pressure measurements at the pump volute in the tongue region and at the discharge pipe. An internal sound propagation model, applied to the industrial pump, is described in this section. Furthermore, the transfer matrix analysis (TMA), applied to both hydraulic circuits, is explained.

4.2.1 Measurements of acoustic pressure

For the unsteady pressure measurements fast-response piezoelectric pressure transducers (Kistler 701 A) with a high sensitivity were used. These pressure transducers were mounted in a casing (see Fig. 4.8). The internal cavity between the transducer and the inlet was previously filled with water. It has a resonance frequency of 8.8 kHz, if a Helmholtz resonator is assumed (Parrondo et al., 2002). This resonance frequency is several times higher than the frequencies considered in this study, which are in the range of 10-500 Hz.

(a) Picture of pressure transducer

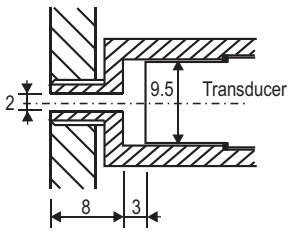

(b) Detail of pressure transducer casing (units in mm)

Figure 4.8: Fast-respone pressure transducer

The pressure signals were amplified using different amplifiers, e.g. charge amplifier Kistler type 5018, and recorded (IMC Cronos-PL2). The signals were processed applying a FFT algorithm. Some basics about signal processing to obtain frequency spectra are explained in this section.

Fourier transforms

Signals in the time domain are processed to transform them into the frequency domain to obtain their spectra. This is done using Fourier transforms (Engelberg, 2008).
A periodic signal $x(t)$ with an arbitrary period T can be written as a sum of various sinusoidal functions, the Fourier series:

$$x(t) = \frac{1}{T} \sum_{n=-\infty}^{\infty} c_n e^{in2\pi f_o t}, \qquad f_o = \frac{1}{T}, \tag{4.11}$$

being c_n the Fourier coefficients given by:

$$c_n = \frac{1}{T} \int_T x(t) e^{-in2\pi f_o t}. \tag{4.12}$$

The Fourier transform of a time signal $h(t)$ is:

$$F[h(t)] = H(f) = \int_{-\infty}^{+\infty} h(t) e^{-i2\pi f t} dt. \tag{4.13}$$

A continuous signal $x(t)$ is sampled:

$$x(n) = x(t) \sum_{-\infty}^{\infty} \delta(t - nT), \tag{4.14}$$

being $\sum_{-\infty}^{\infty} \delta(t - nT)$ a train of periodic impulses and δ the Dirac delta function. The discrete Fourier transform (DFT) is applied to the sampled signal:

$$X(k) = \sum_{n=0}^{N-1} x(n) e^{-in2\pi k/N}, \qquad k = 0, 1, ..., N-1. \tag{4.15}$$

The sampling theorem gives the minimum frequency which is needed to sample a signal, in order to rebuilt it without errors. This minimum frequency is called Nyquist frequency and is two times the maximum frequency that can be represented in a frequency spectrum.
The FFT transforms the time signals into the frequecy domain in a rapid and very efficient way. Symmetry and periodicity characteristics from the DFT are used to save computation time.
The resolution in frequency Δf is obtained by the ratio of f_s to the number of points N taken for the FFT:

$$\Delta f = \frac{f_s}{N} = \frac{1}{t}. \tag{4.16}$$

This means that the resolution in frequency is the inverse of the duration t of the data set, to which the FFT is applied.
As the measurement has a certain duration, discontinuities appear and a phenomenon called leakage occurs, which means that the peaks broaden. To reduce

this phenomenon the measurement time can be increased or an appropriate window function can be applied. Different window functions exist, e.g. the Hann window, which attenuate the time signal at the beginning and at the end.
A filter is a function in the frequency domain to separate the desired part of the signal from the undesired part, e.g. noise. Typical filters are low pass and high pass filters which maintain only the lower frequencies or the higher frequencies, respectively.

Data processing

For the pressure measurements at the transparent pump facility an optical encoder was used to obtain the pump rotational speed. Besides, its electronic signal (one pulse per impeller revolution) was recorded and used as a trigger. The pressure signals were recorded simultaneously with the signal from the encoder during 45 s with a sample rate of $f_s = 1000$ Hz. From each transducer 20 sets of 2048 points were selected by using the encoder signal as trigger, in order to ensure the same phase delay with respect to the impeller angular position. In this way each pressure signal could be averaged to get rid of possible noise. Therefore, the time signal contains basically information on the pump rotation frequency and harmonics, such as the blade-passing frequency f_{BP}. The pressure signals were multiplied by a Hann window to reduce leakage and the FFT algorithm was used to obtain frequency spectra. A high pass filter was used to eliminate the mean pressure signal.
For the pressure measurements at the industrial pump facility the procedure was similar, except that no trigger signal was recorded, as only the amplitude and not the phase was of interest. Therefore, each pressure signal was divided into 20 consecutive data blocks. Each block was multiplied by a Hann window and then FFT processed, to finally result in the average frequency spectra of the recorded pressure signals.

Pressure sensors at pump volute

For the industrial pump a fast-response pressure transducer was placed at the front side of the volute in the narrow region, at $\varphi = 25°$ behind the tongue tip, and at a radial position of $r = 107.5$ mm ($r/r_{tip} = 1.024$).

For the transparent pump five fast-response pressure transducers were placed at the front casing wall of the volute in the zone around the tongue. Two were located in the narrow region of the volute and the other three in the broad region of the volute and pump outlet duct. The exact locations are given in Fig. 4.9 and Table 4.3. A new front volute plate was made, different from the one used for the PIV measurements, as the holes for the pressure transducers would disturb the FOV of the camera. Each hole for the pressure transducers has a diameter of 1 mm.

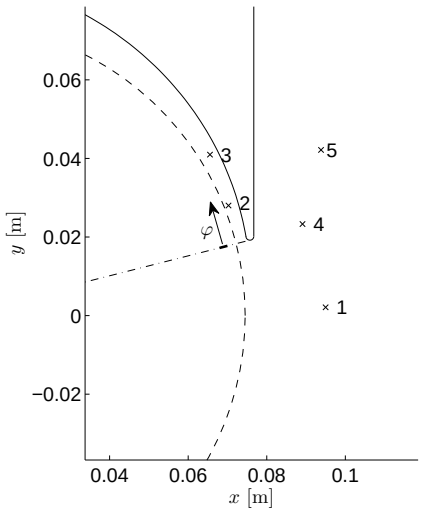

(a) Location of pressure transducers

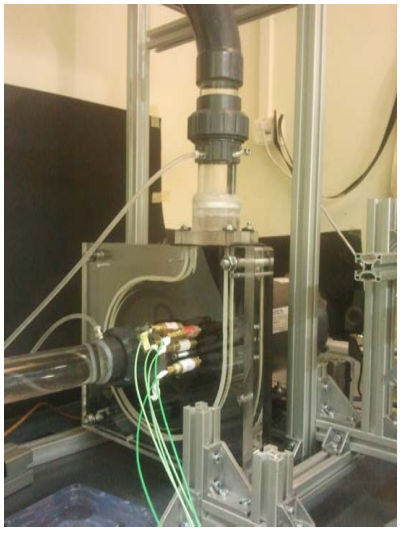

(b) Picture of pressure transducers

Figure 4.9: Pressure transducers at transparent pump volute

Table 4.3: Location of pressure transducers at transparent pump volute

N°	x [m]	y [m]	angle φ [°]	radius [m]	radius* (r/r_{tip}) [-]
1	0.094	0.001	-13	0.094	1.265
2	0.070	0.027	7	0.075	1.004
3	0.065	0.040	18	0.077	1.028
4	0.088	0.023	1	0.091	1.224
5	0.094	0.042	10	0.103	1.377

The uncertainty of the pressure fluctuation data was estimated to be within $\pm$ 2.5 %, based on instrumentation manufacturer's data and on laboratory calibration tests.

4.2.2 Acoustic impedance and speed of sound

In order to measure the acoustic pipe impedance and the pressure fluctuations at the blade-passing frequency, three fast-response pressure transducers were used to monitor the pressure fluctuations along the discharge pipe of the transparent pump facility. The pressure transducers were placed along the discharge pipe between the pump outlet and the dead-end branch. For location of the transducers see Fig. 3.8. As the interest lies in the blade-passing frequency f_{BP}, only the amplitude and phase of each sensor signal at f_{BP} were processed further on. The pressure fluctuations radiated from the pump travel along the pipes as plane pressure waves P^+ with amplitude p^+, frequency f, wavenumber k^+ and phase φ^+:

$$P^+(x,t) = p^+ \mathrm{e}^{\mathrm{i}(2\pi f t - k^+ x + \varphi^+)}. \tag{4.17}$$

Plane waves were assumed, as the wavelengths λ were at least 60 times the pipe diameter for all test cases. Some sound wave attenuation is to be expected, especially for the transparent pump circuit, due to several effects regarding the water stream (viscous shear at walls and turbulence), pipe transmission and pipe absorption, which can be significant if the pipe material has a viscoelastic behaviour that induces retarded strain. In order to consider this attenuation, a complex wavenumber was used, which is defined as $k^+ = 2\pi f/(c+v) - \mathrm{i}\alpha$, with α being an attenuation factor. Reflections in the hydraulic circuit at elements like valves, branches or at the tank lead to returning waves P^- defined as:

$$P^-(x,t) = p^- \mathrm{e}^{\mathrm{i}(2\pi f t + k^- x + \varphi^-)}, \tag{4.18}$$

with $k^- = 2\pi f/(c-v) - \mathrm{i}\alpha$ being the complex wavenumber of the reflected wave. Therefore, the pressure P, measured at any position x along a pipe, results from the combination of the two waves P^+ and P^- that travel in opposite directions:

$$P(x,t) = P^+ + P^- = p^+ \mathrm{e}^{\mathrm{i}(2\pi f t - k^+ x + \varphi^+)} + p^- \mathrm{e}^{\mathrm{i}(2\pi f t + k^- x + \varphi^-)}. \tag{4.19}$$

This needs to be valid for all time instants t, leading to the following equation:

$$P(x) = P^+(x) + P^-(x) = p^+ \mathrm{e}^{\mathrm{i}(-k^+ x + \varphi^+)} + p^- \mathrm{e}^{\mathrm{i}(k^- x + \varphi^-)}. \tag{4.20}$$

Determination of speed of sound

The speed of sound c_w needs to be known with reasonable accuracy in order to keep low uncertainty in determining P^+ and P^-, as it has a direct influence on the wavenumbers. To obtain the speed of sound of water in pipes c_w the following equation is used:

$$c_\mathrm{w} = \frac{1}{\sqrt{\rho_\mathrm{w}\left(\frac{1}{K} + \frac{d}{tE}\right)}}, \tag{4.21}$$

where K is the bulk modulus of water ($K = 2.14 \cdot 10^9$ Pa) and ρ_w the water density ($\rho_\mathrm{w} = 999$ kg/m^3 at 15° C).
For the industrial pump facility with steel pipes, the speed of sound results to be about 1300 m/s. For the transparent pump facility the polycarbonate (PC) pipes have an inner diameter d of 47 mm and a wall thickness t of only 1.5 mm. Assuming that the PC pipes are elastic, with a Young's modulus $E = 2.3 \cdot 10^9$ Pa, the theoretical speed of sound of water in the pipes obtained with Eq. (4.21) results to be 267 m/s. Compared to the speed of sound in unconfined water ($c_\mathrm{w} = 1464$ m/s) or in steel pipes with the same dimensions ($c_\mathrm{w} = 1274$ m/s) the speed of sound for this study appears to be about 5 times smaller.

To obtain P^+ and P^- experimentally the pressure needs to be measured simultaneously in at least two positions x_i along the pipe:

$$\begin{bmatrix} P_1 \\ P_2 \end{bmatrix} = \begin{bmatrix} e^{-ik^+x_1} & e^{ik^-x_1} \\ e^{-ik^+x_2} & e^{ik^-x_2} \end{bmatrix} \begin{bmatrix} P^+ \\ P^- \end{bmatrix}. \tag{4.22}$$

In order to determine the speed of sound experimentally and check the validity of the parameters of Eq. (4.21) for the PC pipes, a series of tests was conducted in which the three pressure transducers were located along the discharge pipe. The pressure waves P^+ and P^- were obtained from Eq. (4.22) assuming different values for the speed of sound and using separately the three possible pairs of sensors (sensor 1 with sensor 2 = S1S2, sensor 1 with sensor 3 = S1S3, sensor 2 with sensor 3 = S2S3). For instance, the resulting ratio between P^+ and P^- for sensors 1 and 2 is

$$\frac{P^+}{P^-} = \frac{P_1 e^{ik^-x_2} - P_2 e^{ik^-x_1}}{-P_1 e^{-ik^+x_2} + P_2 e^{-ik^+x_1}}. \tag{4.23}$$

Figure 4.10 shows the results regarding the phase difference $\varphi^+ - \varphi^-$, which is the argument of the ratio P^+/P^-, for different speeds of sound between 200 and 400 m/s. At a speed of sound of 280 m/s the results of the three pairs coincide. This value obtained experimentally is slightly higher than the theoretical value of 267 m/s. This difference can be attributed to slight variations in pipe wall thickness, bulk modulus of water or Young's modulus of the pipe, and to the non-consideration of the viscoelastic behaviour of the PC pipes. The c_w value of 280 m/s obtained experimentally was used in the following calculations.

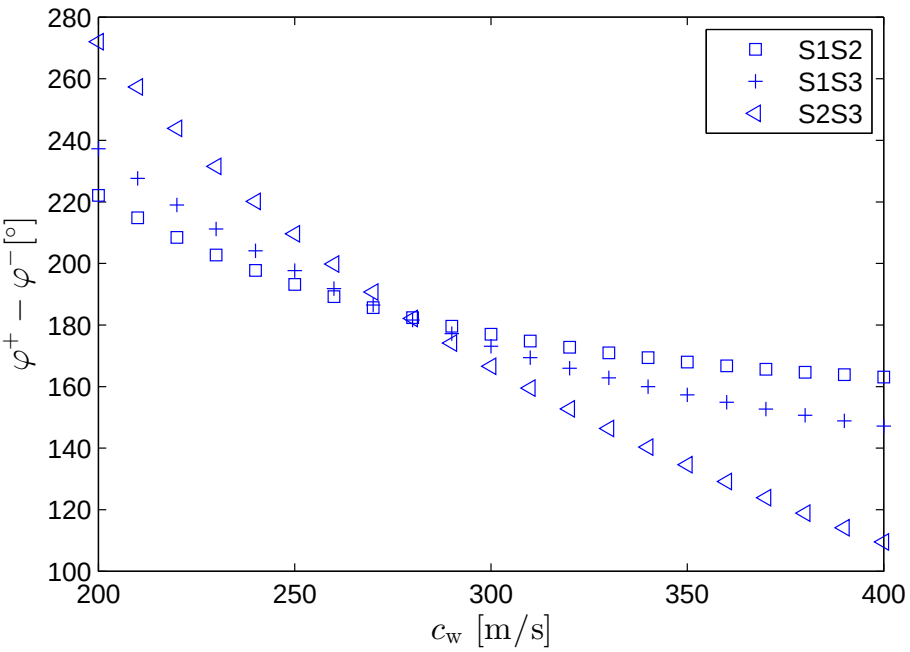

Figure 4.10: Fit of the speed of sound

Overdetermined system

The distance s between two pressure sensors was chosen to always fulfil $0.1\pi(1 - \mathrm{Ma}^2) < ks < 0.8\pi(1 - \mathrm{Ma}^2)$, in order to reduce measurement errors (Allam and Åbom, 2006). Having determined the speed of sound in the pipes, the three pressure transducers were used to solve for P^+ and P^- from an overdetermined equation system by means of a least-square error method:

$$[\varepsilon_{\mathrm{res}}] = \begin{bmatrix} \mathrm{e}^{-\mathrm{i}k^+x_n} & \mathrm{e}^{\mathrm{i}k^-x_n} \end{bmatrix} \begin{bmatrix} P^+ \\ P^- \end{bmatrix} - [P_n], \tag{4.24}$$

where $n = 1, 2, 3$ denotes each sensor and $\varepsilon_{\mathrm{res}}$ is the corresponding residual error.
The acoustic impedance, as ratio of the acoustic pressure fluctuations to the acoustic mass flow ($Z = P/V$), is calculated referred to the pump outlet ($x = 0$). Admittance (V/P) is the reciprocal of the impedance. As from Eq. (4.24) the radiated P^+ and returning pressure wave P^- are obtained, the acoustic impedance is calculated by (Lucas et al., 1997):

$$Z = \zeta \frac{P^+ + P^-}{P^+ - P^-}. \tag{4.25}$$

4.2.3 2-port acoustic model

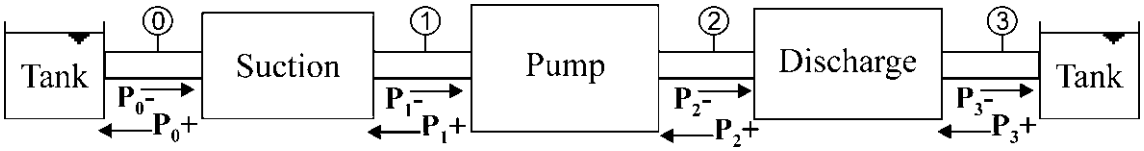

Figure 4.11: Representation of the pump-circuit acoustic coupling

A simplified model of the pump is used to consider the influence of the acoustic characteristics of the hydraulic circuit on the BPF pressure fluctuations generated in the pump. The model is a linear 2-port system (Fig. 4.11), with the two ports being the suction and discharge side of the pump. Two state variables at each port relate the two ports by a transfer matrix. It is common to choose pressure and acoustic mass flow fluctuations (Lucas et al., 1997) or exiting and incoming pressure fluctuations. For this 2-port acoustic pump model the exiting P^+ and incoming P^- pressure waves were chosen as state variables. The relation between the radiated P^+ and returning P^- pressure waves can be expressed as (Lavrentjev et al., 1995):

$$\begin{bmatrix} P_1^+ \\ P_2^+ \end{bmatrix} = \begin{bmatrix} R_{11} & T_{21} \\ T_{12} & R_{22} \end{bmatrix} \begin{bmatrix} P_1^- \\ P_2^- \end{bmatrix} + \begin{bmatrix} P_{\mathrm{G1}} \\ P_{\mathrm{G2}} \end{bmatrix}. \tag{4.26}$$

The 2×2 matrix in Eq. (4.26) is called the scattering matrix. It gives the fraction and phase delay of the incoming pressure waves that are reflected back (R_{ii}) or

transmitted (T_{ij}) to the other port, i.e. it represents the passive acoustic properties of the pump. The active acoustic properties, which describe the sound generation are represented by the vector with elements P_{G1} and P_{G2}. All six complex coefficients, with amplitude and phase, can be obtained from the 2-port acoustic pump model. They all are a function of frequency and, to a lesser extent, of the flow-rate.

Internal sound propagation model

The internal sound propagation model was developed at the Chair of Fluid Mechanics of the University of Oviedo. A brief overview of the model is given here, but a more detailed description can be found in Parrondo et al. (2011).
It was originally designed to model sound propagation inside a pump and, in consequence, to identify the internal sound sources from comparison to experimental pressure fluctuation data. This model uses an iterative procedure which progressively varies amplitude, phase and the internal position of one or more sound sources. The results obtained are compared with pressure signals obtained previously experimentally by the use of fast-response pressure transducers. The iterations end when the calculated sound pressure field is as close as possible to the experimental data on a least square error basis.
The ideal sound sources can be monopole or dipole types. It is assumed that they radiate plane waves at f_{BP} which propagate along the volute, impeller channels, outlet diffuser and pipes in positive (streamwise) and negative directions (see Fig. 4.12). The sound propagation in the volute experiences a continuous exchange with the impeller channels. Therefore, the volute is divided into acoustic cells. Each cell is a three-port linear acoustic system, similar to Lorett and Gopalakrishnan (1986). The relation between incoming and exiting pressure waves for each cell are represented by a 3×3 transmission matrix:

$$\begin{bmatrix} e_x \\ e_y \\ e_y \end{bmatrix} = \begin{bmatrix} T_{xx} & T_{yx} & T_{zx} \\ T_{xy} & T_{yy} & T_{zy} \\ T_{xz} & T_{yz} & T_{zz} \end{bmatrix} \begin{bmatrix} i_x \\ i_y \\ i_z \end{bmatrix}, \tag{4.27}$$

with i_i and e_i being the incoming and exiting pressure waves, respectively (see Fig. 4.12).
The elements T_{ij} can be obtained from sound energy balances in the acoustic cells. For the tongue region a similar three-port cell describes the sound transmission in the tongue region between narrow and wide side of the volute and the diffuser (see grey area at the right side in Fig. 4.12). Sound propagation is partially reflected at the end of the impeller channels due to the sudden change in cross-section. Furthermore, the pressure waves can be reflected in the pipes and return with some attenuation and relative phase delay, depending on the acoustic properties of the circuit. A Mach number effect was not considered in the model, since this parameter is very low (its magnitude based on blade tip speed is below 0.02). Furthermore, the influence of the rotational speed,

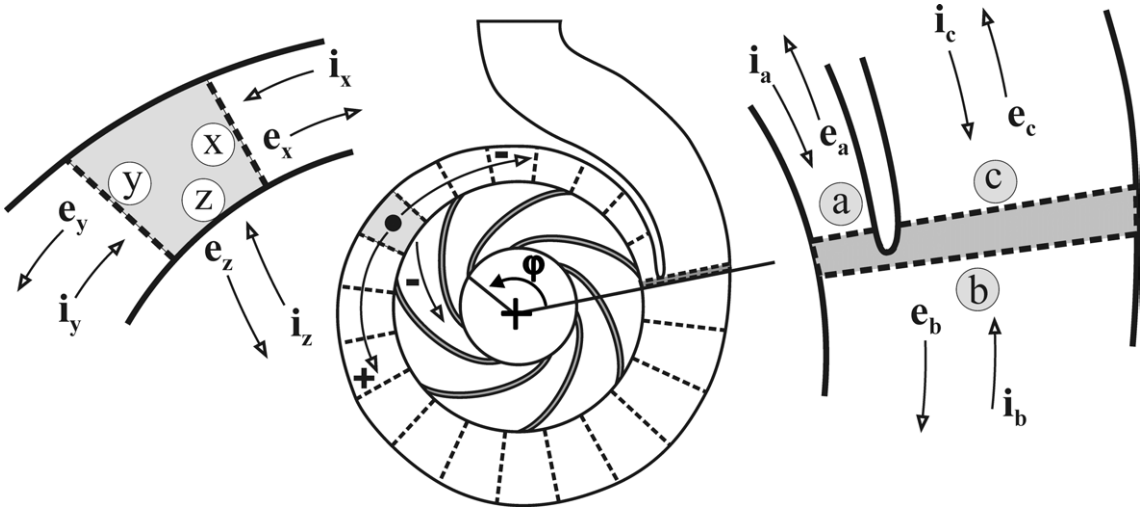

Figure 4.12: Sound emission from an ideal source. Volute is divided into acoustic cells, each with three input-output ports (adapted from Parrondo et al. (2011))

hydraulic torque fluctuation or vibration of the casing was not taken into consideration. None of these parameters are expected to have any significant effect for the range of frequencies of interest, since the impeller rotation itself does not appear to influence the sound transmission data in the pump, according to the studies reported in Carta et al. (2000); Bardeleben and Weaver (2002).

The resulting acoustic fluctuations could be complemented with the pure hydraulic fluctuations in the volute due to the rotating impeller blades and channels. The software code allows systematic variation of the geometrical, physical and calculation parameters. A hill-climbing scheme controls the modification of the acoustic source properties to obtain minimum differences between pressure fluctuation predictions and experimental pressure data. This model was applied to the industrial pump described in section 3.1. It was found that about 30 cells along the volute are sufficient to obtain results insensitive to the discretization degree. Further details about the acoustic model assumptions, complex coefficients of the scattering matrix of each three-port cell and the calculation procedure are described in Parrondo et al. (2011).

Experimental pressure data were previously collected for the industrial pump at 1620 rpm for different operating points (Barrio et al., 2008). Pressure transducers were placed at 36 equally spaced positions along the front side of the volute. More information about the setup, measurement procedure and results can be found in Barrio et al. (2008). The results were used as experimental input data for the ideal source identification software, in order to contrast the pressure fluctuation predictions at f_{BP}.

Two ideal sources in the volute are enough to obtain a reasonable agreement between measurements and predictions at all flow-rates. The identified ideal sound sources for different flow-rates are represented in Table 4.4. It presents the properties of those two sources including type (monopole or dipole), nor-

malized power ($W4c/(\rho A_{\text{tip}} U_{\text{tip}}^4)$), angular position φ and phase delay β, the latter relative to the passage of the blade trailing edge (point Y in Fig. 4.13) in front of the tongue tip. The determination coefficients of each regression fitting, also shown in Table 4.4, are not too far from the ideal value of unity, especially for large flow-rates.

Table 4.4: Ideal sound sources for different flow-rates at industrial pump (Keller et al., 2014)

Flow-rate	40 % Q_N	70 % Q_N	100 % Q_N	130 % Q_N
Source type	Monopole	Monopole	Dipole	Dipole
Regres. Coef.	0.779	0.857	0.866	0.887
Source #1:				
W_1 [-]	0.171	0.0651	0.0038	3.2 E-4
φ_1 [°]	11.7	12.6	5.8	10
β_1 [°]	56.1	62.1	225	267
Source #2:				
W_2 [-]	0.248	0.0955	0.0036	2.1 E-4
φ_2 [°]	15.0	15.0	9.8	15
β_2 [°]	240.4	244.5	43.4	123.2

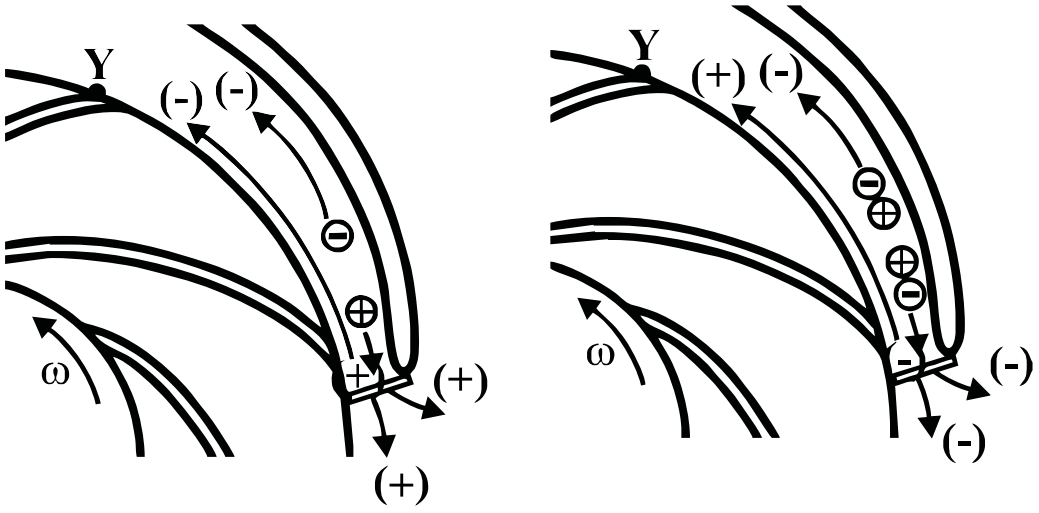

(a) partial flow-rate

(b) nominal and above nominal flow-rate

Figure 4.13: Sound sources in volute (adapted from Pérez Castillo (2009))

The results of Table 4.4 show that at partial flow-rate the ideal sources identified are two monopoles, close to each other, and radiating with opposite phase (Fig. 4.13a). They resemble a dipole, though the second source is about 45 % more powerful than the first one. Combination with the sound reflection effect at the tongue edge consolidates the dipole character of the system.
For the nominal and 130 % Q_N flow-rate, the ideal sources identified are two dipoles, close to each other, which radiate sound with a relative phase delay of

about 180° and not very different sound power W. Hence, they resemble a linear quadrupole at the tongue region (Fig. 4.13b), producing a sharp pressure rise in the middle region. Because of the abrupt change in volute cross-section at the tongue edge, the sound radiated by the quadrupole towards the tongue edge is partially reflected there with a phase of 180°. This reflected sound combines with the sound radiated streamwise by the first source to overcome the negative phase of the sound radiated by the second source. In consequence, the two ideal sources plus the tongue edge represent a dipole-like system that radiates sound with opposite phases along the volute and towards the outlet diffuser.

Transfer matrix analysis

A transfer matrix analysis (TMA) was used to describe the acoustic characteristics of the hydraulic circuit at the suction and discharge side. Each element is represented by a 2×2 matrix, that relates the acoustic pressure P and the acoustic mass flow V (=$\rho_w A U_p$) at the two ports:

$$\begin{bmatrix} P_1 \\ V_1 \end{bmatrix} = \begin{bmatrix} S_{11} & S_{12} \\ S_{21} & S_{22} \end{bmatrix} \begin{bmatrix} P_0 \\ V_0 \end{bmatrix}, \tag{4.28}$$

$$\begin{bmatrix} P_2 \\ V_2 \end{bmatrix} = \begin{bmatrix} S'_{11} & S'_{12} \\ S'_{21} & S'_{22} \end{bmatrix} \begin{bmatrix} P_3 \\ V_3 \end{bmatrix}. \tag{4.29}$$

Thus, Eqs. (4.28) and (4.29) show the relation between pressure and mass flow fluctuations in the suction and discharge pipe, respectively. This representation allows to multiply the matrices of individual components or portions in the hydraulic circuit in order to produce the transfer matrix of the equivalent aggregated system (Munjal, 1987).

The procedure described afterwards is valid for the transparent pump hydraulic circuit. For the industrial pump facility it is similar, but for example there was no need to work with equivalent lengths.
A simple pipe is represented by (Lucas et al., 1997):

$$T_P = e^{-iMakL} \begin{bmatrix} \cos(kL) & i\zeta \sin(kL) \\ \frac{i}{\zeta}\sin(kL) & \cos(kL) \end{bmatrix}, \tag{4.30}$$

where e^{-iMakL} accounts for the attenuation taking place, Ma is the Mach number and $k = 2\pi f/c - i\alpha$. $\zeta = c_w/A$ is the acoustic impedance for a plane wave based on mass flow-rate. L is the geometrical length of the PC pipes or an equivalent acoustic length for other elements like PVC pipe elbows, the flow meter and other connecting elements. This equivalent acoustic length is obtained by multiplying the geometrical length L_g by the ratio of the speed of sound in the PC pipe c_w to the speed of sound at each element c_e: $L = L_g \cdot c_w/c_e$. The curvature of the elbows has a negligible effect on the acoustic waves due to the relatively large curvature radius of 0.10 m, which is more than twice the pipe

diameter. A cavity is a side-branch (shunt) element that modifies the acoustic velocity at the joint, but not the pressure (Munjal, 1987). Its transfer matrix is:

$$T_{\mathrm{C}} = \begin{bmatrix} 1 & 0 \\ \frac{1}{Z} & 1 \end{bmatrix}. \tag{4.31}$$

In the setup of the transparent pump facility the lower part of the cylindrical dead-end branch (cavity) is filled with water and the upper part is filled with air (see Fig. 3.8). It works like a harmonic oscillator with the water volume in the cavity acting as a mass ($\rho_{\mathrm{w}} >> \rho_{\mathrm{a}}$) and the air volume as a spring ($K_{\mathrm{w}} >> K_{\mathrm{a}}$). To represent the transfer matrix for this cavity, it was split into a simple pipe with water and another simple pipe with air, each of them associated to a transfer matrix using Eq. (4.30). The boundary conditions are $V = 0$ at the end of the closed cavity and no change in acoustic pressure P nor acoustic velocity U_{p} at the interface between air and water. As the acoustic mass flow-rate V is used and the cross-section is constant, only the density relationship shows up in the transfer matrix corresponding to the air-water interface:

$$T_{\mathrm{if}} = \begin{bmatrix} 1 & 0 \\ 0 & \frac{\rho_{\mathrm{w}}}{\rho_{\mathrm{a}}} \end{bmatrix}. \tag{4.32}$$

The impedance for the cavity, which appears in Eq. (4.31), can be obtained from the proper matrix product of the transfer matrices for the air and water sections (Eq. (4.30)) including their interface (Eq. (4.32)).
In this way the transfer matrices of the individual elements along the discharge pipe are multiplied to relate the beginning of the duct (pump outlet) with the end of the circuit. The boundary condition considered is acoustic mass flow-rate equal to zero at valve V2 (see Fig. 3.8) for the case of zero flow-rate (V2 totally closed) or acoustic pressure P equal to zero at the discharge tank for non-zero flow-rates. Finally, the acoustic impedance $Z = P/V$ is calculated referred to the pump outlet.

To deal with Eq. (4.26) the pressure waves P^+ and P^- need to be decomposed. From Eqs. (4.28) and (4.29) the ratio of returning to radiated pressure waves, using Eqs. (1.14) and (1.15), is:

$$\frac{P_1^-}{P_1^+} = \frac{S_{12} - \zeta_1 S_{22}}{S_{12} + \zeta_1 S_{22}}, \tag{4.33}$$

$$\frac{P_2^-}{P_2^+} = \frac{S'_{12} - \zeta_2 S'_{22}}{S'_{12} + \zeta_2 S'_{22}}. \tag{4.34}$$

The advantage of working with acoustic mass flow instead of acoustic velocity is that changes in cross-section area do not need to be considered separately. Eqs. (4.26), (4.28) and (4.29) can finally be combined for a direct determination of the radiated P^+ and returning P^- pressure waves.

Part III

Results and Discussion

5 Flow field

In this chapter the results obtained from the PIV measurements are presented for three flow-rates, three field of views with different magnifications and various blade positions. The instantaneous absolute velocity fields are the direct results obtained from processing the PIV images. These velocity fields were further processed using MATLAB® to obtain, among others, phase-averaged relative and absolute velocities, and its tangential u_θ and radial components u_r. Furthermore, other flow variables such as phase-averaged out-of-plane vorticity ω_z and turbulence statistics were calculated to detect flow structures with emphasis on rotor-stator interaction. A FFT analysis of the flow field was carried out, using 32 phase-averaged time instants at low and high magnification.

One FOV was investigated by stereo PIV using two cameras. The advantage is that all three velocity components in the measurement plane were obtained. The other two FOVs are from the low and high magnification measurements described in 4.1.1. The coordinate system is referred to the pump axis and for clarity it is not always shown in the contour maps. The coordinates corresponding to the low magnification FOV are shown in Fig. 5.5 and for the high magnification FOV in Fig. 5.1. All PIV measurements presented in this chapter were taken at a pump rotational speed of 625 rpm, which corresponds to f_{BP} = 62.5 Hz. The three different flow-rates investigated are 40 % Q_N (part load), Q_N and 150 % Q_N (overload). 33 different blade positions which cover one blade passage were recorded for the low and high magnification measurements. For stereo PIV five different blade positions were recorded. At each blade position 500 double images were taken by each camera to obtain converged phase-averaged velocity fields. Velocities were normalized by the impeller blade tip speed U_{tip} of 4.9 m/s, resulting in dimensionless velocities U^* computed by:

$$U^* = \frac{U}{U_{tip}}. \tag{5.1}$$

The time t, which describes the position of the blade relative to the tongue, was normalized by the blade passage period:

$$t^* = \frac{t}{t_{BP}} = t \cdot f_{BP}. \tag{5.2}$$

At $t^* = 0.00$ the blade suction side of the trailing edge aligns with the tongue tip.

5.1 Instantaneous and phase-averaged velocities

An example of instantaneous absolute velocity fields at high magnification and a flow-rate of 150 % Q_N is shown in Fig. 5.1. The time series shown in these figures do not correspond to one blade passage, as they were taken in different runs.
High fluctuation can be observed between the different blade positions, as the flow field is composed basically of turbulence and flow structures associated with the rotation of the impeller blades at f_{BP} and harmonics. To discriminate between turbulence and cyclic flow variation at f_{BP} and harmonics phase-averaged velocity fields were calculated and are presented in section 5.3.
The instantaneous out-of-plane vorticity ω_z was calculated from these instantaneous velocity fields and is shown in Fig. 5.2. Individual vortices can be observed which are shed from the blade trailing edge and tongue tip. However, these vorticity fields are only representing instantaneous vorticity and are not directly related between one blade position to the other, as already pointed out for the instantaneous velocities. Therefore, to obtain a better understanding of the vorticity structures at f_{BP} and harmonics phase-averaged vorticity fields are presented in section 5.5.

The instantaneous velocity in the pump is a function of location x and y, time t and circumferential blade-position ϕ:

$$\vec{u}(x,y,t,\phi) = \vec{U}(x,y,\phi) + \vec{u'}(x,y,t,\phi), \tag{5.3}$$

with $\vec{U}$ being the phase-averaged velocity and $\vec{u'}$ the fluctuating component of the velocity. This turbulent part $\vec{u'}$ is not associated with deterministic unsteadiness, i.e. it is not periodic with the blade-passing frequency and harmonics.
All double images ($n = 500$) recorded were used to obtain phase-averaged velocity fields $\vec{U}$ for 33 blade-positions ϕ (every 1.875°) by

$$\vec{U}(x,y,\phi) = \frac{1}{n}\sum_{m=1}^{n} \vec{u}_m(x,y,\varphi); \qquad \varphi = \phi + 2\pi(3m-1). \tag{5.4}$$

For each blade position successive double images were taken every three impeller rotations, which contributes to a greater statistical independence between instantaneous velocity fields. A convergence analysis was done by progressively increasing the number of double images for one blade position and obtaining the phase-averaged velocity magnitude at three reference points in the tongue region (for location see Fig. 5.3). Figure 5.4 shows that reasonable convergence starts at about 100 double images. Nevertheless, all the results reported herein have been obtained from 500 double images in order to ensure well converged phase-averaged velocity fields. The fluctuations are assumed to have a Gaussian distribution, which would not be the case for phenomena occurring at a frequency different than f_{BP} or harmonics (Cavazzini et al., 2010), such as rotating stall.

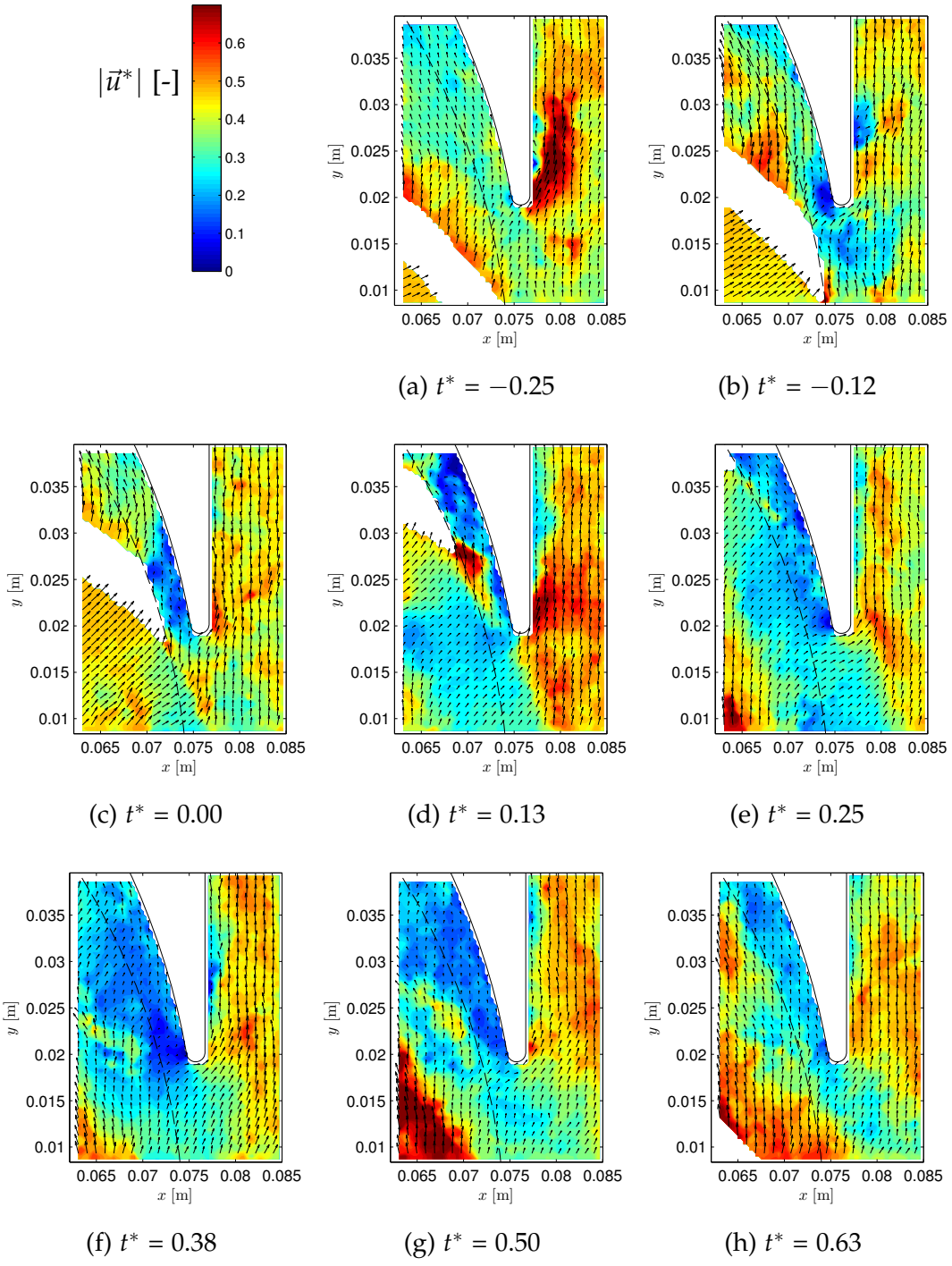

(a) $t^* = -0.25$ (b) $t^* = -0.12$

(c) $t^* = 0.00$ (d) $t^* = 0.13$ (e) $t^* = 0.25$

(f) $t^* = 0.38$ (g) $t^* = 0.50$ (h) $t^* = 0.63$

Figure 5.1: Normalized instantaneous in-plane velocity magnitude $|\vec{u}^*|$ [-] at high M and 150 % Q_N. Every 3rd vector is represented

The velocity field can be transformed from a Cartesian coordinate system (with u and v) to a polar coordinate system with tangential velocities u_θ and radial velocities u_r:

$$\begin{aligned} u_\theta &= -u\sin(\theta) + v\cos(\theta) \\ u_r &= u\cos(\theta) + v\sin(\theta). \end{aligned} \tag{5.5}$$

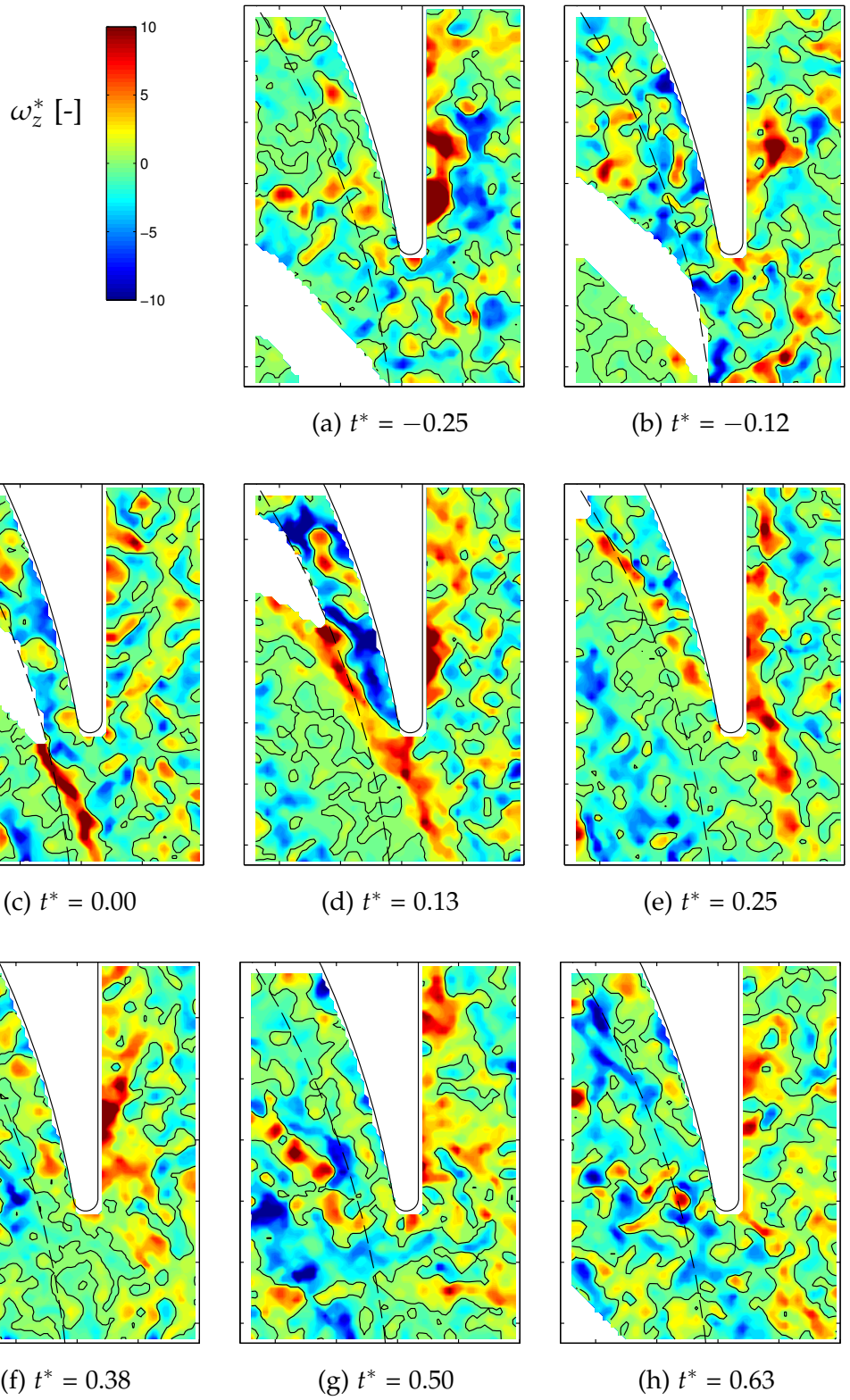

(a) $t^* = -0.25$ (b) $t^* = -0.12$

(c) $t^* = 0.00$ (d) $t^* = 0.13$ (e) $t^* = 0.25$

(f) $t^* = 0.38$ (g) $t^* = 0.50$ (h) $t^* = 0.63$

Figure 5.2: Normalized instantaneous vorticity ω_z^* [-] at high M and 150 % Q_N. Black contours at $\omega_z^* = 0$. Coordinates as in Fig. 5.1

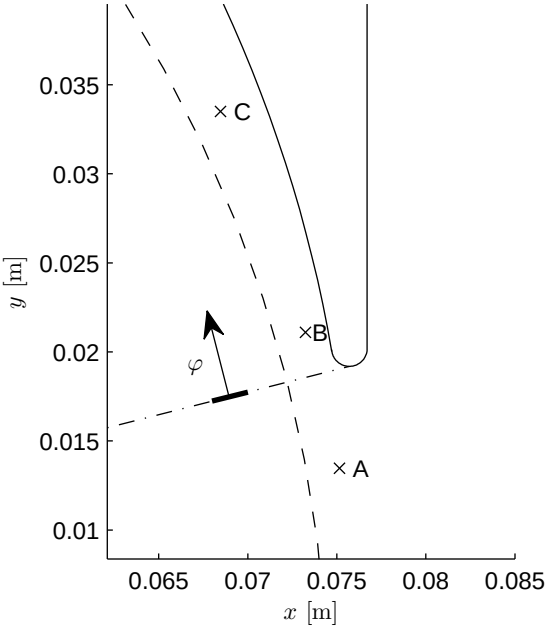

Figure 5.3: Location of reference points (in high magnification FOV) in volute at $1.02 \cdot r_{\text{tip}}$: A ($\varphi = -4°$), B ($\varphi = 2°$) and C ($\varphi = 12°$). Blade angular position φ is with respect to tongue tip and coordinate origin at pump axis. Dashed arc represents impeller outlet

In the polar coordinate system each point is defined by the angle θ and the radial distance r referred to the pump axis.
The complete velocity gradient tensor is (Raffel et al., 2007)

$$\frac{\partial u_i}{\partial x_j} = \begin{pmatrix} \frac{\partial u}{\partial x} & \frac{\partial u}{\partial y} & \frac{\partial u}{\partial z} \\ \frac{\partial v}{\partial x} & \frac{\partial v}{\partial y} & \frac{\partial v}{\partial z} \\ \frac{\partial w}{\partial x} & \frac{\partial w}{\partial y} & \frac{\partial w}{\partial z} \end{pmatrix}. \tag{5.6}$$

For 2D2C PIV only the blue marked velocity gradients can be obtained, which leads to a 2×2 matrix. For stereo PIV the velocity gradients of w in x and y direction are added: $(\partial w/\partial x)$, $(\partial w/\partial y)$. The velocity gradient tensor can be decomposed (Lesieur, 2008) into a symmetric (strain) and an antisymmetric (rotation) part

$$\frac{\partial u_i}{\partial x_j} = S_{ij} + \Omega_{ij}, \tag{5.7}$$

with the rate-of-strain tensor

$$S_{ij} = \frac{1}{2}\left(\frac{\partial u_i}{\partial x_j} + \frac{\partial u_j}{\partial x_i}\right) \tag{5.8}$$

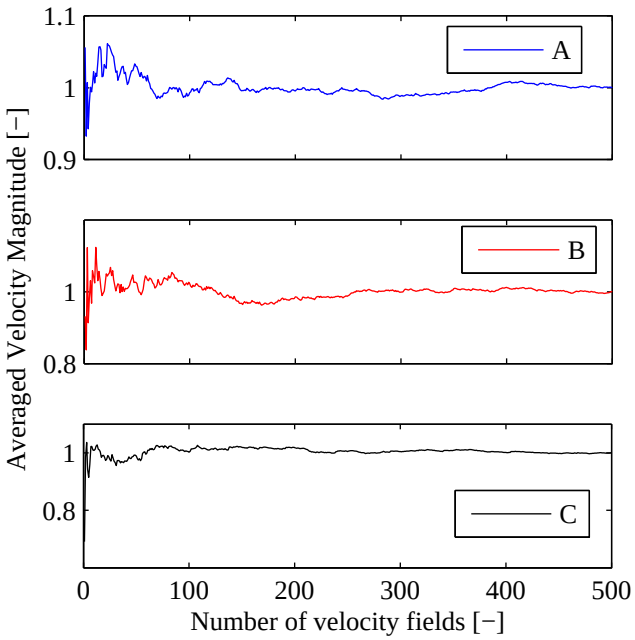

Figure 5.4: Convergence of normalized phase-averaged velocity magnitude as a function of the number of instantaneous velocity fields at three reference points (see Fig. 5.3 for location), for 150 % Q_N and blade at $\varphi = 22.5°$

and the rate-of-rotation tensor

$$\Omega_{ij} = \frac{1}{2}\left(\frac{\partial u_i}{\partial x_j} - \frac{\partial u_j}{\partial x_i}\right). \tag{5.9}$$

The vorticity is (Wu et al., 2006)

$$\vec{\omega} = \nabla \times \vec{U} = \text{curl}\ \vec{U} = \epsilon_{ijk}\frac{\partial u_k}{\partial x_j}. \tag{5.10}$$

For 2D2C PIV, and for stereo PIV, only the vorticity component out of the measurement plane can be computed as

$$\omega_z = \frac{\partial v}{\partial x} - \frac{\partial u}{\partial y}. \tag{5.11}$$

Vorticities were normalized by the vorticity of the impeller due to its solid rotation:

$$\omega_z^* = \frac{\omega_z}{2 \cdot \Omega} = \frac{\omega_z}{2 \cdot 2\pi\frac{f_{BP}}{6}}. \tag{5.12}$$

This means that a positive vorticity of one in the flow field has the same vorticity as the impeller with a counterclockwise rotation. Negative vorticity values mean clockwise rotation.

5.2 Relative phase-averaged velocity fields in impeller

The phase-averaged relative velocity field $\vec{W}$ is obtained by subtracting the local velocity of the impeller at each point from the phase-averaged absolute velocity field:

$$\vec{W} = \vec{U} - \vec{\Omega} \times \vec{r} \tag{5.13}$$

Representing relative velocities is only convenient for regions inside or close to the impeller. The arrow length and the color represent the relative in-plane velocity magnitude normalized by U_{tip} in Fig. 5.5 for 40 % Q_{N} at low magnification (low M).

In the impeller channels high relative velocities occur in the middle of the impeller channels (see Fig. 5.5a). After the blade has passed the tongue tip this zone of relatively high velocities deviates towards the suction side of the blade and leads to high radial velocities with high outflow (see Fig. 5.5e). The highest relative velocities are situated at the outlet of the impeller with values of about 0.5 U_{tip}, pointing in the negative tangential direction (opposite direction of the impeller rotation). In general, outflow with positive radial velocities (leaving the impeller) takes place at the impeller outlet behind the blade suction side, up to about half of the impeller channel. Whereas backflow at the impeller outlet occurs in the other half, except very close to the blade pressure side where radial velocities are positive again (see also radial velocity maps in appendix, Fig. B.14). The radial velocities at the impeller outlet in the channel ahead of the tongue are negative from $t^* = -0.25$ to -0.12 and from 0.13 to 0.75. This means that flow at the impeller outlet is modulated with a jet-wake pattern, so that periodic fluctuations are perceived in the volute, especially in the narrow region close to the tongue tip.

Depending on the blade position relative to the tongue, up to four different vortices can be found inside one impeller channel. A vortex is situated near the impeller outlet at the blade pressure region and is rotating clockwise, i.e. contrary to the impeller rotation. As the channel passes by the tongue tip this recirculation vortex gets larger and is observed best between $t^* = -0.25$ (see Fig. 5.5a) and $t^* = -0.12$ (see Fig. 5.5b). In the blade pressure region there is backflow with negative radial velocities. This leads to another clockwise rotating vortex which is situated at the blade pressure region close to the impeller inlet. A third vortex is situated between the two vortices described and is turning counterclockwise. The vortices are often hard to detect in the relative velocity maps due to the low relative velocities in these regions. However, they are also visible observing the vorticity fields described in section 5.5, with the clockwise rotating vortices having negative vorticity and the counterclockwise rotating vortices having positive vorticity.

Another vortex, which is always present, is situated in the blade suction region with backflow near the blade and turns counterclockwise (best observed at

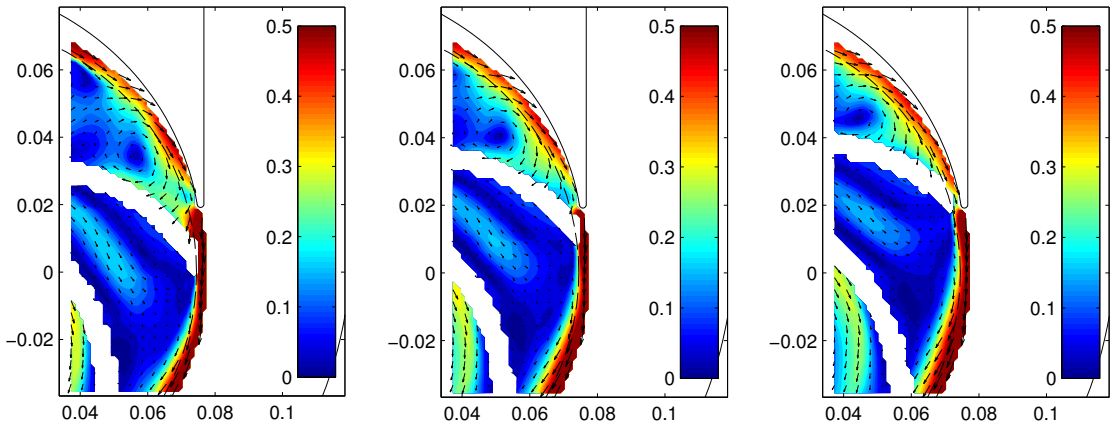

(a) $t^* = -0.25$ (b) $t^* = -0.12$ (c) $t^* = 0.00$

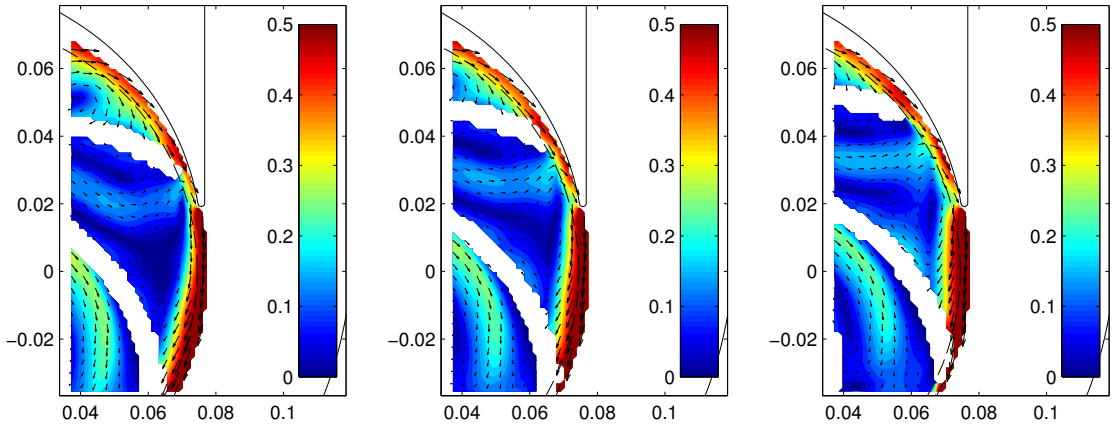

(d) $t^* = 0.13$ (e) $t^* = 0.25$ (f) $t^* = 0.38$

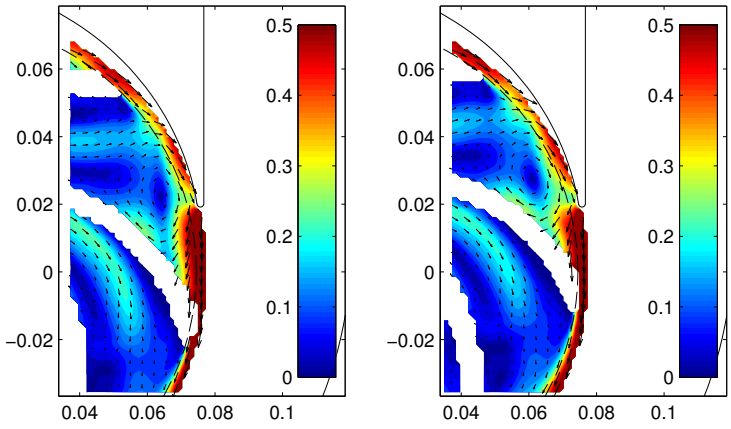

(g) $t^* = 0.50$ (h) $t^* = 0.63$

Figure 5.5: Normalized phase-averaged in-plane relative velocity magnitude W^* [-] at low M and 40 % Q_N. Region shown up to $1.05 \cdot r_{tip}$. Every 3rd vector is represented

$t^* = 0.13$ in Fig. 5.5d). The vortices at the suction and at the pressure region are independent, which means that they are not moving from the suction to the pressure region or vice versa. The vortices coexist, e.g. at $t^* = 0.38$ (see Fig. 5.5f), separated by the principal flow stream which concentrates in the central zone of the channel. The vortices result from the adverse pressure gradient ($\partial p/\partial r > 0$, as pressure is rising from inlet to outlet), from flow separation at the leading edge on the blade suction side due to the low flow-rate and from the fact that the flow tries to maintain its angular momentum and therefore rotates contrary to the impeller rotation.

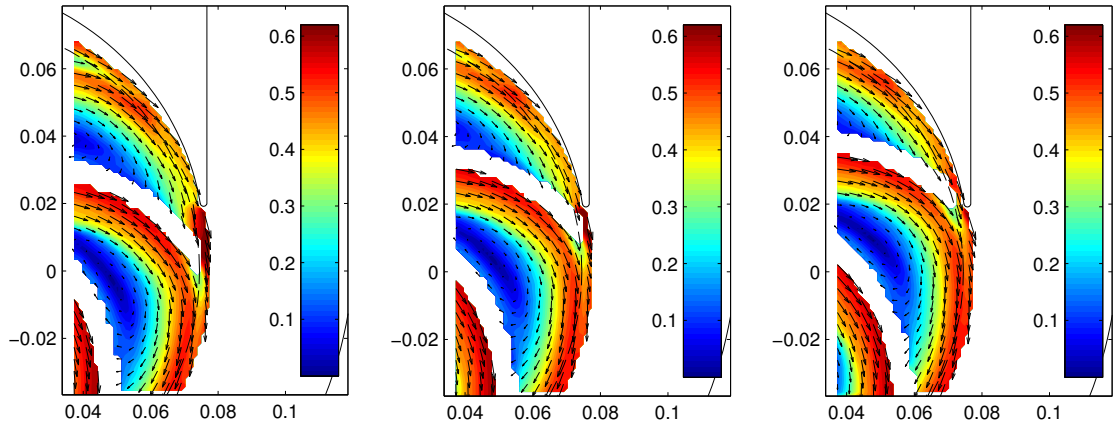

(a) $t^* = -0.25$ (b) $t^* = -0.12$ (c) $t^* = 0.00$

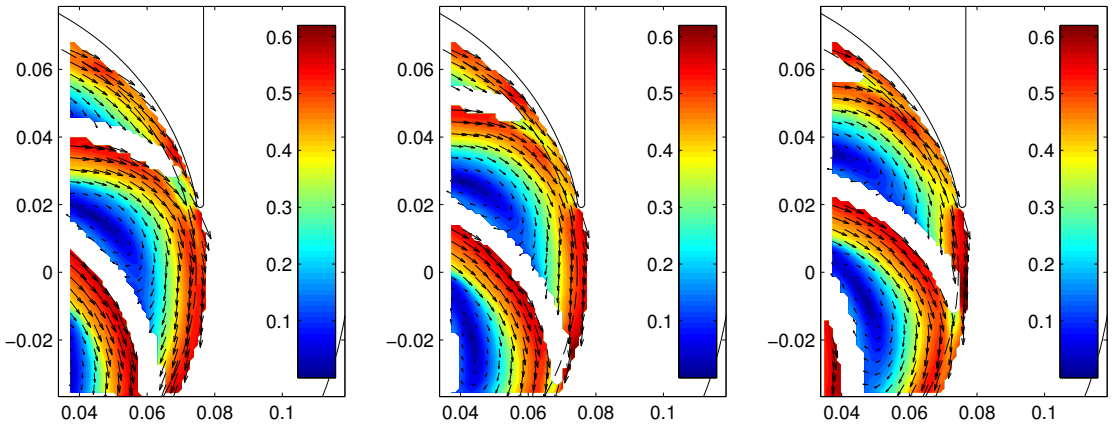

(d) $t^* = 0.13$ (e) $t^* = 0.38$ (f) $t^* = 0.63$

Figure 5.6: Normalized phase-averaged in-plane relative velocity magnitude W^* [-] at low M and Q_N. Region shown up to $1.05 \cdot r_{tip}$. Every 3rd vector is represented

The flow patterns of the relative velocities for Q_N are shown in Fig. 5.6. The flow through the impeller consists mainly of two flow structures *(i)* a throughflow which is basically a uniform flow through the channels resulting in the flow-rate measured in the pipes and *(ii)* a counterrotating flow due to the trend of

the flow to maintain its angular momentum (Brennen, 1994). For this pump this leads to a clockwise rotating movement. The combination of these two flow structures leads to higher velocities at the blade suction region and lower velocities with backflow at the pressure region. This results in a large (elliptical shaped) clockwise rotating vortex covering the whole channel. However, the negative radial velocities (backflow) at the blade pressure side are low.

The highest velocities occur in the blade suction region with a high radial component. Furthermore, relative velocities are high at the impeller outlet, but with the main velocity component pointing in the negative tangential direction. As the blade passes the tongue tip a zone of high relative velocity builds up ahead of the tongue tip (Fig. 5.6d). After the blade has passed the tongue the relative flow pattern in the impeller is basically the same, but with lower relative velocities at the impeller outlet. The radial velocity component at the impeller outlet is small and positive almost all the time. Only in a small zone near the inner side of the tongue u_r is negative from $t^* = -0.25$ to -0.03 and from 0.22 to 0.75.

For a flow-rate of 150 % Q_N Fig. 5.7 shows the relative velocity map obtained for the impeller region at different time instants during one blade passage period. The flow pattern of the relative velocities is similar to Q_N, but with a larger extension of the principal flow current inside the impeller channels. The relative velocities are higher than for Q_N, reaching values of up to about the absolute blade tip speed (U_{tip}).

The relative flow in the rotating channels concentrates in the region close to the blade suction side, whereas low velocity backflow can be observed on the blade pressure side. The result is a large clockwise rotating vortex. This is an expectable behaviour, already seen for the nominal flow-rate. The two main flow structures are a throughflow related to the pumped flow and a counterrotating flow due to the trend of the flow trying to maintain its angular momentum. Additionally, this behaviour is reinforced by the early flow detachment from the pressure side of the blade leading edge, as corresponds to flow-rates above the nominal flow-rate.

In general, the radial velocity component at the channel outlet tends to diminish from the suction to the pressure side, so that close to the pressure side velocity becomes almost tangential (see Fig. 5.7c). Hence, flow at the impeller outlet is modulated with a jet-wake pattern. This means that periodic fluctuations are perceived at any position in the volute. In the tongue region, once the blade has passed the tongue tip (see Fig. 5.7f), the relative velocity magnitude at the impeller outlet increases though it remains mostly tangential in the negative direction. This is because flow in the volute close to the tongue tip tends to leak towards the pump outlet for very high flow-rates, like the present one. The flow is always exiting the impeller outlet, even near the tongue tip (u_r>0). After the blade has passed the tongue the relative flow pattern in the impeller is basically the same, but with higher relative velocities at the impeller outlet. This is contrary to the observations made for the nominal flow-rate.

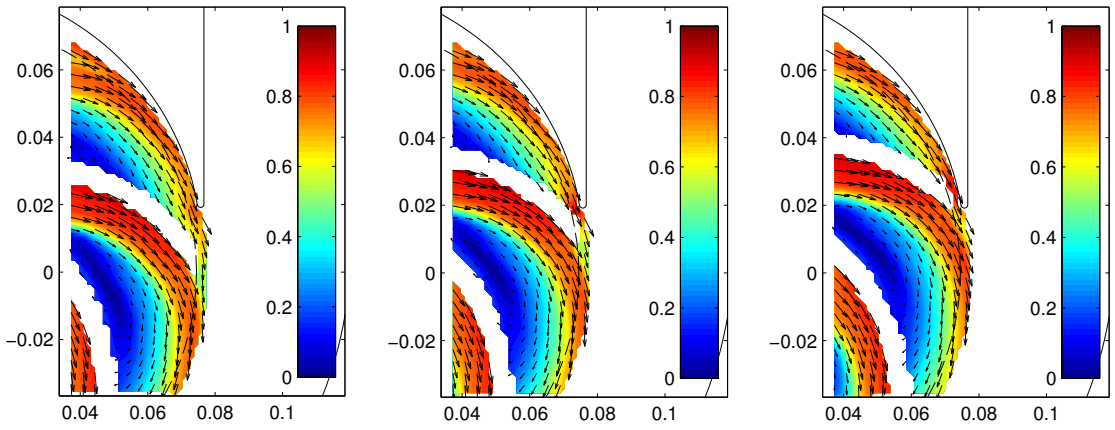

(a) $t^* = -0.25$ (b) $t^* = -0.12$ (c) $t^* = 0.00$

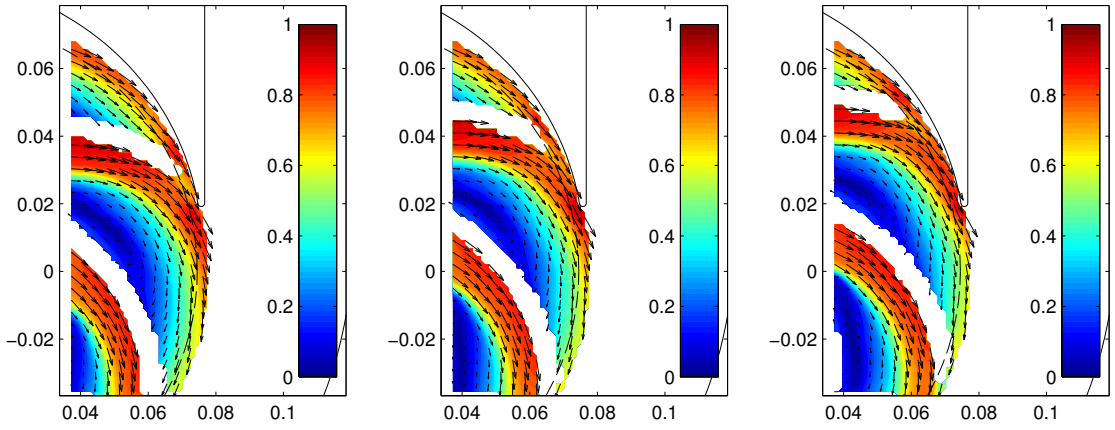

(d) $t^* = 0.13$ (e) $t^* = 0.25$ (f) $t^* = 0.38$

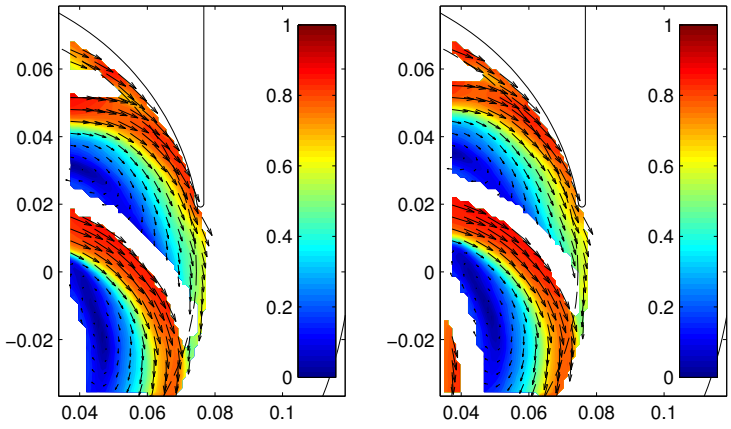

(g) $t^* = 0.50$ (h) $t^* = 0.63$

Figure 5.7: Normalized phase-averaged in-plane relative velocity magnitude W^* [-] at low M and 150 % Q_N. Region shown up to 1.05·r_{tip}. Every 3rd vector is represented

5.3 Absolute phase-averaged velocity fields

The absolute in-plane velocity maps for 40 % Q_N, normalized by U_{tip}, are shown in Fig. 5.8 (low magnification) and in Fig. 5.9 (high magnification). The time history of the absolute velocity is summarized in eight instants. Absolute velocities for 40 % Q_N inside the impeller are higher than for the other flow-rates, namely up to about U_{tip}. As the flow through the impeller is low, the absolute velocity (in magnitude and direction) is close to the tangential blade velocity. This is particularly visible at the blade suction region, where the flow velocities are very similar to the blade velocities in direction and magnitude.

For 40 % Q_N absolute velocities are highest right behind the blade trailing edge in the blade suction region, before the blade aligns with the tongue tip (Fig. 5.8b). This zone of high velocity starts to extend as the blade moves on and reaches the blade pressure side (Fig. 5.8f). It splits up, with the larger zone of high velocities corresponding now to the blade pressure side (Fig. 5.8h). Absolute velocities reduce towards the pump exit, as the flow-rate is low.

The details of flow evolution in the tongue region, where most of the rotor-stator interaction takes place, can be better observed in the velocity fields obtained from the high magnification measurements. For 40 % Q_N a stagnation zone is situated at the exit side of the tongue. This leads to flow separation from the tongue tip (see Fig. 5.9) and a small zone with very high velocities in the narrow region of the volute next to the tongue tip. High velocity gradients in the tangential direction are found in the narrow volute channel between the impeller and the tongue tip, especially when the blade lines up with the tongue tip at $t^* = 0.00$ (Fig. 5.9c). The high velocities in the narrow zone of the volute correspond to low pressure which leads to this flow recirculation due to the low flow-rate. The flow is accelerated as it enters the volute through the narrow impeller-tongue gap and recirculates. Just afterwards velocities reduce to a minimum in the wake region of the tongue tip (Fig. 5.9d).

For Q_N the results of the normalized absolute in-plane velocity magnitude at low magnification are shown in Fig. 5.10. Absolute velocities only achieve about 70 % of the blade tip speed. High absolute velocities are found in the blade pressure region, which indicates flow separation from the blade leading edge.

In the high magnification FOV it can be seen that velocities for Q_N are also high on the suction side near the blade tip (see Fig. 5.11). This is due to the wake behind the blade with relative velocities being close to zero (see also Fig. 5.14b). There is also an increment in velocity magnitude in the narrow channel between impeller and tongue tip as for 40 % Q_N, but less pronounced, as it is the nominal flow-rate. The stagnation point does not move for the nominal flow-rate and is always situated at the tongue tip, as expected, leading to a much more uniform outflow in the outlet duct compared to the other flow-rates.

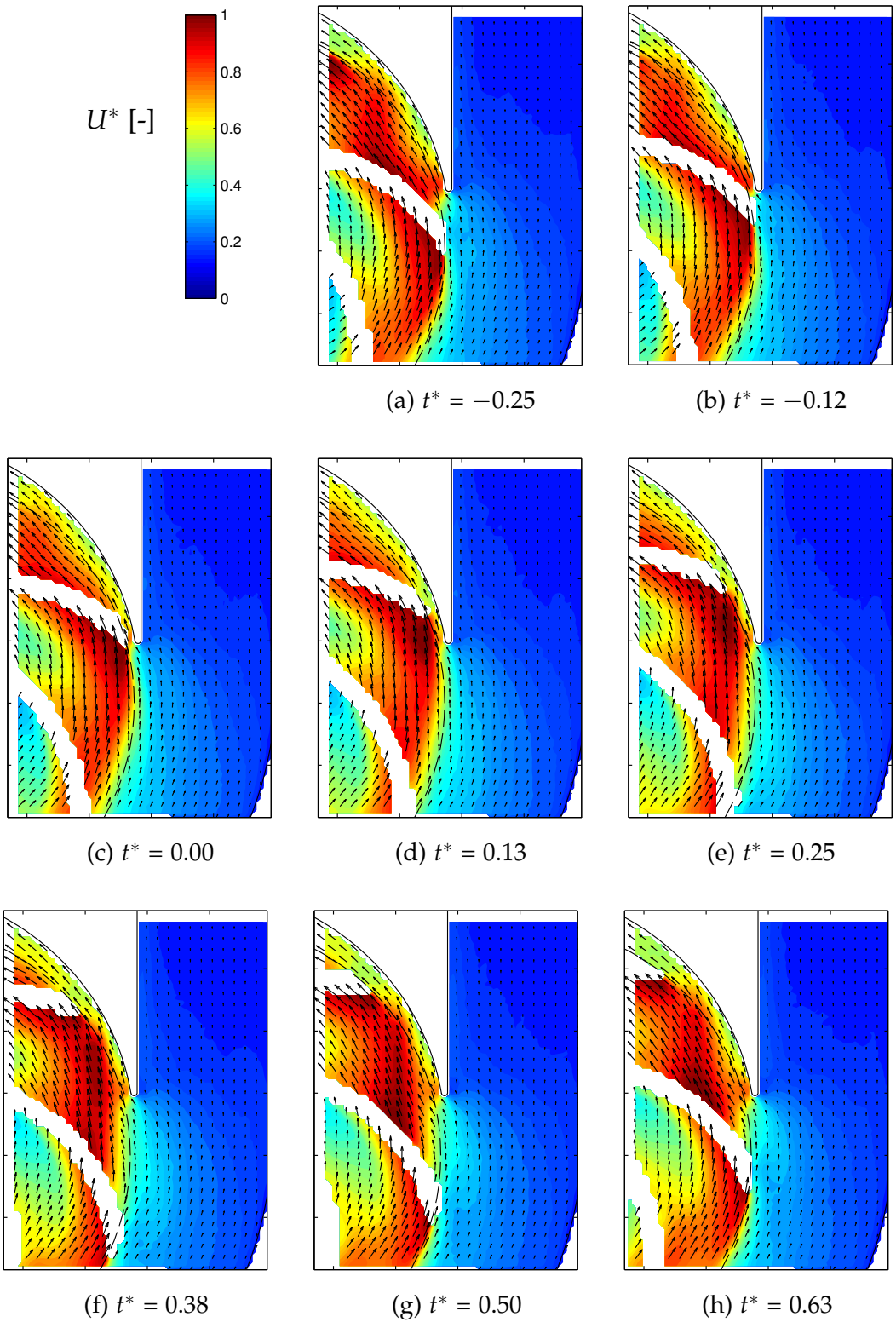

(a) $t^* = -0.25$ (b) $t^* = -0.12$

(c) $t^* = 0.00$ (d) $t^* = 0.13$ (e) $t^* = 0.25$

(f) $t^* = 0.38$ (g) $t^* = 0.50$ (h) $t^* = 0.63$

Figure 5.8: Normalized phase-averaged in-plane velocity magnitude U^* [-] at low M and 40 % Q_N. Every 3rd vector is represented

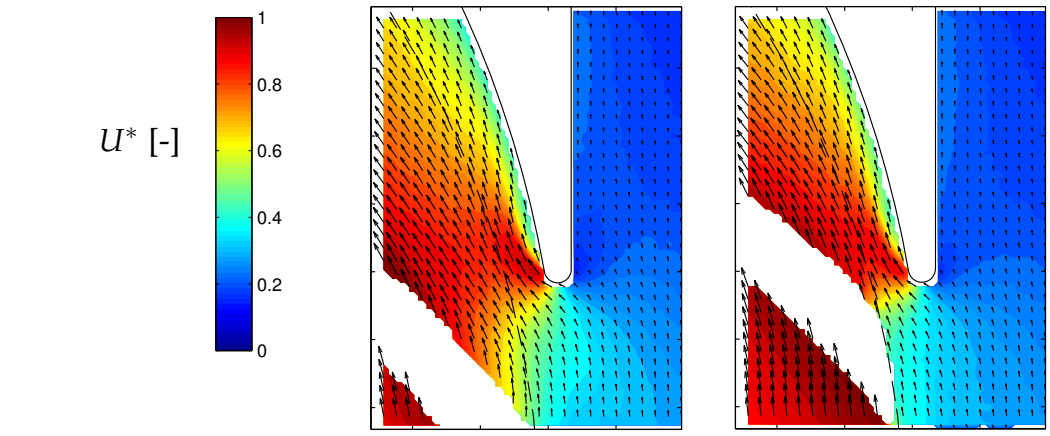

(a) $t^* = -0.25$ (b) $t^* = -0.12$

(c) $t^* = 0.00$ (d) $t^* = 0.13$ (e) $t^* = 0.25$

(f) $t^* = 0.38$ (g) $t^* = 0.50$ (h) $t^* = 0.63$

Figure 5.9: Normalized phase-averaged in-plane velocity magnitude U^* [-] at high M and 40 % Q_N. Every 3rd vector is represented

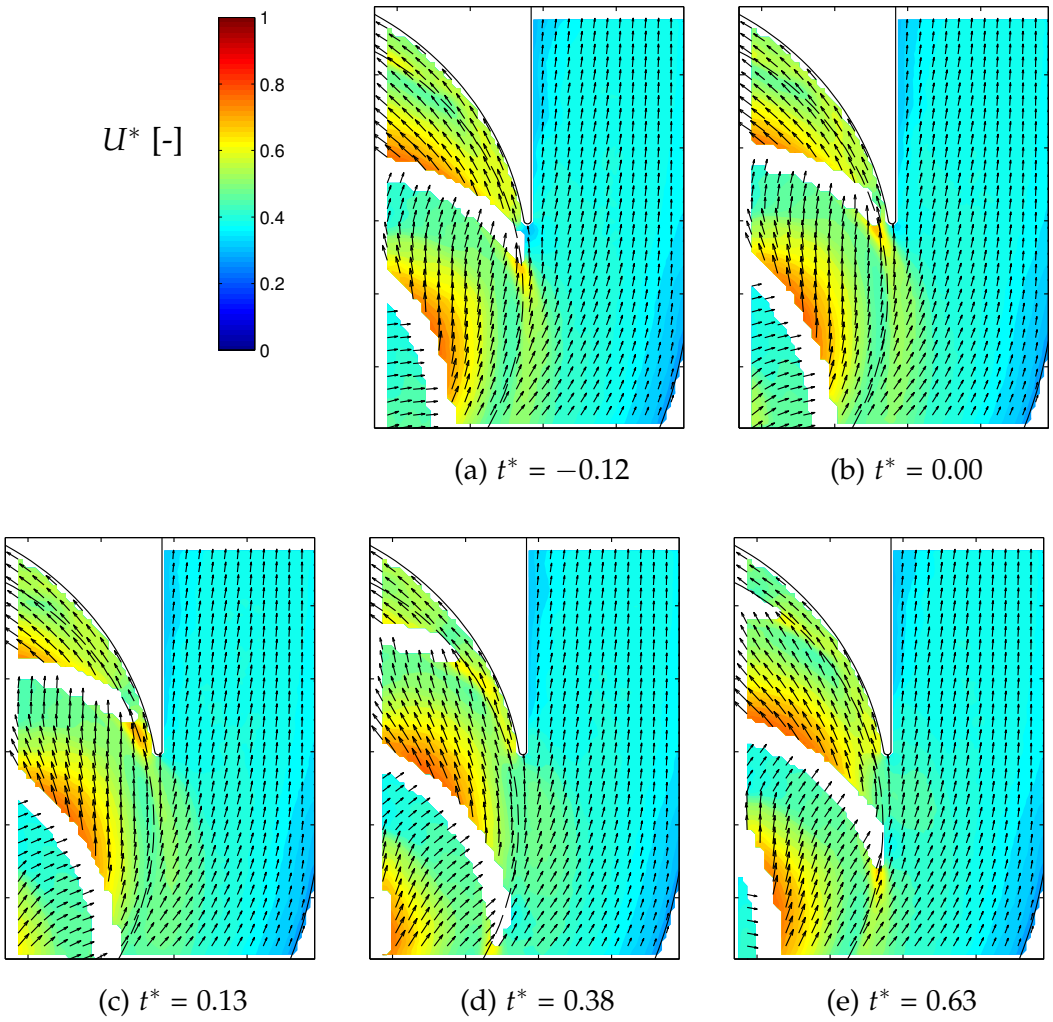

(a) $t^* = -0.12$ (b) $t^* = 0.00$

(c) $t^* = 0.13$ (d) $t^* = 0.38$ (e) $t^* = 0.63$

Figure 5.10: Normalized phase-averaged in-plane velocity magnitude U^* [-] at low M and Q_N. Every 3rd vector is represented

For 150 % Q_N the time history of the absolute velocity maps at low magnification is shown in Fig. 5.12. Absolute velocities achieve about 80 % of U_{tip}. Along the middle of the impeller channels there is a low velocity zone that progressively shifts towards the blade suction side and then, at the impeller outlet, continues extending along the negative tangential direction while reducing further in magnitude. At the impeller outlet, velocity is particularly low in the narrow region of the volute (see Fig. 5.12c), with minimum values at the blade pressure side and close to the tongue tip (see Fig. 5.12f). Again, this is the foreseeable behaviour for high flow-rates: velocity is expected to increase along the volute, so that maximum values are achieved at the outlet duct. Also, stagnation at the tongue tip is located on its interior side (see Fig. 5.12f), so that a wake is formed on its exterior side, thus contributing to shift the outcoming flow away from the tongue.

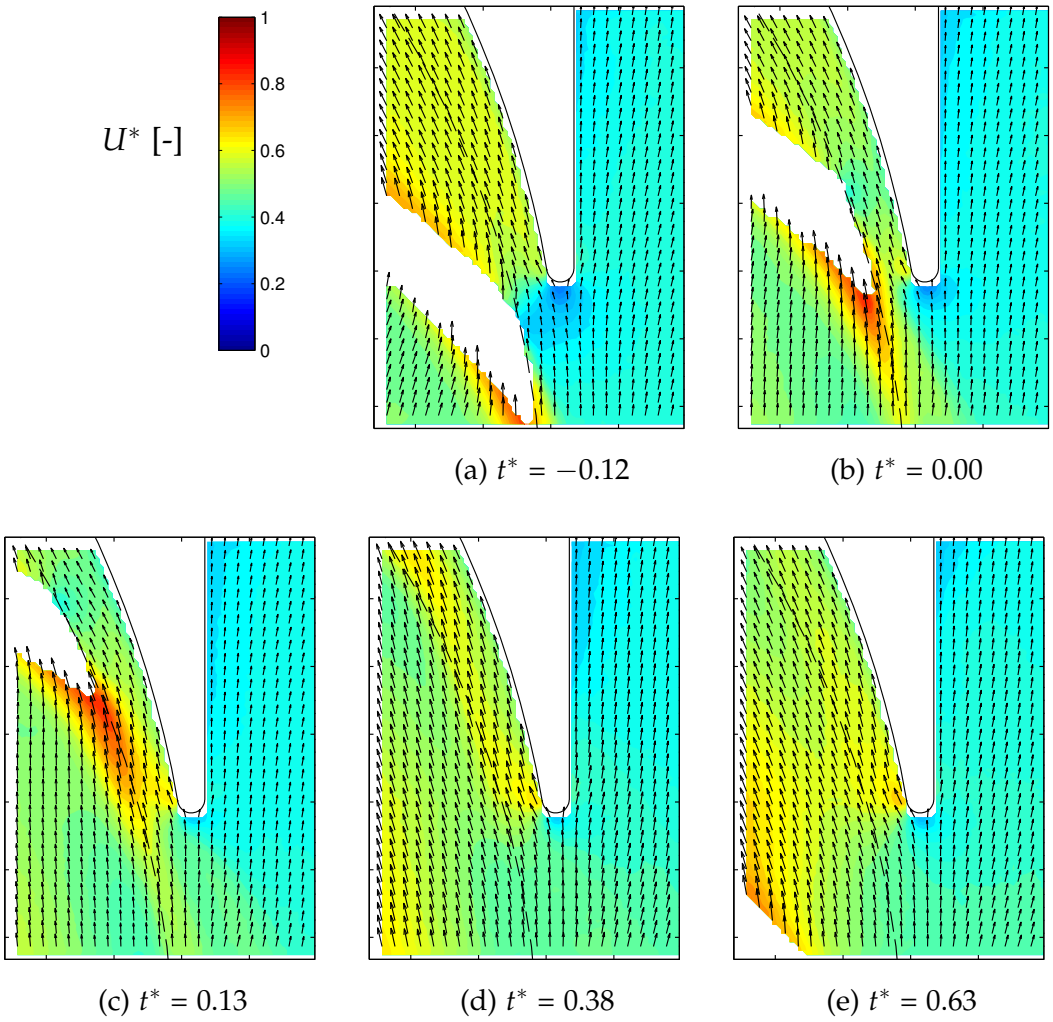

(a) $t^* = -0.12$ (b) $t^* = 0.00$

(c) $t^* = 0.13$ (d) $t^* = 0.38$ (e) $t^* = 0.63$

Figure 5.11: Normalized phase-averaged in-plane velocity magnitude U^* [-] at high M and Q_N. Every 3rd vector is represented

Figure 5.13 presents the normalized absolute in-plane velocity fields for 150 % Q_N at high magnification summarized in eight instants. This high magnification FOV shows that, as the blade reaches the tongue tip ($t^* = -0.12$), the low velocity zones corresponding to the pressure side of the blade trailing edge and to the stagnation point on the tongue get closer until coinciding just before $t^* = 0.00$. Therefore, at that instant the blockage for the leakage flow becomes maximum. This implies that the flow exiting the impeller behind that blade, including the high velocity sheet that is associated to the blade wake in the relative frame, has to deviate towards the pump outlet. Hence, the velocity magnitude at the external side of the tongue tip reaches a maximum at about $t^* = 0.13$. The wake of the blade, characterized by high absolute velocity, counteracts the low velocity region surrounding the stagnation point on the tongue, so that velocities in this zone achieve a maximum at that instant. With the blade further away from the tongue ($t^* = 0.38$) the flow on the internal side of the tongue develops again

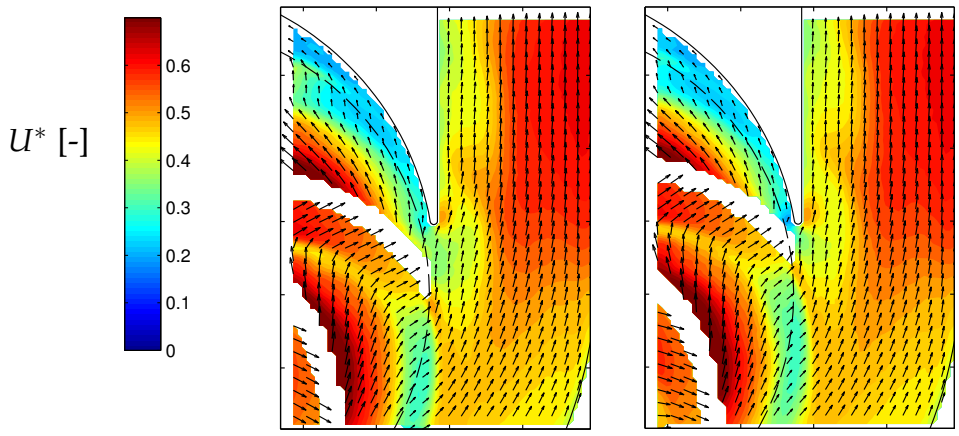

(a) $t^* = -0.25$ (b) $t^* = -0.12$

(c) $t^* = 0.00$ (d) $t^* = 0.13$ (e) $t^* = 0.25$

(f) $t^* = 0.38$ (g) $t^* = 0.50$ (h) $t^* = 0.63$

Figure 5.12: Normalized phase-averaged in-plane velocity magnitude U^* [-] at low M and 150 % Q_N. Every 3rd vector is represented

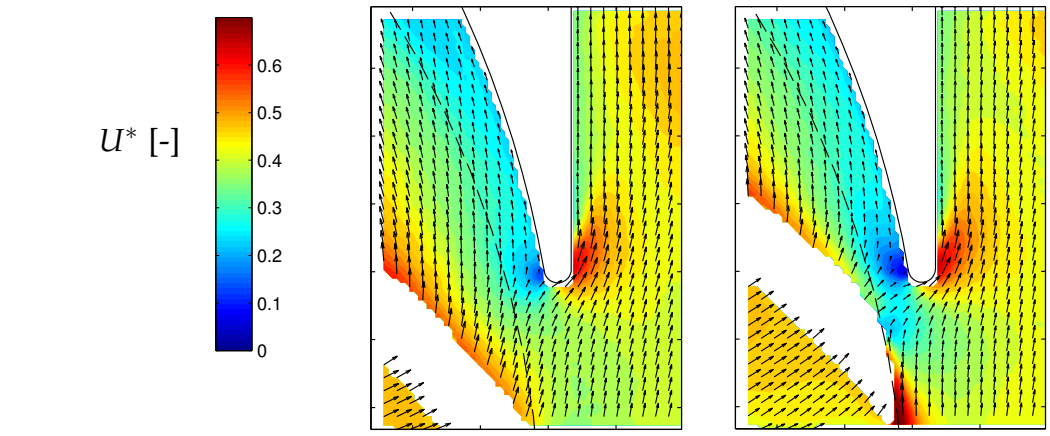

(a) $t^* = -0.25$ (b) $t^* = -0.12$

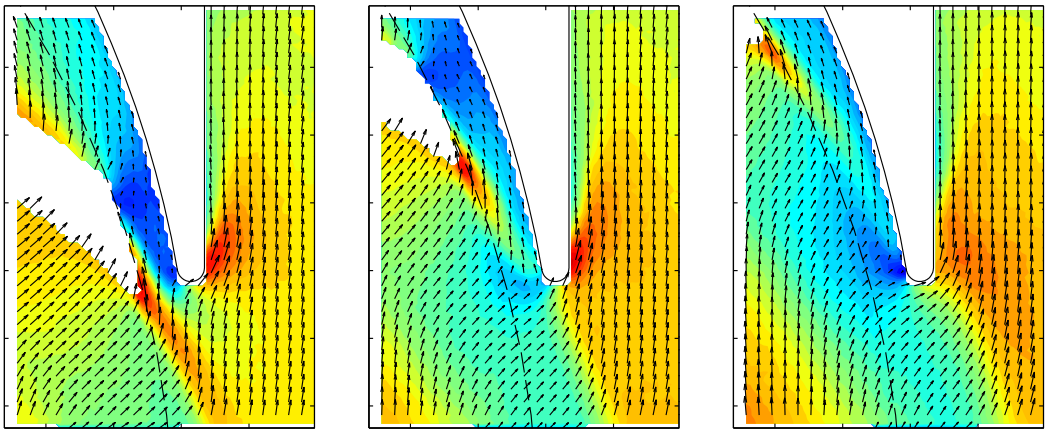

(c) $t^* = 0.00$ (d) $t^* = 0.13$ (e) $t^* = 0.25$

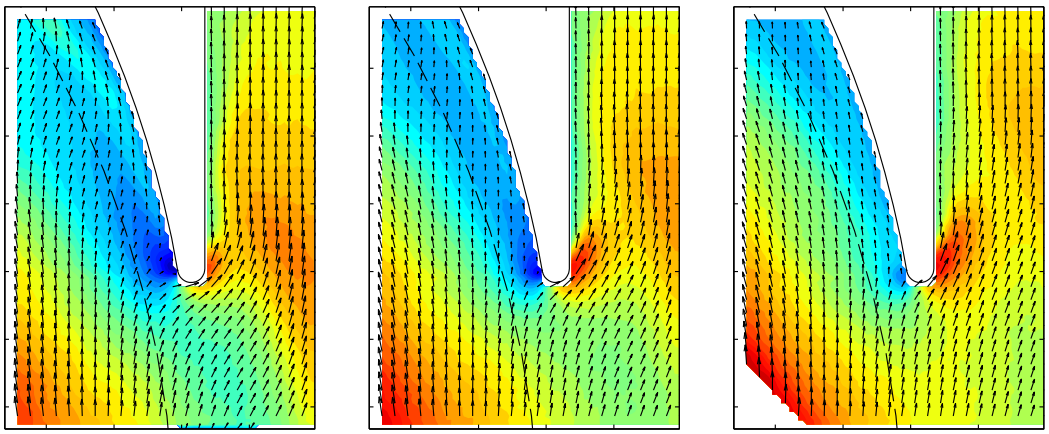

(f) $t^* = 0.38$ (g) $t^* = 0.50$ (h) $t^* = 0.63$

Figure 5.13: Normalized phase-averaged in-plane velocity magnitude U^* [-] at high M and 150 % Q_N. Every 3rd vector is represented

a pronounced stagnation region. Afterwards, as the next blade approaches the tongue ($t^* = 0.63$), the flow impelled by it reaches the tongue region so that velocity increases all around the tongue and the stagnation point gets less distinctive.

A zoom of the relative in-plane velocity with the blade lining up with the tongue tip ($t^* = 0.00$) is shown in Fig. 5.14 for the three different flow-rates.
For 40 % Q_N relative velocities behind the blade suction side are very low and are pointing in the tangential direction (see Fig. 5.14a). Behind the impeller outlet they are pointing in the negative tangential direction. This leads to high velocity gradients in the radial direction ($\partial u_\theta / \partial r$).
For Q_N the boundary layer can be clearly identified. At the suction side of the blade trailing edge, the blade wake with low relative velocities is well delimited and is situated inside the impeller channel (see Fig. 5.14b).
For 150 % Q_N the boundary layer can be observed at the blade suction side (see Fig. 5.14c) with higher relative velocities than for the nominal flow-rate. Downwards the blade trailing edge, the wake is very well delimited, showing sharp velocity gradients with respect to the flow exiting the impeller from both sides of the blade. The high velocity zone on the inner side of the tongue tip actually corresponds to the stagnation region in the absolute frame (Fig. 5.13c). Similarly, the blade wake in the relative frame appears as a high velocity jet once in the absolute frame.

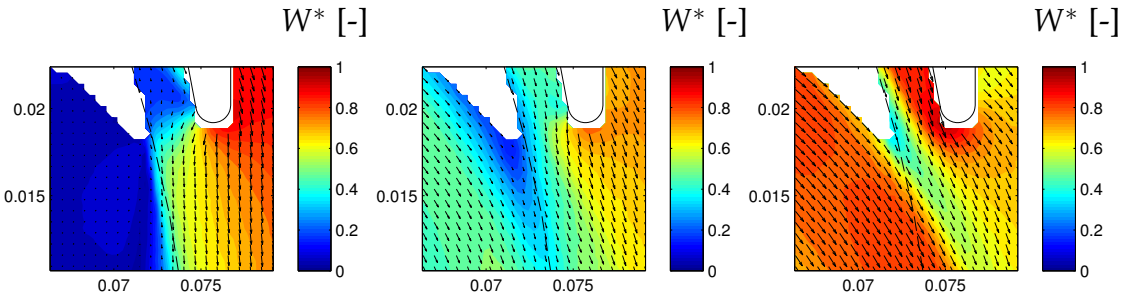

(a) 40 % Q_N (b) Q_N (c) 150 % Q_N

Figure 5.14: Normalized phase-averaged relative in-plane velocity magnitude W^* [-] at $t^* = 0.00$ with zoom into high M. Every 2nd vector is represented

5.4 Results of stereo PIV

All three velocity components, including the out-of-plane velocity component w, can be obtained in the measurement plane using two cameras with an oblique viewing angle (see section 4.1.3 for a description of the setup). Figures 5.15, 5.16 and 5.17 show the out-of-plane velocity component w normalized by U_{tip} for

the three different flow-rates. Positive w is pointing towards the pump inlet, i.e. towards the suction pipe.

For 40 % Q_N the out-of-plane velocity component w is relatively high, about 10% of the blade tip speed U_{tip}, in the blade tip vicinity (see Fig. 5.15). For $t^* = -0.25$, before the blade arrives at the tongue tip, there is a high out-of-plane component on the blade pressure side at the blade tip, i.e. in the narrow gap between blade tip and tongue tip. After the blade has passed the tongue tip, positive w is found in the wake of the blade and stretches along the impeller outlet. Further away from the impeller (at $1.11r_{tip}$) w becomes negative in the pump exit. Above the tongue tip, positive w extends up to about half of the pump exit. This means that the flow describes a longitudinal stretched vorticity tube.

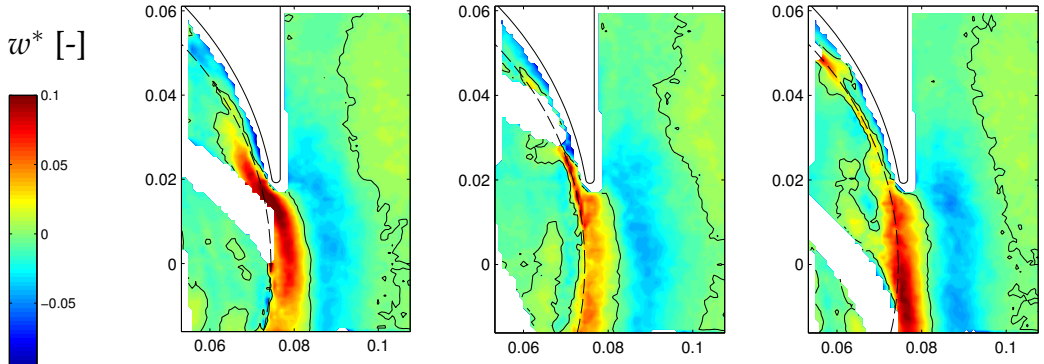

(a) $t^* = -0.25$ (b) $t^* = 0.13$ (c) $t^* = 0.44$

Figure 5.15: Normalized phase-averaged out-of-plane velocity component w^* [-] using stereo PIV at 40 % Q_N

For Q_N (Fig. 5.16) maximum positive values of w are lower than for 40 % Q_N. At $t^* = -0.25$ a distinctive positive zone with high w stretches from the tongue downwards and shifts along the pump exit wall of the tongue as the impeller turns (Fig. 5.16b). A zone with negative w is situated at $t^* = -0.25$ behind the blade tip. At $t^* = 0.06$ this zone hits the tongue tip and is convected afterwards towards the pump outlet ($t^* = 0.44$). Behind the blade tip at the suction side w is positive again. In the pump exit channel w is mainly positive at the half closer to the tongue and mainly negative at the other half. This means that a vorticity tube with axis in the tangential direction is formed at the periphery of the impeller close to the tongue, which progresses towards the outlet duct while extending. For this flow-rate it is rotating the other way (signs of w are changed) compared to 40 % Q_N.

For 150 % Q_N (Fig. 5.17) w is positive at the blade suction side and changing to negative values at about the middle of the impeller channel. This leads to negative values of w along the blade pressure side. However, along the impeller outlet w is predominantly positive. In the outlet channel w is mainly negative

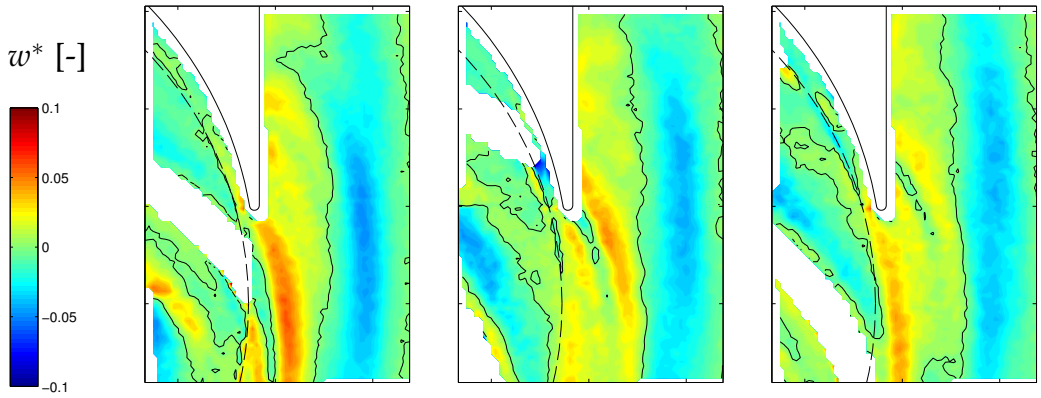

(a) $t^* = -0.25$ (b) $t^* = 0.13$ (c) $t^* = 0.44$

Figure 5.16: Normalized phase-averaged out-of-plane velocity component w^* [-] using stereo PIV at Q_N

and attenuates towards the pump outlet. Positive values are situated along the exit wall away from the tongue. w is also high in the outlet channel in the tongue wake (see Figs. 5.17a and 5.17c) due to the flow separation from the tongue tip. At $t^* = 0.13$ w is negative in most of the tongue wake due to the negative zone coming from the impeller. The zone of positive w, situated before at the tongue tip (Fig. 5.17a), has moved closer to the outlet due to this zone of negative w (Fig. 5.17b). At $t^* = 0.44$ (Fig. 5.17c) two zones of positive w are visible. One is near the pump outlet, already described, and has been convected with the stream. The other one with high w is situated again in the wake region of the tongue tip.

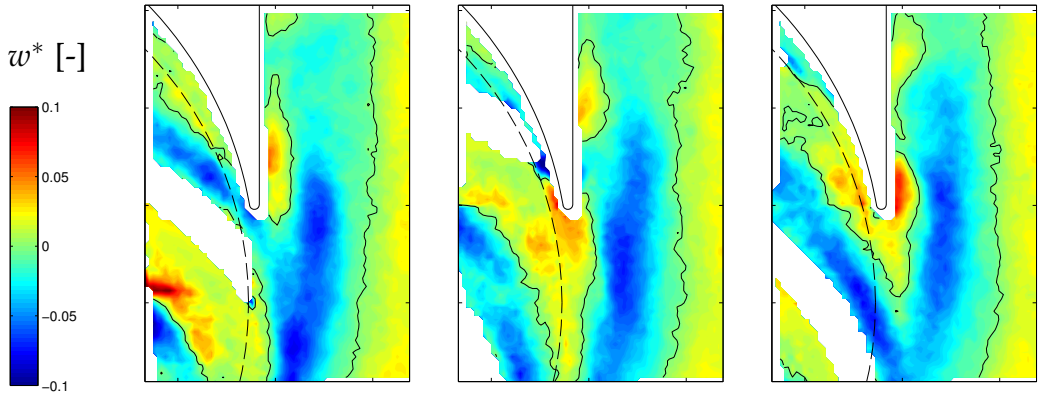

(a) $t^* = -0.25$ (b) $t^* = 0.13$ (c) $t^* = 0.44$

Figure 5.17: Normalized phase-averaged out-of-plane velocity component w^* [-] using stereo PIV at 150 % Q_N

Due to the oblique viewing angle of the cameras the velocity could not be measured close to the blade and volute walls. This also means that the velocities in the gap between impeller and tongue could not be resolved properly. For

all three flow-rates the out-of-plane velocity component w is relatively small ($\leq 0.1 U_{tip}$). To be able to describe the flow near the walls and in the narrow impeller-volute gap the other results presented were made with one camera.

5.5 Phase-averaged vorticity fields

Due to the phase-averaging of the velocity fields the individual vortices, such as these shed from the blade trailing edge or tongue tip, cannot be seen directly in the vorticity fields. This is because the frequencies of the shedding of vortices are normally several times higher than the rotation frequency f_R or its harmonics. However, the locations where these vortices are formed coincide with high vorticity sheets in the phase-averaged vorticity fields.

Figure 5.18 shows the evolution of the normalized phase-averaged out-of-plane vorticity field ω_z^* for 40 % Q_N at eight time instants during one blade passage period. Vorticities were normalized by the vorticity of the impeller due to its solid rotation ($2 \cdot \Omega$).
The vorticity in the impeller is mainly positive and higher at the blade suction region than at the blade pressure region. The positive vorticity in the blade suction region is due to the adverse pressure gradient ($\partial p / \partial r > 0$). This leads to a rapid increase of the boundary layer and therefore to flow separation with a counterclockwise rotating vortex. This generates backflow near the blade suction side (see also section 5.2). The adverse pressure gradient and therefore the ease of flow separation is especially strong for low flow-rates, as the pressure rise is higher than for nominal or above nominal flow-rate.
Behind the blade trailing edge a region with high negative vorticity is observed. It starts at the blade tip of the suction side (see also high M in Fig. 5.19c). It is mainly due to the high radial velocity gradient from the high absolute velocities behind the blade to low absolute velocities behind the impeller outlet ($\partial u_\theta / \partial r$), see also Fig. 5.9. It extends over the whole blade passage having mainly a negative tangential direction following the impeller outlet. This is valid when the blade has not arrived at the tongue tip (Figs. 5.18a and 5.18b). As soon as the blade passes the tongue tip this negative vorticity zone moves towards the inner zone of the impeller channel ($t^* = 0.38$ to 0.63) and hits the pressure side of the following blade. It extends over a large portion of the blade (see upper half of Fig. 5.18b). This vorticity zone corresponds to the vortex visible near the blade pressure side in the relative velocity maps (see Fig. 5.5).
The interaction of the different vorticity zones in the tongue region can be better seen at the high magnification FOV in Fig. 5.19 for 40 % Q_N. Note the change in scale which now ranges from -12 to 4 times the impeller vorticity. The strong negative vorticity zone next to the tongue tip in the narrow region of the volute is due to the flow detachment from the tongue tip. This could not be properly seen in the low magnification vorticity maps of Fig. 5.18 because of the low

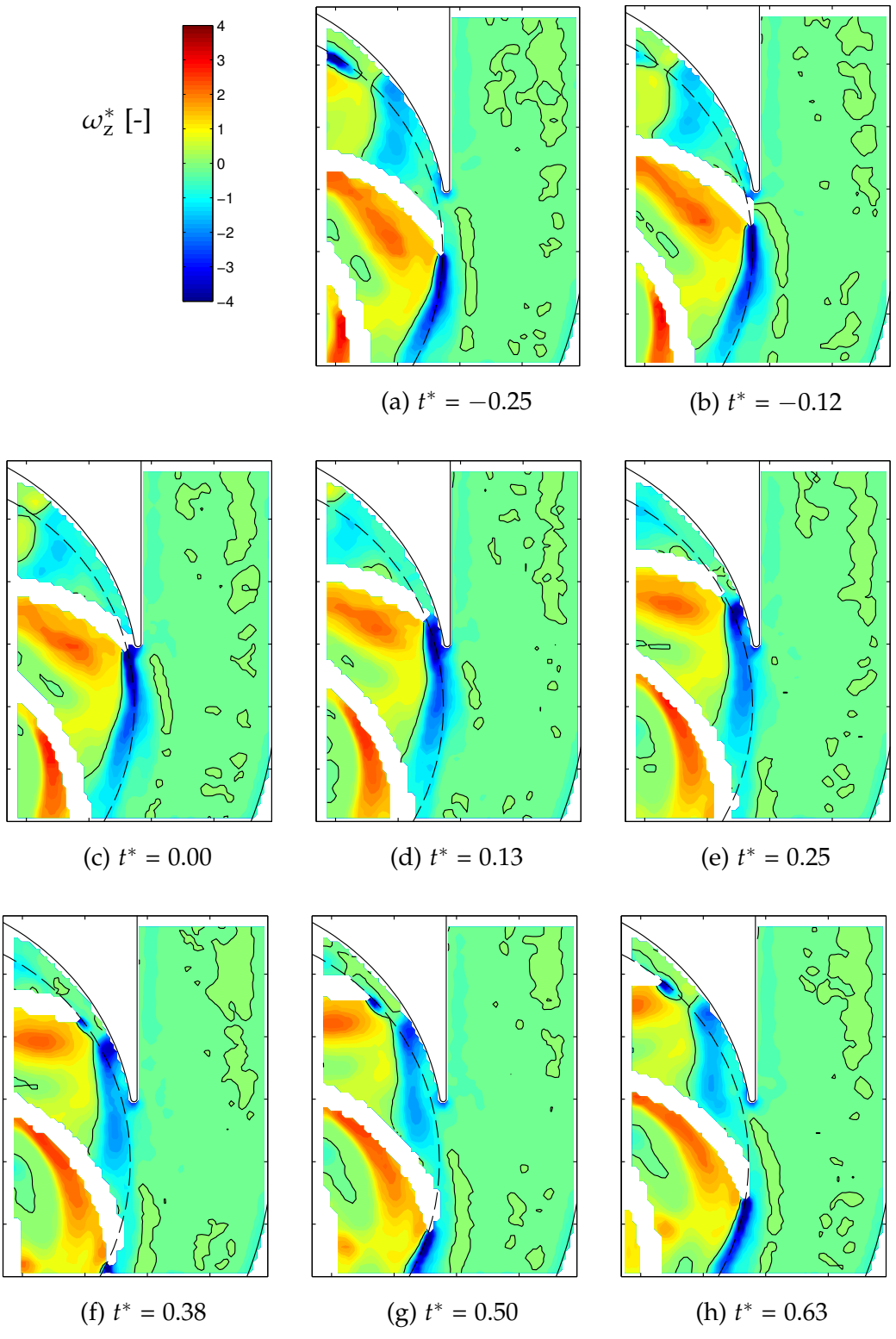

(a) $t^* = -0.25$ (b) $t^* = -0.12$

(c) $t^* = 0.00$ (d) $t^* = 0.13$ (e) $t^* = 0.25$

(f) $t^* = 0.38$ (g) $t^* = 0.50$ (h) $t^* = 0.63$

Figure 5.18: Normalized phase-averaged vorticity ω_z^* [-] at low M and 40 % Q_N. Black contours at $\omega_z^* = 0$

spatial resolution. As the blade passes the tongue tip flow detachment from the tongue tip is reduced, leading to vorticity values closer to zero (see Fig. 5.19c).

As the blade passes the tongue the negative vorticity sheet behind the blade tip changes its shape and deviates towards the volute. It separates from the blade tip (Fig. 5.19d) due to the high radial velocities. The positive vorticity zone at the blade suction side extends slightly over the impeller radius into the volute channel with high absolute velocities (Fig. 5.9d). The negative vorticity zone changes from a vorticity sheet (longitudinal stretched shape), situated at the blade tip, to a circular vorticity shape which moves to the centre of the volute channel. There it decays, while a new negative vorticity sheet starts to form from the blade tip at the suction side (see Fig. 5.19e). It gets larger as the blade rotates further away from the tongue (see Fig. 5.18h). Extreme normalized vorticity values range from about -18 in the narrow zone of the volute up to about +4 times the impeller vorticity.

For Q_N the vorticity evolution is shown in Fig. 5.20 using the low magnification FOV. Vorticity in nearly the whole impeller channel is negative with values close to zero ($-1 < \omega_z < 0$). This means that the flow in the impeller tries to oppose the impeller rotation. An exception is a small zone in the middle of the channel with more negative values, which suggests flow detachment from the blade leading edge. This means that the blade inlet angle should be slightly higher. Adjacent to the blade suction side is a layer with positive vorticity which grows in extension and in intensity as it moves towards the trailing edge. There it turns into an intense positive vorticity sheet due to the velocity gradients from low absolute velocities in the impeller channel to high absolute velocities in the blade wake. This wake with low relative velocities can be seen in detail in Fig. 5.14b. The centre of this layer continues along the inner side of the blade tip wake, i.e. along the edge closer to the impeller inlet, in the negative tangential direction with decreasing intensity. It deviates slightly towards the pump outlet, so that it leaves the impeller channel.

Next to this positive vorticity sheet towards the blade pressure side a negative vorticity sheet is situated which is better observed in the high magnification FOV in Fig. 5.21. This negative vorticity zone splits up, with a small positive vorticity zone in between (Fig. 5.21b). The negative vorticity sheet hits the tongue tip (Fig. 5.21c). Part of it continues behind the blade tip and the other part is transported towards the pump outlet.

At the tongue wall in the narrow region of the volute the boundary layer is visible with negative vorticity. Along the pump exit wall at the tongue the boundary layer with relatively high positive vorticity is visible.

Figure 5.22 shows the phase-averaged vorticity field ω_z for 150 % Q_N at several time instants. For this high flow-rate the vorticity patterns are similar to Q_N, but with higher vorticity magnitudes. As the blades move towards the tongue tip several vorticity layers can be observed following the blade rotation. A strong

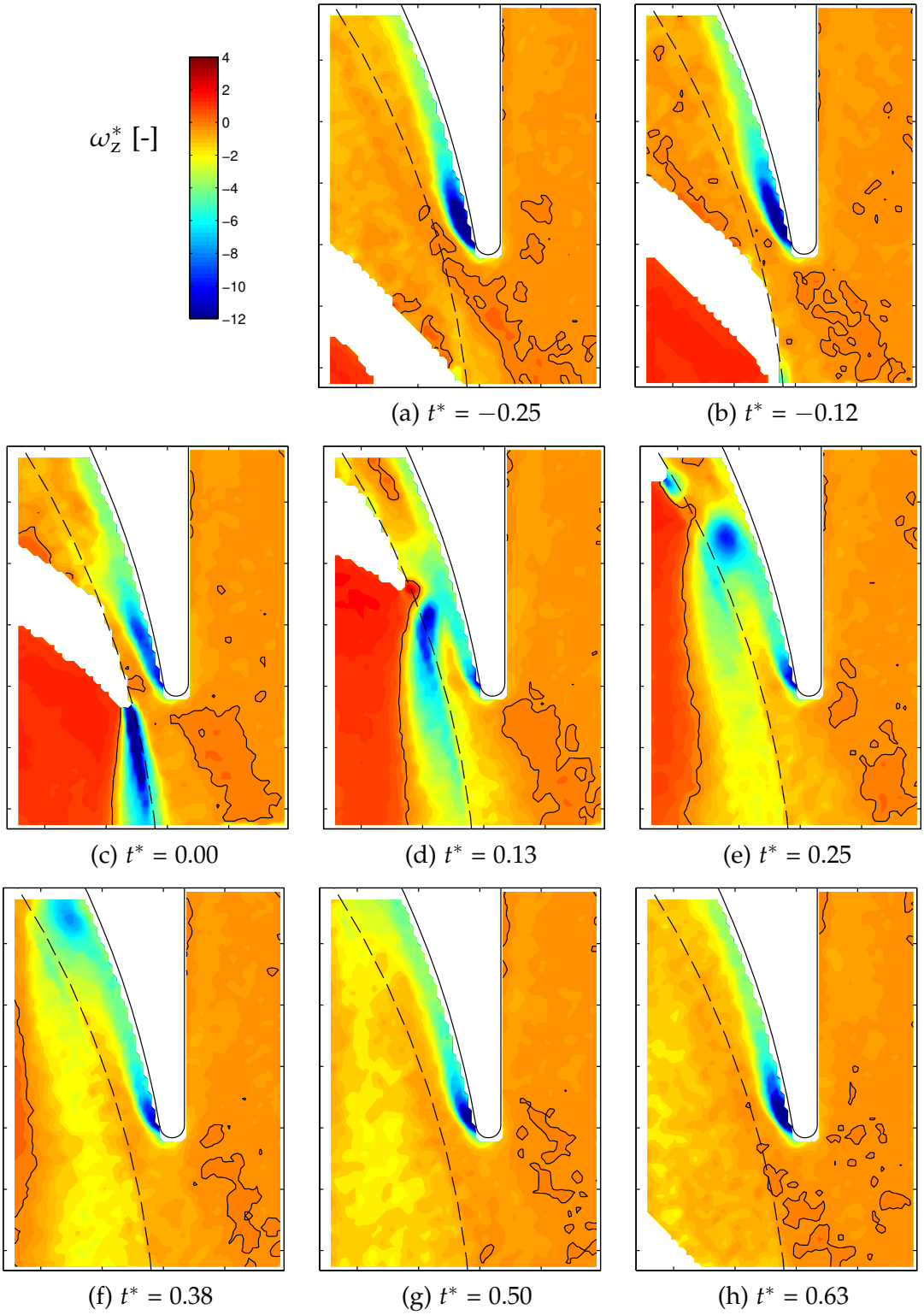

(a) $t^* = -0.25$ (b) $t^* = -0.12$

(c) $t^* = 0.00$ (d) $t^* = 0.13$ (e) $t^* = 0.25$

(f) $t^* = 0.38$ (g) $t^* = 0.50$ (h) $t^* = 0.63$

Figure 5.19: Normalized phase-averaged vorticity ω_z^* [-] at high M and 40 % Q_N. Black contours at $\omega_z^* = 0$. Note the change in scale compared to the low magnification FOV

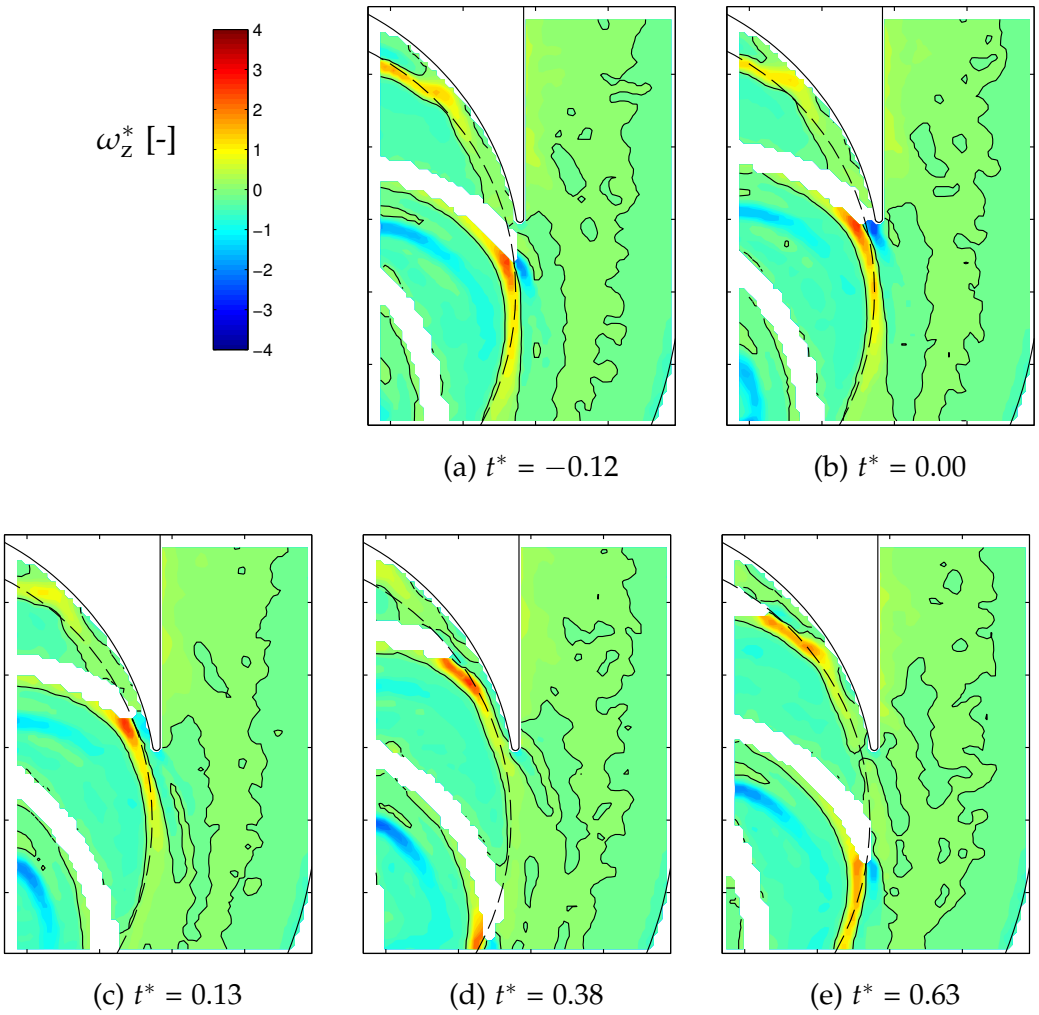

(a) $t^* = -0.12$ (b) $t^* = 0.00$

(c) $t^* = 0.13$ (d) $t^* = 0.38$ (e) $t^* = 0.63$

Figure 5.20: Normalized phase-averaged vorticity ω_z^* [-] at low M and Q_N. Black contours at $\omega_z^* = 0$

negative vorticity sheet (indicating rotation opposite to the impeller) is formed along the central zone of the impeller channels, with the transversal relative velocity gradient being maximum (see Fig. 5.7). Though not shown in the images, this sheet starts from the pressure side of the blade leading edge due to the flow detachment at that position. Close to the channel inlet its magnitude is maximum with about four times the vorticity associated to the impeller rotation. Though not so strong, a second negative vorticity sheet can be observed close to the blade pressure side, in coincidence with the core of the counterrotating vortex observed in Fig. 5.7 for each impeller channel. Clearly, vorticity in the impeller channels is mostly negative, i.e. the throughflow tries to oppose the impeller rotation. Positive vorticity can be observed at the suction side of the blades which, at the trailing edge, turns into a very intense positive vorticity sheet that is being shed along the border of the blade wake. Again, maximum values are close to four times the vorticity associated to the impeller rotation.

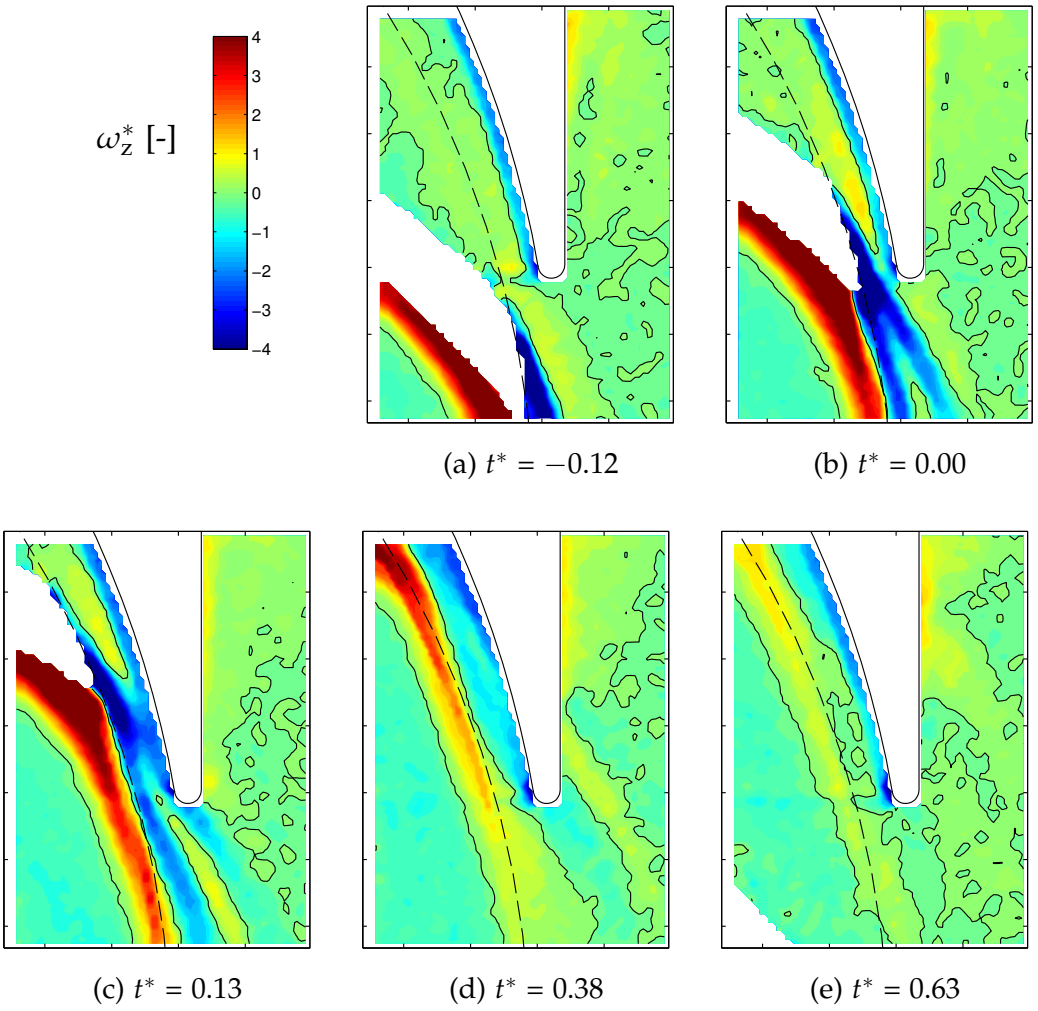

(a) $t^* = -0.12$ (b) $t^* = 0.00$

(c) $t^* = 0.13$ (d) $t^* = 0.38$ (e) $t^* = 0.63$

Figure 5.21: Normalized phase-averaged vorticity ω_z^* [-] at high M and Q_N. Black contours at $\omega_z^* = 0$

This positive vorticity sheet is partly due to the boundary layer developed on the blade surface, but overall, it is due to the velocity gradient from low absolute velocity at the impeller outlet to high velocity at the blade wake (Fig. 5.12c). Once in the outlet duct the vorticity remains mostly positive, but with values in the order of 10 % of the vorticity associated to the impeller rotation.

During the impeller rotation each of the vorticity sheets is eventually cut by the volute tongue, so that the two resultant vorticity zones continue their motion along the narrow region of the volute and towards the pump outlet, respectively, while undergoing some distortion. The positive vorticity sheet hits the tongue tip at about $t^* = 0.13$ (Fig. 5.22d) and then the part torn off to the outlet duct becomes progressively weaker and more concave. This is due to the bending and streamwise stretching of the vorticity sheet around the tongue and its mixing with the more external flow with low vorticity values. The sequence of images in Fig. 5.22 shows the convection of several positive vorticity sheets (named

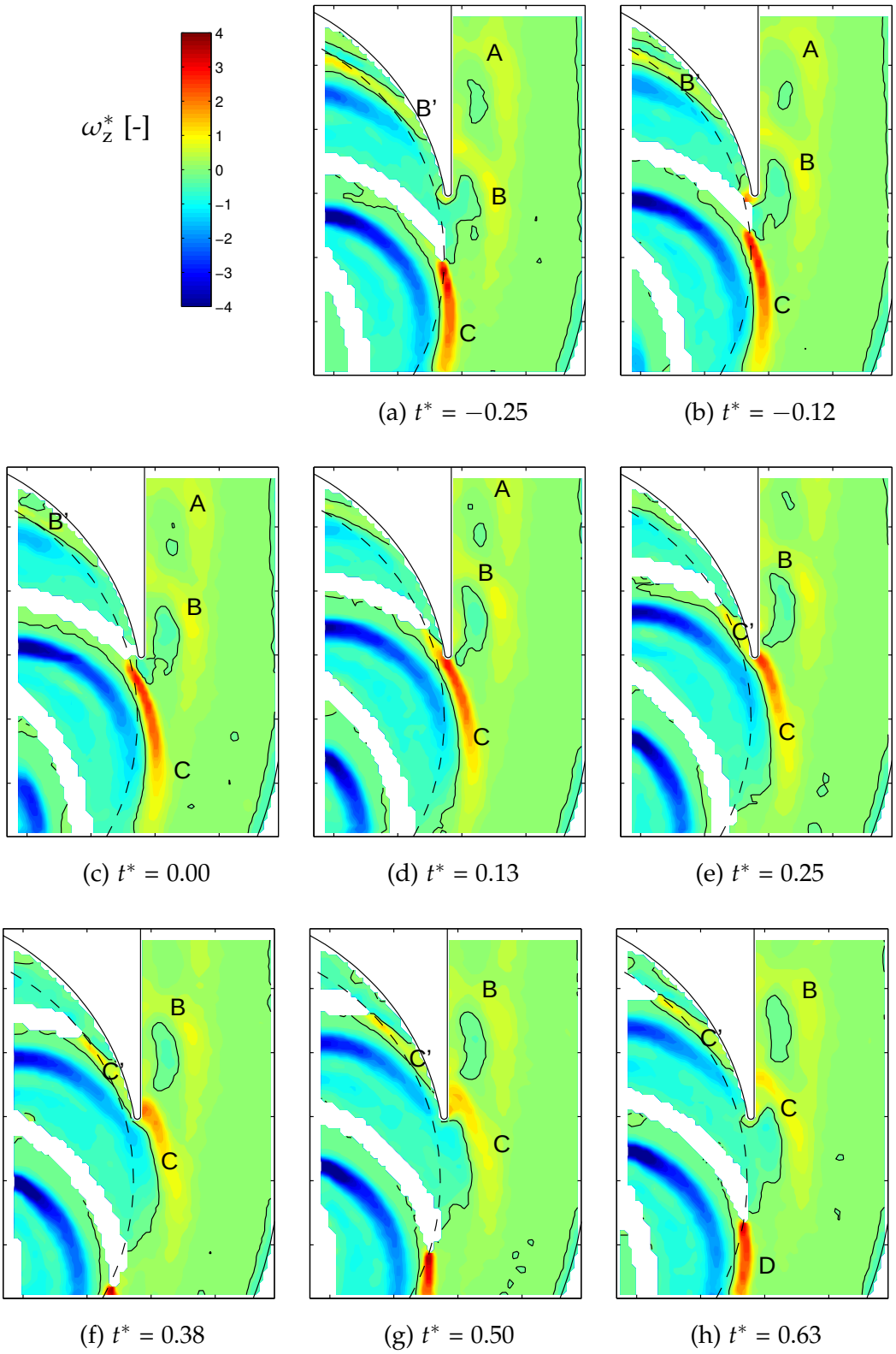

(a) $t^* = -0.25$ (b) $t^* = -0.12$

(c) $t^* = 0.00$ (d) $t^* = 0.13$ (e) $t^* = 0.25$

(f) $t^* = 0.38$ (g) $t^* = 0.50$ (h) $t^* = 0.63$

Figure 5.22: Normalized phase-averaged vorticity ω_z^* [-] at low M and 150 % Q_N. Black contours at $\omega_z^* = 0$

A, B, C and D), each corresponding to a different blade wake. Vorticity zones A and B have been generated from blades that already left the FOV. Also, the passage of the negative vorticity sheet in front of the tongue (starting at about $t^* = 0.38$) results in a small island-like fluid portion that is convected with the main stream while decaying. The positive vorticity portions dragged by the leakage flow between impeller and tongue (denoted as B' and C' in Fig. 5.22) also undergo a reduction in magnitude due to stretching effects in the tangential direction, see change in zone C' from $t^* = 0.13$ to $t^* = 0.38$.

The rotor-stator interaction in the tongue region and the influence on the vorticity fields for 150 % Q_N can be better seen in Fig. 5.23 using the high magnification FOV. The transverse velocity gradients along the bounds of the blade wake at the blade trailing edge result in two vorticity layers generated by the blade, one positive and one negative. Considering the instant $t^* = 0.00$, the change from the positive to the negative vorticity layer ($\omega_z = 0$) runs through the centre of the wake observed in Fig. 5.14c, i.e. the line where the transverse gradient of velocity is zero and hence the relative velocities are minimum.

Just after $t^* = 0.00$ the tail of the short negative vorticity sheet (extreme values of about 9 times the impeller vorticity) hits the tongue tip and a small portion is transported into the outlet channel ($t^* = 0.13$). The other part is dragged by the blade along the narrow passage between impeller and tongue, reinforcing the negative vorticity along the thin boundary layer on the internal tongue surface (t^* =0.13 to 0.38). The positive vorticity layer developing from the boundary layer at the blade suction side (maximum values of about 11 times the impeller vorticity) deforms slightly before it hits the tongue tip (Fig. 5.23d). It splits and detaches from the tongue tip (Fig. 5.23g), leaving a small positive vorticity spot right on the tongue tip.

Another zone of high positive vorticity, with maximum values up to 8 times the impeller vorticity, is near the tongue tip on the outlet side due to the flow detachment from the tongue tip, as the stagnation point is situated on the inner volute channel side (see section 5.3). This zone is displaced towards the outlet by the negative vorticity layer ($t^* = 0.13$) and afterwards by the positive vorticity layer coming from the blade. It grows again as the negative and positive vorticity layer from the blade have passed by with a maximum at about $t^* = 0.63$.

The maximum vorticity values are about four times higher than the maximum values obtained by the low magnification measurements. This is in correspondence with the spatial resolution of the velocity fields, as the vector spacing is four times higher in the high magnification measurements.

These vorticity maps at 150 % Q_N can be compared with the ones reported by Chu et al. (1995b) for a centrifugal pump operating at 135 % Q_N. Though not so clearly as in the present study, they also observed the shedding of positive and negative vorticity layers from the impeller channels. However, their study shows significant differences both in magnitude and pattern. For instance, in their case the vorticity in the region ahead of the blade pressure side was positive while

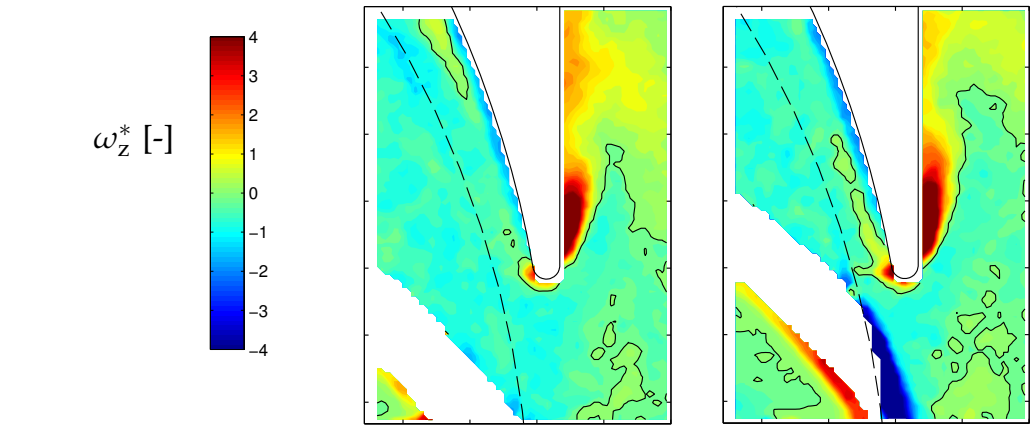

(a) $t^* = -0.25$ (b) $t^* = -0.12$

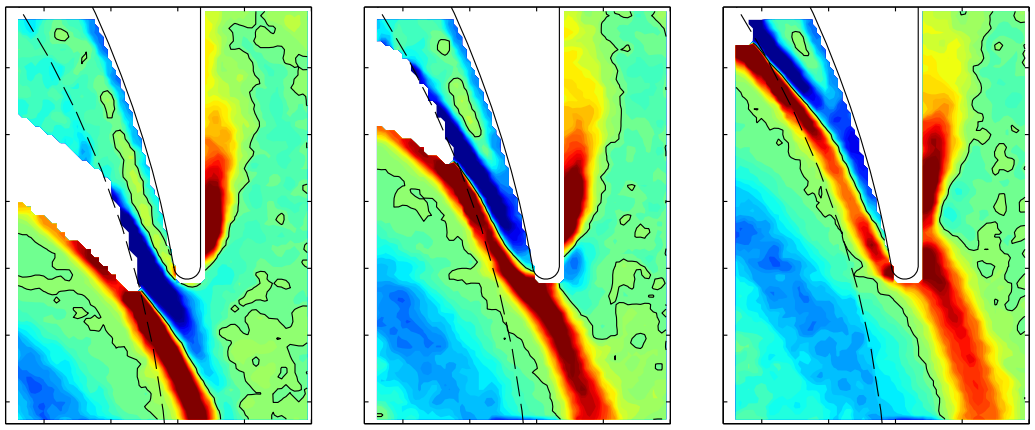

(c) $t^* = 0.00$ (d) $t^* = 0.13$ (e) $t^* = 0.25$

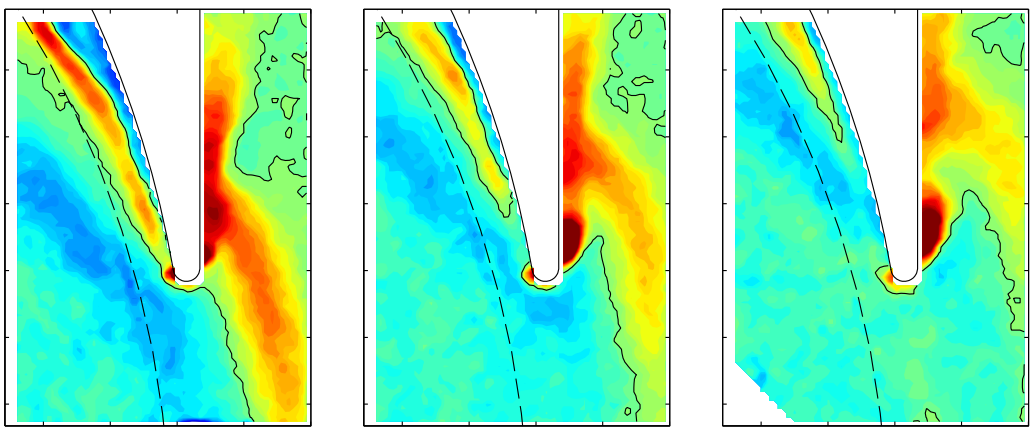

(f) $t^* = 0.38$ (g) $t^* = 0.50$ (h) $t^* = 0.63$

Figure 5.23: Normalized phase-averaged vorticity ω_z^* [-] at high M and 150 % Q_N. Black contours at $\omega_z^* = 0$

Fig. 5.22 shows negative values. These differences can be partially attributed to the different relative flow-rate used (135 % Q_N against 150 % Q_N in the present case). This also suggests that the details of pump design and construction may have a significant effect on the vorticity field pattern.

5.6 Turbulence results

Turbulence data obtained from series of 500 velocity maps, acquired for each blade position and FOV, are shown in this section. The Reynolds stress tensor is derived from Eq. (5.3) for the fluctuating velocity part as

$$\tau_{ij} = \overline{u_i' u_j'}. \tag{5.14}$$

For 2D2C PIV four components of Reynolds stresses can be computed as

$$\tau = \begin{pmatrix} \overline{u'u'} & \overline{u'v'} \\ \overline{v'u'} & \overline{v'v'} \end{pmatrix}. \tag{5.15}$$

5.6.1 Phase-averaged TKE

Reynolds stresses can be seen as a measure of the velocity variance in the measurement plane. They can be used to represent in-plane contribution to turbulent kinetic energy (TKE) as (Wu et al., 2011a)

$$k_{2D} = \frac{1}{2} \cdot (\overline{u'u'} + \overline{v'v'}). \tag{5.16}$$

The in-plane phase-averaged TKE is normalized by the blade tip velocity:

$$k^*_{2D} = \frac{1}{2} \cdot \frac{\overline{u'u'} + \overline{v'v'}}{U^2_{tip}}. \tag{5.17}$$

In this way k^*_{2D} represents the in-plane TKE as a fraction of the kinetic energy of the blade tip. In PIV measurements the finite interrogation region size works as a low-pass filter (Spencer and Hollis, 2005), i.e. turbulence scales smaller than the interrogation region size are not resolved. Therefore the TKE values for the low magnification measurements are in general lower than the values for the high magnification measurements.
For 40 % Q_N the in-plane phase-averaged TKE fields for several time instants at low magnification are shown in Fig. 5.24 and at high magnification in Fig. 5.25. The turbulence level is very low in nearly the whole impeller channel before the blade reaches the tongue tip (Fig. 5.24a). Behind the trailing edge at the suction side of the blade there is a high turbulent zone extending along the negative

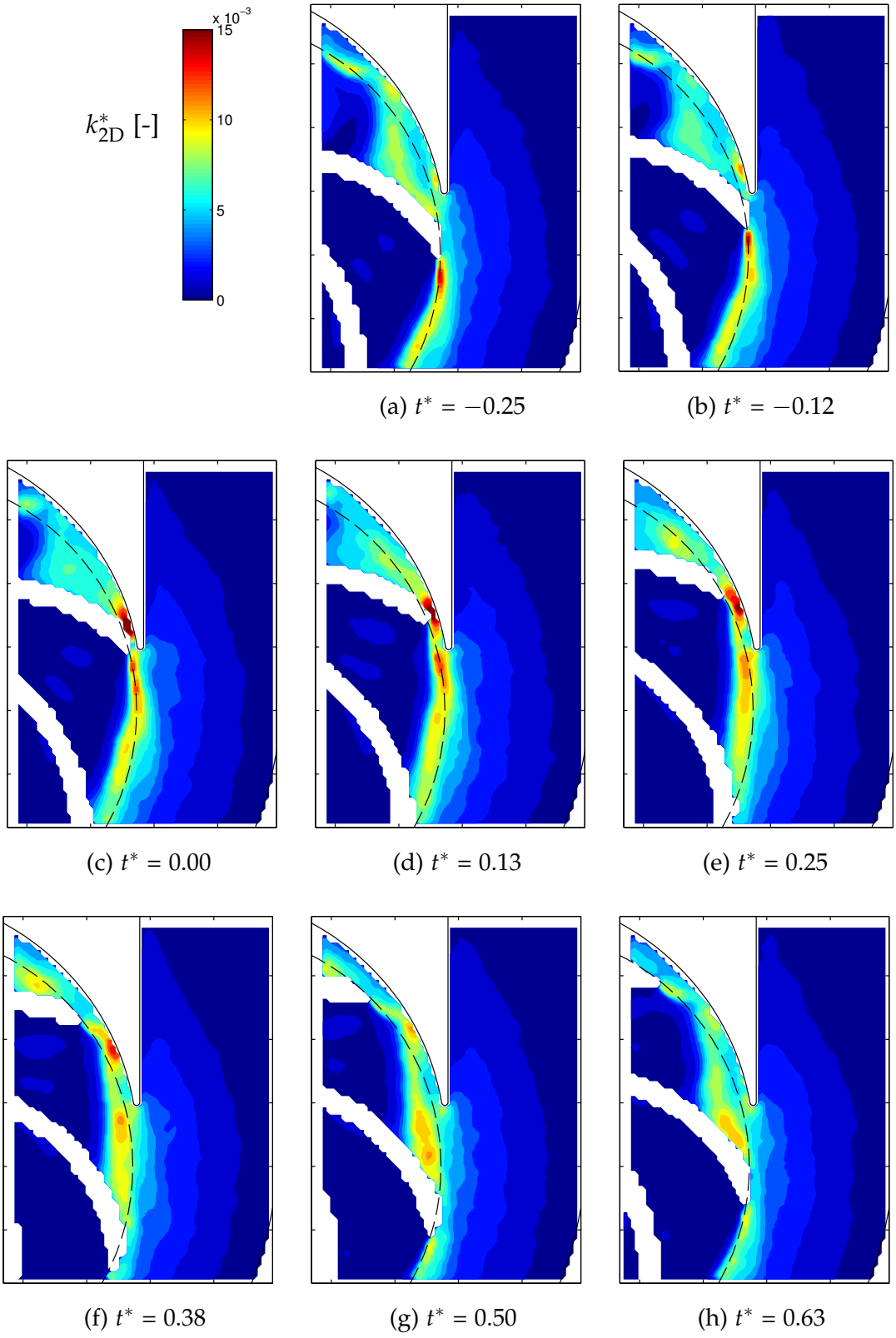

(a) $t^* = -0.25$ (b) $t^* = -0.12$

(c) $t^* = 0.00$ (d) $t^* = 0.13$ (e) $t^* = 0.25$

(f) $t^* = 0.38$ (g) $t^* = 0.50$ (h) $t^* = 0.63$

Figure 5.24: Normalized in-plane TKE k^*_{2D} [-] at low M and 40 % Q_N

tangential direction while reducing intensity. This zone coincides in extension and intensity variation reasonably well with the negative vorticity sheet (see Fig. 5.18). It hits the pressure side of the next blade (Fig. 5.24d). As the blade passes the tongue tip, a higher turbulent zone at the impeller outlet stays ahead of the tongue tip (Fig. 5.24c) until it hits, with still high TKE values, the next blade (Fig. 5.24g). Inside the impeller channel, with the channel being at the narrow region of the volute, higher TKE values are found next to the blade pressure side (Fig. 5.24a), as the positive vorticity zone moves towards the impeller inlet (see Fig. 5.18a).

In the high magnification FOV it can be observed that for 40 % Q_N the turbulent zone starts right next to the tongue tip on the volute side (Fig. 5.25). This is due to the flow separation from the tongue tip towards the narrow region of the volute for flow-rates below Q_N. Zones of high TKE values correspond often to flow detachment, where vorticity is usually high. Turbulence is also high behind the blade trailing edge, as already seen on the low magnification FOV, but lower than in the flow separation zone of the tongue tip.
After the blade has passed the tongue tip, the TKE zone in the blade wake is seen to separate from the blade tip and it stays ahead of the tongue tip (Fig. 5.25d). Furthermore, turbulence in the flow separation zone decreases, as vorticity decreases due to flow reattachment to the tongue wall. As the next blade approaches the tongue tip the wake with high TKE increases again in amplitude and extension (Fig. 5.25h), in concordance with the growth of the negative vorticity zone (Fig. 5.19h).

TKE for Q_N is shown in Fig. 5.26 using the low magnification FOV. Turbulence is very low, as expected, therefore the color scale used for its representation was reduced. However, in the middle of the impeller channels TKE is higher than at 40 % Q_N. This suggests some flow separation at the blade leading edge, as also seen in the vorticity fields (Fig. 5.20). The turbulence zone behind the blade trailing edge is associated with the negative vorticity sheet. In the positive vorticity sheet, which extends from the blade suction side, TKE is particularly low (Fig. 5.26a). The turbulence level in the blade wake is significantly smaller than at 40 % Q_N. After the blade has passed the tongue tip TKE is lower, which can be better seen at high magnification in Fig. 5.27. As it is the nominal flow-rate no flow separation takes place at the tongue tip. This is confirmed by the very low turbulence levels in this region, except when the blade passes by and the negative vorticity sheet behind the blade trailing edge leaves a small turbulent spot in front of the tongue tip (Fig. 5.27c).

Figure 5.28 shows the TKE evolution for 150 % Q_N using the low magnification FOV. TKE is high along the central zone of the impeller channels, with maximum values close to each channel inlet. This confirms the flow detachment from the pressure side of the blade leading edge, as already suggested by the vorticity fields of Fig. 5.22. However, close to the blade suction side TKE is very small

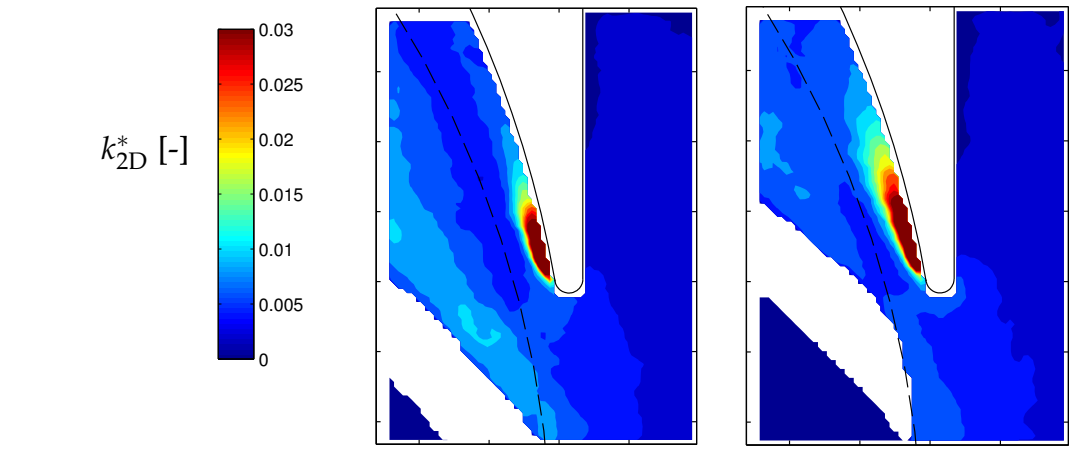

(a) $t^* = -0.25$ (b) $t^* = -0.12$

(c) $t^* = 0.00$ (d) $t^* = 0.13$ (e) $t^* = 0.25$

(f) $t^* = 0.38$ (g) $t^* = 0.50$ (h) $t^* = 0.63$

Figure 5.25: Normalized in-plane TKE k^*_{2D} [-] at high M and 40 % Q_N

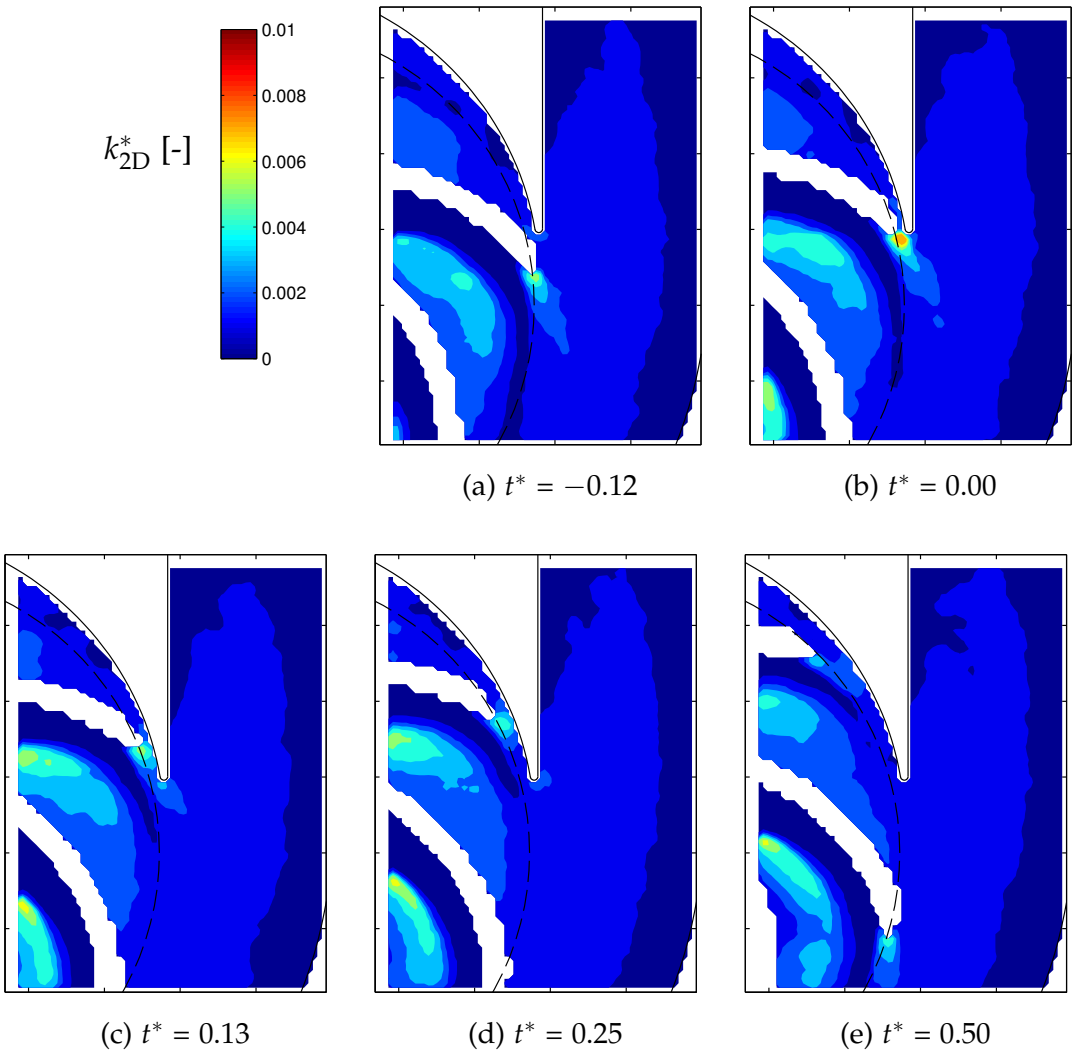

(a) $t^* = -0.12$ (b) $t^* = 0.00$

(c) $t^* = 0.13$ (d) $t^* = 0.25$ (e) $t^* = 0.50$

Figure 5.26: Normalized in-plane TKE k^*_{2D} [-] at low M and Q_N

in spite of the high magnitude of relative velocity (see Fig. 5.7). This is also the case in the exit channel (high absolute velocity, low TKE).

TKE evolution for 150 % Q_N at high magnification is shown in Fig. 5.29. High TKE values are found in the wake of the blade which become maximum when the blade aligns with the tongue tip ($t^* = 0.00$), i.e. when the negative vorticity at that position becomes most intense. Just below, another turbulence sheet but with less TKE can be observed in Fig. 5.29c, which corresponds to the positive vorticity layer being shed from the suction side of the blade trailing edge. TKE in this zone is lower, denoting that the relative flow remains well adhered to the blade suction side up to the trailing edge and that it joins smoothly the secondary flow around the blade tip, i.e. the bulk of the flow structure is well periodic with the blade passage. High TKE values are also observed in the wake region behind the tongue during most of the cycle, with a maximum at about

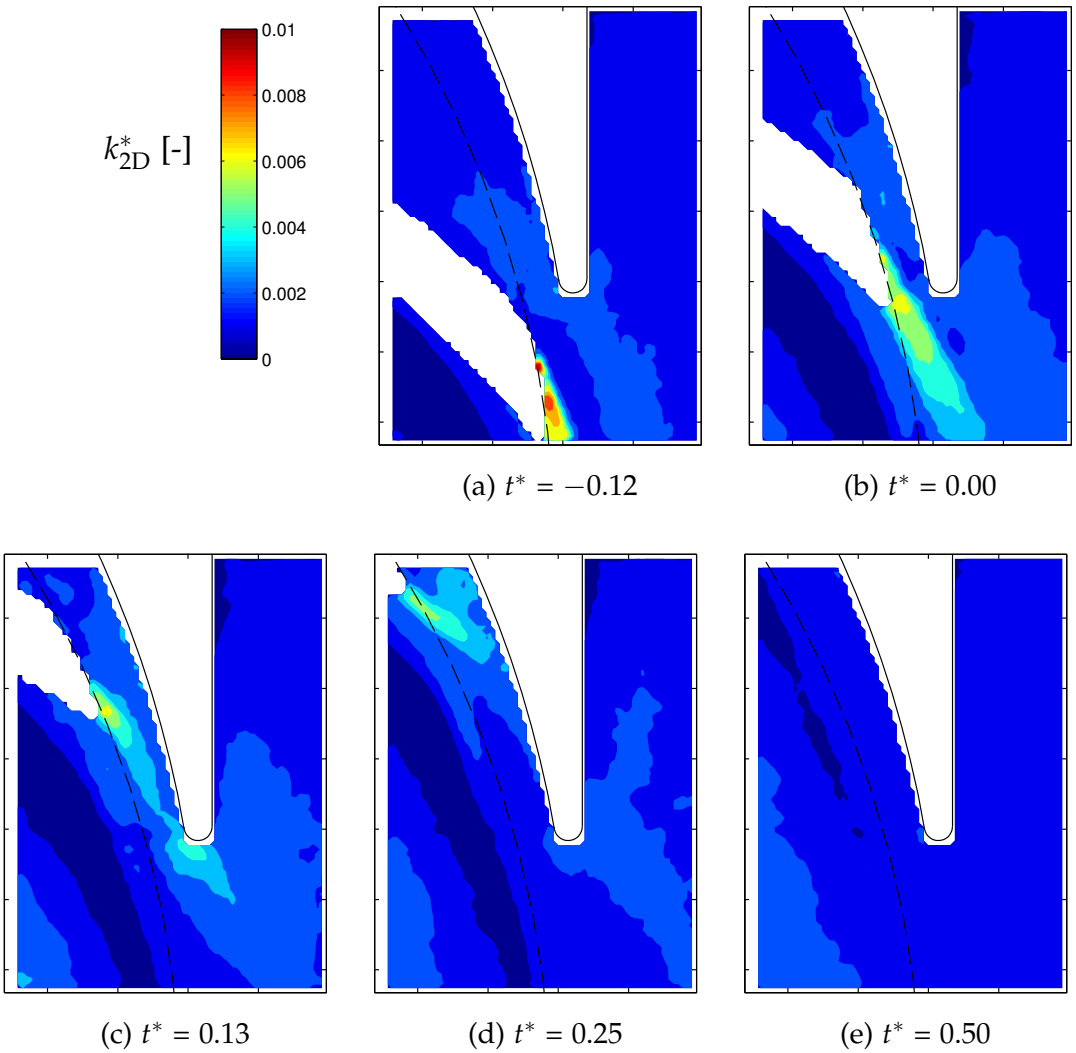

(a) $t^* = -0.12$ (b) $t^* = 0.00$

(c) $t^* = 0.13$ (d) $t^* = 0.25$ (e) $t^* = 0.50$

Figure 5.27: Normalized in-plane TKE k^*_{2D} [-] at high M and Q_N

$t^* = 0.63$ (like the positive vorticity shown in Fig. 5.23). However, TKE values in the tongue wake are lower for this flow-rate than for 40 % Q_N. At that instance some relatively high TKE is also observed close to the stagnation point, due to the arrival of the high TKE sheet coming from the impeller channel (see Fig. 5.28h). Once the negative vorticity sheet from the blade reaches the tongue tip ($t^* = 0.13$) it displaces the wake (with positive vorticity) slightly towards the pump exit, so that flow tends to reattach to the tongue wall, thus reducing the turbulence in this zone. Then the positive vorticity sheet from the blade with low turbulence reinforces this effect, reducing TKE behind the tongue to a minimum at about $t^* = 0.38$.

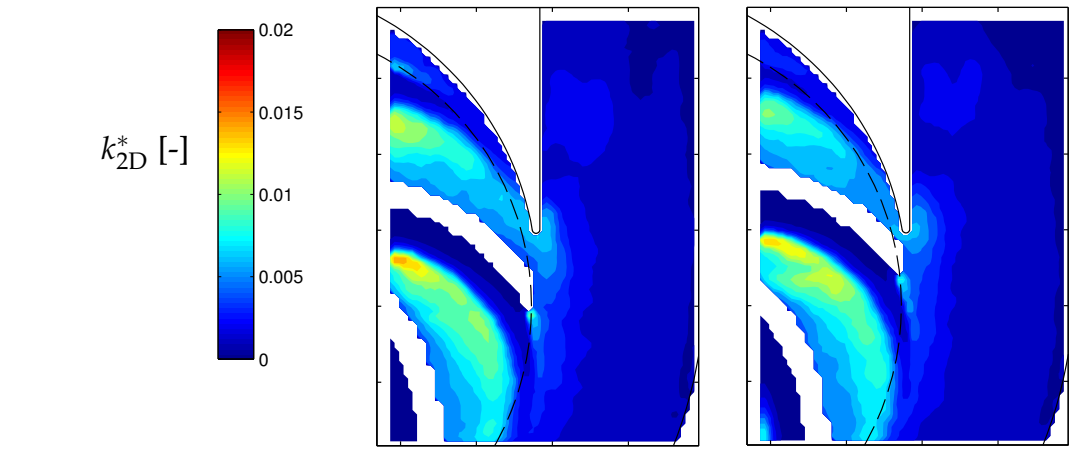

(a) $t^* = -0.25$ (b) $t^* = -0.12$

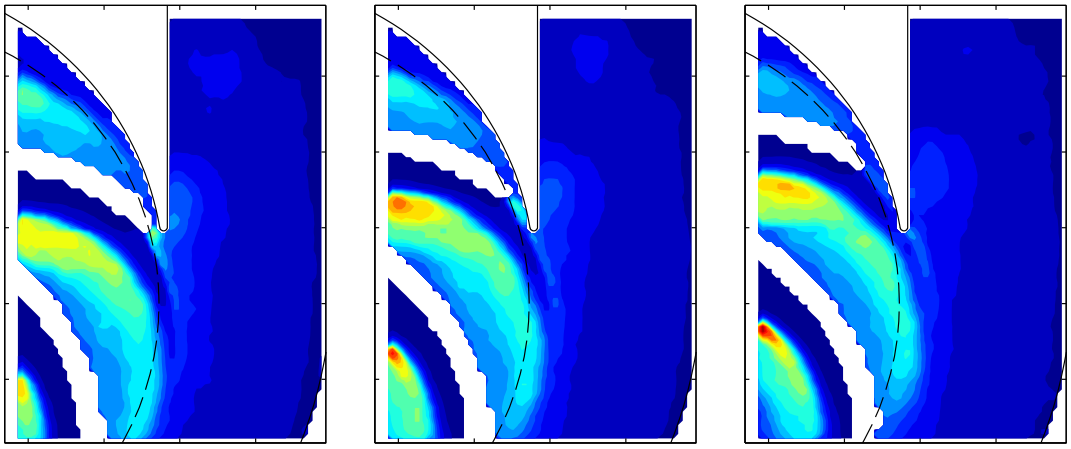

(c) $t^* = 0.00$ (d) $t^* = 0.13$ (e) $t^* = 0.25$

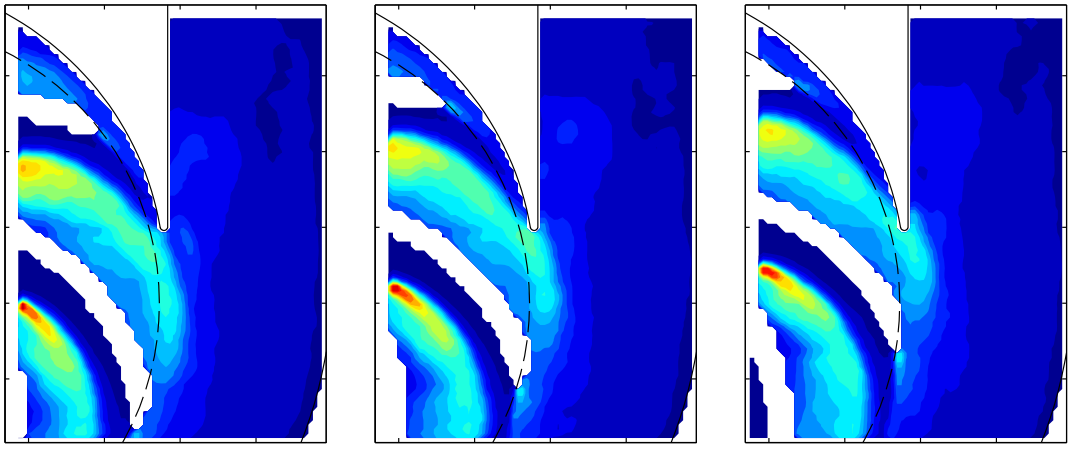

(f) $t^* = 0.38$ (g) $t^* = 0.50$ (h) $t^* = 0.63$

Figure 5.28: Normalized in-plane TKE k^*_{2D} [-] at low M and 150 % Q_N

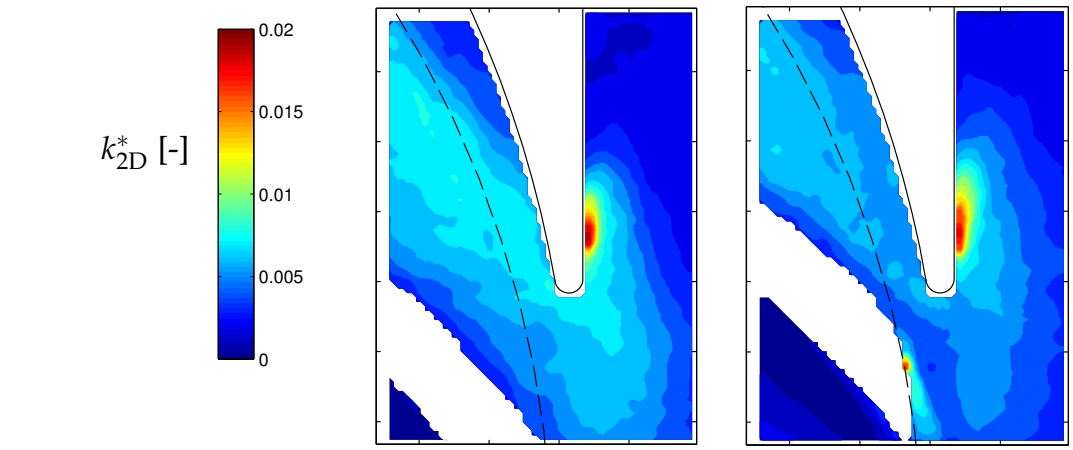

(a) $t^* = -0.25$ (b) $t^* = -0.12$

(c) $t^* = 0.00$ (d) $t^* = 0.13$ (e) $t^* = 0.25$

(f) $t^* = 0.38$ (g) $t^* = 0.50$ (h) $t^* = 0.63$

Figure 5.29: Normalized in-plane TKE k^*_{2D} [-] at high M and 150 % Q_N

5.6.2 TKE production rate

The phase-averaged production tensor of the turbulent kinetic energy (TKE) is (Pope, 2000)

$$P_{ij} = -\overline{u_i' u_k'} \frac{\partial \bar{u}_j}{\partial x_k} - \overline{u_j' u_k'} \frac{\partial \bar{u}_i}{\partial x_k}. \tag{5.18}$$

The in-plane terms of TKE production (Miorini et al., 2012) are normalized by the impeller radius and blade tip speed:

$$P_{2D}^* = -(\overline{u'u'} S_{11} + 2\overline{u'v'} S_{12} + \overline{v'v'} S_{22}) \cdot \frac{r_{tip}}{U_{tip}^3}, \tag{5.19}$$

with S_{ij} being the elements of the strain rate tensor formed by the in-plane phase-averaged velocities (see Eq. (5.8)).

The TKE production P_{2D}^*, obtained by Eq. (5.19), is shown for 40 % Q_N in Fig. 5.30 using the low magnification FOV and in Fig. 5.31 using the high magnification FOV. As expected, TKE production appears to be particularly intense in the zones of flow separation. In the low magnification FOV the production is seen to be highest just behind the blade trailing edge in the blade wake (Fig. 5.30b). It looses intensity while extending in the negative tangential direction towards the next blade. However, TKE production is maintained even as the turbulent zone hits the pressure side of the next blade (Fig. 5.30f), producing more turbulence in this region (Fig. 5.30g).
The TKE production in the tongue region can be better observed in the high magnification FOV (see Fig. 5.31). TKE production in the flow separation zone of the tongue tip is about three times higher than in the blade wake (Fig. 5.31c). It is particularly intense before the blade arrives at the tongue tip (Fig. 5.31a). As the blade passes the tongue tip, TKE production in the tongue wake is reduced signifcantly, reaching a minimum shortly afterwards at $t^* = 0.13$ (Fig. 5.31d). Furthermore, after the blade has passed the tongue tip, a zone of TKE production, associated with the negative vorticity sheet which extends from the blade tip, is situated ahead of the tongue tip (Fig. 5.31d) and hits on the pressure side of the next blade (Fig. 5.31a). TKE production increases in this zone, i.e. that new TKE is produced due to the impingement on the pressure side of the next blade.

TKE production at Q_N is shown in Fig. 5.32 using the low magnification FOV. It is low compared to the other flow-rates, as expected and observed in the TKE maps. The highest TKE production zones correspond to flow separation from the pressure side at the entrance of the impeller channels and to the blade wake. The TKE production in the blade wake at Q_N is better observed in the high magnification FOV (see Fig. 5.33), being highest at the blade trailing edge and

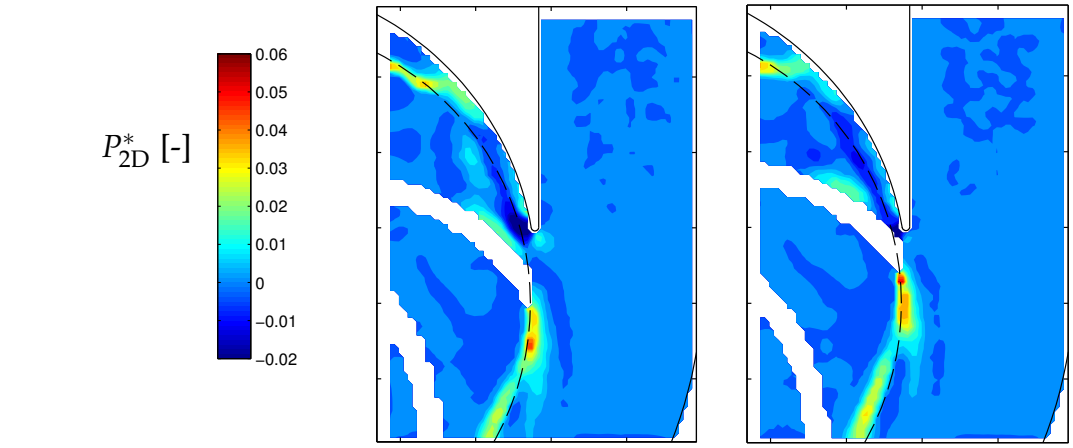

(a) $t^* = -0.25$ (b) $t^* = -0.12$

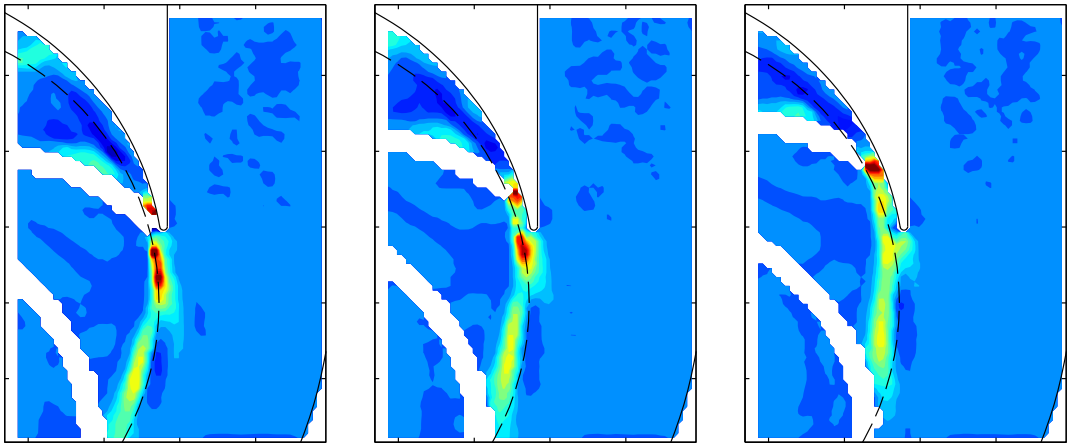

(c) $t^* = 0.00$ (d) $t^* = 0.13$ (e) $t^* = 0.25$

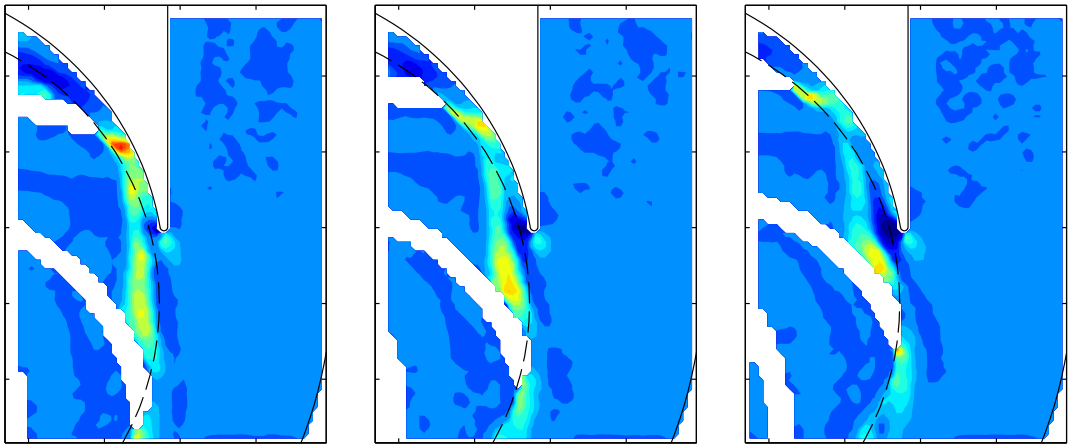

(f) $t^* = 0.38$ (g) $t^* = 0.50$ (h) $t^* = 0.63$

Figure 5.30: Normalized in-plane TKE production P^*_{2D} [-] at low M and 40 % Q_N

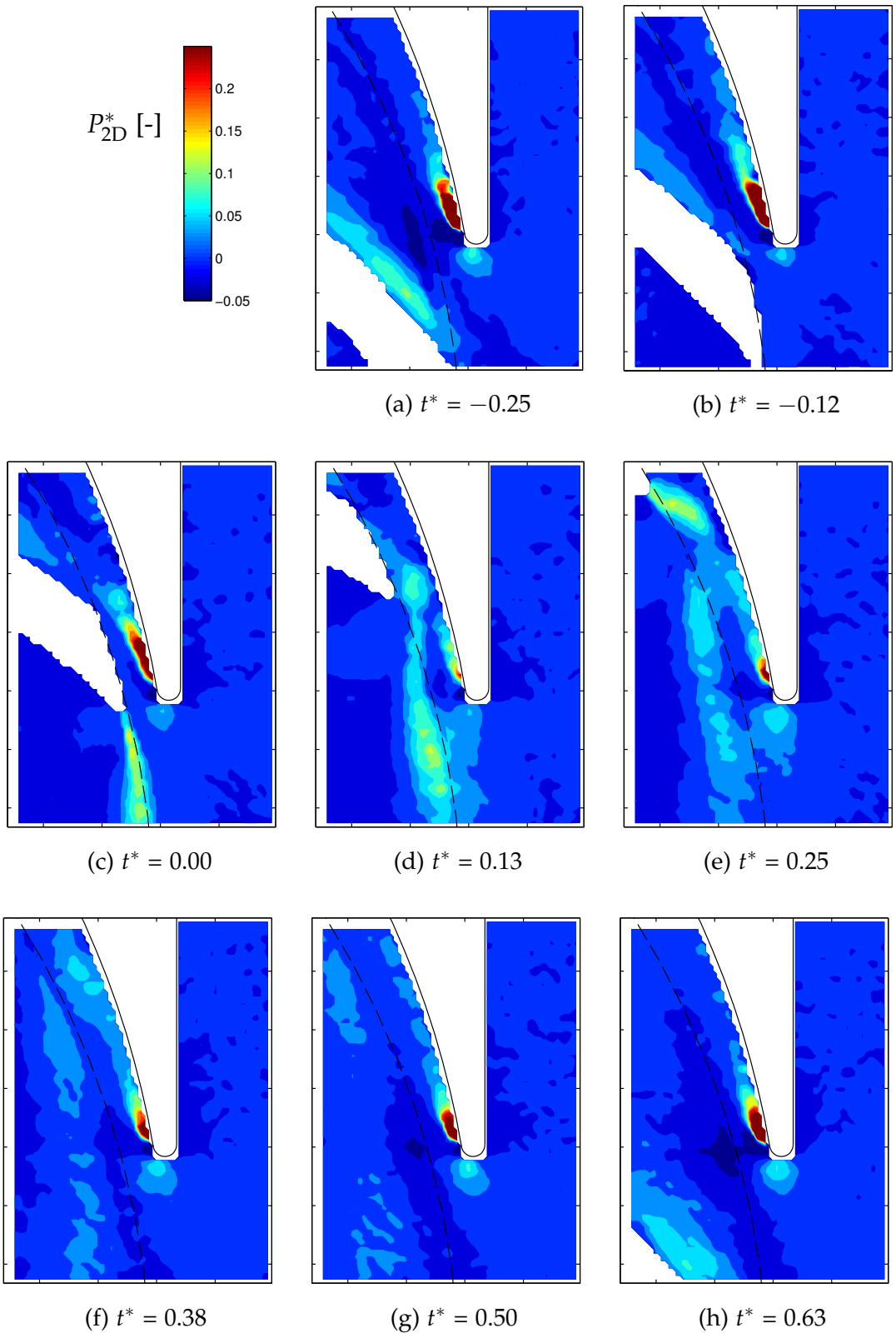

(a) $t^* = -0.25$ (b) $t^* = -0.12$

(c) $t^* = 0.00$ (d) $t^* = 0.13$ (e) $t^* = 0.25$

(f) $t^* = 0.38$ (g) $t^* = 0.50$ (h) $t^* = 0.63$

Figure 5.31: Normalized in-plane TKE production P^*_{2D} [-] at high M and 40 % Q_N

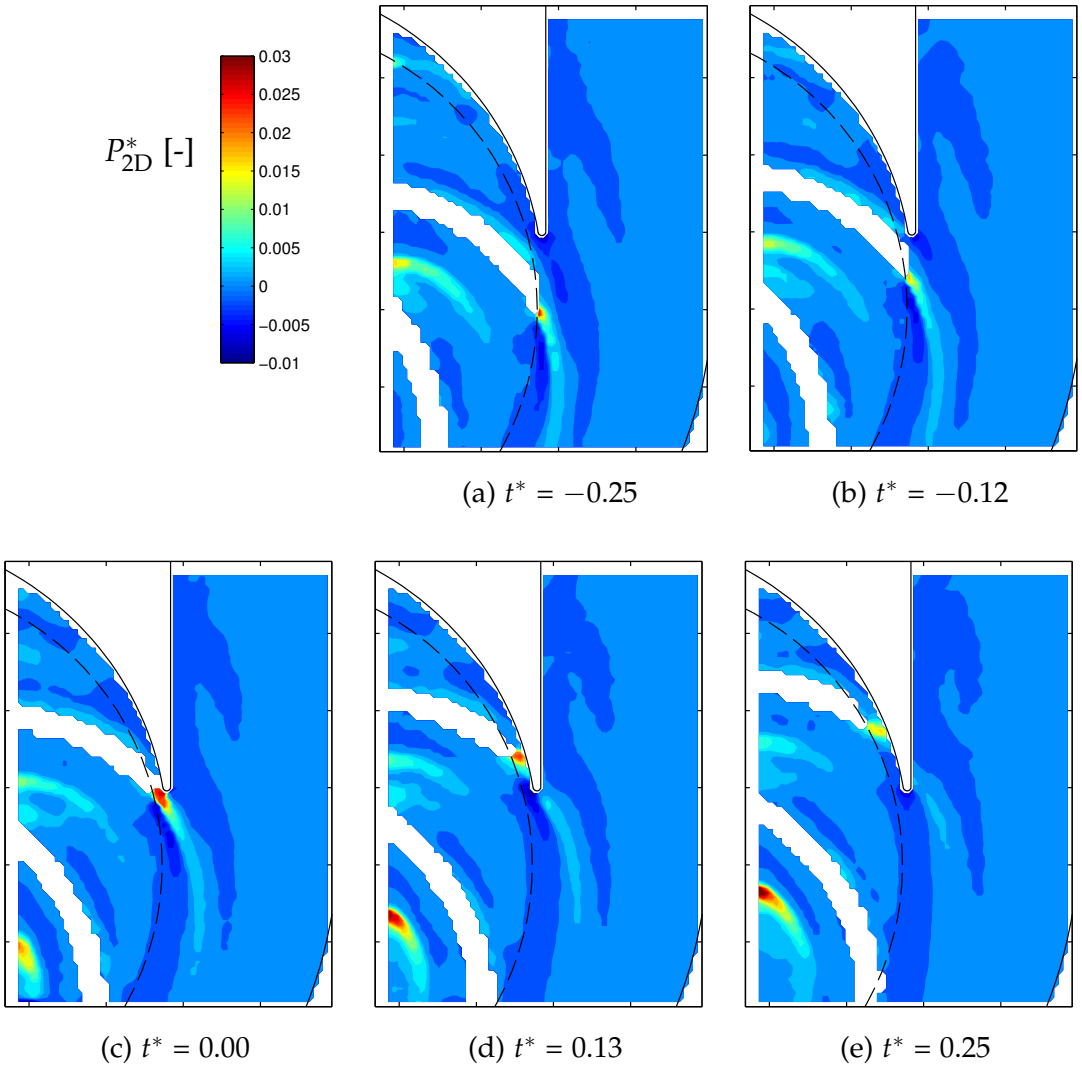

(a) $t^* = -0.25$ (b) $t^* = -0.12$

(c) $t^* = 0.00$ (d) $t^* = 0.13$ (e) $t^* = 0.25$

Figure 5.32: Normalized in-plane TKE production P^*_{2D} [-] at low M and Q_N

high on the blade pressure side (Fig. 5.33b). As the blade passes the tongue tip, a small zone of higher TKE production stays at the tongue tip (Fig. 5.33d).

TKE production for 150 % Q_N is shown in Fig. 5.34 using the low magnification FOV. It is about three times higher than at Q_N. As seen at the other flow-rates, TKE production at 150 % Q_N is particularly intense in the zones of flow separation. This is the case of the flow detached from the pressure side at the entrance of the impeller channels, though significant TKE production still takes place during some extension along the central zone of the channels.
TKE production in the blade wake and tongue region is better observed using the high magnification FOV (see Fig. 5.35). Regarding the wake from the blades, TKE production is seen to be initially concentrated just behind the pressure side of the blade trailing edge (Fig. 5.35b) and becomes maximum when the blade aligns with the tongue tip (Fig. 5.35c). Afterwards this zone of TKE production

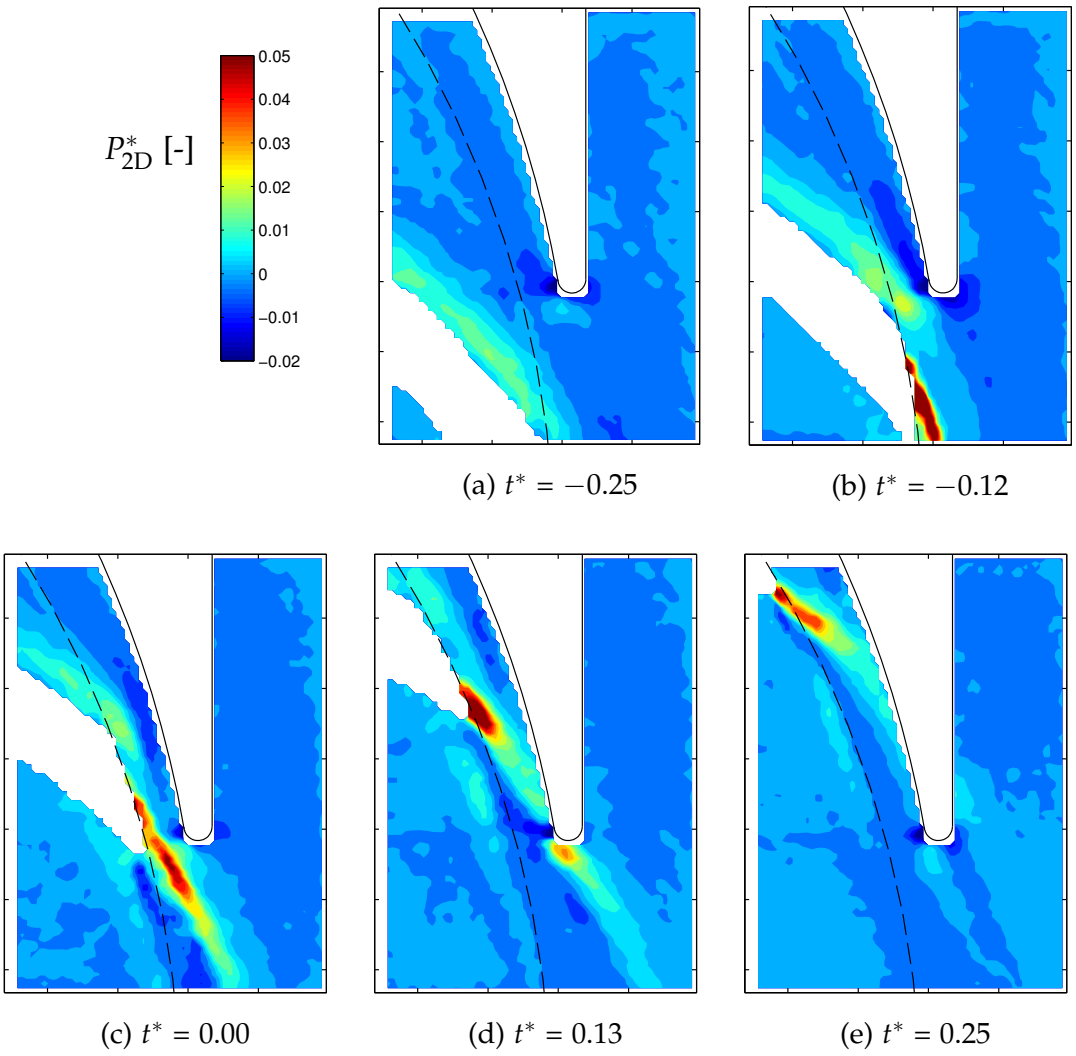

(a) $t^* = -0.25$ (b) $t^* = -0.12$

(c) $t^* = 0.00$ (d) $t^* = 0.13$ (e) $t^* = 0.25$

Figure 5.33: Normalized in-plane TKE production P^*_{2D} [-] at high M and Q_N

continues shifting towards the blade suction side while losing intensity (Fig. 5.35d).

Finally, high production of turbulence takes place in the wake of the tongue tip during most of the blade passage period. Only from $t^* = 0.13$ to 0.44 the production reduces until nearly vanishing at $t^* = 0.38$ due to the effect described in section 5.5 of the vorticity layers shed from the blade trailing edge. These TKE production maps also show negative values at different zones throughout the flow. The most significant one corresponds to the stagnation region at the tongue, where high viscous stresses can be expected. The most pronounced TKE dissipation occurs at about $t^* = 0.63$, coinciding with the arrival of the highly turbulent stream generated at the blade leading edge (Fig. 5.29h).

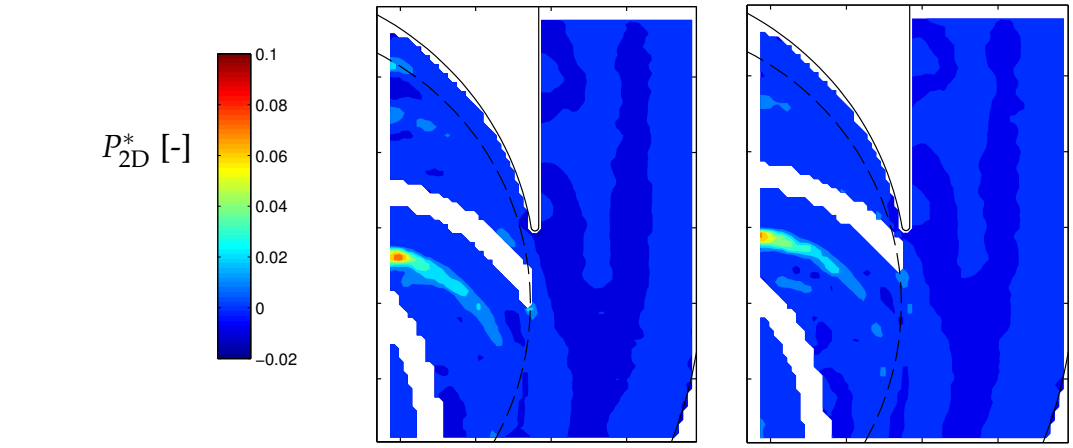

(a) $t^* = -0.25$ (b) $t^* = -0.12$

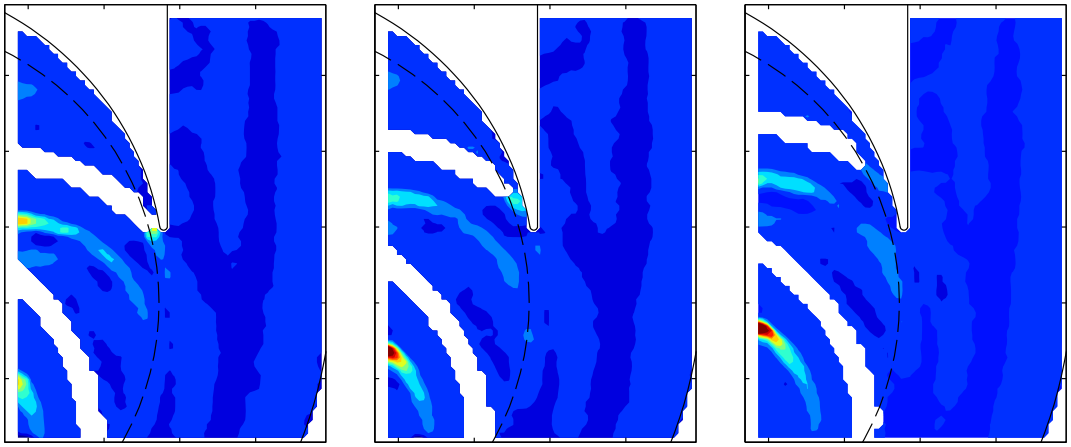

(c) $t^* = 0.00$ (d) $t^* = 0.13$ (e) $t^* = 0.25$

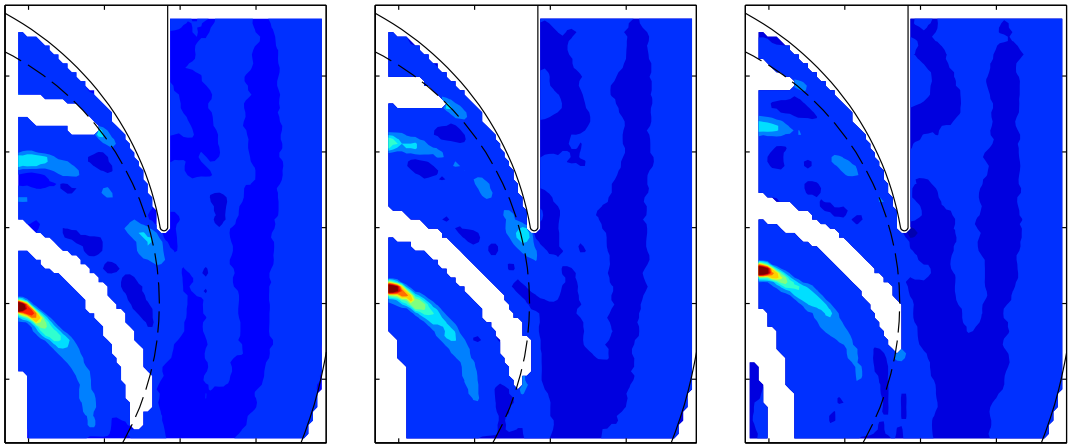

(f) $t^* = 0.38$ (g) $t^* = 0.50$ (h) $t^* = 0.63$

Figure 5.34: Normalized in-plane TKE production P^*_{2D} [-] at low M and 150 % Q_N

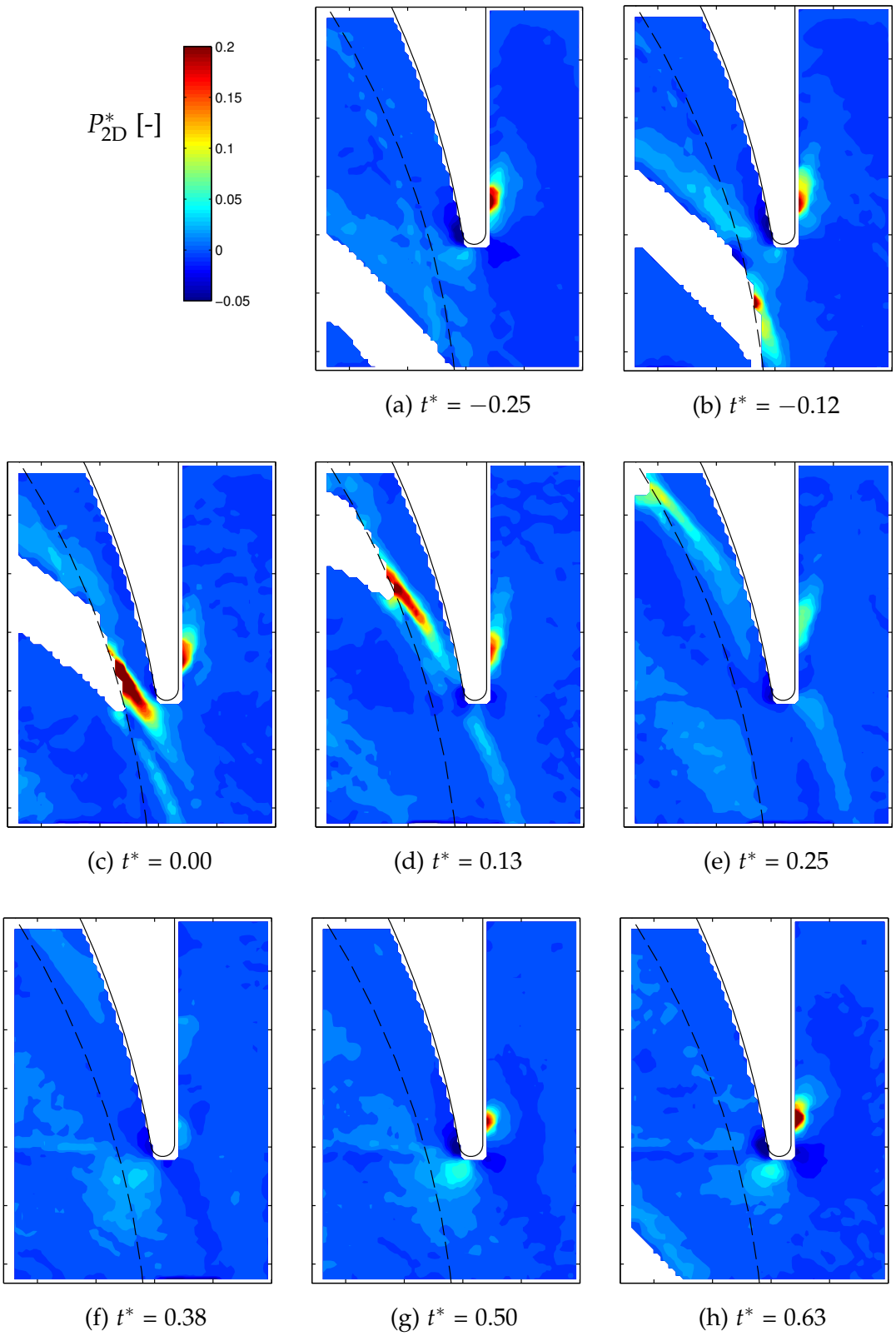

(a) $t^* = -0.25$ (b) $t^* = -0.12$

(c) $t^* = 0.00$ (d) $t^* = 0.13$ (e) $t^* = 0.25$

(f) $t^* = 0.38$ (g) $t^* = 0.50$ (h) $t^* = 0.63$

Figure 5.35: Normalized in-plane TKE production P^*_{2D} [-] at high M and 150 % Q_N

5.7 Time evolution and spectral analysis

Since the flow field data obtained corresponds to 33 time instants during one blade passage cycle, the flow evolution can be analysed in detail at any position in the low and high magnification FOVs. The time evolution and the associated frequency spectra of phase-averaged velocity, vorticity and TKE are discussed in this section.

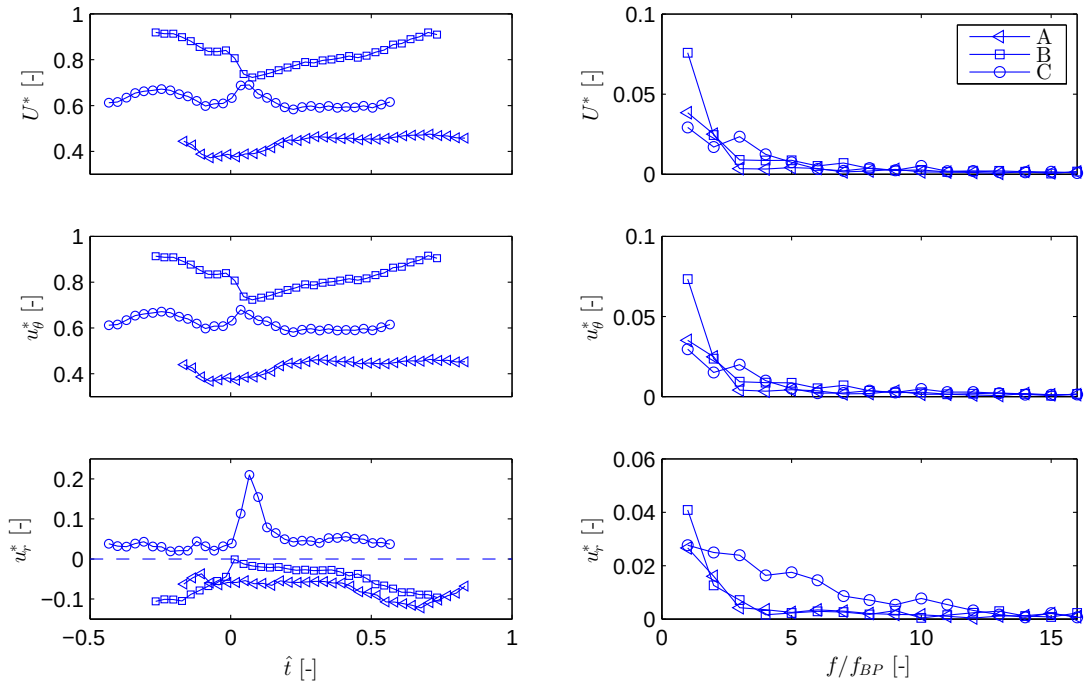

(a) Time signals (b) Spectra

Figure 5.36: Time signals and spectra at 40 % Q_N of phase-averaged velocity magnitude, tangential and radial components at positions A (◁), B (□) and C (○). Positions as in Fig. 5.3

The time evolution of in-plane velocity magnitude U, its tangential u_θ and radial component u_r is shown at 3 positions in the gap region between impeller and tongue at $1.02r_{tip}$, one 4° ahead of the tongue tip (A) and the other two at 2° behind (B) and 12° behind (C) the tongue tip (see Fig. 5.3 for location). The results presented in this section were taken from the high magnification FOV data, as all three points are inside this FOV. Each time signal t^* has been shifted, so that for $\hat{t} = 0$ the trailing edge of the blade suction side aligns with either A, B or C; $\hat{t} = 1$ corresponds to one blade passage, i.e. a blade has moved 60° with respect to $\hat{t} = 0$.

The right side of the figures presents the frequency spectra obtained by FFT analysis of each time signal. 32 points were used, as the first and the last (33rd) instants are the same blade position but for different blades. As 32 data points

were taken a FFT can be done without the need of adding zeros or eliminating data. Frequency values correspond to f_{BP} and harmonics (the static value for $f = 0$ is not represented). The first value represented is at f_{BP} and the next points all correspond to harmonics of f_{BP}. As expected, most of the signal content is concentrated on the low frequency range, with highest peaks either at f_{BP} or $2f_{BP}$ depending on the time signal pattern.

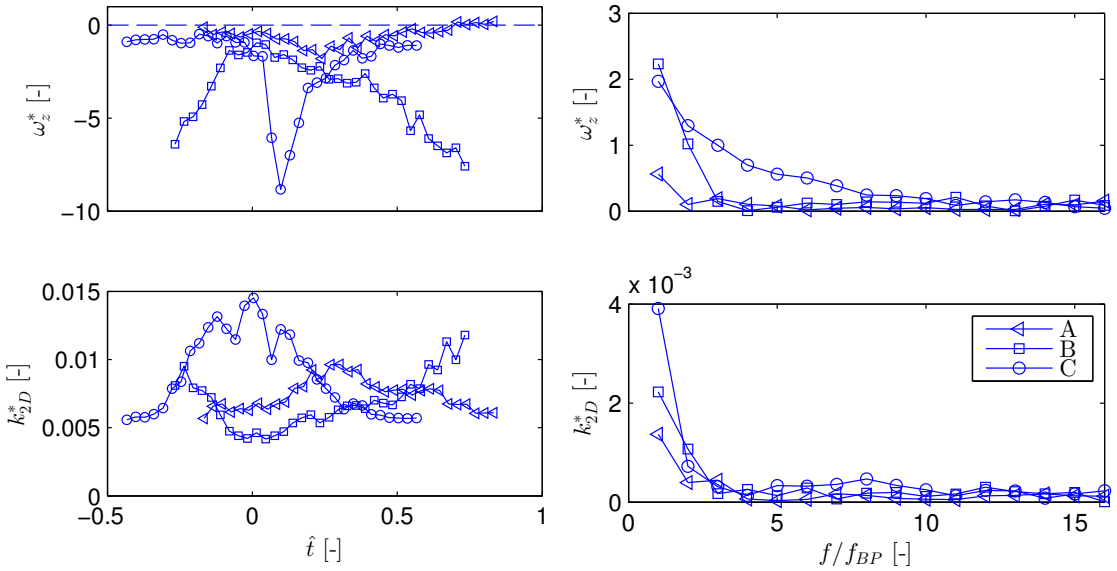

(a) Time signals

(b) Spectra

Figure 5.37: Time signals and spectra at 40 % Q_N of vorticity and TKE. Positions A (◁), B (□) and C (○) as shown in Fig. 5.3

For 40 % Q_N the velocity magnitude is always highest in point B (2° behind the tongue tip) and always lowest in point A (4° in front of the tongue tip), as shown in Fig. 5.36. A minimum in B, just after the blade has passed by (at about $\hat{t} = 0.1$), coincides with a maximum in C, so that at this time instant the velocity magnitude is nearly the same. A similar pattern is observed for the tangential velocity component. The radial velocity component is always positive (outflow) for point C and negative (backflow) for the other two points. In C there is a pronounced peak at $\hat{t} = 0.07$ which coincides with the absolute maximum velocity at this instant. This is due to the high outflow in the suction side of the blade behind the tongue tip, as explained in section 5.2.

In the frequency spectra of the velocities the highest peak for all three points is situated at f_{BP} (see Fig. 5.36b). For point C there is a significant peak at the third harmonic ($3f_{BP}$) in the absolute velocity and the tangential component. For the radial component in point C there is significant spectral content up to the 6th harmonic.

The vorticity in these three points is always negative (clockwise rotation contrary to impeller rotation), except for point A from $\hat{t} = 0.71$ to 0.83. For point A vorticity is moderate as it is situated ahead of the tongue tip with normalized

extreme values of -2 times the impeller vorticity. However, behind the tongue tip normalized vorticity values of -8 in B at $\hat{t} = 0.73$, due to flow separation from the tongue tip, and -9 in C, after the blade has passed ($\hat{t} = 0.1$), are achieved. In the frequency spectra the highest peaks are always at f_{BP}, as vorticity signals have only one pronounced minimum and maximum during one blade passage. TKE values are maximum in C as the blade passes by ($\hat{t} = 0.0$). In point A the maximum is achieved at $\hat{t} = 0.3$ due to the turbulence generated in the blade trailing edge wake. The evolution of the TKE curves with one broad peak leads always to the highest peak situated at f_{BP}.

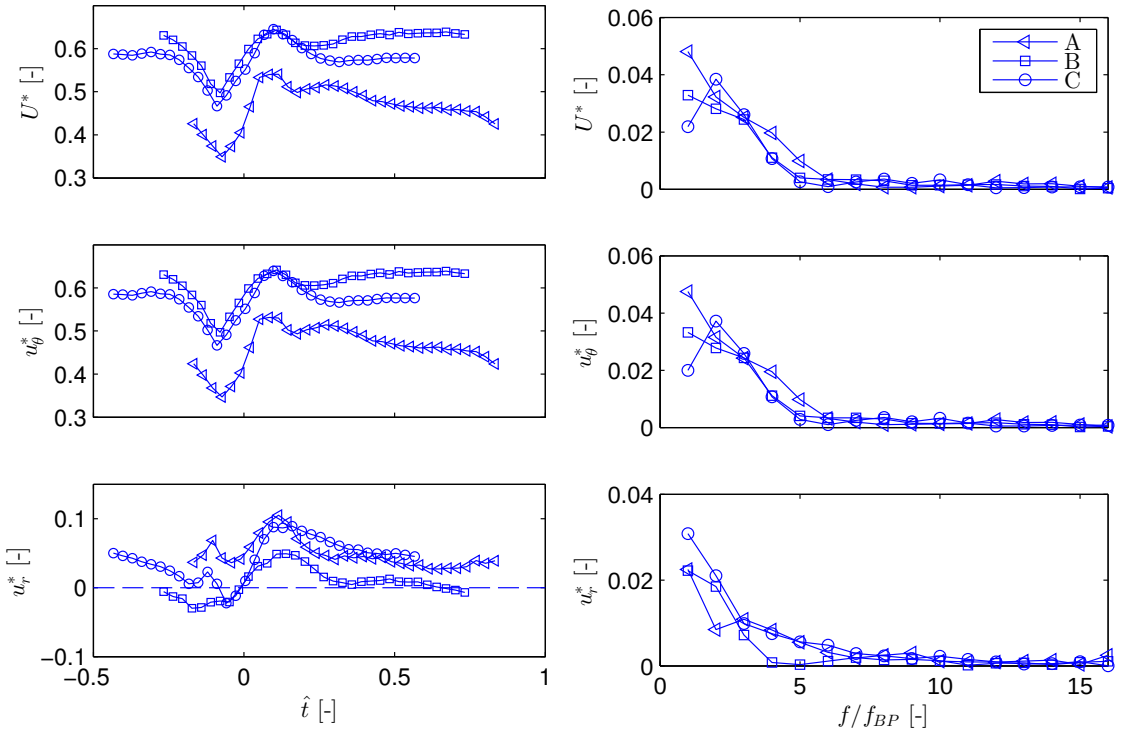

(a) Time signals

(b) Spectra

Figure 5.38: Time signals and spectra at Q_N of phase-averaged velocity magnitude, tangential and radial components at positions A (◁), B (□) and C (○). Positions as in Fig. 5.3

The time evolution of the velocity for Q_N (see Fig. 5.38a) is similar to 40 % Q_N, with lowest velocities in point A, ahead of the tongue tip. However, velocities in C are very similar to velocities in B. This is to be expected, as for the nominal flow-rate velocities in the volute are supposed to be very similar for different circumferential positions. Furthermore, the minimum velocity corresponds in all three points to the same time instant ($\hat{t} = -0.1$), just before the blade trailing edge aligns with these points. The maximum occurs after the blade has passed by ($\hat{t} = 0.1$). This behaviour of the jet-wake having the minimum and maximum close together leads to a higher spectral content at $2f_{BP}$ (see Fig. 5.38b). For point C the spectral content at the second harmonic ($2f_{BP}$) is even higher than at f_{BP}.

The tangential velocity component u_θ is very similar to the absolute velocity, as the radial component u_r is small (maximum of 0.1 U_{tip}). Only slight backflow ($u_r < 0$) occurs in B and C, before the blade arrives at these points.

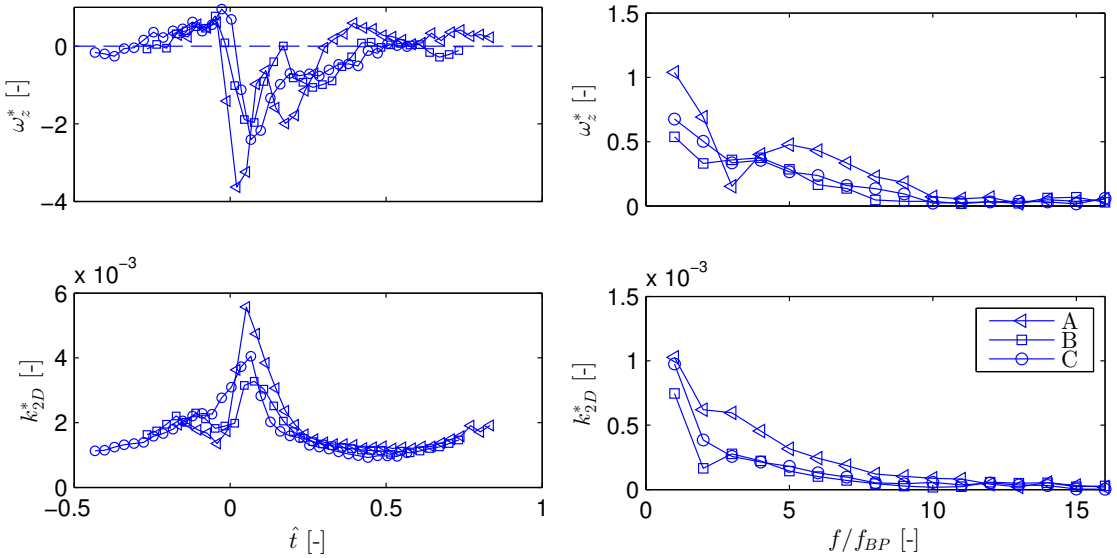

(a) Time signals (b) Spectra

Figure 5.39: Time signals and spectra at Q_N of vorticity and TKE. Positions A (◁), B (□) and C (○) as in Fig. 5.3

The vorticity is mainly positive before the blade arrives at each point (see Fig. 5.39a). As the blade passes by, vorticity drops abruptly to extreme minimum values due to the wake in the blade trailing edge.
The maximum TKE occurs in the blade trailing edge wake, coinciding with the extreme negative vorticity peak. With the blade further away TKE is very low, as it is the nominal flow-rate. Vorticity and TKE have the highest spectral content at f_{BP} (see Fig. 5.39b).

The absolute velocity magnitude with its tangential and radial velocity components and the corresponding frequency spectra at 150 % Q_N are presented in Fig. 5.40. The velocity signals for the three positions show two relative maxima and minima. As the blade pressure side passes each point, minimum velocities are achieved, indicating high negative tangential velocity in the relative frame, i.e. secondary flow from blade pressure to suction side. Soon afterwards, during the passage of the blade wake in the relative frame, the absolute and tangential velocity reach a maximum. Then U and u_θ reach another minimum which is more pronounced for points A and B and less pronounced for point C, as it is located further away from the tongue. For point A the highest velocity fluctuations occur at f_{BP} with strong components in the next three harmonics. However, for point B and C the strongest component is the second harmonic ($2f_{BP}$) due to the described time evolution with two maxima and two minima.
The behaviour of the tangential velocity is similar to the velocity magnitude.

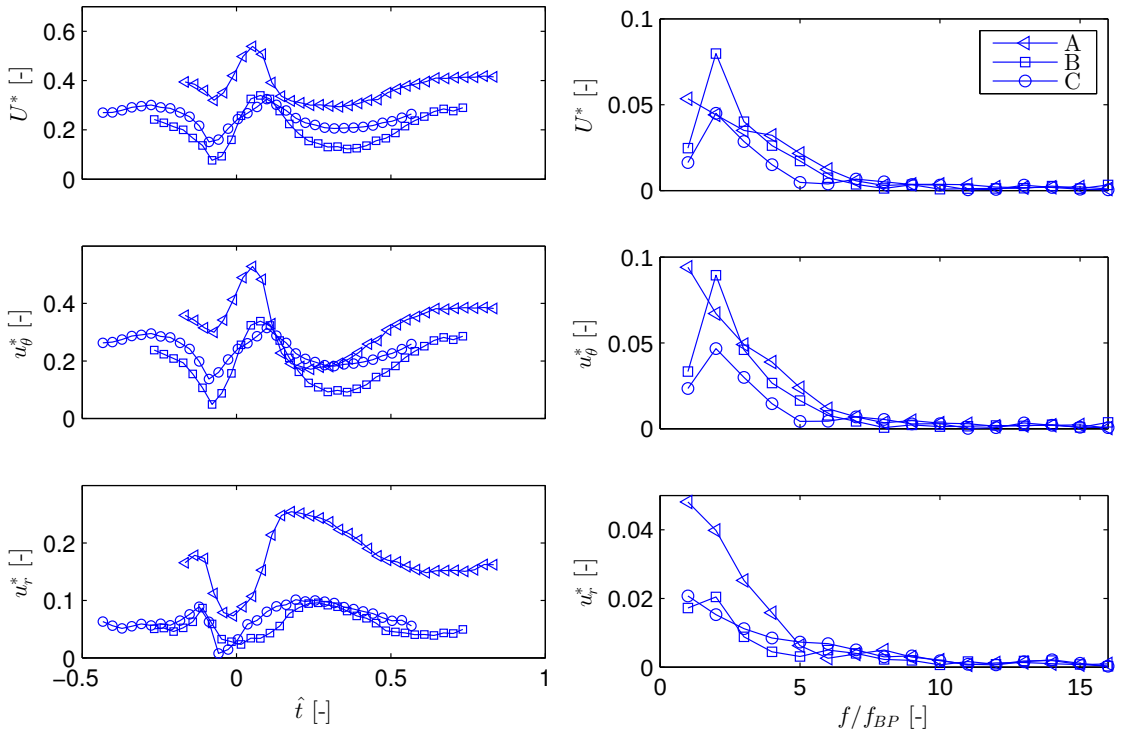

(a) Time signals (b) Spectra

Figure 5.40: Time signals and spectra at 150 % Q_N of phase-averaged velocity magnitude, tangential and radial components at positions A (◁), B (□) and C (○). Positions as in Fig. 5.3

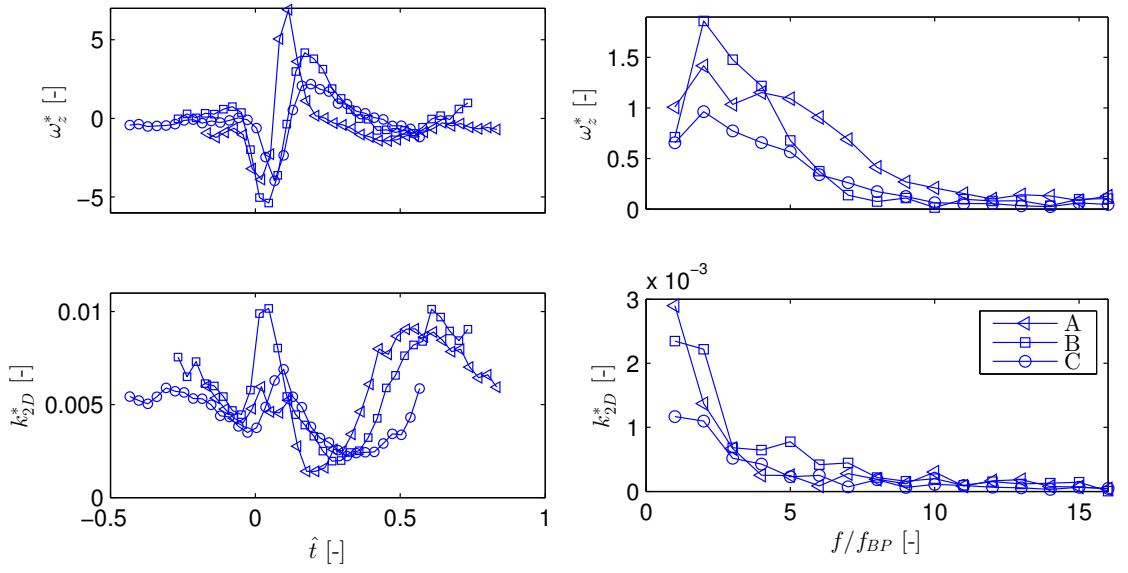

(a) Time signals (b) Spectra

Figure 5.41: Time signals and spectra at 150 % Q_N of vorticity and TKE. Positions A (◁), B (□) and C (○) as in Fig. 5.3

The highest velocities occur in point A, except between $\hat{t} = 0.13$ and 0.3 due to the high radial velocities. In general, the radial velocities are lower than the tangential velocities, especially for points B and C. Point A has one pronounced minimum and one maximum which results in the highest peak situated at f_{BP}. For $\hat{t} = 0.15$ to 0.36 the radial component is larger than the tangential component in A. The radial components (especially at A) reach their maxima due to the jet (in the relative frame), which is situated behind the blade suction side (see Fig. 5.14c).
As the flow with low relative velocity from the region on the pressure side of the next blade approaches each position, the radial velocity achieves a minimum while the tangential velocity gets maximum again.
The passing of the blade trailing edge leads to sharp variations of the vorticity (see Fig. 5.41a), coinciding with the passage of the negative and positive vorticity sheets shed from the blade. The vorticitiy fluctuations are seen to be particularly intense and abrupt at position A, ahead of the tongue tip. For the rest of the cycle the three vorticity signals show values close to zero. The vorticity values are smaller after the blade has passed the tongue tip (points B and C). The TKE shown in Fig. 5.41a has two distinctive maxima and two minima. The first maximum is due to the passing of the blade trailing edge (at about $\hat{t} = 0.05$) and the second (between $\hat{t} = 0.5$ and 0.6) due to the arrival of the turbulent zone generated at the blade leading edge. The highest peaks in the vorticity spectra always correspond to $2f_{BP}$, but significant spectral content is distributed to higher frequencies (see Fig. 5.41b). The most extreme case is found for position A, for which the vorticity amplitude at $7f_{BP}$ is still half the amplitude at $2f_{BP}$. On the contrary, in the TKE spectra all the amplitudes above $2f_{BP}$ are very small. In general, the fluctuations for 150 % Q_N close to the tongue tip (A and B) are similar in magnitude and significantly larger (about twice) than the fluctuations at C.

5.8 Amplitude and phase at f_{BP} and harmonics

The same FFT processing as in section 5.7 has been applied to all the nodes in the low and high magnification FOVs, so that the spectral content at f_{BP} and harmonics of the in-plane velocity magnitude, out-of-plane vorticity and in-plane TKE can be exhibited in contour maps.

5.8.1 Maps for 40 % Q_N

Figure 5.42 shows the amplitude and phase of the absolute velocity magnitude at f_{BP} and $2f_{BP}$ for 40 % Q_N with the high magnification FOV. In this and subsequent figures, lines with phase equal to zero indicate the positions for which the maximum value is achieved at $t^* = 0.00$, i.e. when the blade suction side aligns with the tongue tip.

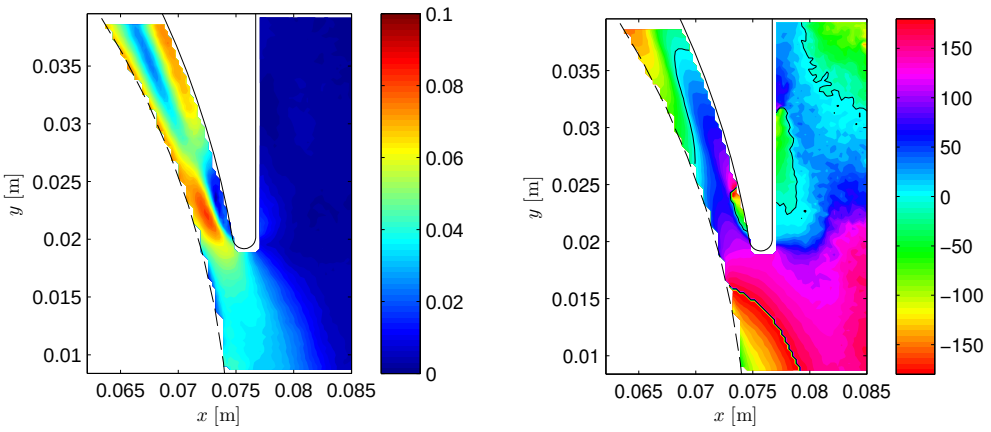

(a) Amplitude [-] at f_{BP}

(b) Phase [°] at f_{BP}

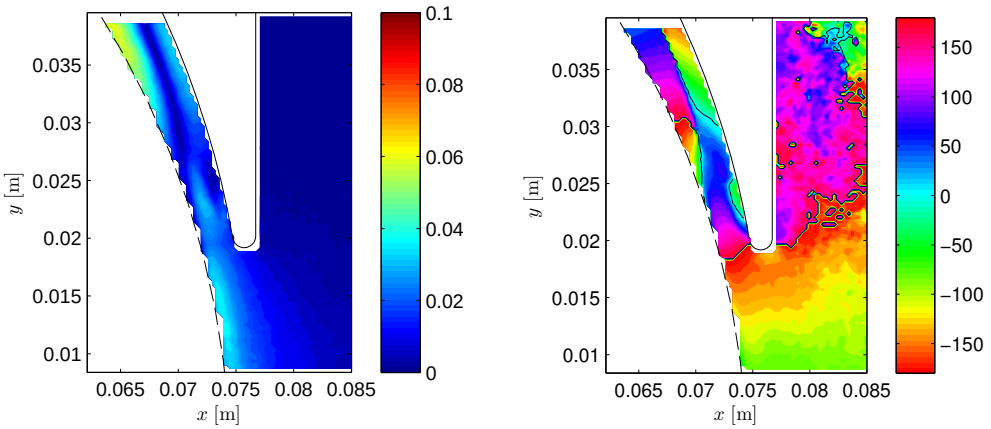

(c) Amplitude [-] at $2f_{BP}$

(d) Phase [°] at $2f_{BP}$

Figure 5.42: Amplitude and phase distribution at f_{BP} and $2f_{BP}$ of normalized phase-averaged in-plane velocity magnitude U^* at high M and 40 % Q_N

The main velocity fluctuations in the whole high magnification FOV occur at f_{BP}, as already shown for three points in section 5.7 (see Fig. 5.36). Fluctuations are particularly high in the narrow region of the volute and very low in the pump exit duct (see Fig. 5.42a). Velocity fluctuations at $2f_{BP}$ are low for this flow-rate, except close to the impeller outlet. Phase maps show the propagation of the unsteady velocity field. The colour bands in the phase maps indicate how the velocity fluctuations are convected along the stream. The thicker the color band, the higher the associated wavelength, i.e. the higher the stream velocity.

Vorticity fluctuations are shown in Fig. 5.43. They are especially high, up to 5 times the impeller vorticity, in the flow separation zone of the tongue tip in the narrow region of the volute. The phase map (Fig. 5.43b) helps to distinguish between maximum vorticity fluctuations in the narrow region of the volute associated with the flow separation zone (next to the tongue tip) and associated

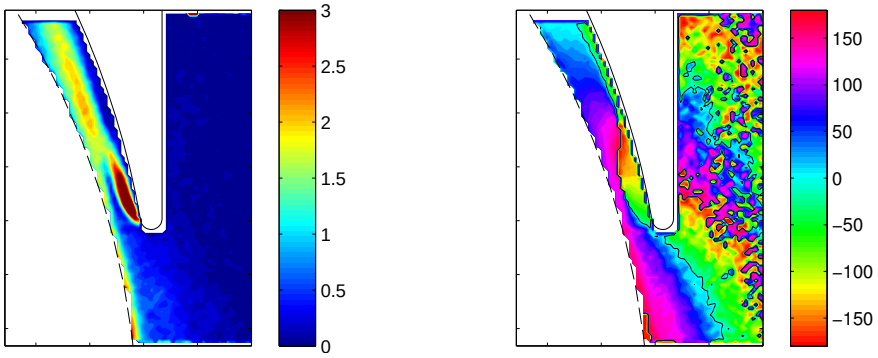

(a) Amplitude [-] at f_{BP} (b) Phase [°] at f_{BP}

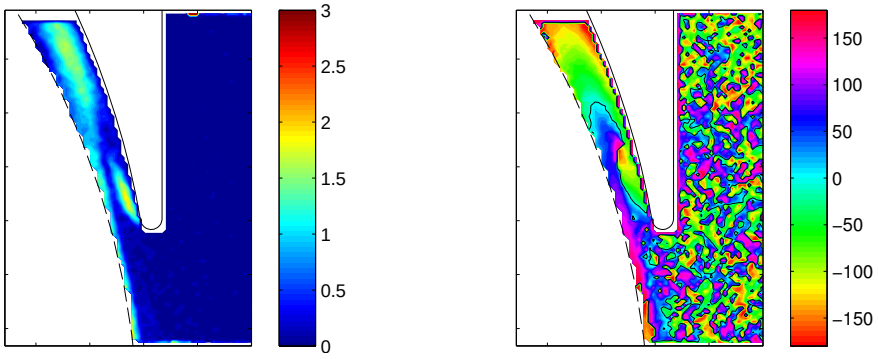

(c) Amplitude [-] at $2f_{BP}$ (d) Phase [°] at $2f_{BP}$

Figure 5.43: Amplitude and phase distribution at f_{BP} and $2f_{BP}$ of normalized phase-averaged vorticity ω_z^* at high M and 40 % Q_N

with the blade wake (next to the impeller outlet). The black line at phase equal to zero limits these two regions. The maximum values of vorticity fluctuations at $2f_{BP}$ (see Fig. 5.43c) occur in about the same places as for f_{BP}, but with about half of the amplitude in the flow separation zone and 75 % further away (in the upper region of the FOV).

TKE fluctuations, shown in Fig. 5.44, are highest for 40 % Q_N at f_{BP} in the narrow region of the volute due to the flow separation from the tongue tip. In the pump outlet duct TKE fluctuations are very low. For the TKE fluctuations at $2f_{BP}$ the same pattern occurs, but with less amplitude.

The results of the velocity fluctuations for 40 % Q_N at low magnification are shown in Fig. 5.45. In the low magnification FOV the pattern is similar to the high magnification FOV, with highest fluctuations at f_{BP} close to the impeller outlet and very low fluctuations in the whole pump outlet duct.

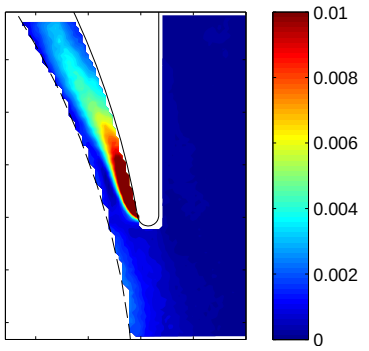

(a) Amplitude [-] at f_{BP}

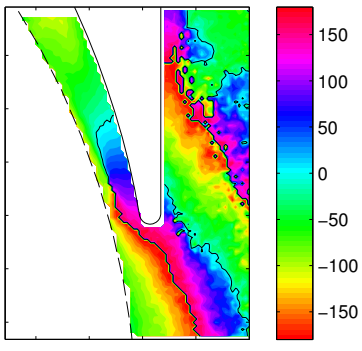

(b) Phase [°] at f_{BP}

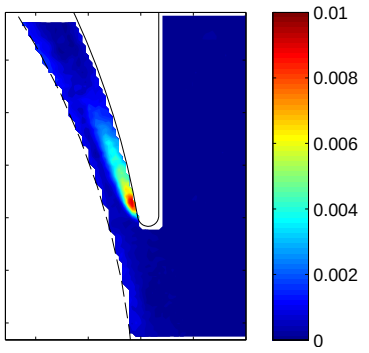

(c) Amplitude [-] at $2f_{BP}$

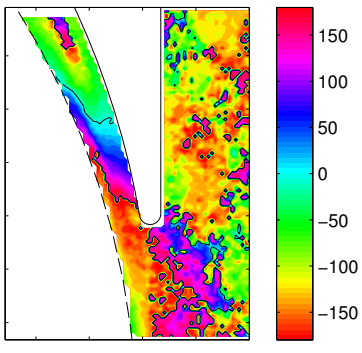

(d) Phase [°] at $2f_{BP}$

Figure 5.44: Amplitude and phase distribution at f_{BP} and $2f_{BP}$ of normalized in-plane TKE k^*_{2D} at high M and 40 % Q_N

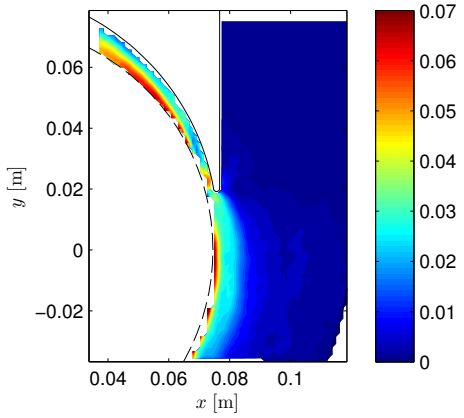

(a) Amplitude [-] at f_{BP}

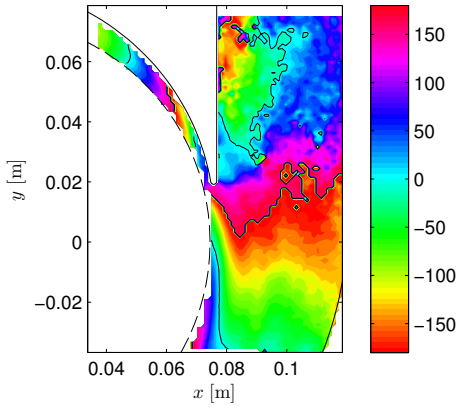

(b) Phase [°] at f_{BP}

Figure 5.45: Amplitude and phase distribution at f_{BP} of normalized phase-averaged in-plane velocity magnitude U^* at low M and 40 % Q_N

For the vorticity (Fig. 5.46) and TKE (Fig. 5.47) at low magnification the same behaviour as for the velocity is detected regarding the fluctuations in amplitude. In the phase map of the vorticity fluctuations at f_{BP} (Fig. 5.46b) a flow structure

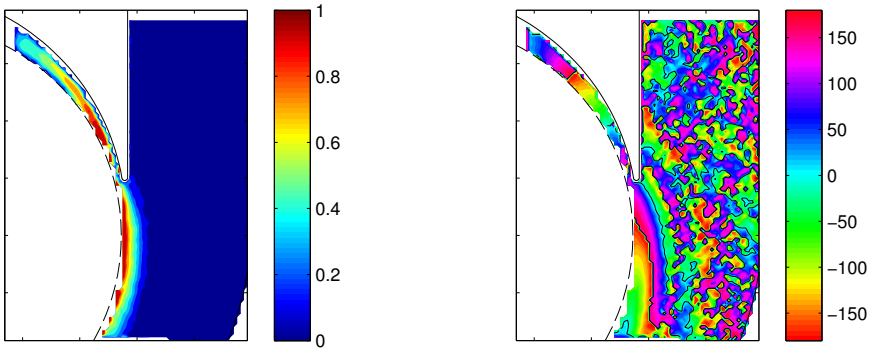

(a) Amplitude [-] at f_{BP} (b) Phase [°] at f_{BP}

Figure 5.46: Amplitude and phase distribution at f_{BP} of normalized phase-averaged vorticity ω_z^* at low M and 40 % Q_N

can be identified which starts at the tongue tip and bends into the broad region of the volute towards the pump exit. However, this flow structure decays fast as vorticity fluctuations at f_{BP} in the rest of the pump exit are not distinguishable due to the low signal to noise ratio (SNR).

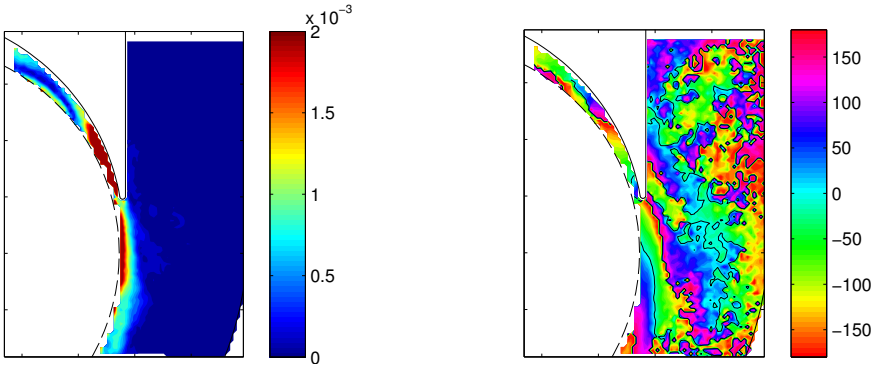

(a) Amplitude [-] at f_{BP} (b) Phase [°] at f_{BP}

Figure 5.47: Amplitude and phase distribution at f_{BP} of normalized in-plane TKE k_{2D}^* at low M and 40 % Q_N

5.8.2 Maps for Q_N

The velocity fluctuations for Q_N using the high magnification FOV are shown in Fig. 5.48. Velocity fluctuations are highest at f_{BP} at the impeller outlet ahead of the tongue tip (see Fig. 5.48a). Behind the tongue tip in the narrow region of the volute fluctuations are higher at $2f_{BP}$ than at f_{BP} (Fig. 5.48c). The phase of the fluctuations are better distinguishable than for 40 % Q_N, as more flow structures from the impeller are convected towards the volute and pump exit. In the phase maps a mainly uniform phase shift is observed for the nominal flow-rate compared to the other flow-rates. A region with slightly higher velocities

(less phase shift) in the outlet duct behind the tongue tip can be observed. This is due to flow acceleration from the blade trailing edge wake with high absolute velocities.

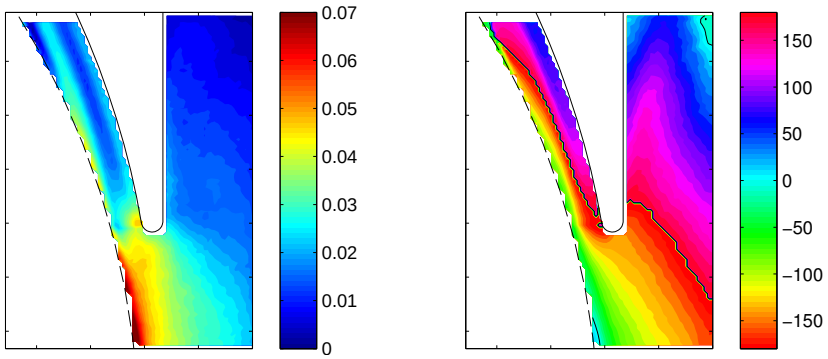

(a) Amplitude [-] at f_{BP} (b) Phase [°] at f_{BP}

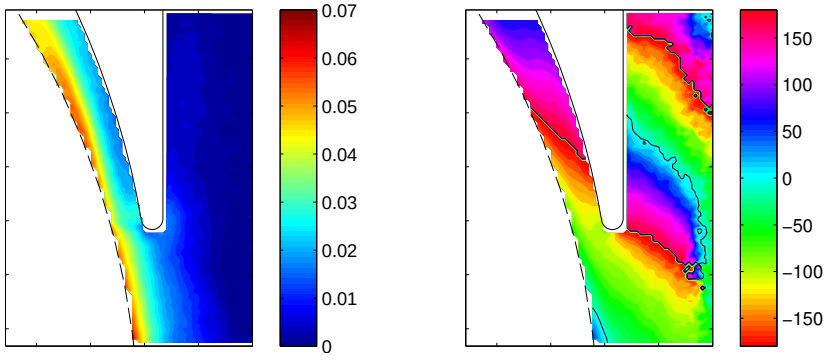

(c) Amplitude [-] at $2f_{BP}$ (d) Phase [°] at $2f_{BP}$

Figure 5.48: Amplitude and phase distribution at f_{BP} and $2f_{BP}$ of normalized phase-averaged in-plane velocity magnitude U^* at high M and Q_N

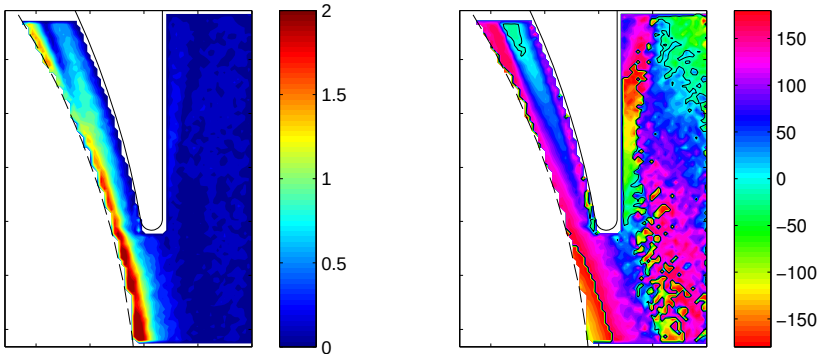

(a) Amplitude [-] at f_{BP} (b) Phase [°] at f_{BP}

Figure 5.49: Amplitude and phase distribution at f_{BP} of normalized phase-averaged vorticity ω_z^* at high M and Q_N

The vorticity (Fig. 5.49) and TKE fluctuations (Fig. 5.50) at Q_N are highest at f_{BP}, as already observed in section 5.7 (Fig. 5.39). Contour maps at $2f_{BP}$ can be found for comparison in the appendix (Figs. B.23 and B.24). Fluctuations are lower than at off-design conditions, which lead to a higher noise level. This noise is especially visible in the phase maps.

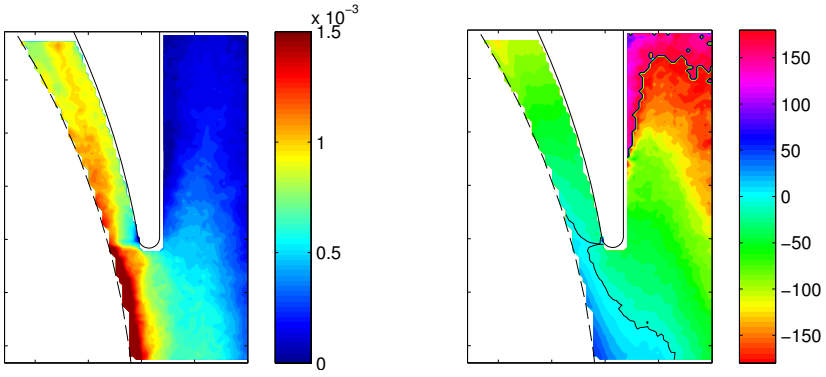

(a) Amplitude [-] at f_{BP} (b) Phase [°] at f_{BP}

Figure 5.50: Amplitude and phase distribution at f_{BP} of normalized in-plane TKE k^*_{2D} at high M and Q_N

Flow structures in the volute and pump outlet duct can be better observed in the low magnification FOV. Figure 5.51 shows the velocity fluctuations with highest amplitudes at the impeller outlet ahead of the tongue tip. In the phase map (see Fig. 5.51b) flow structures which are cyclic with f_{BP} can be clearly observed and extend up to about half of the outlet duct width.

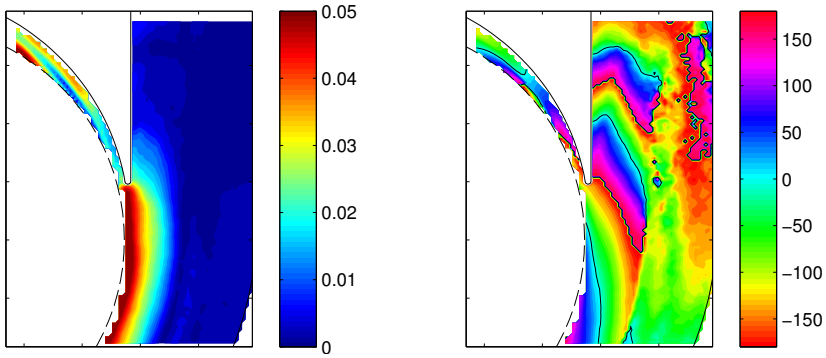

(a) Amplitude [-] at f_{BP} (b) Phase [°] at f_{BP}

Figure 5.51: Amplitude and phase distribution at f_{BP} of U^* at low M and Q_N

Similar flow structures as for the velocity fluctuation can be seen in the vorticity fluctuation maps in Fig. 5.52. They have very similar extension but the shape is slightly different, as they are due to the vorticity sheets shed from the impeller with the main component being the tangential direction.

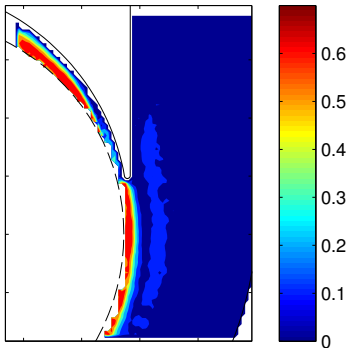

(a) Amplitude [-] at f_{BP}

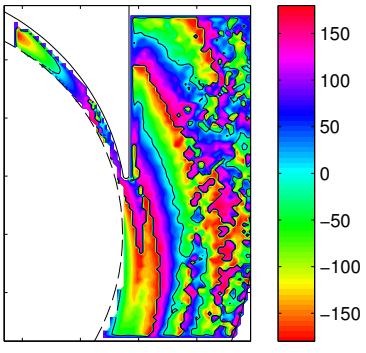

(b) Phase [°] at f_{BP}

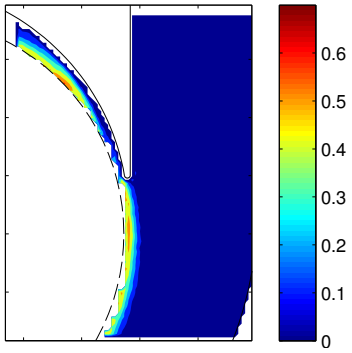

(c) Amplitude [-] at $2f_{BP}$

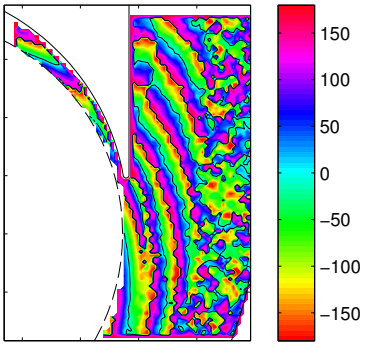

(d) Phase [°] at $2f_{BP}$

Figure 5.52: Amplitude and phase distribution at f_{BP} and $2f_{BP}$ of normalized phase-averaged vorticity ω_z^* at low M and Q_N

The TKE fluctuations are low, especially in the outlet duct (see Fig. 5.53). This leads to a lower SNR in the phase maps, so that flow structures are harder to detect (Fig. 5.53b).

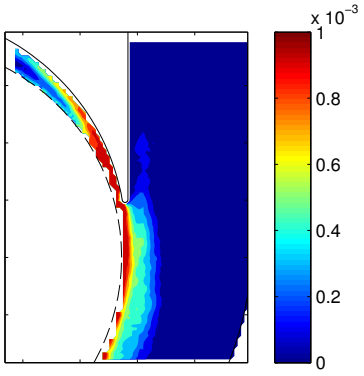

(a) Amplitude [-] at f_{BP}

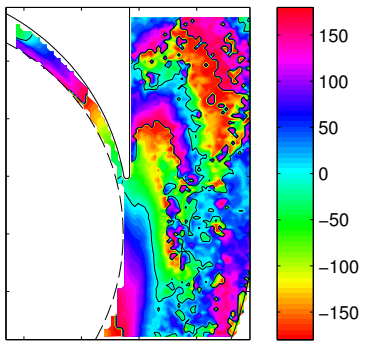

(b) Phase [°] at f_{BP}

Figure 5.53: Amplitude and phase distribution at f_{BP} of normalized in-plane TKE k_{2D}^* at low M and Q_N

5.8.3 Maps for 150 % Q_N

For 150 % Q_N Fig. 5.54 shows the velocity fluctuations at f_{BP} and $2f_{BP}$. The velocity fluctuations at the impeller outlet are mainly associated to f_{BP} in the region ahead of the tongue tip, whereas the dominant frequency in the narrow region of the volute is $2f_{BP}$, most remarkably in the tongue stagnation region. Also, significant fluctuations appear at both frequencies in the tongue wake region, whereas they are very small at the tongue tip. The phase map for f_{BP} (see Fig. 5.54b) reveals the jet-like flow formed from the tongue tip towards the outlet duct as well as the low velocity on the tongue exit side, which can be attributed to the detachment of this jet.

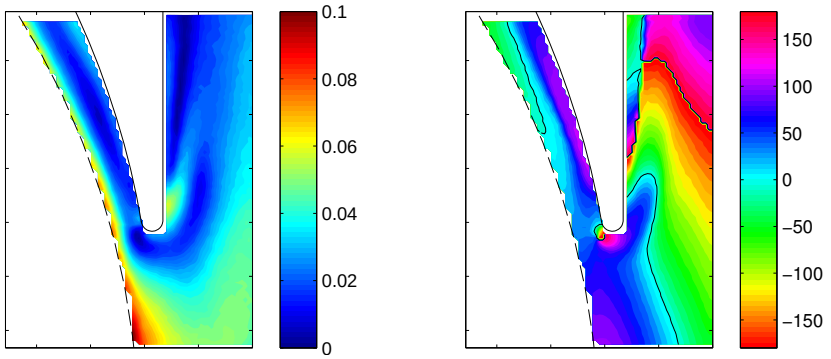

(a) Amplitude [-] at f_{BP} (b) Phase [°] at f_{BP}

(c) Amplitude [-] at $2f_{BP}$ (d) Phase [°] at $2f_{BP}$

Figure 5.54: Amplitude and phase distribution at f_{BP} and $2f_{BP}$ of normalized phase-averaged in-plane velocity magnitude U^* at high M and 150 % Q_N

In line with the vorticity spectra of Fig. 5.41b, Fig. 5.55 shows that vorticity fluctuations at the impeller outlet are much higher for $2f_{BP}$ than for f_{BP}, with particularly high values in the region close to the tongue tip. Besides, high vorticity values can be seen from the wake tongue region at both f_{BP} and $2f_{BP}$.

Again, the phase maps show the jet-wake effects for the flow past the tongue towards the outlet duct. Besides, the colour bands at both sides of the tongue

exhibit a fault-like phase shift of 180°, which is caused by the trend of the vorticity sheets shed from the rotating blade to stretch due to stickiness effects on the tongue stagnation region (Fig. 5.23 from $t^* = 0.00$ to 0.38).

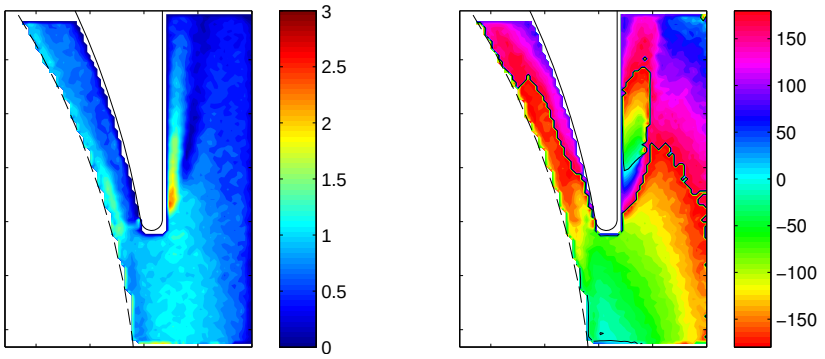

(a) Amplitude [-] at f_{BP} (b) Phase [°] at f_{BP}

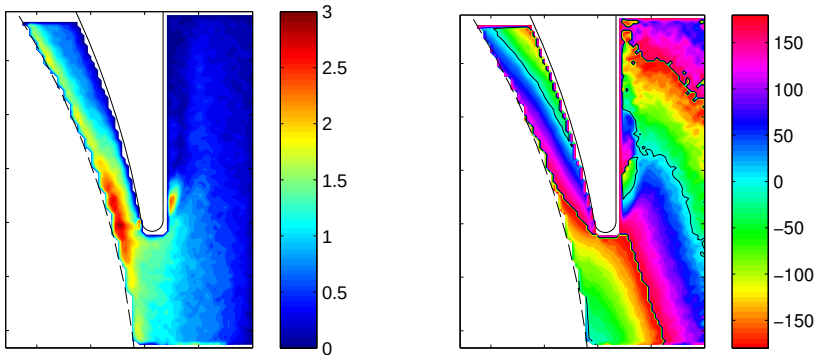

(c) Amplitude [-] at $2f_{BP}$ (d) Phase [°] at $2f_{BP}$

Figure 5.55: Amplitude and phase distribution at f_{BP} and $2f_{BP}$ of normalized phase-averaged vorticity ω_z^* at high M and 150 % Q_N

The TKE fluctuations (Fig. 5.56) at the impeller outlet are intense at f_{BP} ahead of the tongue and also at $2f_{BP}$ in the region close to the tongue tip. The TKE fluctuations appear to be particularly high at the wake tongue region for both frequencies. The TKE phase maps show how the TKE fluctuations are convected with the stream. Nearly no shifting effects occur when comparing the regions at both sides of the tongue.

As shown in Fig. 5.56b and 5.56d, maximum TKE values at f_{BP} in the tongue wake region occur when the blade is passing the tongue tip, whereas the maximum values at $2f_{BP}$ take place twice during the cycle: first slightly after the passage of the blade in front of the tongue tip and second when the next blade has moved half-way towards the tongue (at about $t^* = 0.15$ and 0.65 respectively). This is motivated by the turbulence generated at the wake tongue (see Fig. 5.35) and, especially, by the arrival of the high TKE strips, either shed from

the blade trailing edge or carried by the stream coming from the mid-region of the impeller channels.

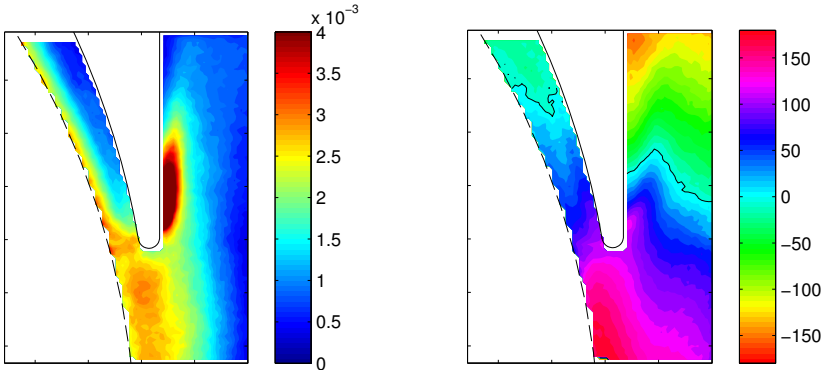

(a) Amplitude [-] at f_{BP} (b) Phase [°] at f_{BP}

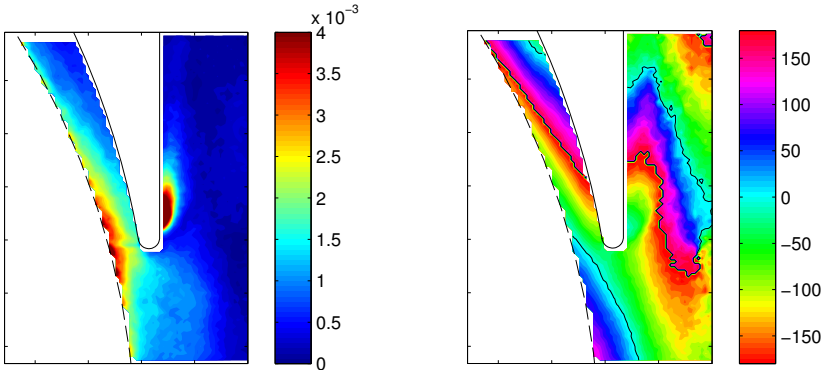

(c) Amplitude [-] at $2f_{BP}$ (d) Phase [°] at $2f_{BP}$

Figure 5.56: Amplitude and phase distribution at f_{BP} and $2f_{BP}$ of normalized in-plane TKE k^*_{2D} at high M and 150 % Q_N

Figure 5.57 presents the distribution of the velocity fluctuations at f_{BP} and $2f_{BP}$ for the low magnification FOV. In spite of the loss of resolution as compared to the previous high magnification FOV maps, the results confirm that the fluctuations are remarkably high around the impeller outlet ahead of the tongue tip and that they diminish quickly in the radial direction. With respect to the f_{BP} amplitude just behind the impeller outlet, at a radius of 1.25 r_{tip}, there is a reduction to about 10 % for the velocity magnitude, vorticity (Fig. 5.58a) and TKE (Fig. 5.59a). This is in agreement with previous results by Miner et al. (1989) and Dong et al. (1992b). In the exit channel, relatively high fluctuations can still be seen since fluctuations are dragged with the stream along the half of the exit channel on the tongue side. On the contrary, nearly no fluctuations appear on the side opposite the tongue. The convection of the velocity fluctuations is well exposed in the phase maps of Fig. 5.57, where the trace of up to three blade passages is clearly visible (see Fig. 5.57b). Also, these phase maps show the extension of the region where fluctuations are distinguishable from the background noise.

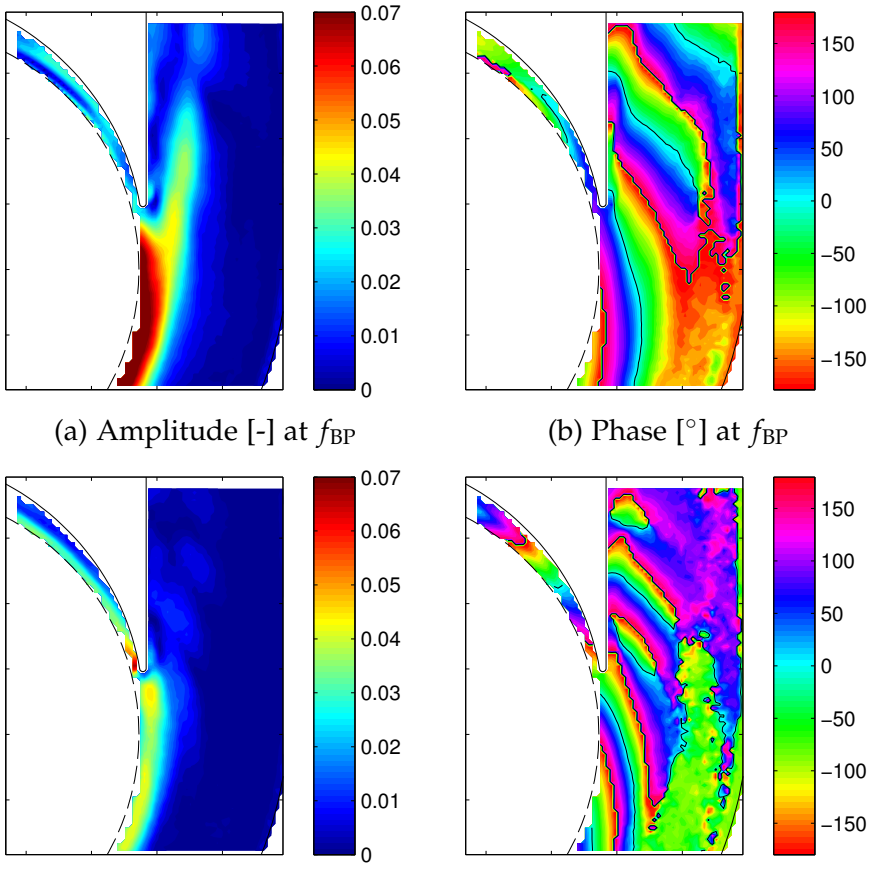

(a) Amplitude [-] at f_{BP} (b) Phase [°] at f_{BP}

(c) Amplitude [-] at $2f_{BP}$ (d) Phase [°] at $2f_{BP}$

Figure 5.57: Amplitude and phase distribution at f_{BP} and $2f_{BP}$ of normalized phase-averaged in-plane velocity magnitude U^* at low M and 150 % Q_N

Figure 5.58 presents the distributions of vorticity fluctuations in the low magnification FOV, including f_{BP}, $2f_{BP}$ and $3f_{BP}$. Unlike the results plotted in the high magnification FOV (Fig. 5.55) for the flow exiting the impeller in front of the tongue tip, where the dominant frequency is $2f_{BP}$, in the extended FOV the highest amplitudes correspond to f_{BP}. Although, significant amplitudes exist at the impeller exit at $2f_{BP}$ and even at $3f_{BP}$.

Again, the vorticity (Fig. 5.58) and TKE fluctuations (Fig. 5.59) are seen to progressively decay in amplitude while being convected towards the pump exit, the higher the frequency the quicker the decay and the smaller the area where fluctuations are noticeable. The latter can be better observed in the phase maps, for which the number of colour sheets is proportional to the harmonic order.

The fluctuation amplitudes in the pump outlet duct are highest for 150 % Q_N. The extension of the flow structures are also highest for 150 % Q_N, occupying nearly the whole outlet duct, followed by Q_N. For 40 % Q_N hardly any flow structures are convected into the pump outlet duct.

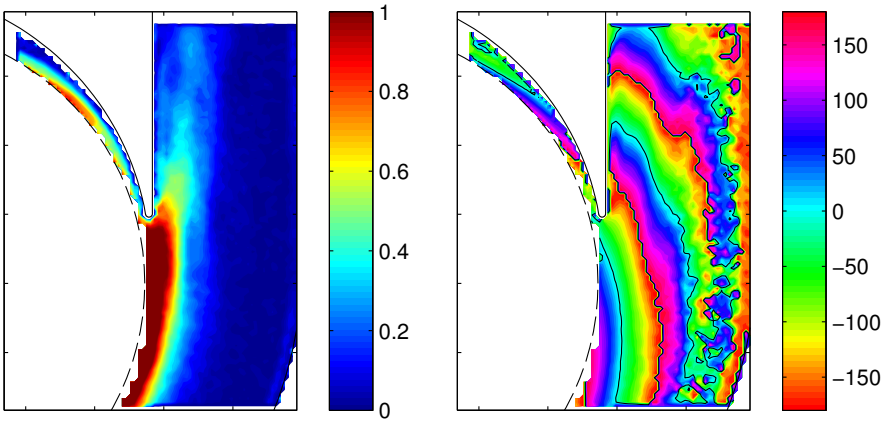

(a) Amplitude [-] at f_{BP} (b) Phase [°] at f_{BP}

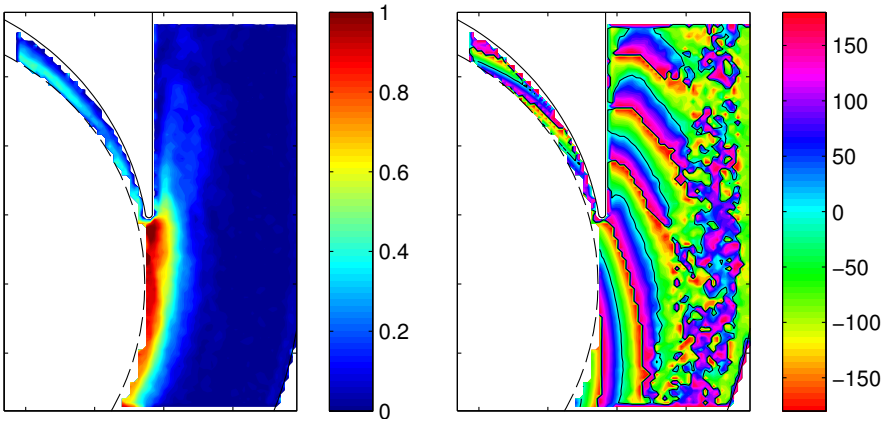

(c) Amplitude [-] at $2f_{BP}$ (d) Phase [°] at $2f_{BP}$

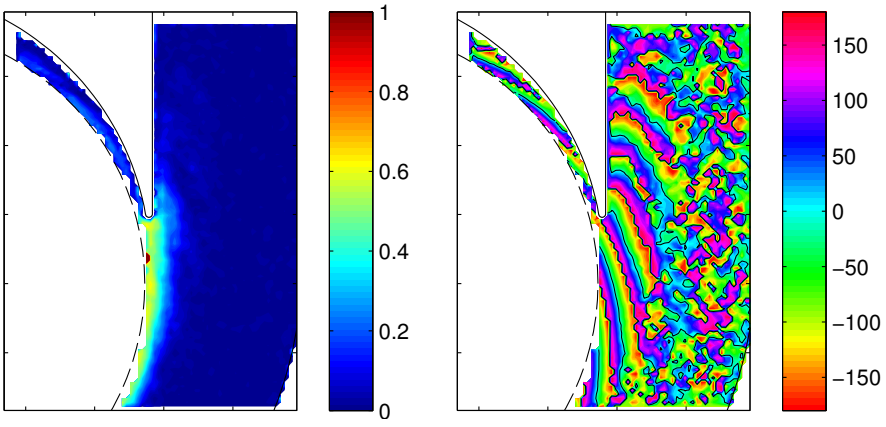

(e) Amplitude [-] at $3f_{BP}$ (f) Phase [°] at $3f_{BP}$

Figure 5.58: Amplitude and phase distribution at f_{BP}, $2f_{BP}$ and $3f_{BP}$ of normalized phase-averaged vorticity ω_z^* at low M and 150 % Q_N

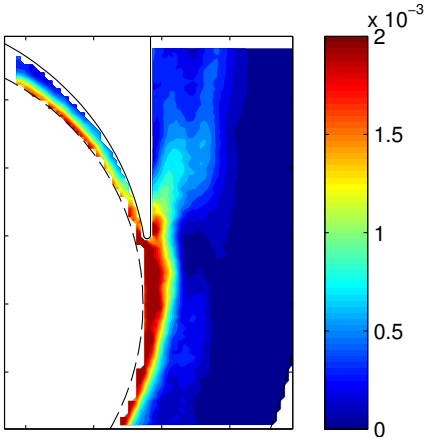

(a) Amplitude [-] at f_{BP}

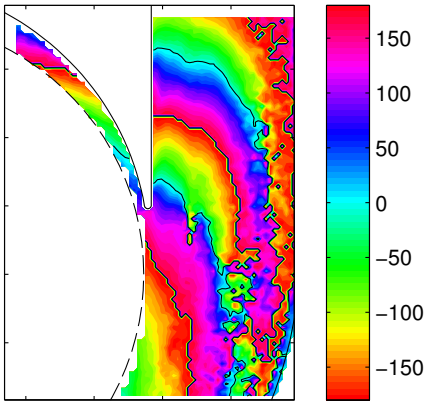

(b) Phase [°] at f_{BP}

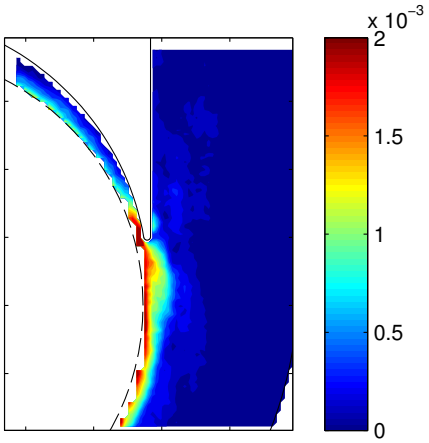

(c) Amplitude [-] at $2f_{BP}$

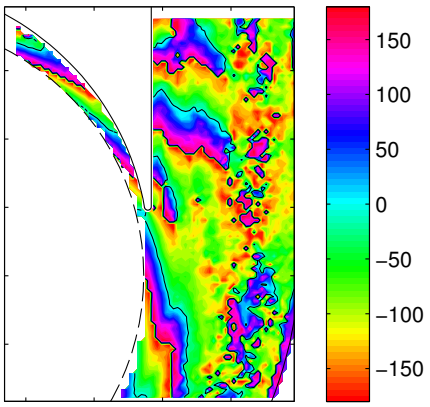

(d) Phase [°] at $2f_{BP}$

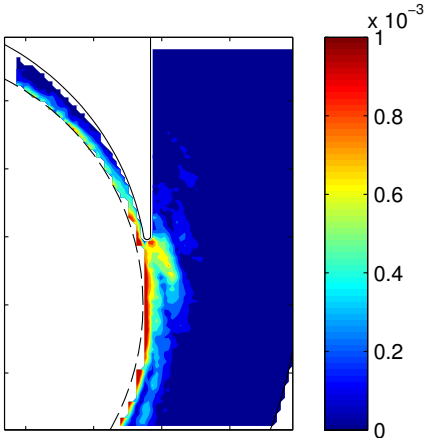

(e) Amplitude [-] at $3f_{BP}$

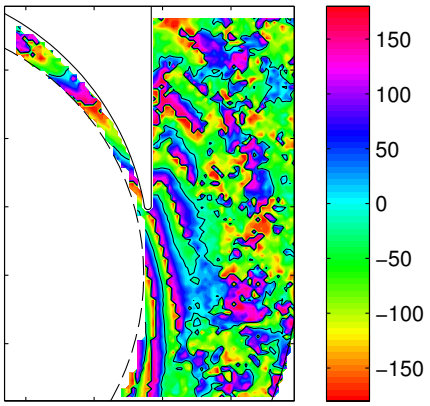

(f) Phase [°] at $3f_{BP}$

Figure 5.59: Amplitude and phase distribution at f_{BP}, $2f_{BP}$ and $3f_{BP}$ of normalized in-plane TKE k^*_{2D} at low M and 150 % Q_N

6 Acoustic coupling with hydraulic circuit

In this chapter the results regarding the acoustic coupling with the hydraulic circuit of two different centrifugal pumps are presented. The first pump is an industrial pump with double-curved impeller blades and is described in section 3.1. The second pump is the transparent pump which was specifically designed and built (see description in section 3.2) to obtain optical access for the PIV measurements. The methodologies applied and the measurement procedures are described in section 4.2.

6.1 Acoustic results for industrial pump

The internal sound propagation model described in section 4.2.3 was used to estimate the scattering matrix (Fig. 6.1) and the source vector (Fig. 6.2) of the industrial pump. Figure 6.1 shows the calculated magnitude and phase of the four elements of the scattering matrix for the test pump. They were obtained by imposing appropriate auxiliary acoustic sources at the boundaries and anechoic pipelines. Several pump rotational speeds were investigated. The frequency is normalized by a reference pump rotation frequency $f_{\text{ref}} = 27$ Hz ($\widehat{=}$1620 rpm). Whereas the magnitude of the reflection elements must lie between 0 and 1, the transmission elements can be greater than unity if, like in the present case, the cross-sections of both ports are different. In the present case, the section of port #2, which corresponds to the inlet of the discharge diffuser, is 4.5 times smaller than the section of port #1, at the impeller inlet. According to the reciprocity principle (Rossing, 2007), if both sections were equal then the scattering matrix would be symmetric, except for the very slight effect of the water stream on the effective speed of sounds along the positive and the negative directions. In fact, because of the assumptions of the pump acoustic model, that very small effect is the only one that can be attributable to variations in the pump operating point. Moreover, Fig. 6.1 shows that the effect of the sound frequency on the elements of the scattering matrix is relatively small. Basically all the elements except R_{22} have some reduction in magnitude for increasing frequency, thus indicating a somewhat greater internal acoustic energy dissipation.

The results in Fig. 6.1 can be compared to the experimental data exposed by Bardeleben and Weaver (2002) for a centrifugal pump with a single inlet and single volute. The performance data reported by them suggest a specific speed

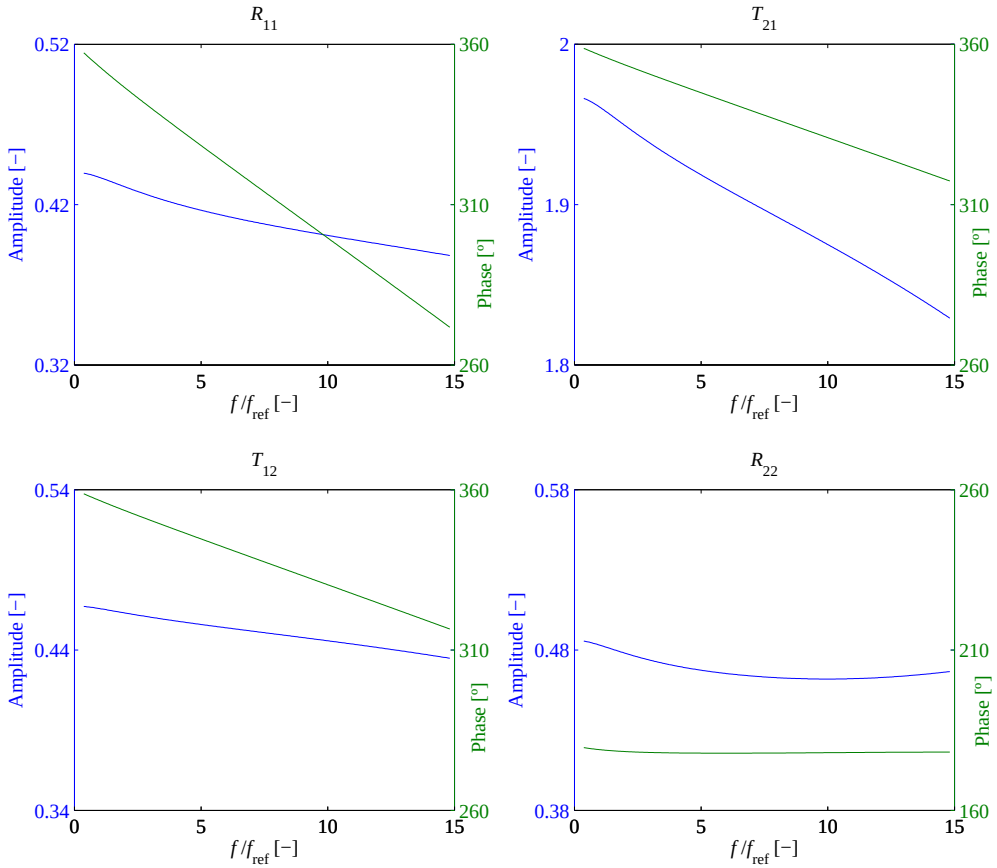

Figure 6.1: Scattering matrix of the industrial pump

for that pump of about 0.3, whereas the specific speed for the pump used in this thesis is 0.46. In spite of that, the predictions of Fig. 6.1 show similar trends to the experimental results reported by Bardeleben and Weaver (2002). The agreement between predictions and measurements regarding the phase of the scattering matrix is particularly satisfactory. Besides, the reflection coefficients now calculated for the pump inlet and outlet are respectively about 50 % and 30 % smaller than those measured in Bardeleben and Weaver (2002). However, this is not surprising because for pumps with low specific speed the width of the internal passageways is usually very small in comparison with the diameter and, additionally, the change from axial to radial direction at the impeller inlet becomes more abrupt, i.e. sound transmission becomes more difficult and so sound reflection is favoured.

Figure 6.2 represents the source elements P_{G1} and P_{G2} as a function of frequency for three different flow-rates (40 % Q_N, Q_N and 140 % Q_N). They were obtained by imposing in the pump the ideal sound sources that characterize the f_{BP} acoustic excitation, together with anechoic piping (as boundary condition). The frequency in the bottom axis is shown normalized by a reference pump rotation

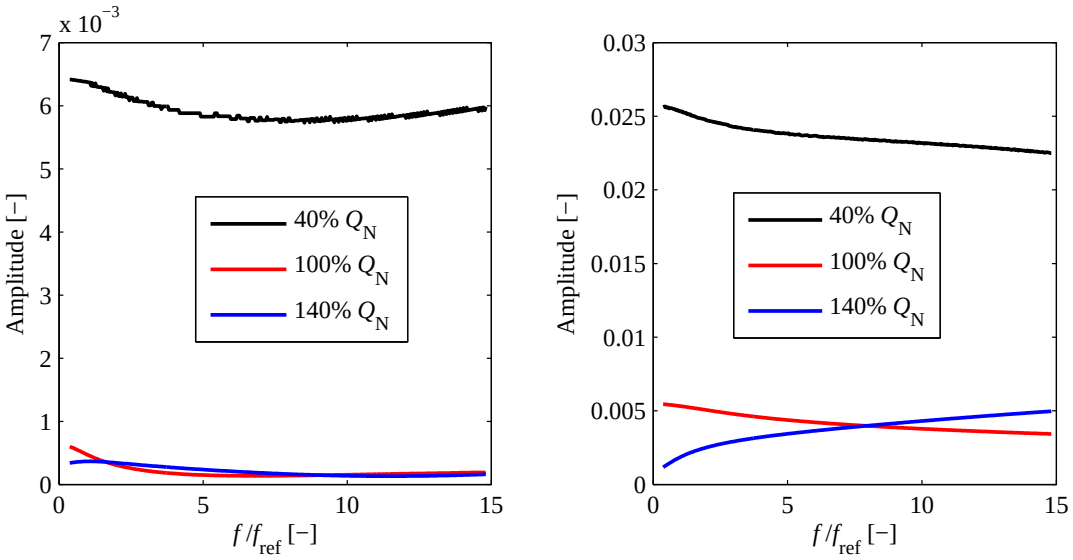

(a) Modulus of P_{G1} (b) Modulus of P_{G2}

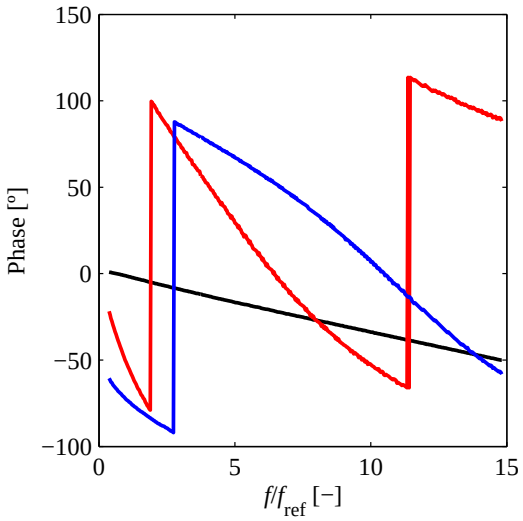

(c) Phase between P_{G1} and P_{G2}

Figure 6.2: Source vector elements P_{G1} and P_{G2}

frequency $f_{ref} = 27$ Hz and the amplitude by $\rho/2U_{tip}^2$. For part load (40 % Q_N) the amplitude of the two source elements is particularly high. It is also higher at the discharge port than at the suction port, this is partially caused by different cross-sectional areas of the ports.

Special attention was taken during the modification of the acoustic properties of the hydraulic system when opening or closing valves at lateral branches. This did not change the operating point of the pump, as the flow-rate in these lateral branches was zero due to second closed valves. An example is the lateral branch shown in Fig. 3.2 with valves V3 and V4 in the suction part of the hydraulic sys-

tem. Valve V3 is always closed, so by opening or closing valve V4 the operating point is not changed, although it modifies the circuit acoustic characteristics.

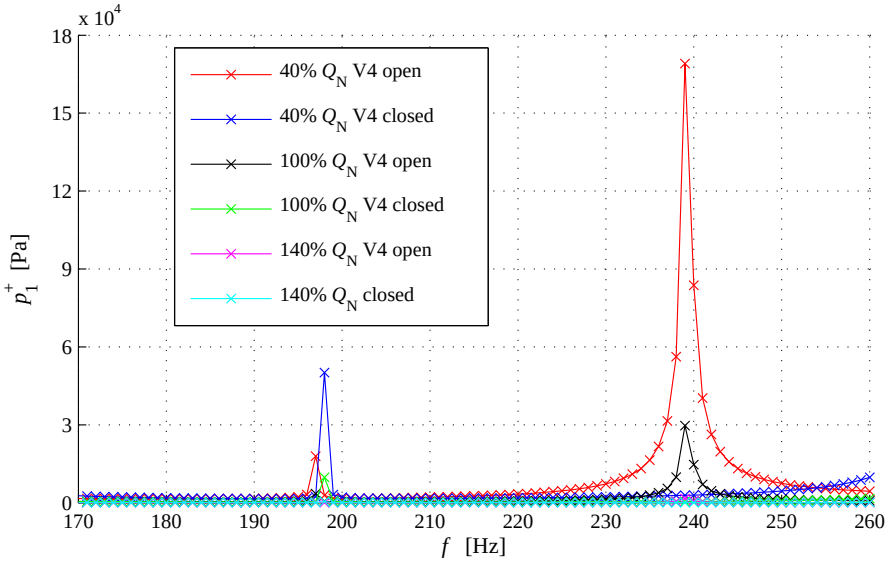

(a) p^+ at pump inlet

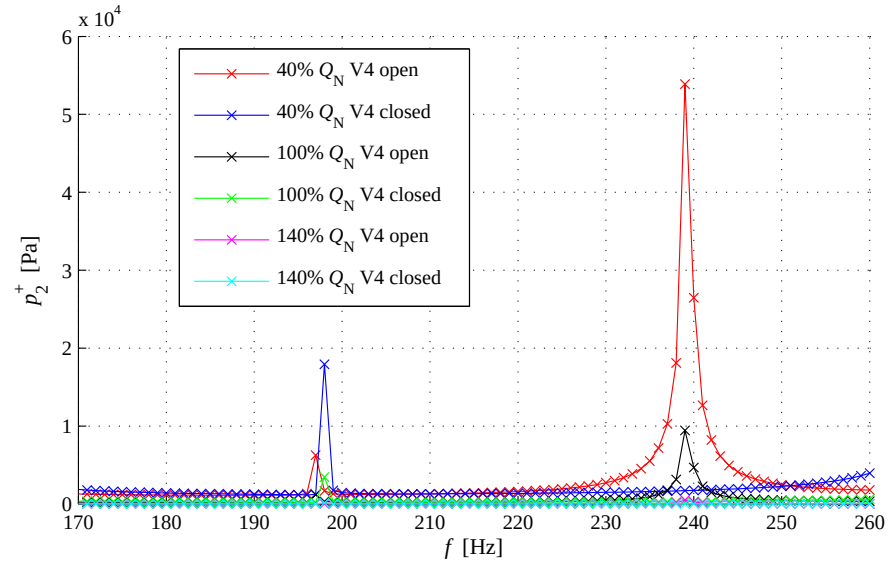

(b) p^+ at pump outlet

Figure 6.3: Amplitude of radiated pressure waves p_1^+ and p_2^+ for different f_{BP}, flow-rates and valve V4 open or closed, obtained from pump-circuit model. Note the different scale of the pressure between a) and b)

Figure 6.3 represents the amplitude of the exiting pressure waves P_1^+ and P_2^+ calculated for the test pump when operating at three different flow-rates (part load, nominal and overload) and each of them under two conditions, with valve V4 open or closed. It is seen that, with valve V4 open, a large resonant peak is produced at 239 Hz, especially when operating at part load. The phenomenon

affects the suction and the discharge side, but at the suction side the peak is three times higher than at the discharge side. This is reasonable, as the valve V4 is situated at the suction part. Closing valve V4 results in the vanishing of the 239 Hz resonant peak for all flow-rates, but a new resonant peak appears at about 198 Hz. Though its magnitude is not so high, again it is more evident for the low flow-rate and affects similarly both pump ports.

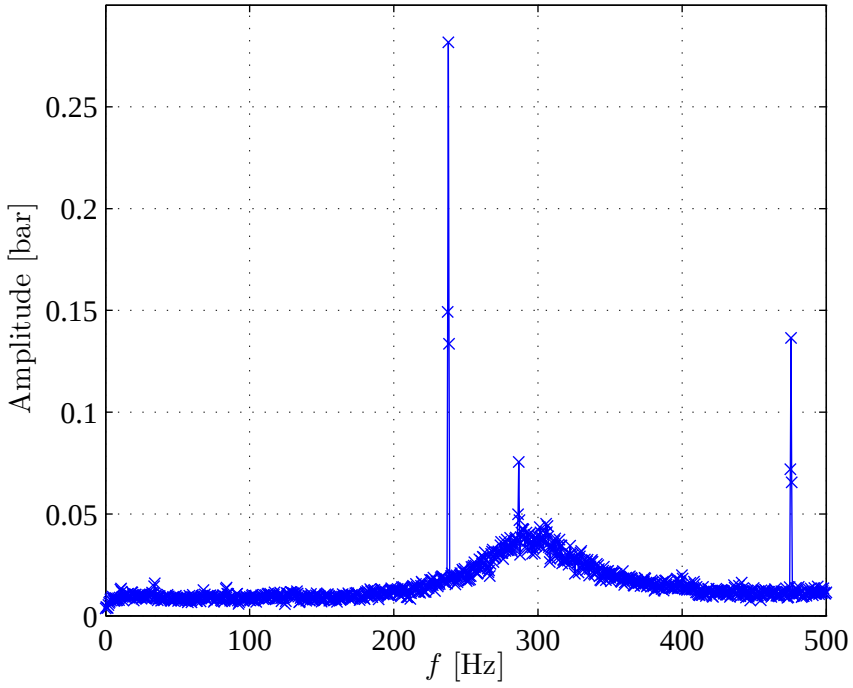

Figure 6.4: Example of pressure spectrum at pump

An example of a typical frequency spectrum of the pressure signal obtained in the system, either at the pipes or at the pump, is represented in Fig. 6.4. The highest peak corresponds to f_{BP} at 238 Hz followed by the second harmonic ($2f_{BP} = 476$ Hz).

Figure 6.5 compares the f_{BP} pressure amplitude measured at the tongue region of the volute of the test pump for different pump rotational speeds (1620 rpm and 2040 rpm), operating points and with valve V4 either open or closed. The effect of manoeuvring valve V4 is significant when the flow-rate is small and the pump rotates at 2040 rpm ($\widehat{=} f_{BP} = 238$ Hz), as expected from the theoretical calculations by the pump-circuit model where a peak is situated at 239 Hz (Fig. 6.3). This means that the acoustic coupling is capable of modifying the pressure fluctuations registered even at the location where the fluctuations are generated. This effect is especially evident at 20 % of the nominal flow-rate, with a difference of 15 % between V4 open or closed, and to a lesser extent at 40 % Q_N, with a difference of 9 %.

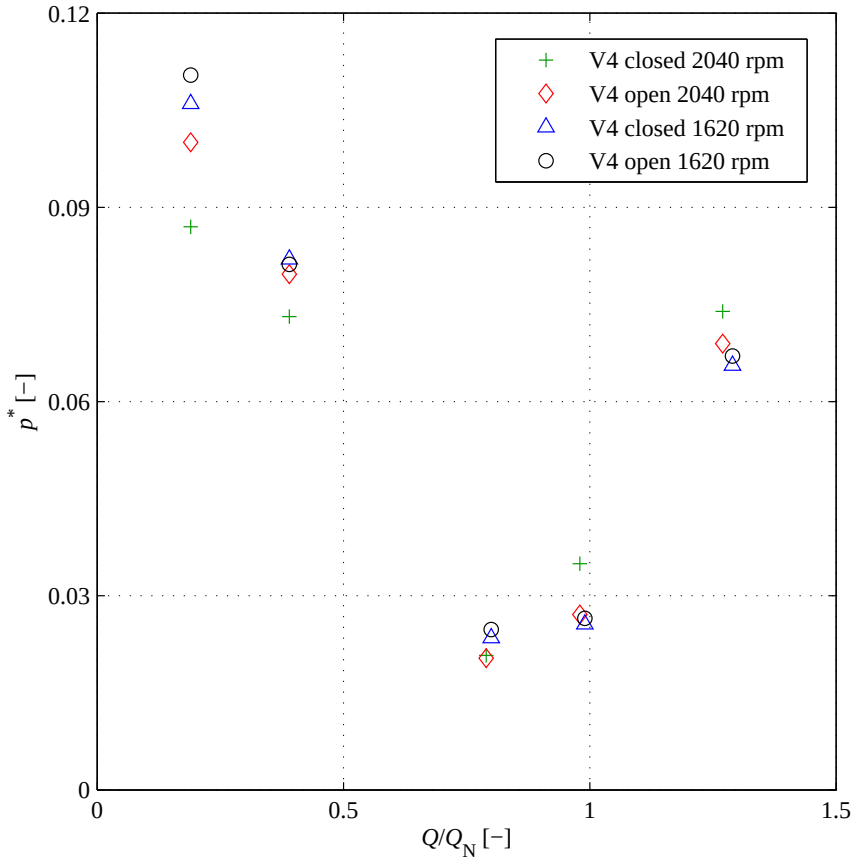

Figure 6.5: Experimental pressure fluctuations at the tongue region of the volute for different flow-rates, pump rotational speeds and valve V4 of dead-end branch open or closed

6.2 Acoustic results for transparent pump

The transparent pump used for the PIV measurements was also employed to study the pressure fluctuations in the tongue region of the pump. Therefore, pressure measurements were taken using fast-response pressure transducers at the volute in the tongue region and at the discharge pipe. First, a detailed analysis of the pressure signals for three flow-rates at a pump rotational speed of 625 rpm is given. The operating points and rotational speed correspond to those of the PIV measurements, whose results are presented in section 5. Second, the acoustic impedance was changed by investigating different pump rotational speeds and by opening or closing the dead-end branch at the discharge pipe. The effects of the acoustic coupling of the pump with the hydraulic circuit on the pressure fluctuations are shown.

6.2.1 Pressure at pump volute

Five pressure sensors were placed at the front casing wall of the pump to measure the pressure fluctuations in the tongue region. Two (sensors 2 and 3) were situated in the narrow region of the volute and the other three in the broad region of the volute (sensor 1) and pump outlet duct (sensor 4 and 5). For exact location of the sensors see Fig. 4.9 and Table 4.3.

Results at 625 rpm

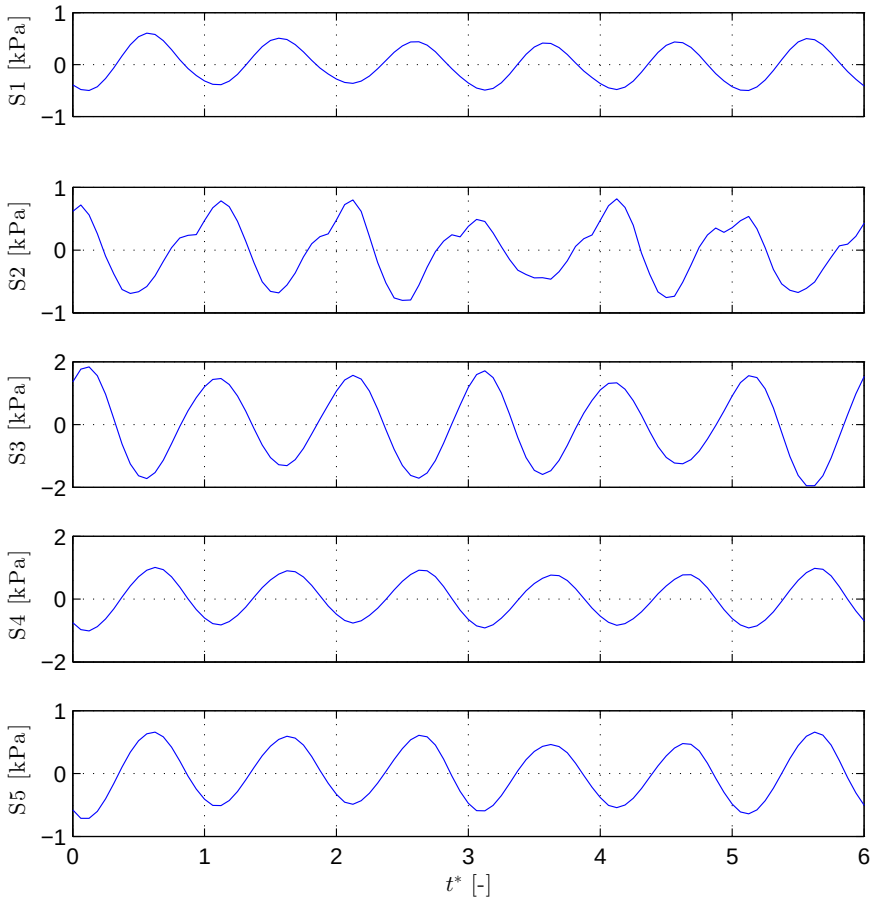

Figure 6.6: Averaged pressure time signals at transparent pump volute for 40 % Q_N

Three different flow-rates have been investigated, namely 40 % Q_N, Q_N and 150 % Q_N, with the pump running at 625 rpm (f_{BP} = 62.5 Hz). The averaged time signals at 40 % Q_N flow-rate are presented in Fig. 6.6. The averaged time signals were shifted, so that $t^* = 0.0$ corresponds to the time instant of the blade trailing edge at the suction side aligning with the tongue tip. Furthermore, the time was normalized by the blade-passing period, i.e. $t^* = 1$ corresponds to one

blade passage and $t^* = 6$ to one impeller rotation. This means that the same time reference as for the PIV measurements was used. The results presented here for 625 rpm were all obtained with the valve of the dead-end branch open. For the other two flow-rates the averaged time signals are shown in Figs. 6.7 and 6.8.

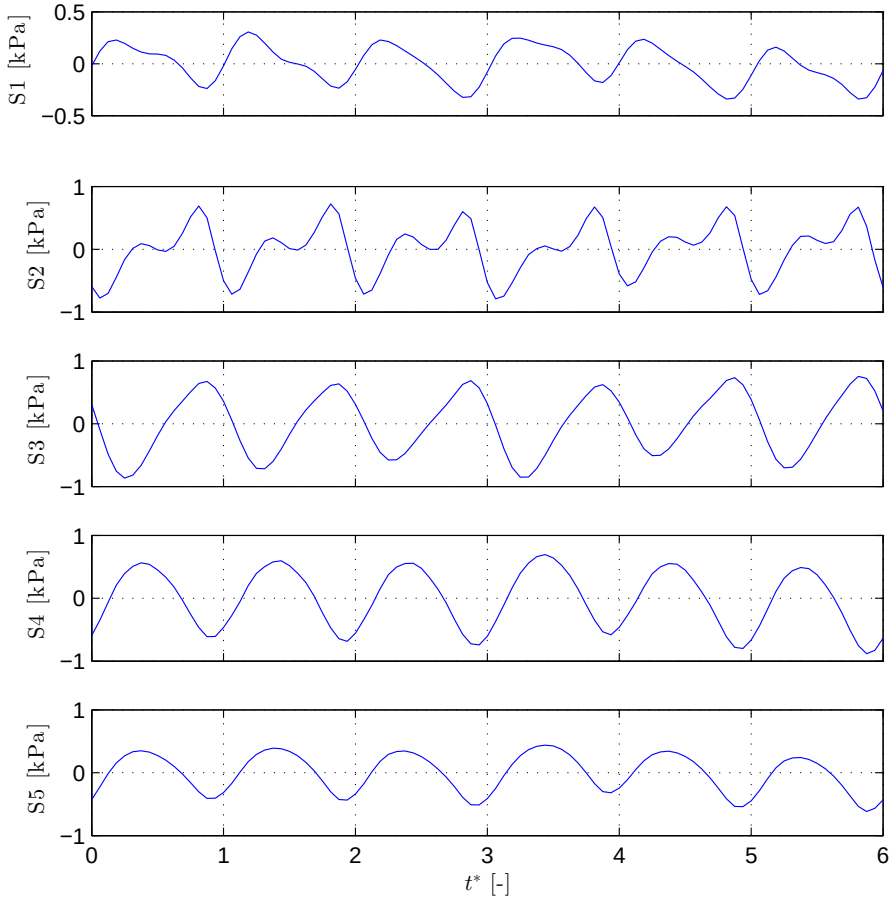

Figure 6.7: Averaged pressure time signals at transparent pump volute for Q_N

As the averaged time signals were obtained by the use of the trigger signal to overlap the individual time signals, as explained in section 4.2.1, the averaged time signals contain only components at the pump rotation frequency f_R and harmonics, with the main component being the f_{BP}. This is shown in the frequency spectra of the different pressure sensors for 40 % Q_N in Fig. 6.9. The frequency was normalized by the rotation frequency f_R, so that $f/f_R = 6$ corresponds to the f_{BP}, as the pump has six blades. Instantaneous time signals and frequency spectra are shown for comparison in appendix C. The second highest peak is situated at the second harmonic ($2f_{BP}$).
The frequency spectra for the nominal flow-rate (Q_N) are shown in Fig. 6.10 and for 150 % Q_N in Fig. 6.11. The pressure fluctuations are always highest at f_{BP}. At Q_N pressure amplitudes at f_{BP} are smallest compared to the other flow-rates,

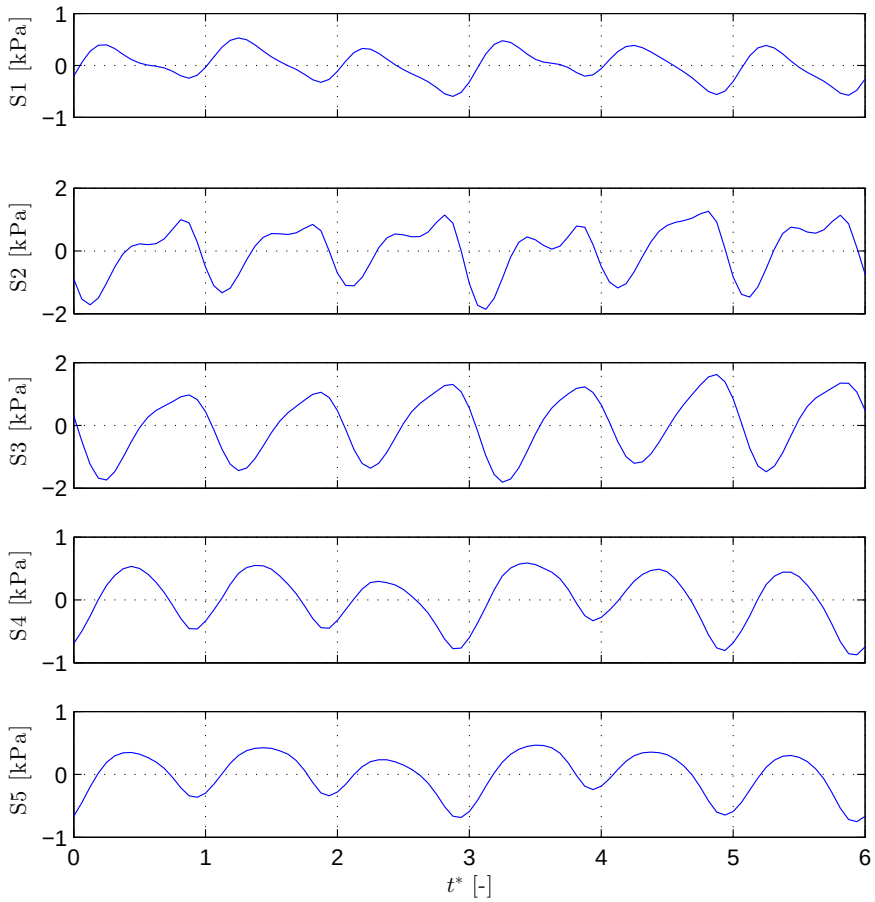

Figure 6.8: Averaged pressure time signals at transparent pump volute for 150 % Q_N

as expected. An exception is the frequency spectrum of sensor 4 for 150 % Q_N, where pressure fluctuations at f_{BP} are 15 % smaller than at Q_N. However, it has higher spectral content at f_R and harmonics than at nominal flow-rate.

The results of the pressure measurements for the three flow-rates at 625 rpm are summarized in Table 6.1, showing the amplitude and phase at f_{BP} and at the second harmonic ($2f_{BP}$). For 150 % Q_N the amplitude for sensor 2 (close to the impeller outlet and 7° behind the tongue tip) is more than half the amplitude at f_{BP} and at Q_N the amplitude for sensor 2 at $2f_{BP}$ is even 0.9 of the amplitude at f_{BP}. The pressure fluctuations are always highest for sensor 3, which is situated 18° behind the tongue tip in the narrow region of the volute.

The amplitudes at $2f_{BP}$ increase for increasing flow-rate. There is a nearly linear relation between the amplitude at $2f_{BP}$ and the flow-rate for sensors 1,2 and 4. This is in accordance with the increasing extension of flow structures leaving the impeller for increasing flow-rates, as described in section 5.8.

The phase of the pressure signals for 40 % Q_N can be classified into two groups. In the first group with sensors 1,4 and 5, all situated in the broad volute region

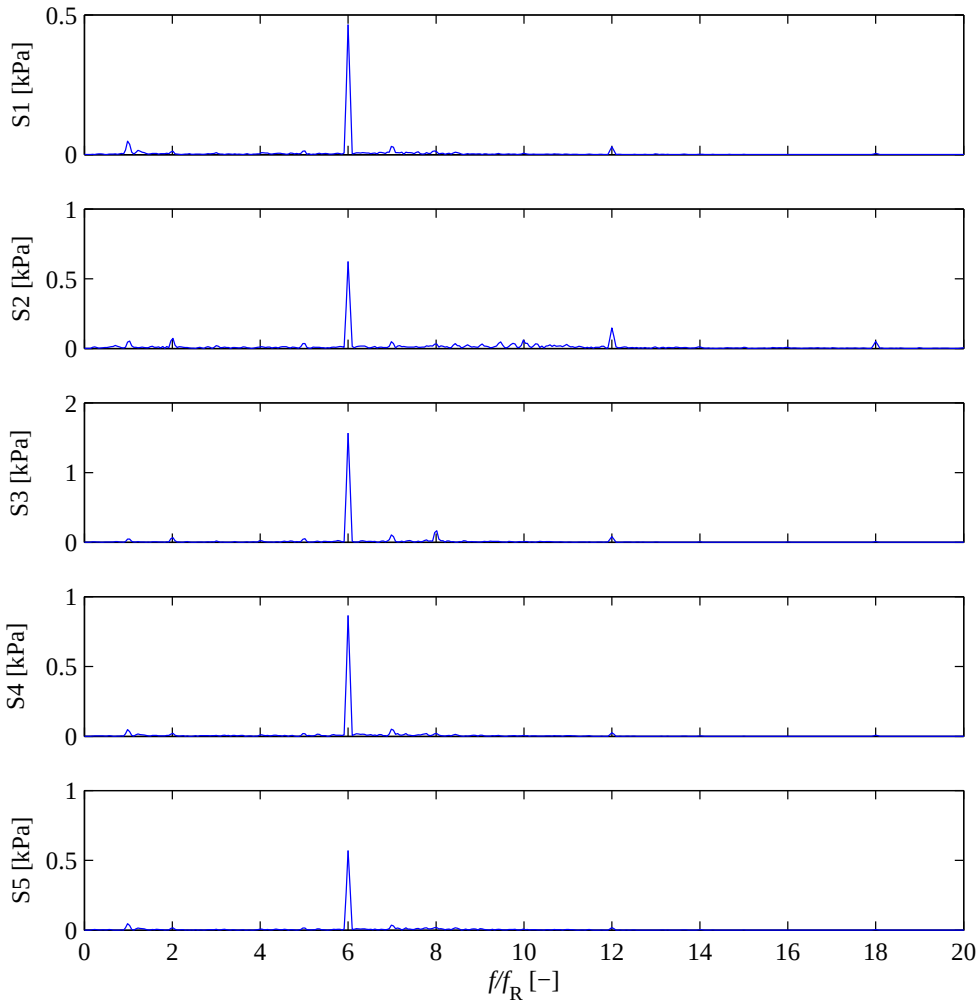

Figure 6.9: Spectra of time-averaged signal for 40 % Q_N

and outlet duct, the pressure signals have similar phases (139°-154° at f_{BP} referred to the tongue tip). In the second group the sensors 2 and 3 (situated in the narrow region of the volute) have a phase of -6° and -30°, respectively. This means that maximum pressure occurs just after the blade has passed the tongue tip. The phase of sensor 3 is smaller, as the sensor is located further upstream (18° behind the tongue tip) than sensor 2. There is a phase shift of about 160° between these two groups, which are separated by the narrow channel at the tongue tip.

Comparing the phase for Q_N and 40 % Q_N a high shift, between 88° and 141°, can be observed (see Table 6.1). The phases between S4 and S5 are very similar ($\leq$ 3° at f_{BP} and $2f_{BP}$). However, the phase difference of these sensors to S1 have increased about three times, compared to 40 % Q_N. The phase difference

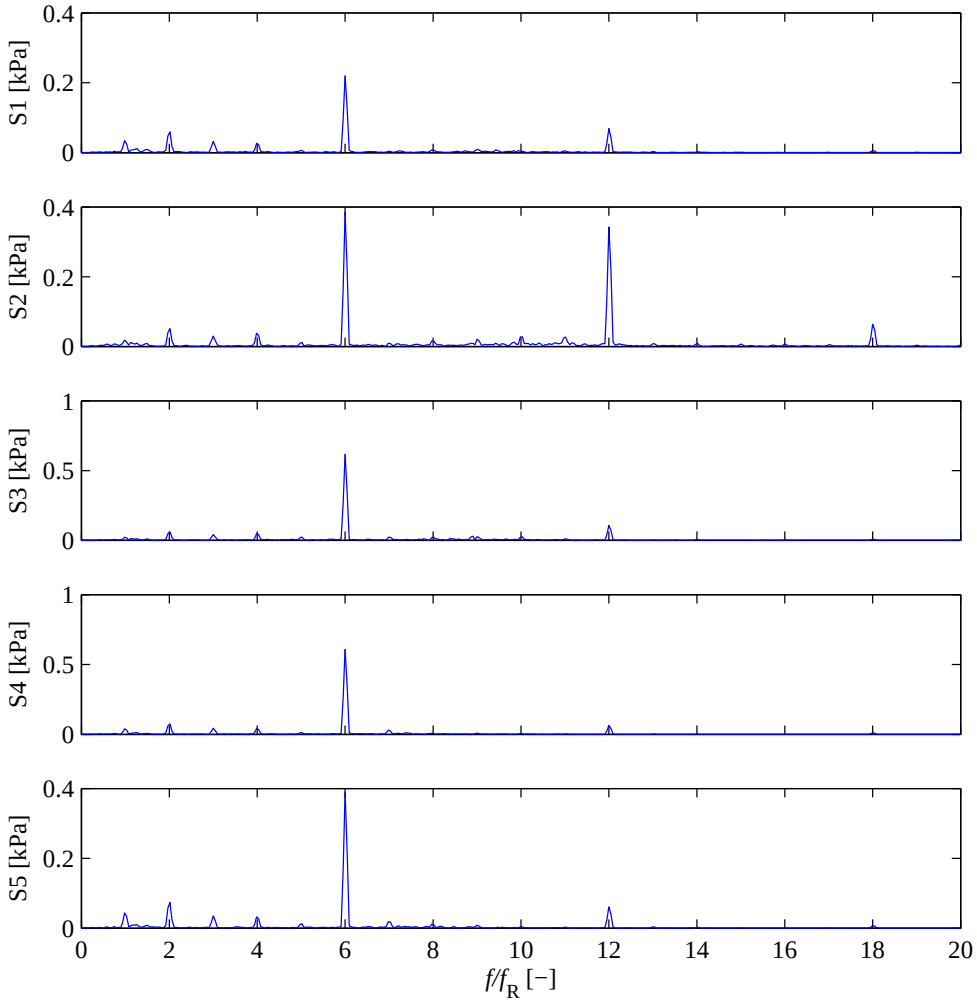

Figure 6.10: Spectra of time-averaged signal for Q_N

between the two sensors located in the narrow region of the volute (S2 and S3) have increased about two times.

The same pattern is noticed for the maximum flow-rate (150 % Q_N), having very similar phase differences between the pressure signals, compared to Q_N. However, the phases at 150 % Q_N have reduced about 20° for sensors 2 and 3 (in the narrow region of the volute) and 30° for sensors 1,4, and 5. This means that maximum pressure occurs later for 150 % Q_N than for Q_N, with respect to the blade aligning with the tongue tip. For higher flow-rates the stagnation point moves towards the narrow region of the volute, as described in the PIV results (see section 5.3). Therefore, the impeller blades and associated velocities encounter the stagnation region later, which is a possible explanation for the pressure maximum taking place later.

There is always a noticeable phase shift between the sensors located in the narrow region of the volute and the ones in the broad region. For instance, the

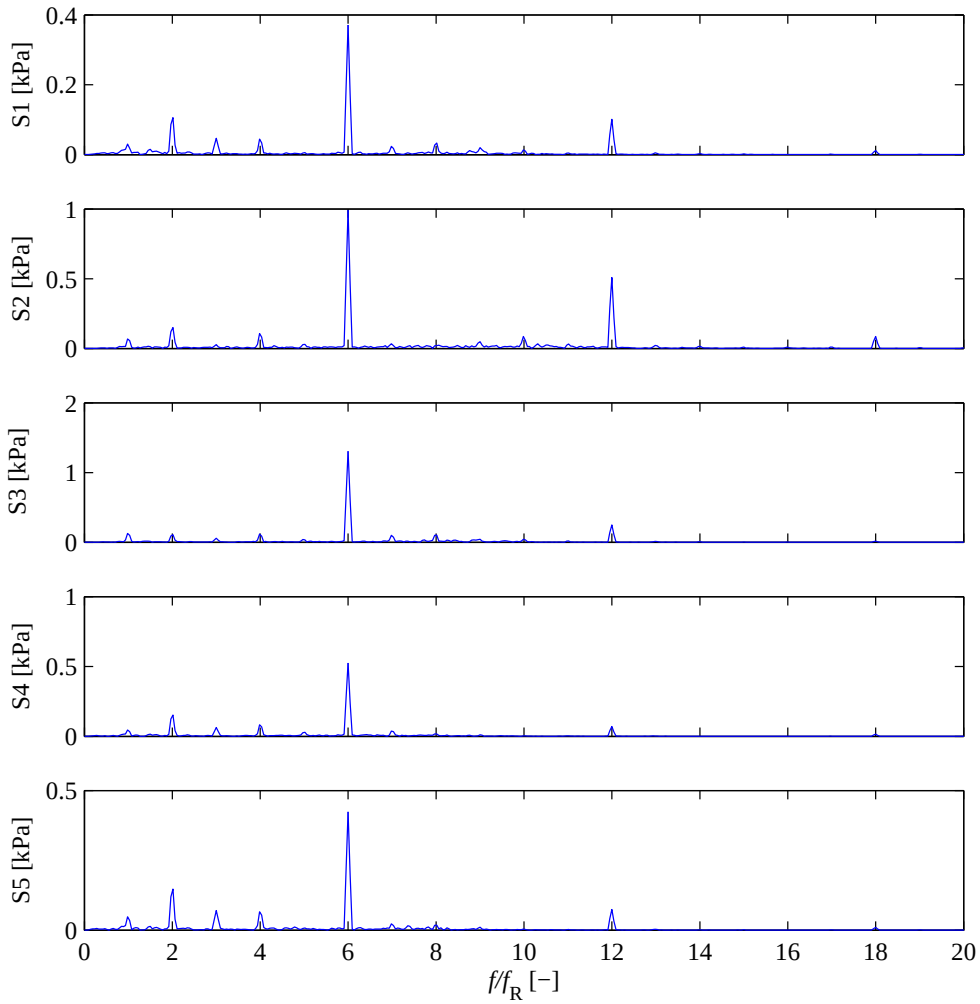

Figure 6.11: Spectra of time-averaged signal for 150 % Q_N

phase shift between sensor 1 and sensor 3 is about 180° for all three flow-rates. There is also a systematic phase shift between the pressure signals at 40 % Q_N compared to the pressure signals at Q_N and 150 % Q_N. This suggests that noise generation patterns at Q_N and 150 % Q_N are more related between each other than compared to the patterns at 40 % Q_N. The maximum pressure in S2 and S3 for 40 % Q_N, at f_{BP} and at $2f_{BP}$, occur earlier than for the other two flow-rates.

For Q_N and 150 % Q_N the minimum pressure in S1, S2 and S3 occurs approximately when the blade trailing edge aligns with these pressure measurement points. This coincides with high relative velocities, corresponding to low absolute velocities (see section 5.3), due to the relative flow between blade pressure and suction side. This confirms the results observed by Barrio et al. (2011) for Q_N and 160 % Q_N. The minimum pressure has a strong effect on the volute wall at the narrow region of the volute, due to the small impeller-tongue gap. This

Table 6.1: Amplitude and phase at f_{BP} and $2f_{BP}$ of pressure sensors in tongue region, with pump at 625 rpm, referred to tongue tip

		f_{BP}	f_{BP}	$2f_{BP}$	$2f_{BP}$
		Ampl. [kPa]	Phase [°]	Ampl. [kPa]	Phase [°]
40 % Q_N	S1	0.47	154	0.03	-1
	S2	0.62	-6	0.15	-121
	S3	1.56	-30	0.08	-143
	S4	0.87	139	0.03	-171
	S5	0.57	143	0.02	177
Q_N	S1	0.22	-86	0.07	-69
	S2	0.39	135	0.34	153
	S3	0.62	83	0.11	65
	S4	0.61	-132	0.06	-97
	S5	0.39	-129	0.06	-99
150 % Q_N	S1	0.37	-115	0.1	-148
	S2	0.99	115	0.51	83
	S3	1.31	67	0.25	8
	S4	0.52	-161	0.07	-147
	S5	0.42	-162	0.07	-150

leads to successive compression and decompression to generate acoustic waves at f_{BP}.

For part load (40 % Q_N) the minimum pressure in the narrow region of the volute (S2 and S3) occurs with the arrival of the recirculation vortex close to the blade pressure side at the impeller outlet, described in section 5.2. Maximum pressure occurs just before the blade aligns with each point in the narrow region of the volute. Barrio et al. (2011) found the minimum pressure occurring when the vortex centre aligns with each point and maximum pressure when the blade is approaching and leaving each point. The fact that the phase difference between S4 and S5, which are situated in the outlet duct, is very small for all three flow-rates suggests that there the hydraulic pressure fluctuations already have attenuated and that pressure fluctuations propagate at the speed of sound. This suggests that acoustic pressure waves already dominate in this zone. These acoustic waves are composed of the radiated P^+ and reflected P^- pressure waves. The fact that the phase of S1 is close to the phase of S4 and S5 only for 40 % Q_N suggests that the hydraulic pressure fluctuations are not transported far away from the impeller outlet into the volute, as it is the case for Q_N and 150 % Q_N. This confirms the results obtained from the PIV measurements, where fluctuations in the volute and outlet duct increased for increasing flow-rate.

Influence of impedance

The influence of the acoustic impedance of the hydraulic circuit on the pressure fluctuations at the tongue region was investigated. Therefore, measurements were taken at different f_{BP}s by changing the pump rotational speed. Furthermore, the impedance was changed by opening or closing a valve at the bifurcation to the vertical dead-end branch situated at the discharge pipe (see Fig. 3.8). The pump rotational speed was changed in a range from 350 rpm (f_{BP} = 35 Hz) to 625 rpm (f_{BP} = 62.5 Hz) for 40 % Q_N and for some selected rotational speeds also for Q_N. The exact locations of the five pressure transducers at the volute are shown in Fig. 4.9 and Table 4.3.

The amplitude, at each pump rotational speed, was normalized by the dynamic pressure referred to the blade tip speed:

$$p^* = \frac{p}{0.5\rho U_{tip}^2}. \tag{6.1}$$

The pressure fluctuation amplitudes at f_{BP} for each sensor are shown in Fig. 6.12. Even with the normalization of the pressure amplitude, there is a trend of increasing amplitude for increasing frequency. This trend is reduced between 45 Hz and 55 Hz and even inverted for some sensors. Particularly for sensor 2 and sensor 3, which are situated in the narrow channel of the volute, with the valve closed, the amplitude of pressure fluctuations drops between 45 and 50 Hz.

The difference in pressure amplitude fluctuation at f_{BP} between valve of dead-end branch open and closed is highest between 45 Hz and 49 Hz. To investigate in detail the difference of pressure fluctuations further measurements between 45 Hz and 48 Hz were carried out and are represented in Fig. 6.13.

For the pressure sensors situated in the narrow region of the volute (sensor 2 and 3) the pressure fluctuation amplitudes at f_{BP} are reduced when the valve is closed. On the contrary, for the pressure signals in the broad region (sensor 1,4 and 5) the amplitude reduces with the valve of the dead-end branch open. The highest differences are found for 47 Hz. At this f_{BP} the pressure fluctuations reduce in amplitude with the valve open by 30 % for S1, by 16 % for S4 and by 10 %, for S5, compared to the pressure amplitudes with the valve closed. In the narrow region of the volute f_{BP} pressure fluctuations increase 16 % for S2 and 10 % for S3, respectively, with valve open compared to valve closed. However, there is no noticeable phase shift due to opening or closing the valve. The phase maps are shown in appendix C.

For the nominal flow-rate some selected pump rotational speeds were investigated. Figure 6.14 shows the amplitude of pressure fluctuations at f_{BP}. The pattern is similar to the one obtained for the flow-rate of 40 % Q_N, i.e. that

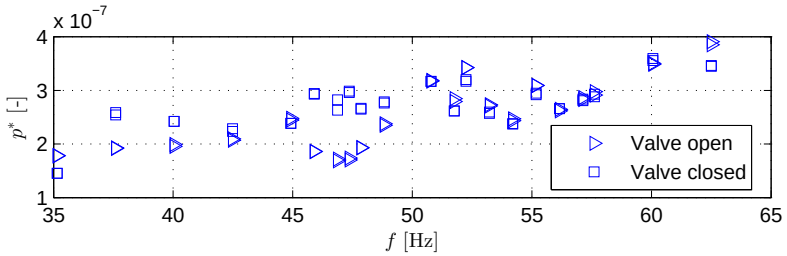

(a) Sensor 1

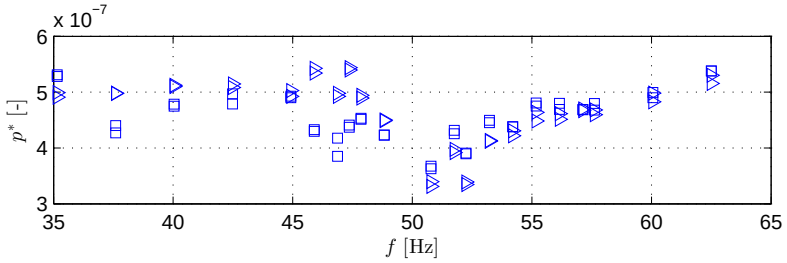

(b) Sensor 2

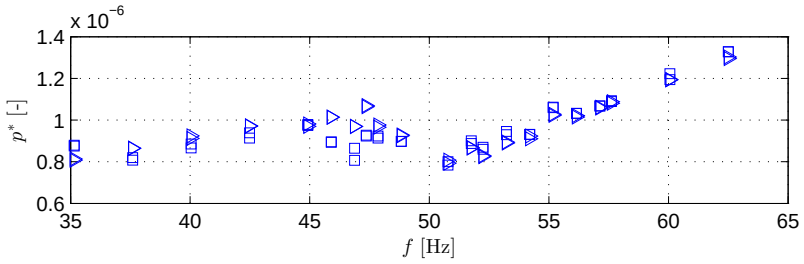

(c) Sensor 3

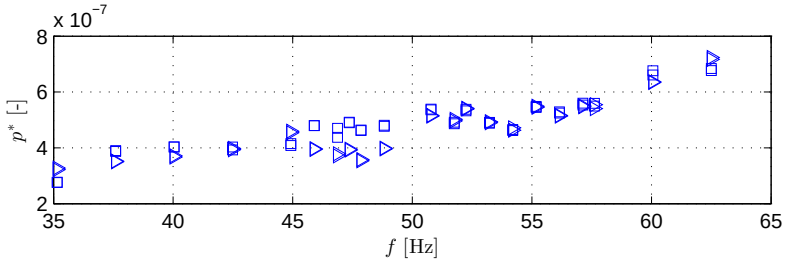

(d) Sensor 4

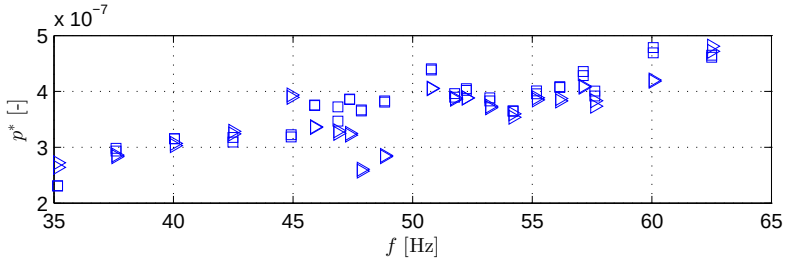

(e) Sensor 5

Figure 6.12: Influence of valve open (▷) and closed (□) at 40 % Q_N on amplitude at f_{BP} of pressure sensors at pump volute for different pump rotational speeds

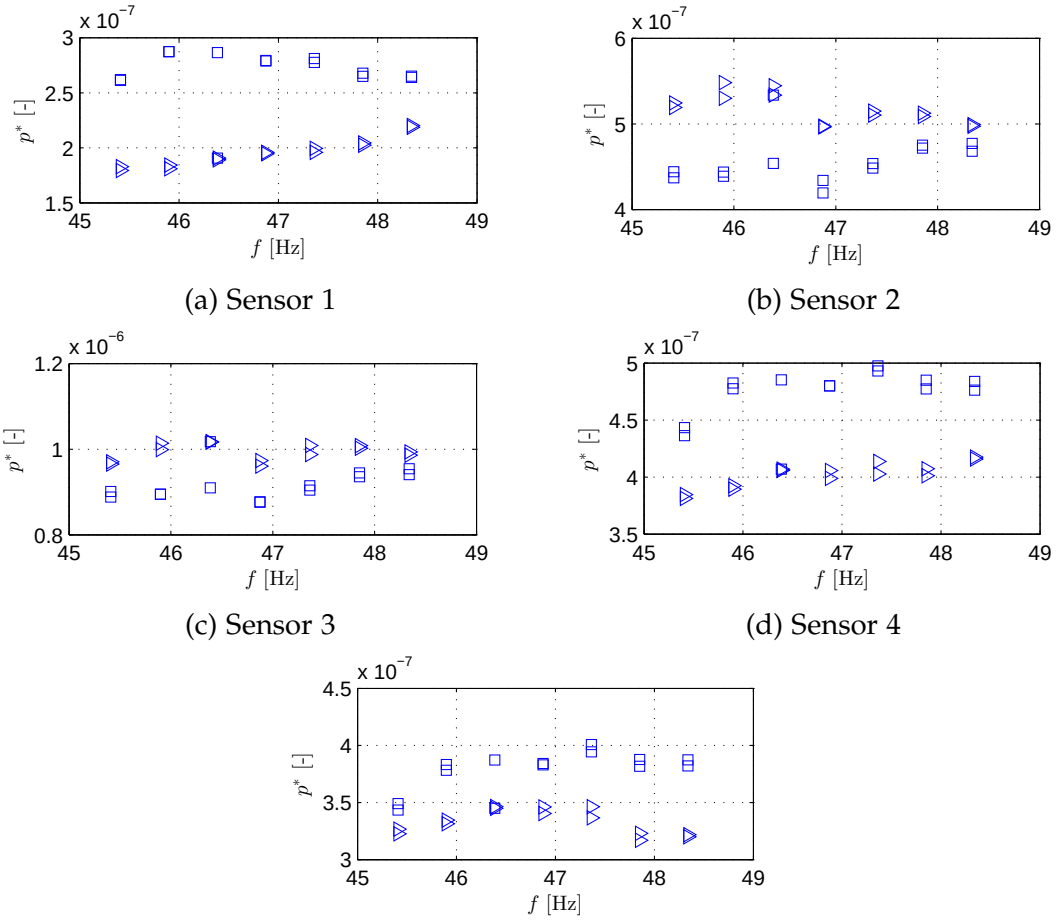

(a) Sensor 1

(b) Sensor 2

(c) Sensor 3

(d) Sensor 4

(e) Sensor 5

Figure 6.13: Influence of valve open (▷) and closed (□) at 40 % Q_N on amplitude at f_{BP} of pressure sensors at pump volute for different pump rotational speeds between 45 and 48 Hz

pressure fluctuation amplitudes at f_{BP} with the valve of dead-end branch closed are higher than with the valve open in the broad region of the volute and pump outlet (sensor 1,4, and 5). In the narrow region of the volute (sensor 1 and 2) the pressure fluctuation amplitudes increase when the valve is opened. Difference in pressure fluctuation amplitude is found to be particularly high for 45 Hz ($\Omega = 450$ rpm) and 47 Hz ($\Omega = 470$ rpm). For sensor 1 the amplitude is reduced by 36 % when the valve of the dead-end branch is opened, compared to the valve being closed. In the narrow region of the volute there is an increase of 18 % for sensor 2 and 29 % for sensor 3 when the valve is opened (see Fig. 6.14b and 6.14c).

Therefore, to investigate the influence of the pressure fluctuations on the velocity fields, PIV measurements were done at 470 rpm for 40 % Q_N and Q_N. PIV measurements were taken at 33 different blade positions, covering one blade passage, with the valve of the dead-end branch open and closed at low and high

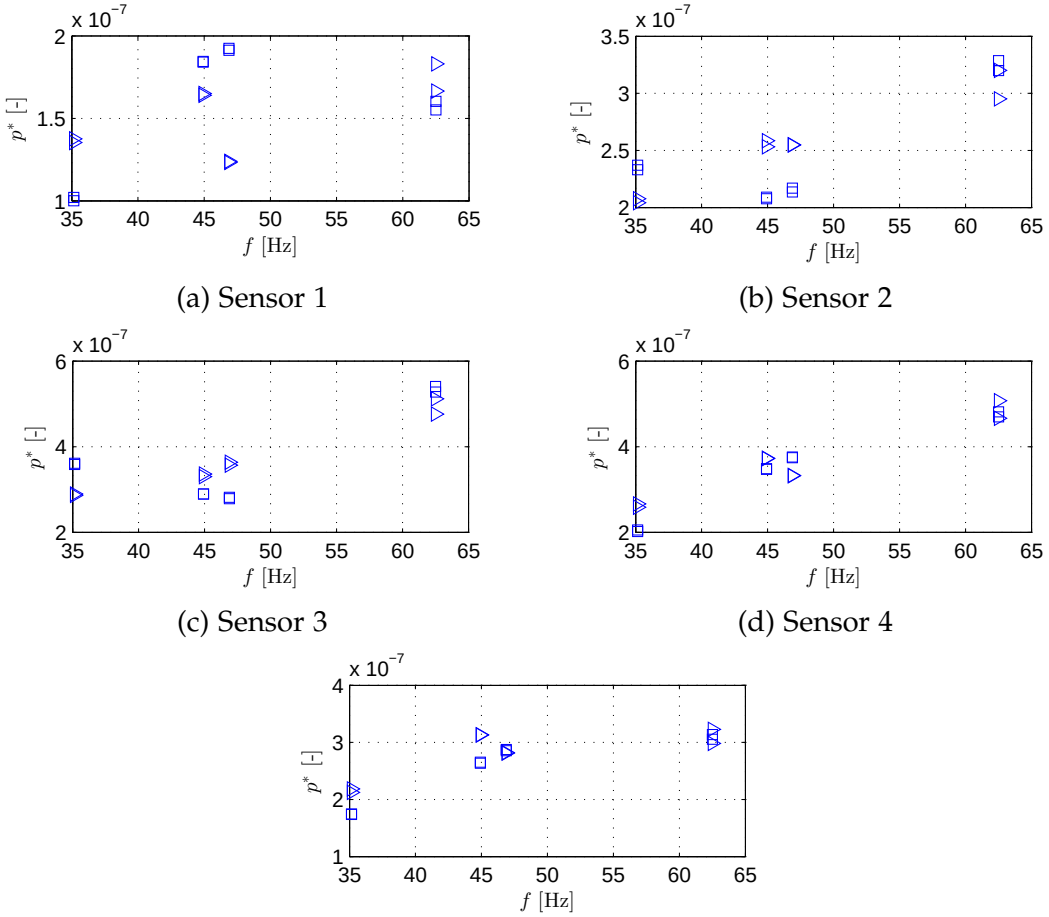

(a) Sensor 1

(b) Sensor 2

(c) Sensor 3

(d) Sensor 4

(e) Sensor 5

Figure 6.14: Influence of valve open (▷) and closed (□) at Q_N on amplitude at f_{BP} of pressure sensors at pump volute for different pump rotational speeds

magnification, as the ones described in section 4.1.1. However, no significant difference was found on the phase-averaged velocity, vorticity or TKE fields. This confirms the results found by Morgenroth (1995). The reason is that the acoustic particle velocity is very small (in the order of $p/(\rho c) = 0.004$ m/s), so that with the PIV measurements a difference cannot be measured, as it is below the measurement accuracy.

6.2.2 Acoustic response of hydraulic circuit

To obtain the acoustic impedance ($Z = P/V$) of the hydraulic circuit, experimental tests were conducted and a transfer matrix analysis (TMA) was used.

For the pressure measurements three fast-response pressure transducers were placed at the discharge pipes. The methodology is explained in section 4.2.2. Frequencies of f_{BP} between 36 and 70 Hz were investigated for 0 % Q_N and 40 % Q_N. In the vertical dead-end branch the water level was maintained at a

height of 0.5 m for all test cases. In the rest of that vertical branch (1.0 m) there was still air at a pressure, that varied from -1.4 kPa to 8.6 kPa, depending on the pump rotational speed. Speed of sound of water in these PC pipes was determined to 280 m/s, as explained in section 4.2.2. The attenuation factor α was estimated to be 0.07 rad/m by comparing the experimental amplitudes of the impedances $Z = P/V$ with the ones obtained from the transfer matrix analysis (TMA).

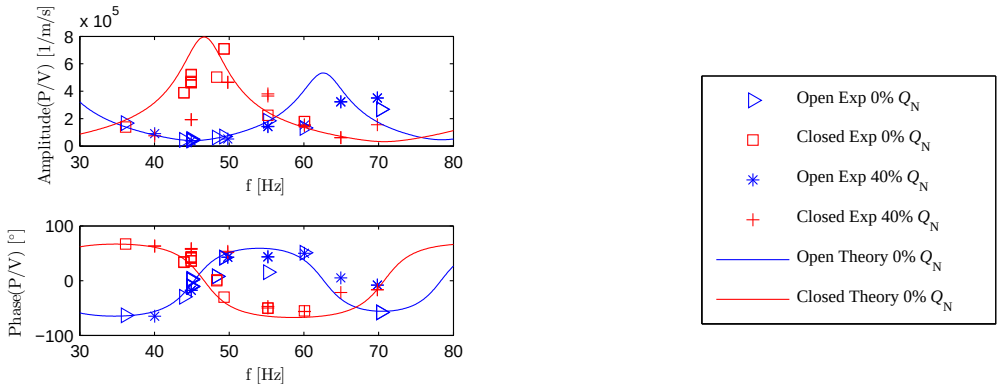

(a) Impedance

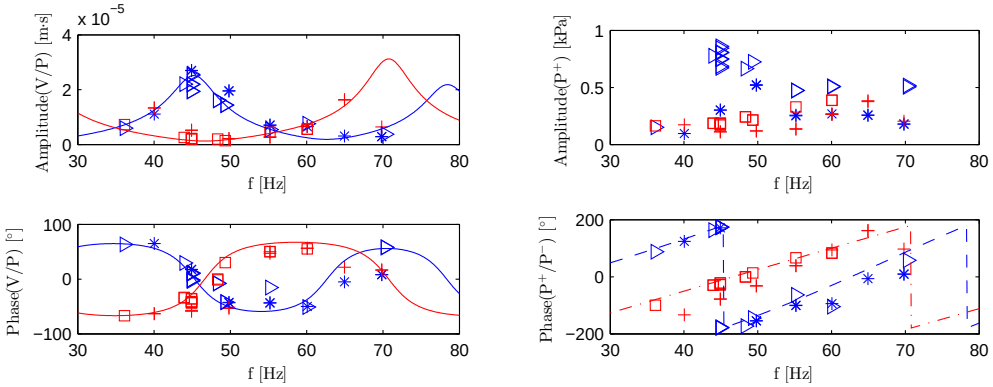

(b) Admittance (c) P^+/P^-

Figure 6.15: Acoustic characteristics at pump discharge

In Fig. 6.15a the amplitude and phase of the impedance referred to the pump outlet are presented for different frequencies and for the valve of the dead-end branch open or closed. Solid lines correspond to the prediction of the TMA and the dots correspond to the experimental results. Experimental and theoretical results for 0 % Q_N coincide reasonably well, especially the phase. The phase of the impedance in the case of an open dead-end branch has usually a phase shift of nearly 180° compared to the case of a closed dead-end branch. For the closed dead-end branch a resonance peak is observed experimentally at 49 Hz and for the theoretical impedance this peak is situated at a slightly lower frequency, namely at 47 Hz. This is in concordance with the results obtained in section 6.2.1, where the highest pressure differences between an open or closed dead-end branch, measured directly at the pump, were also found at $f_{BP} = 47$ Hz.

For the open dead-end branch the amplitude of the impedance for frequencies between 45 and 50 Hz is minimum. This can be observed better in Fig. 6.15b, corresponding to a peak in the amplitude of the admittance ($1/Z = V/P$), which is the reciprocal of the impedance. Without considering attenuation the impedance would always be imaginary (with the real part being 0) and this would lead to values for the phase of only 90° and -90°. By considering attenuation there is a softer transition between minimum and maximum phases. The transition zone, when the phase is zero, always corresponds to a minimum or maximum in the impedance amplitude. This also corresponds to values of 0° or 180° in the phase of P^+/P^- (see Fig. 6.15c). For the 40 % Q_N case, the experimental results differ only slightly from the theoretical results (0 % Q_N) for an open dead-end branch. For the closed dead-end branch the difference is higher. A maximum in the admittance amplitude (V/P) corresponds to maximum radiated pressure amplitudes p^+ (Fig. 6.15c).

Part IV

Conclusions

7 Conclusions

In this thesis the interaction of the impeller with the volute (rotor-stator interaction), taking place in a centrifugal pump with volute casing, has been studied in detail. The interaction of the blades with the volute tongue has been shown and described exhaustively. Furthermore, the influence of the acoustic characteristics of the hydraulic circuit on the pressure fluctuations generated at the pump was investigated.

7.1 Summary

A special hydraulic setup with a transparent centrifugal pump has been designed and built to conduct PIV measurements. The impeller blades and the volute of the test pump have a 2D-shape in order to measure the velocity fields by 2D2C PIV with low uncertainty.
High and low magnification PIV measurements in the centerplane perpendicular to the pump axis of a centrifugal pump at three different flow-rates allowed to observe the flow structures originated in the impeller channels and their interaction with the volute. The flow-rates investigated were below (40 % Q_N), at and above (150 % Q_N) nominal flow-rate.
Reliable velocity fields even close to solid boundaries were achieved by avoiding reflections and reducing background noise by using fluorescent seeding particles.
High magnification PIV measurements allowed to obtain a high spatial resolution to study the flow in the small impeller-tongue gap and close to the impeller blades and volute tongue. Low magnification measurements revealed the flow structure in the impeller and the pump outlet duct.
Selection of the adequate seeding particles and other PIV parameters were described. 500 double images at 33 blade positions covering one whole blade passage were taken to obtain converged phase-averaged velocity fields. The instantaneous velocity fields were processed to obtain, among others, phase-averaged absolute and relative velocities, out-of-plane vorticity and in-plane TKE fields with its production. Stereo PIV complemented the flow field measurements, to obtain also the out-of-plane velocity component. All this allowed the detailed investigation of the flow structures due to rotor-stator interaction in the tongue region of this pump.

Furthermore, the influence of the acoustic characteristics of the hydraulic system on the pressure fluctuations radiated by a pump at BPF was investigated

theoretically and experimentally. Particular attention was paid to the influence of the acoustic characteristics at the suction side of an industrial pump on the pressure fluctuations at BPF. The acoustic impedance was changed by activating a dead-end branch at the suction side, with no mean flow through it, with the pump operating at different rotational speeds and flow-rates.
The acoustic pump-circuit coupling was studied theoretically by means of a 2-port model including a transfer matrix analysis (TMA). Furthermore, an acoustic model developed at the Chair of Fluid Mechanics at the University of Oviedo was used to simulate the internal sound field in an industrial centrifugal pump. The components of the scattering matrix (sound reflection and transmission coefficients) were determined for different frequencies and flow-rates. This study was complemented by unsteady pressure measurements conducted at the centrifugal pump.

The acoustic pump-circuit coupling has also been studied at the hydraulic circuit of the transparent pump. A TMA was used to describe the hydraulic system theoretically. Attenuation was considered using complex wavenumbers. Three fast-response pressure transducers were placed along the pipes at the discharge side of the pump to decompose the pressure signal into the radiated and reflected pressure waves. Five pressure transducers were also placed at the pump volute in the tongue region, with two transducers situated in the narrow region of the volute and three in the broad volute region and pump outlet duct. The acoustic impedance could be easily changed without affecting the flow-rate, i.e. without changing the pump rotational speed, by activating a dead-end branch. This vertical dead-end branch, which was partially filled with air, was connected to the circuit at the discharge pipe. The influence of the activation of the dead-end branch on the pressure fluctuations for various BPFs was investigated. The speed of sound in the circuit was determined experimentally by the use of three pressure transducers.
PIV measurements were also conducted at 470 rpm, since a high influence of the state of the dead-end branch on the pressure pulsations was detected for that speed. In particular, at 40 % Q_N and Q_N 33 different blade positions with the dead-end branch open and closed at low and high magnification FOV were investigated.

7.2 Flow field

The main conclusions regarding the flow field in the pump from rotor-stator interaction (RSI) are:

1. The stereo PIV measurements showed that the axial velocity component is equal to or less than 10% of the blade tip velocity, due to the two-dimensional shape of impeller and volute. However, longitudinal stretched

vorticity tubes were found, which change their rotation direction depending on the flow-rate.

2. For 40 % Q_N the flow is characterized by:

   - Several vortices inside each impeller channel in the phase-averaged relative velocity fields.
   - These vortices lead to several positive and negative vorticity zones. An intense negative vorticity sheet, starting at the blade trailing edge, hits the next blade on its pressure side. This sheet has high TKE and also high TKE production, and as it reaches the next blade still TKE is produced.
   - In the narrow region of the volute absolute velocities are highest for 40 % Q_N, compared to the other flow-rates, due to the recirculation and flow separation from the tongue tip.
   - The results of the high magnification FOV show how the vorticity sheet from the blade trailing edge interacts with the wake region formed by flow detachment from the tongue tip, resulting in high values of counter-rotating vorticity and of TKE.
   - The high radial velocities just behind the blade trailing edge at the suction side cause the longitudinal stretched vorticity sheet to separate from the blade and to change to a circular shape, while moving to the centre of the volute channel.

3. The stagnation point moves considerably depending on the flow-rate:

   - For the flow-rate below Q_N (40 % Q_N) the stagnation point moves along the tongue towards the pump outlet. This leads to flow separation from the tongue tip into the narrow region of the volute with high negative vorticity producing high TKE. As the blade passes the tongue tip, flow detachment from the tongue tip is reduced. TKE production reaches a minimum shortly afterwards and has its maximum before the blade pressure side arrives at the tongue tip, in concordance with the vorticity development in the tongue wake.
   - For the flow-rate above Q_N (150 % Q_N) the stagnation point is shifted along the tongue towards the internal zone near the impeller. Flow separation occurs and high positive vorticity is extending from the tongue into the outlet channel. High TKE production takes place in the tongue wake during most of the cycle, except during the arrival of the vorticity sheets shed from the blade trailing edge, which forces the tongue wake to shrink. The high TKE zone in the tongue wake due to flow separation from the tongue is reduced, in amplitude and extension, and shifted towards the pump outlet.

- The development of the stagnation zone and the tongue wake could be observed in detail and for certain time instants the flow separation reduces considerably, leading to lower vorticity and lower TKE levels. TKE values in the tongue wake are lower for 150 % Q_N than for 40 % Q_N.

4. For 150 % Q_N the flow is characterized by the following phenomena:
   - The relative flow along impeller channels is dominated by a counterrotating vortex and conditioned by flow detachment at the pressure side of the blade leading edge, where high TKE production takes place. The zone of high TKE is subsequently convected with the main stream.
   - Flow exiting the impeller channels is characterized by two very intense vorticity sheets, one negative and one positive, shed from the blade trailing edge, plus another negative broad sheet related to the counterrotating vortex in the impeller channels.
   - As these vorticity sheets hit the tongue, they are cut by the tongue tip. They split and are convected by the stream, though the vorticity sheet portions at the blade side undergo some stretching due to stickiness effects at the tongue stagnation region.
   - The maximum TKE production observed occurs at the blade-tongue interaction region. TKE production is initially concentrated just behind the pressure side of the blade trailing edge and becomes maximum when the blade aligns with the tongue tip. Afterwards, this zone of TKE production shifts towards the blade suction side.
   - The positive vorticity sheet has far less TKE and TKE production than the negative vorticity sheet, as the main flow structure is well periodic with the blade passage.

7.3 Spectral analysis of flow variables

The main conclusions drawn from the FFT processing of the flow fields, available for 32 time instants at low and high magnification, are:

1. For 40 % Q_N the flow variables (velocity magnitude, vorticity and TKE) have the highest spectral content at f_{BP}. At Q_N these variables also exhibit the highest peak at f_{BP}, except for the velocity magnitude in most of the narrow region of the volute, where the peak at $2f_{BP}$ is higher.

2. In the tongue region, for 150 % Q_N, due to the blade-tongue interaction the flow variables have a high spectral content at f_{BP} and $2f_{BP}$. However, there is still significant spectral content at higher harmonics, particularly for the vorticity. A general trend is that in the volute ahead of the tongue

tip the main fluctuations occur at f_{BP}, whereas behind the tongue tip the fluctuations at $2f_{BP}$ are dominant (for velocity magnitude and radial and tangential velocity components) or are of similar magnitude (TKE). For the vorticity the dominant component in the tongue region is at $2f_{BP}$, due to the intense negative and positive vorticity sheets shed from the blade trailing edge. However, further away from the tongue tip, in the pump outlet duct, the dominant frequency is f_{BP}.

3. Maps of fluctuation distribution (amplitude and phase) at f_{BP} and harmonics (up to $3f_{BP}$) clearly show how fluctuations are convected with the stream, as well as the amplitude decay and the extension where fluctuations are noticeable. With respect to the f_{BP} amplitude behind the impeller outlet, at a radius of 1.25 r_{tip}, there is a reduction to about 10 % for the velocity magnitude, vorticity and TKE for 150 % Q_N. Therefore, the zone of high fluctuations extends to about 1.25 r_{tip} outside the impeller and continues along the outlet duct close to the tongue side.

4. Comparing the three different flow-rates investigated, it could be clearly observed how the fluctuations at f_{BP} and harmonics become more perceptible in the broad region of the volute and in the pump outlet duct when increasing the flow-rate. For Q_N, fluctuation amplitudes in general are smaller than at off-design conditions, especially the ones from TKE. However, in the phase maps the fluctuations at the pump outlet are better noticeable than at 40 % Q_N. For 150 % Q_N the fluctuations at f_{BP} and harmonics occupy nearly the whole pump outlet duct of the low magnification FOV.

7.4 Acoustic coupling

The main conclusions derived from the acoustic coupling of the hyraulic circuit with the pump are:

1. For the industrial centrifugal pump run at a reference rotational speed of 1620 rpm, the change of the acoustic impedance at the suction side, by activating a dead-end branch, has almost no influence on the pressure fluctuations at the tongue region of the pump. In contrast, at 2040 rpm a significant change of the amplitude of pressure fluctuations at the tongue region occurs when closing the valve at the bifurcation of this dead-end branch. A reduction of 15 % is achieved for deep part load. This tendency is confirmed by the results from the acoustic models, that predict in this BPF region a resonance frequency of the system, depending on the state of the dead-end branch.

   This suggests that, although significant noise at BPF may be generated when a pump is operating at off-design conditions, the impact of this noise

can be mitigated by proper design of the associated circuit in order to reduce acoustic feedback.

2. Results suggest that noise generation patterns between Q_N and 150 % Q_N are more similar than noise generation patterns at 40 % Q_N:
   - For part load the minimum pressure in the narrow region of the volute coincides with the arrival of the recirculation vortex close to the blade pressure side at the impeller outlet.
   - For Q_N and 150 % Q_N the minimum pressure occurs approximately when the blade trailing edge passes by each point. This coincides with high relative velocities, corresponding to low absolute velocities.

3. The phase difference between the sensors situated in the outlet duct is very small for all three flow-rates. This suggests that there the hydraulic fluctuations have already decreased and pressure fluctuations propagate at the speed of sound. These acoustic waves are composed of the radiated and reflected pressure waves.

4. Only for 40 % Q_N the phase of the sensor in the broad region of the volute is close to the phase of the sensors in the outlet duct. This suggests that the hydraulic fluctuations are not transported far away from the impeller outlet into the volute, as it is the case for Q_N and 150 % Q_N. This confirms the results from PIV measurements, where the extension of the fluctuations in the volute and outlet channel increases for increasing flow-rate.

5. The theoretical results from the transfer matrix analysis (TMA) agree reasonably well with the experimental results for the investigated BPF range. They can be used to predict acoustic resonance with maximum impedance.

6. The pressure field, even at the pump, changes in amplitude for certain frequencies when changing the acoustic impedance by the dead-end branch. The pressure fluctuations at BPF were reduced up to 29 % in the narrow region of the volute for a certain pump rotational speed. In the broad region of the volute the pressure fluctuations reduce even by 36 % at nominal flow-rate.

7. For the PIV measurements taken at 470 rpm, no significant influence of activating the dead-end branch was found on the velocity, vorticity or TKE fields. The reason is the very small acoustic particle velocity, which is below the measurement accuracy.

8. The influence of the acoustic impedance on the magnitude of the pressure fluctuations generated in a pump was demonstrated for an industrial pump and for a two-dimensional shaped pump. The 2-port models can be used to predict successfully resonance frequencies, as confirmed by the experimental results.

7.5 Future work

During the research for this thesis several topics arose, which are worth studying with more detail, but are beyond the scope of this thesis. Some possible future research studies are:

1. Estimation of the pressure fields from the PIV measurements. In fact, there is ongoing research to obtain the pressure fields from the phase-averaged velocity fields and the in-plane Reynolds stresses. This is performed in two steps: *(i)* calculation of the time and spatial derivatives of the velocity components and the Reynolds stresses to finally estimate the in-plane components of the pressure gradient by using the phase-averaged URANS equations (van Oudheusden, 2013); *(ii)* integration of the pressure gradient distribution, taking as reference the pressure signals obtained from the five transducers at the pump volute (see Fig. 4.9), by following the omnidirectional integration strategy introduced by Liu and Katz (2006).

2. Experimental measurements of 3D flow structures. This can be achieved by:

   - Multi-plane stereo PIV to obtain phase-averaged flow variables in several measurement planes.
   - Tomographic PIV to obtain the complete instantaneous velocity fields in a volume inside the pump.

   Also, time-resolved PIV would allow to capture flow structures not associated with BPF or harmonics. These techniques might be applied on a test pump with double-curved blades, which is the usual case for industrial pumps. Besides, to be able to obtain reliable velocity fields inside the impeller channels another facility with optical index-matching would be needed.

3. Validation of theoretical calculations of the internal flow fields. The current PIV measurements constitute a valuable database to contrast the predictions of numerical models (CFD). For instance, this allows to verify calculation parameters, such as boundary conditions or turbulence models. Additionally, the internal sound field in the transparent pump can be further investigated by means of the internal propagation model, used in this thesis for the industrial pump.

8 Conclusiones

The conclusions in English are in chapter 7.

En esta tesis doctoral se ha estudiado con detalle la interacción del rodete con la voluta (interacción rotor-estator) en una bomba centrífuga. Se ha descrito de forma exhaustiva la interacción de los álabes con la lengüeta de la voluta. Además, se estudió la influencia de las características acústicas del circuito hidráulico en las fluctuaciones de presión originadas por la bomba.

8.1 Trabajo realizado

Se diseñó y construyó un banco hidráulico con una bomba centrífuga transparente para medidas PIV. Los álabes del rodete y la voluta de la bomba tienen una geometría 2D para poder medir los campos de velocidad mediante 2D2C PIV con baja incertidumbre.
Las medidas PIV con alta y baja ampliación en el plano central perpendicular al eje de la bomba para tres caudales diferentes permitieron observar las estructuras del flujo originadas en los canales del rodete y su interacción con la voluta. Los caudales investigados estaban por debajo (40 % Q_N), por encima (150 % Q_N) y en el propio caudal nominal.
Los campos de velocidades con baja incertidumbre, incluso cerca de los contornos sólidos, se consiguieron mediante el uso de partículas fluorescentes al no haber reflexiones y al reducir el ruido de fondo.
Las medidas PIV de alta ampliación permitieron obtener una resolución espacial alta para así estudiar el flujo en el pequeño espacio entre el rodete y la lengüeta y cerca de los álabes del rodete. Las medidas de baja ampliación revelaron las estructuras del flujo en el rodete y en el conducto de salida de la bomba.
Se describió la selección de las partículas adecuadas de sembrado y otros parámetros del PIV. Se tomaron 500 imágenes dobles en 33 posiciones del mismo, cubriendo un paso completo del álabe, para obtener campos de velocidad convergidos y promediados para una cierta posición del rodete. Se procesaron los campos de velocidad instantáneos para obtener, entre otros: los campos de velocidad absolutos y relativos promediados para una cierta posición del rodete, la componente de la vorticidad fuera del plano y TKE (energía cinética turbulenta) en el plano junto con su producción. El PIV estéreo completó las medidas del flujo para obtener la componente de la velocidad fuera del plano. Todo esto permitió la investigación detallada de las estructuras del flujo debido a la interacción rotor-estator.

Además, se estudió teórica y experimentalmente la influencia de las características acústicas del sistema hidráulico en las fluctuaciones radiadas por la bomba a la frecuencia de paso de álabe (BPF). Se consideró especialmente la influencia de las características acústicas del lado de succión en una bomba industrial. Se modificó la impedancia acústica mediante la activación de una rama sin salida en el lado de succión, con flujo medio nulo, y con la bomba operando a distintas velocidades y caudales.
Se estudió teóricamente el acoplamiento entre bomba y circuito mediante un modelo de dos puertos, incluyendo un TMA (análisis matricial de transferencia). Además, se utilizó un modelo acústico desarrollado en el Área de Mecánica de Fluidos de la Universidad de Oviedo para simular el campo sonoro interno en una bomba centrífuga industrial. Se determinaron los componentes de la matriz de dispersión (coeficientes sonoros de reflexión y transmisión) para distintas frecuencias y caudales. Este estudio se complementó con mediciones de la presión no estacionaria en la bomba centrífuga.

Se estudió también el acoplamiento acústico entre la bomba transparente y su circuito hidráulico. Se describió el sistema teóricamente mediante un TMA. La atenuación se incluyó en el modelo mediante el uso de números de onda complejos. Se instalaron tres transductores de presión de respuesta rápida a lo largo del conducto de impulsión, para descomponer la señal de presión en onda radiada y reflejada. De forma complementaria, se colocaron cinco transductores de presión en la voluta de la bomba cerca de la lengüeta: dos en la zona estrecha de la voluta y tres en la zona ancha y en el conducto de salida. Se consiguió modificar fácilmente la impedancia acústica sin cambiar el caudal, es decir, sin cambiar la velocidad de la bomba, mediante la activación de una rama vertical sin salida. Esta rama se encontraba parcialmente llena con aire, y estaba conectada al circuito en la zona de impulsión. Se investigó la influencia de activar esta rama en las fluctuaciones de presión para distintas BPFs. Se determinó la velocidad del sonido experimentalmente mediante el uso de tres transductores de presión.
Se tomaron medidas PIV a 470 rpm debido a que se detectó una alta influencia del estado de la rama en las fluctuaciones de presión para esta velocidad. En concreto, se investigaron 33 posiciones distintas del álabe al 40 % Q_N y Q_N con la rama abierta y cerrada a alta y baja ampliación.

8.2 Campo del flujo

Las conclusiones principales respecto al campo del flujo en la bomba debido a la interacción rotor-estator son:

1. Las medidas PIV estéreo mostraron que la componente axial de la velocidad es pequeña, igual o menor que el 10 % de la velocidad en la punta del álabe, debido a la geometría 2D del rodete y de la voluta. Sin embargo, se

encontraron tubos de vorticidad longitudinales que cambian su sentido de rotación en función del caudal.

2. Para el caudal del 40 % Q_N se concluye que:
   - Se observaron varios vórtices en cada canal del rodete en los campos de velocidad relativa promediados para una cierta posición del rodete.
   - Estos vórtices generan varias zonas de vorticidad positiva y negativa. Una capa de vorticidad intensa, que empieza en el borde de salida del álabe, incide sobre el siguiente álabe en su cara de presión. Esta capa tiene la TKE alta y también alta producción de TKE, y cuando llega al siguiente álabe todavía se produce TKE.
   - En la zona estrecha de la voluta las velocidades absolutas son más altas para este caudal, debido a la recirculación y a la separación del flujo desde la lengüeta.
   - Los resultados de alta ampliación muestran cómo la capa de vorticidad del borde de salida interactúa con la zona de estela formada por la separación del flujo desde la lengüeta, generando altos valores de vorticidad con sentido de rotación contrario y de TKE.
   - Las altas velocidades radiales justo detrás del borde de salida en la cara de succión llevan a la capa longitudinal de vorticidad a separarse del álabe y a cambiar a una geometría circular mientras se mueve hacia el centro del canal de la voluta.

3. El punto de estancamiento se mueve considerablemente dependiendo del caudal. Se observó que:
   - Para el caudal por debajo de Q_N (40 % Q_N) el punto de estancamiento se desplaza hacia la salida de la bomba. Esto causa la separación del flujo hacia la zona estrecha de la voluta con alta vorticidad negativa, produciendo alta TKE. Mientras el álabe pasa por la punta de la lengüeta se reduce la separación del flujo desde esta zona. La producción de TKE alcanza un mínimo poco después y su máximo antes de que la cara de presión del álabe llegue a la punta de la lengüeta, en concordancia con el desarrollo de vorticidad en la estela de la misma.
   - Para el caudal por encima de Q_N (150 % Q_N) el punto de estancamiento se mueve a lo largo de la lengüeta hacia la zona interior, cerca del rodete. Tiene lugar la separación del flujo y una zona con alta vorticidad positiva se extiende desde la lengüeta hacia el conducto de salida. La alta producción de TKE se concentra en la estela de la lengüeta para casi todo el ciclo, excepto durante la llegada de las capas de vorticidad desprendidas del borde de salida, que fuerzan la estela de la lengüeta a disminuir su tamaño. Se reduce la zona de alta TKE en la estela de la lengüeta, en amplitud y extensión, debido a la separación desde la misma y se desplaza hacia la salida de la bomba.

- Se pudo observar con detalle el desarrollo de la zona de estancamiento y la estela de la lengüeta y, para ciertos instantes del tiempo, se constató una reducción considerable de la separación del flujo, que generaba menos vorticidad y menos TKE. Los valores de TKE son más bajos para 150 % Q_N que para 40 % Q_N.

4. Para 150 % Q_N el flujo se caracteriza por los siguientes fenómenos:
   - El flujo relativo entre los canales del rodete se encuentra condicionado por un vórtice que rota en dirección contraria a la del rodete y por la separación del flujo desde la cara de presión en el borde de ataque, donde se produce alta TKE. La zona de alta TKE es arrastrada por convección con el flujo principal.
   - El flujo que sale por los canales del rodete tiene dos capas de alta vorticidad, una negativa y otra positiva, que se desprenden del borde de salida, además de una ancha zona negativa relacionada con el vórtice con sentido de rotación contrario al del rodete indicado con anterioridad.
   - En cuanto estas capas de vorticidad inciden sobre la lengüeta, el borde de la misma las trocea, se dividen y son arrastradas por convección junto con el flujo. Aunque las partes de las capas de vorticidad cercanas al álabe sufren alargamiento debido a efectos de adherencia en la zona de estancamiento de la lengüeta.
   - La máxima producción de TKE observada se corresponde con la zona de interacción del álabe con la lengüeta. La producción de TKE se concentra inicialmente justo detrás de la cara de presión en el borde de salida y alcanza su máximo cuando el álabe se alinea con la punta de la lengüeta. Después, esta zona de producción de TKE se desplaza hacia la cara de succión.
   - La capa de vorticidad positiva tiene menos TKE y menos producción de TKE que la zona de vorticidad negativa, debido a que la estructura del flujo principal es bastante periódica con el paso del álabe.

8.3 Análisis espectral de las variables del flujo

Las conclusiones principales derivadas del procesado FFT de los campos de flujo, disponible para 32 instantes de tiempo a alta y baja ampliación, son:

1. Para 40 % Q_N las variables del flujo (magnitud de velocidad, vorticidad y TKE) tienen su contenido espectral más alto a f_{BP}. A Q_N estas variables también tienen su pico más alto a f_{BP}, excepto para la magnitud de la velocidad en casi toda la zona estrecha de la voluta, donde el pico a $2f_{BP}$ es más alto.

2. Para 150 % Q_N en la zona de la lengüeta, debido a la interacción del álabe, las variables del flujo tienen un contenido alto de su señal a f_{BP} y $2f_{BP}$. Todavía hay contenido espectral significativo en armónicos más altos, especialmente para la vorticidad. Una tendencia general es que en la voluta, antes de la punta de la lengüeta, las fluctuaciones principales ocurren a f_{BP}, mientras que detrás de la punta de la lengüeta las fluctuaciones a $2f_{BP}$ son dominantes (para la magnitud de la velocidad y sus componentes radiales y tangenciales), o son de magnitud similar (TKE). Para la vorticidad la componente dominante es a $2f_{BP}$, debido a las capas intensas de vorticidad negativa y positiva generadas desde el borde de salida del álabe. Sin embargo, lejos de la punta de la lengüeta la frecuencia dominante es la f_{BP}.

3. Los mapas de distribución de la fluctuación (amplitud y fase) a f_{BP} y sus armónicos (hasta $3f_{BP}$) muestran claramente cómo las fluctuaciones son arrastradas por convección con el flujo, además de la atenuación de la amplitud y la extensión hasta donde las fluctuaciones son visibles. Con respecto a la amplitud a f_{BP} se observó que, detrás de la salida del rodete, a un radio de 1.25 r_{tip}, hay una reducción hasta aproximadamente un 10 % para la magnitud de la velocidad, vorticidad y TKE. Esto significa que la zona de altas fluctuaciones se extiende hasta aproximadamente 1.25 r_{tip} fuera del rodete y continúa a lo largo del conducto de salida en el lado de la lengüeta.

4. Comparando los tres caudales investigados se pudo observar claramente cómo las fluctuaciones a f_{BP} y armónicos son más notables en la zona ancha de la voluta y en el conducto de salida para caudales crecientes. Para Q_N las fluctuaciones en amplitud son generalmente más pequeñas que en condiciones fuera de diseño, especialmente para la TKE. Sin embargo, las fluctuaciones en la salida de la bomba son más notables en los mapas de fase para Q_N que para 40 % Q_N. Para 150 % Q_N las fluctuaciones a f_{BP} y armónicos ocupan casi todo el conducto de salida de la bomba en el campo de visión con baja ampliación.

8.4 Acoplamiento acústico

Las conclusiones principales respecto al acoplamiento acústico del circuito hidráulico con la bomba son:

1. Para la bomba industrial, operando a una velocidad de referencia de 1620 rpm, el cambio de la impedancia acústica en el lado de succión mediante la activación de una rama sin salida casi no tiene ninguna influencia en las fluctuaciones de presión en la zona de la lengüeta. En cambio, para 2040 rpm hay una variación significativa en la amplitud de las fluctuaciones de presión en esta zona si se cierra la válvula en la bifurcación de esta rama sin salida: se consigue una reducción de un 15 % para baja carga

parcial. Esta tendencia se confirma mediante los modelos acústicos, que predicen en esta zona de frecuencia de paso de álabe (BPF) una frecuencia de resonancia del sistema que depende del estado de la rama sin salida.

Esto sugiere que, aunque se puede generar un ruido significativo, si la bomba opera fuera de sus condiciones de diseño, se puede reducir el impacto de este ruido mediante un diseño adecuado del circuito que reduzca el efecto del acoplamiento acústico.

2. Los resultados sugieren que los patrones de generación de ruido entre Q_N y 150 % Q_N son más similares que al 40 % Q_N debido a que:
   - A carga parcial la presión mínima en la zona estrecha de la voluta coincide con la llegada del vórtice de recirculación cerca de la cara de presión en la salida del rodete.
   - Para Q_N y 150 % Q_N la presión mínima ocurre aproximadamente cuando el borde de salida del álabe pasa por cada punto. Esto coincide con velocidades relativas altas, correspondiendo con velocidades absolutas bajas.

3. La diferencia de fase entre los sensores situados en la salida del conducto es muy pequeña para los tres caudales. Esto sugiere que las fluctuaciones hidráulicas ya se han atenuado en esta zona y que las fluctuaciones de presión se propagan a la velocidad del sonido. Estas ondas acústicas están compuestas por la onda radiada y la reflejada.

4. Solamente para el 40 % Q_N la fase del sensor en la zona ancha de la voluta está cerca de la fase de los sensores en el conducto de salida. Esto sugiere que las fluctuaciones hidráulicas no son transportadas lejos de la salida del rodete hacia la voluta, como ocurre para Q_N y 150 % Q_N. Esto confirma los resultados de las medidas PIV, donde la extensión de las fluctuaciones en la voluta y en el conducto de salida aumenta si se aumenta el caudal.

5. Los resultados teóricos de TMA concuerdan razonablemente bien con los resultados experimentales para el rango investigado de BPF. Se pueden utilizar para predecir resonancias acústicas con impedancia máxima.

6. El campo de presión, incluso en la propia bomba, cambia en amplitud para ciertas frecuencias si se cambia la impedancia acústica mediante la rama sin salida. Las fluctuaciones de presión a BPF se redujeron hasta en un 29 % en la zona estrecha de la voluta para una cierta velocidad de la bomba. En la zona ancha de la voluta las fluctuaciones se redujeron incluso en un 36 % al caudal nominal.

7. En las medidas PIV a 470 rpm no se encontró ninguna diferencia significativa en los campos de velocidad, vorticidad y TKE al activar la rama sin salida. Esto se debe a que la velocidad acústica de las partículas es muy pequeña, debajo de la precisión de las medidas PIV.

8. Se demostró la influencia de la impedancia acústica en la magnitud de las fluctuaciones de presión generadas para una bomba industrial y otra bomba con una geometría bidimensional. Se pueden utilizar los modelos de dos puertos para predecir frecuencias de resonancia con éxito, como confirman los resultados experimentales.

8.5 Trabajo futuro

Algunos trabajos futuros posibles que no se han podido cubrir en esta tesis son:

1. Estimación de los campos de presión a partir de las medidas PIV. De hecho, actualmente se está investigando para obtener los campos de presión a partir de los campos de velocidades promediados para una cierta posición del rodete y las tensiones de Reynolds de los componentes en el plano. Esto se hace en dos pasos: *(i)* cálculo de las derivadas temporales y espaciales de las componentes de la velocidad y de las tensiones de Reynolds, para finalmente estimar las componentes en el plano de los gradientes de presión utilizando las ecuaciones URANS promediadas para una cierta posición del rodete (van Oudheusden, 2013); *(ii)* integración de la distribución de los gradientes de presión, tomando como referencia las señales de presión obtenidas mediante los cinco transductores en la voluta de la bomba (ver Fig. 4.9), mediante la estrategia omnidireccional de integración según Liu and Katz (2006).

2. Medidas experimentales de estructuras 3D del flujo. Esto se puede conseguir mediante:
   - Multi-plano estéreo PIV para obtener variables del flujo promediadas para una cierta posición del rodete en varios planos de medida.
   - PIV tomográfico para obtener el campo de velocidad instantáneo completo en un volumen dentro de la bomba.

   Además, el PIV de alta velocidad permitiría capturar estructuras del flujo no asociadas con BPF o armónicos. Se podrían aplicar estas técnicas en una bomba de laboratorio con álabes curvados en dos direcciones, que es lo típico para bombas industriales. Además, para poder obtener campos de velocidad dentro de los canales del rodete, sería conveniente utilizar otra instalación experimental con coincidencia del índice óptico.

3. Validación de cálculos teóricos de los campos de flujo internos. Estas medidas PIV constituyen una importante base de datos para contrastar las predicciones de modelos numéricos (CFD). Por ejemplo, esto permite verificar parámetros de cálculo como condiciones de contorno o los modelos de turbulencia. Adicionalmente, se puede investigar el campo sonoro interno en la bomba transparente mediante el uso del modelo de propagación interno usado en esta tesis para la bomba industrial.

Bibliography

Adrian, R. and Yao, C. (1985). Pulsed laser technique application to liquid and gaseous flows and the scattering power of seed materials. *Applied Optics*, 24(1):44–52.

Akin, O. and Rockwell, D. (1994). Flow structure in a radial flow pumping system using high-image-density particle image velocimetry. *Journal of Fluids Engineering - Transactions of the ASME*, 116(3):538–544.

Allam, S. and Åbom, M. (2006). Investigation of damping and radiation using full plane wave decomposition in ducts. *Journal of Sound and Vibration*, 292:519–534.

Arndt, N., Acosta, A., Brennen, C., and Caughey, T. (1988). Rotor-stator interaction in a diffuser pump. In *ASME, Gas Turbine and Aeroengine Congress and Exposition, Nº 88-GT-55*. Amsterdam, Netherlands.

Bachert, R., Ludwig, G., and Stoffel, B. (2005). Three dimensional, impressed cavitation effects at the tongue of the volute in a radial pump. In *Proceedings of ASME Fluid Engineering Division Summer Meeting and Exhibition, Nº 2005-77373*. Houston, USA.

Bardeleben, M. and Weaver, D. (2002). Investigation into the passive acoustic properties of a centrifugal pump. In *Proceedings of 1000 Islands Fluids Mechanics Meeting*. Alexandria Bay, Canada.

Barrio, R., Blanco, E., Keller, J., Parrondo, J., and Fernández, J. (2011). Numerical determination of the acoustic impedance of a centrifugal pump. In *Proceedings of ASME-JSME-KSME Joint Fluids Engineering Conference, Nº 06074*. Hamamatsu, Japan.

Barrio, R., Blanco, E., Parrondo, J., and Fernández, J. (2008). The effect of impeller cutback on the fluid-dynamic pulsations and load at the blade-passing frequency in a centrifugal pump. *Journal of Fluids Engineering*, 130:111102–1–11.

Barrio, R., Parrondo, J., and Blanco, E. (2010). Numerical analysis of the unsteady flow in the near-tongue region in a volute-type centrifugal pump for different operating points. *Computers & Fluids*, 39:859–870.

Berten, S. (2010). *Hydrodynamics of High Specific Power Pumps for Off-Design Operating Conditions*. PhD thesis, STI, Lausanne.

Berten, S., Dupont, P., Farhat, M., and Avellan, F. (2007). Rotor-stator interaction induced pressure fluctuations: CFD and hydroacoustic simulations in the stationary components of a multistage centrifugal pump. In *Proceedings of FEDSM 2007, N° 37549*. San Diego, USA.

Bolleter, U. (1993). Interaction of pumps and piping systems with regard to pressure pulsations. In *Proceedings of 1st International Symposium on "Pump Noise and Vibrations"*. Clamart, France.

Braun, O. (2009). *Part Load Flow in Radial Centrifugal Pumps*. PhD thesis, STI, Lausanne.

Brennen, C. E. (1994). *Hydrodynamics of Pumps*. Concepts ETI, Inc. and Oxford University Press.

Carta, F., Charley, J., and Caignaert, G. (2000). Transfer matrices of single volute centrifugal pumps. *Int. J. Acoust. Vib*, 5(4):159–166.

Cavazzini, G., Dupont, P., Pavesi, G., Dazin, A., Bois, G., Atif, A., and Cherdieu, P. (2011). Analysis of unsteady flow velocity fields inside the impeller of a radial flow pump: PIV measurements and numerical calculation comparisons. In *Proceedings of ASME-JSME-KSME Joint Fluids Engineering Conference, N° 22055*. Hamamatsu, Japan.

Cavazzini, G., Pavesi, G., and Ardizzon, G. (2010). Validation of an analysis method for particle image velocimetry of turbulent unsteady flows in turbomachinery. *Proceedings of the Institution of Mechanical Engineers, Part A: Journal of Power and Energy*, 224(5):679–689.

Choi, J.-S., McLaughlin, D. K., and Thompson, D. E. (2003). Experiments on the unsteady flow field and noise generation in a centrifugal pump impeller. *Journal of Sound and Vibration*, 263(3):493 – 514.

Chu, S., Dong, R., and J., K. (1995a). Relationship between unsteady flow, pressure fluctuations, and noise in a centrifugal pump - part A: Use of PDV data to compute the pressure field. *Journal of Fluids Engineering*, 117:24–29.

Chu, S., Dong, R., and J., K. (1995b). Relationship between unsteady flow, pressure fluctuations, and noise in a centrifugal pump - part B: Effects of blade-tongue interactions. *Journal of Fluids Engineering*, 117:30–35.

Curle, N. (1955). The influence of solid boundaries upon aerodynamic sound. *Proceedings of the Royal Society of London. Series A. Mathematical and Physical Sciences*, 231(1187):505–514.

Davies, P. and Holland, K. (2004). The measurement and prediction of sound waves of arbitrary amplitude in practical flow ducts. *Journal of Sound and Vibration*, 271:849–861.

Dazin, A., Cavazzini, G., Pavesi, G., Dupont, P., Coudert, S., Ardizzon, G., Caignaert, G., and Bois, G. (2011). High-speed stereoscopic PIV study of rotating instabilities in a radial vaneless diffuser. *Experiments in Fluids*, 51(1):83–93.

Dong, R., Chu, S., and Katz, J. (1992a). Quantative visualization of the flow within the volute of a centrifugal pump. Part A: Technique. *Journal of Fluids Engineering*, 114:390–395.

Dong, R., Chu, S., and Katz, J. (1992b). Quantative visualization of the flow within the volute of a centrifugal pump. Part B: Results and analysis. *Journal of Fluids Engineering*, 114:396–403.

Dong, R., Chu, S., and Katz, J. (1997). Effect of modification to tongue and impeller geometry on unsteady flow, pressure fluctuations, and noise in a centrifugal pump. *Journal of Turbomachinery*, 119:506–515.

Dupont, P., Caignaert, G., Bois, G., and Schneider, T. (2005). Rotor-stator interactions in a vaned diffuser radial flow pump. In *Proceedings of FEDSM, Nº 77038*. Houston, USA.

Engelberg, S. (2008). *Digital Signal Processing: An Experimental Approach*, chapter 1 "Understanding Sampling", pages 3–16. Springer, London.

Feng, J., Benra, F.-K., and Dohmen, H. J. (2009a). Comparison of periodic flow fields in a radial pump among CFD, PIV, and LDV results. *International Journal of Rotating Machinery*, 2009.

Feng, J., Benra, F.-K., and Dohmen, H. J. (2009b). Unsteady flow visualization at part-load conditions of a radial diffuser pump: By PIV and CFD. *Journal of Visualization*, 12(1):65–72.

Friedrichs, J. and Kosyna, G. (2003). Unsteady PIV flow field analysis of a centrifugal pump impeller under rotating cavitation. In *Proceedings of the Fifth International Symposium on Cavitation, Nº Cav03-OS-6-005*. Osaka, Japan.

Guelich, J. (2010). *Centrifugal Pumps*. Springer, Berlin Heidelberg, 2nd edition.

Guelich, J. and Bolleter, U. (1992). Pressure pulsations in centrifugal pumps. *Journal of Vibration and Acoustics*, 114:272–279.

Howe, M. S. (1991). On the estimation of sound produced by complex fluid-structure interactions, with application to a vortex interacting with a shrouded rotor. *Proceedings: Mathematical and Physical Sciences*, 433(1889):pp. 573–598.

Howe, M. S. (2003). *Theory of Vortex Sound*. Cambridge University Press.

Huang, H., Dabiri, D., and Gharib, M. (1997). On errors of digital particle image velocimetry. *Measurement Science and Technology*, 8(12):1427.

Karassik, I. J., Krutzsch, W. C., Fraser, W. H., and Messina, J. P. (1986). *Pump Handbook*. McGraw-Hill NewYork, 2nd edition.

Kaupert, K. and Staubli, T. (1999). The unsteady pressure field in a high specific speed centrifugal pump impeller-part I: Influence of the volute. *Journal of Fluids Engineering*, 121:621–626.

Keane, R. and Adrian, R. (1990). Optimization of particle image velocimeters. Part I: Double pulsed systems. *Measurement Science and Technology*, 1:1202–1215.

Kearney, D., Grimes, R., and Punch, J. (2009). An experimental investigation of the flow fields within geometrically similar miniature-scale centrifugal pumps. *Journal of Fluids Engineering*, 131(10):101101–1–10.

Keller, J., Parrondo, J., Barrio, R., Fernández, J., and Blanco, E. (2014). Effects of the pump-circuit acoustic coupling on the blade-passing frequency perturbations. *Applied Acoustics*, 76(0):150 – 156.

Krause, N., Pap, E., and Thévenin, D. (2006). Investigation of off-design conditions in a radial pump by using time-resolved-PIV. In *Proceedings of 13th Int Symp on Applications of Laser Techniques to Fluid Mechanics*. Lisbon, Portugal.

Krause, N., Zähringer, K., and Pap, E. (2005). Time-resolved particle imaging velocimetry for the investigation of rotating stall in a radial pump. *Experiments in Fluids*, 39:192–201.

Langthjem, M. and Olhoff, N. (2004a). A numerical study of flow-induced noise in a two-dimensional centrifugal pump. Part I. Hydrodynamics. *Journal of Fluids and Structures*, 19:349–368.

Langthjem, M. and Olhoff, N. (2004b). A numerical study of flow-induced noise in a two dimensional centrifugal pump. Part II. Hydroacoustics. *Journal of Fluids and Structures*, 19:369–386.

Lavrentjev, J., Åbom, M., and Bodén, H. (1995). A measurement method for determining the source data of acoustic two-port sources. *Journal of Sound and Vibration*, 183(3):517 – 531.

Lawson, N. J. and Wu, J. (1997). Three-dimensional particle image velocimetry: error analysis of stereoscopic techniques. *Measurement Science and Technology*, 8(8):894.

Lesieur, M. (2008). *Turbulence in Fluids*. Springer, Berlin Heidelberg, 4th edition.

Liu, X. and Katz, J. (2006). Instantaneous pressure and material acceleration measurements using a four-exposure PIV system. *Experiments in Fluids*, 41(2):227–240.

Lorett, J. A. and Gopalakrishnan, S. (1986). Interaction between impeller and volute of pumps at off-design conditions. *Journal of Fluids Engineering*, 108(1):12–18.

Lucas, M. J., Noreen, R. A., Sutherland, L. C., Cole III, J. E., and Junger, C. M. (1997). *Handbook of the acoustic characteristics of turbomachinery cavities*. ASME Press, New York.

Miner, S., Beaudoin, R., and Flack, R. (1989). Laser velocimeter measurements in a centrifugal flow pump. *Journal of Turbomachinery*, 111:205–212.

Miorini, R. L., Huixuan, W., and Katz, J. (2012). The internal structure of the tip leakage vortex within the rotor of an axial waterjet pump. *Journal of Turbomachinery*, 134(3):031018.1–12.

Morgenroth, M. (1995). *Sound Generation by a Centrifugal Volute Pump at Blade Pass Frequency*. PhD thesis, McMaster University.

Morgenroth, M. and Weaver, D. (1998). Sound generation by a centrifugal pump at blade passing frequency. *Journal of Turbomachinery*, 120:736–743.

Mulleners, K. and Raffel, M. (2013). Dynamic stall development. *Experiments in Fluids*, 54(2):1–9.

Munjal, M. (1987). *Acoustics of Ducts and Mufflers*. John Wiley & Sons., 1st edition.

Neise, W. (1992). Review of fan noise generation mechanisms and control methods. In *Proceedings of FAN NOISE symposium*, pages 45–56. Senlis, France.

Nicolet, C., Ruchonnet, N., Alligné, S., Koutnik, J., and Avellan, F. (2010). Hydroacoustic simulation of rotor-stator interaction in resonance conditions in Francis pump-turbine. In *IOP Conference Series: Earth and Environmental Science*, volume 12, page 012005. IOP Publishing.

Oro, J. M. F., Marigorta, E. B., Díaz, K. M. A., and Ballesteros-Tajadura, R. (2009). Forced and unforced unsteadiness in an axial turbomachine. *Experimental Thermal and Fluid Science*, 33(3):449 – 459.

Paone, N., Riethmuller, M., and Braembussche, R. (1989). Experimental investigation of the flow in the vaneless diffuser of a centrifugal pump by particle image displacement velocimetry. *Experiments in Fluids*, 7(6):371–378.

Parrondo, J., González, J., and Fernández, J. (2002). The effect of the operating point on the pressure fluctuations at the blade passage frequency in the volute of a centrifugal pump. *Journal of Fluids Engineering*, 124:784–790.

Parrondo, J., Pérez, J., Barrio, R., and González, J. (2011). A simple acoustic model to characterize the internal low frequency sound field in centrifugal pumps. *Applied Acoustics*, 72:59–64.

Pavesi, G., Cavazzini, G., and Ardizzon, G. (2008). Time–frequency characterization of the unsteady phenomena in a centrifugal pump. *International Journal of Heat and Fluid Flow*, 29(5):1527 – 1540.

Pedersen, N., Larsen, P., and Jacobsen, C. (2003). Flow in a centrifugal pump impeller at design and off-design conditions - part I: Particle image velocimetry (PIV) and laser doppler velocimetry (LDV) measurements. *Journal of Fluids Engineering*, 125(1):61–72.

Pope, S. B. (2000). *Turbulent flows*. Cambridge University Press, Cambridge.

Prasad, A. K. and Jensen, K. (1995). Scheimpflug stereocamera for particle image velocimetry in liquid flows. *Applied optics*, 34(30):7092–7099.

Pérez Castillo, J. (2009). *Generación de Ruido Tonal en Bombas Centrífugas por Interacción Fluidodinámica entre Rodete y Voluta [in spanish]*. PhD thesis, University of Oviedo.

Raffel, M., Willert, C., Wereley, S., and Kompenhans, J. (2007). *Particle Image Velocimetry*. Springer, Berlin Heidelberg, 2nd edition.

Rossing, T. D. (2007). *Springer Handbook of Acoustics*. Springer, Berlin Heidelberg.

Roth, G. I. and Katz, J. (2001). Five techniques for increasing the speed and accuracy of PIV interrogation. *Measurement Science and Technology*, 12(3):238–245.

Rzentkowski, G. and Zbroja, S. (2000). Experimental characterization of centrifugal pumps as an acoustic source at the blade-passing frequency. *Journal of Fluids and Structures*, 14(4):529 – 558.

Schwartz, R. and Nelson, R. (1984). Acoustic resonance phenomena in high energy variable speed centrifugal pumps. In *Proceedings of 1st Intl Pump Symposium*, pages 23–28. Houston, USA.

Sciacchitano, A., Wieneke, B., and Scarano, F. (2013). PIV uncertainty quantification by image matching. *Measurement Science and Technology*, 24(4):045302.

Sinha, M. and Katz, J. (2000). Quantitative visualization of the flow in a centrifugal pump with diffuser vanes - I: On flow structures and turbulence. *Journal of Fluids Engineering, Transactions of the ASME*, 122(1):97–107.

Sinha, M., Katz, J., and Meneveau, C. (2000). Quantitative visualization of the flow in a centrifugal pump with diffuser vanes - II: Addressing passage-averaged and large-eddy simulation modeling issues in turbomachinery flows. *Journal of Fluids Engineering, Transactions of the ASME*, 122(1):108–116.

Sinha, M., Pinarbasi, A., and Katz, J. (2001). The flow structure during onset and developed states of rotating stall within a vaned diffuser of a centrifugal pump. *Journal of Fluids Engineering, Transactions of the ASME*, 123:490–499.

Spencer, A. and Hollis, D. (2005). Correcting for sub-grid filtering effects in particle image velocimetry data. *Measurement Science and Technology*, 16(11):2323–2335.

Srivastav, O., Pandu, K., and Gupta, K. (2003). Effect of radial gap between impeller and diffuser on vibration and noise in a centrifugal pump. *Journal of the Institution of Engineers, Part MC, Mechanical Engineering Division*, 84:36–39.

Stickland, M., Scanlon, T., Fernandez-Francos, J., Blanco-Marigorta, E., and Parrondo, J. (2002). A numerical and experimental analysis of flow in a centrifugal pump. In *Proceedings of ASME FEDSM, Nº 31175*. Montreal, Canda.

Stickland, M., Scanlon, T., Waddell, P., Fernandez-Francos, J., and Blanco, E. (2003). Measurement of rotating flows using PIV and image derotation. *Experiments in Fluids*, 34:304–306.

Talha, A., Barrand, J., and Caignaert, G. (2002). Pressure fluctuations on the impeller blades of a centrifugal turbomachine: a comparative analysis between air and water tests. *International Journal of Acoustics and Vibration*, 7(1):45–51.

Timouchev, S. and Tourret, J. (2002). Numerical simulation of BPF pressure pulsation field in centrifugal pumps. In *Proceedings of the 19th International Pump Users Symposium*, pages 85–106. Texas, USA.

TSI (2011). *Insight 3G and Insight 4G User's Guide*. TSI Incorporated, USA.

Ubaldi, M., Zunino, P., and Ghiglione, A. (1998). Detailed flow measurements within the impeller and the vaneless diffuser of a centrifugal turbomachine. *Experimental Thermal and Fluid Science*, 17(1–2):147 – 155.

van Oudheusden, B. W. (2013). PIV-based pressure measurement. *Measurement Science and Technology*, 24(3):032001.

Wernet, M. (2000). Application of DPIV to study both steady state and transient turbomachinery flows. *Optics and Laser Technology*, 32:497–525.

Wu, H., Miorini, R., and Katz, J. (2011a). Measurements of the tip leakage vortex structures and turbulence in the meridional plane of an axial water-jet pump. *Experiments in Fluids*, 50(4):989–1003.

Wu, J. Z., Ma, H. Y., and Zhou, M. D. (2006). *Vorticity and vortex dynamics*. Springer, Berlin Heidelberg.

Wu, Y., Liu, S., Yuan, H., and Shao, J. (2011b). PIV measurement on internal instantaneous flows of a centrifugal pump. *Science China Technological Sciences*, 54(2):270–276.

Wuibaut, G., Bois, G., Dupont, P., and Caignaert, G.and Stanislas, M. (2002). PIV measurements in the impeller and the vaneless diffuser of a radial flow pump in design and off-design operating conditions. *Journal of Fluids Engineering, Transactions of the ASME*, 124(3):791–797.

Wuibaut, G., Bois, G., El Hajem, M., Akhras, A., and Champagne, J. (2006). Optical PIV and LDV comparisons of internal flow investigations in SHF impeller. *International Journal of Rotating Machinery*, 2006:69521.1–9.

Publications during the research

The following publications are the result of work conducted during my research studies. Several figures and ideas have appeared previously in some of these publications:

Barrio, R., Blanco, E., Keller, J., Parrondo, J., and Fernández, J. (2011). Numerical determination of the acoustic impedance of a centrifugal pump. In *Proceedings of ASME-JSME-KSME Joint Fluids Engineering Conference, Nº 06074*. Hamamatsu, Japan.

Barrio, R., Blanco, E., Keller, J., Fernández, J., and Parrondo, J. (2012). Including pump-circuit interactions in CFD simulations by means of user-defined functions. In *Proceedings of ISROMAC, Nº 1150*. Honolulu, USA.

Keller, J., Barrio, R., Parrondo, J., Fernández, J., and Pérez, J. (2011). Effects of the pump-circuit acoustic coupling on the blade-passing frequency perturbations. In *Proceedings of ASME-JSME-KSME Joint Fluids Engineering Conference, Nº 06071*. Hamamatsu, Japan.

Keller, J., Parrondo, J., Barrio, R., Blanco, E., and Fernández, J. (2012). Experimental analysis of pump-circuit coupling at blade-passing frequency. In *Proceedings of ISROMAC, Nº 1183*. Honolulu, USA.

Keller, J., Parrondo, J., Blanco, E., Barrio, R., and Suárez, C. (2013a). Influence of pump-circuit coupling on acoustic waves in pipelines and pump velocity fields. In *Proceedings of ASME-PVP, Nº 97958*. Paris, France.

Keller, J., Blanco, E., Fernández, J., Barrio, R., and Parrondo, J. (2013b). CFD and PIV characterization of the rotor-stator-interaction of a centrifugal pump and acoustic emission to the hydraulic circuit. In *Proceedings of CIIEM*. Lisboa, Portugal.

Keller, J., Parrondo, J., Barrio, R., Fernández, J., and Blanco, E. (2014). Effects of the pump-circuit acoustic coupling on the blade-passing frequency perturbations. *Applied Acoustics*, 76(0):150 – 156.

Tan, D. Y., Miorini, R. L., Keller, J., and Katz, J. (2012a). Flow visualization using cavitation within blade passage of an axial waterjet pump rotor. In *Proceedings of ASME FEDSM, Nº 72108*. Rio Grande, Puerto Rico.

Tan, D. Y., Miorini, R. L., Keller, J., and Katz, J. (2012b). Flow visualization using cavitation within the rotor and stator blade passages of an axial waterjet pump rotor at and below best efficiency point. In *29th Symposium in Naval Hydrodynamics*. Gothenburg, Sweden.

Tan, D. Y., Miorini, R. L., Keller, J., and Katz, J. (2012c). Investigation of flow phenomena within an axial waterjet pump at off-design conditions. In *CAV 2012, Eighth International Symposium on Cavitation, N^o 255*. Singapore.

Part V

Appendix

A Pump geometry

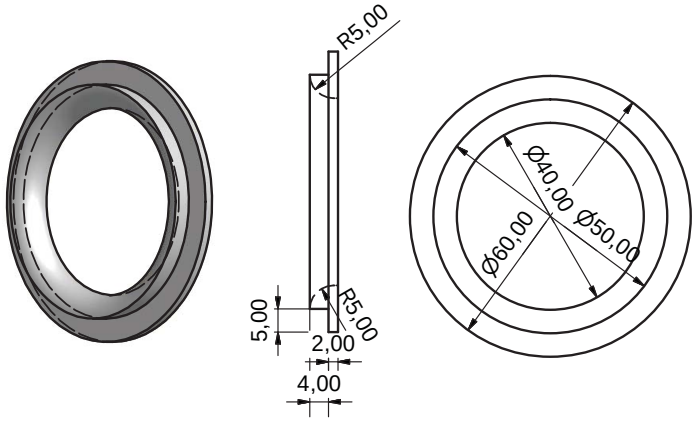

Figure A.1: Metal piece at impeller entrance (units in mm)

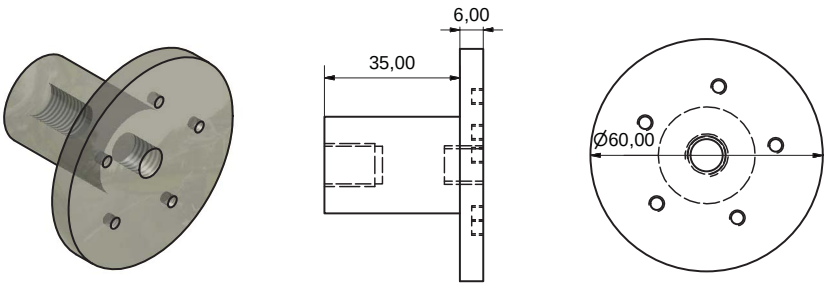

Figure A.2: Metal piece connecting impeller with motor (units in mm)

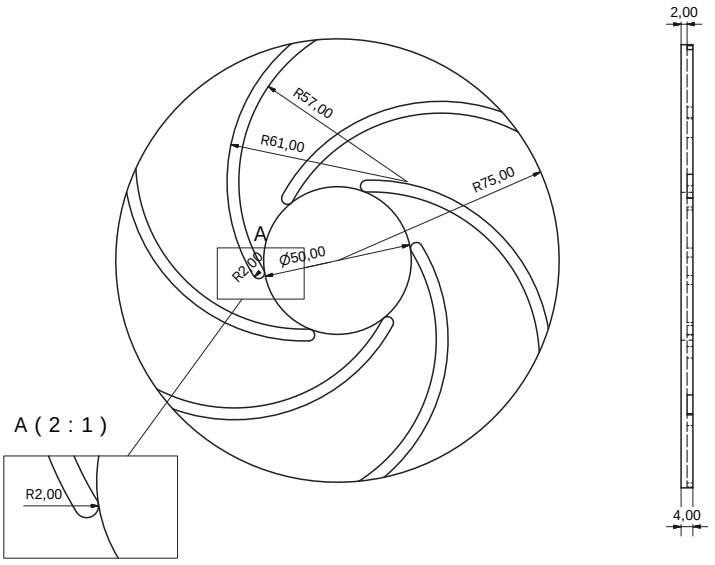

Figure A.3: Front impeller disc (units in mm)

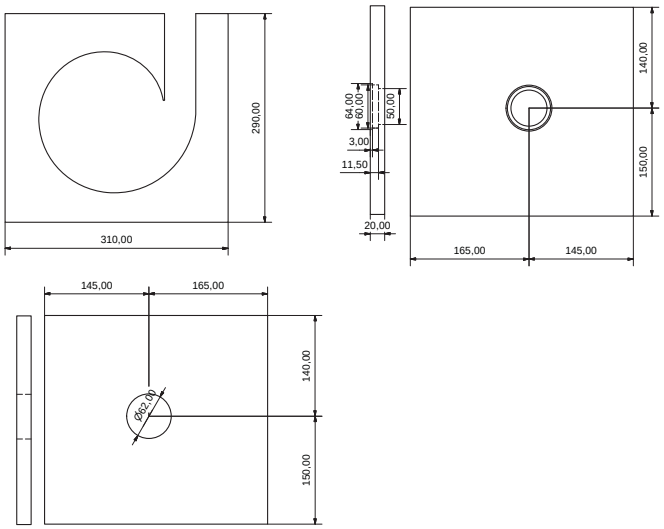

Figure A.4: Volute casing (units in mm)

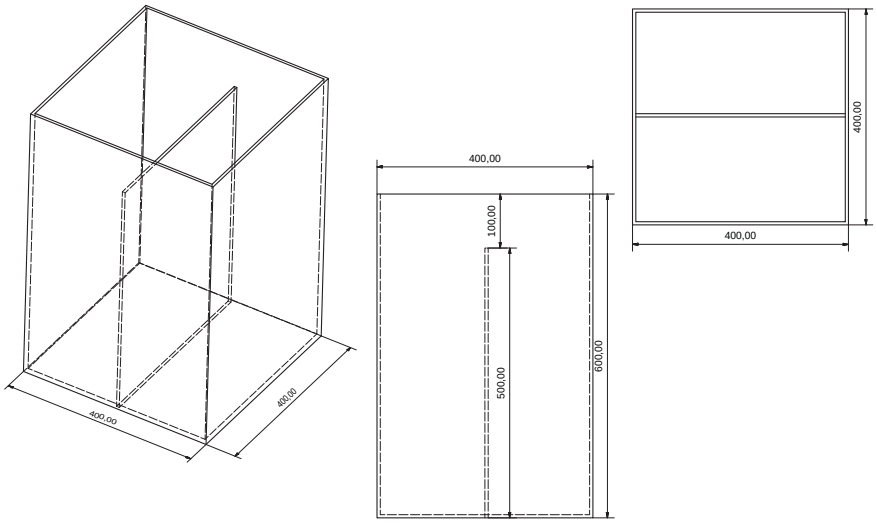

Figure A.5: Water tank (units in mm)

B PIV results

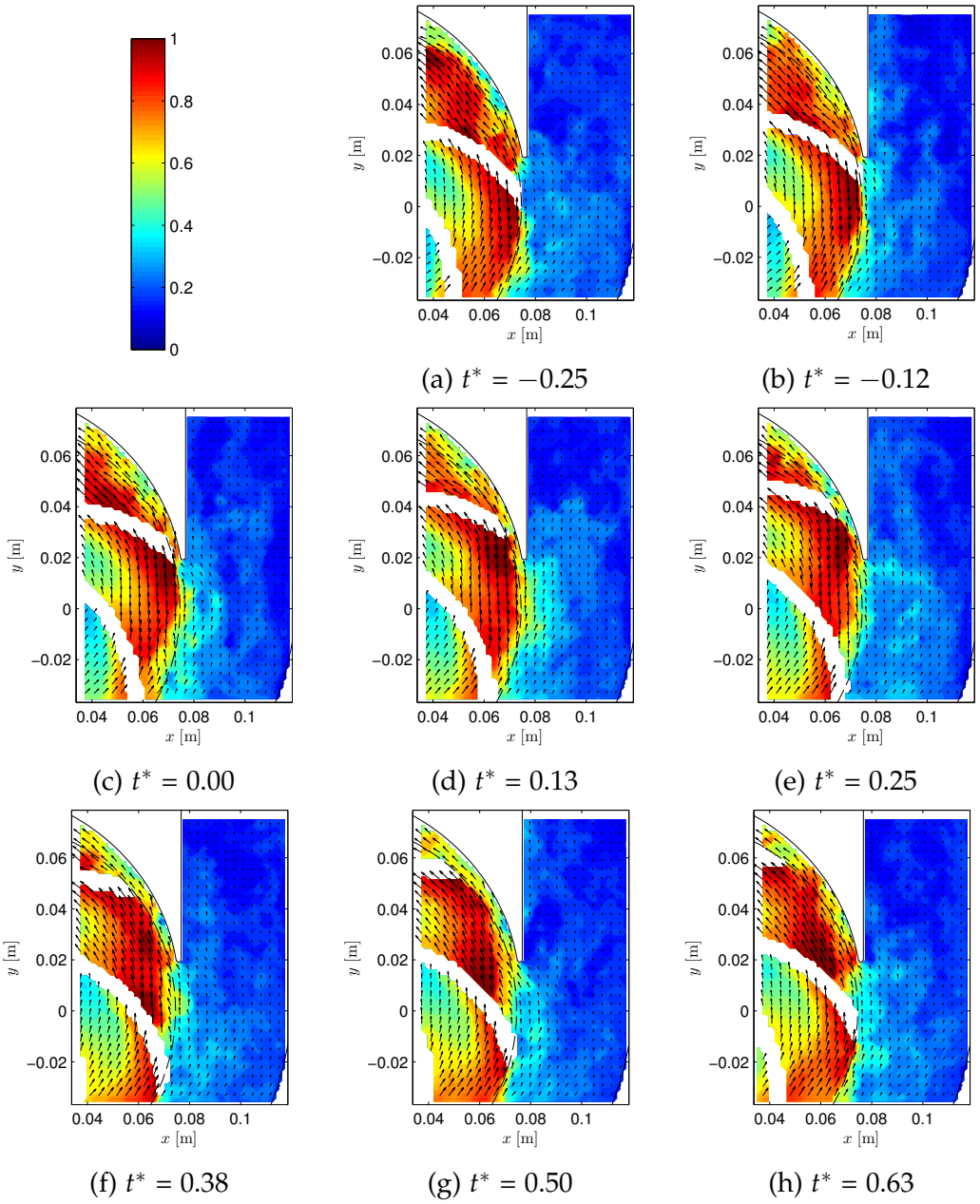

(a) $t^* = -0.25$ (b) $t^* = -0.12$

(c) $t^* = 0.00$ (d) $t^* = 0.13$ (e) $t^* = 0.25$

(f) $t^* = 0.38$ (g) $t^* = 0.50$ (h) $t^* = 0.63$

Figure B.1: Normalized instantaneous in-plane velocity magnitude u^* [-] at low M and 40 % Q_N. Every 3rd vector is represented

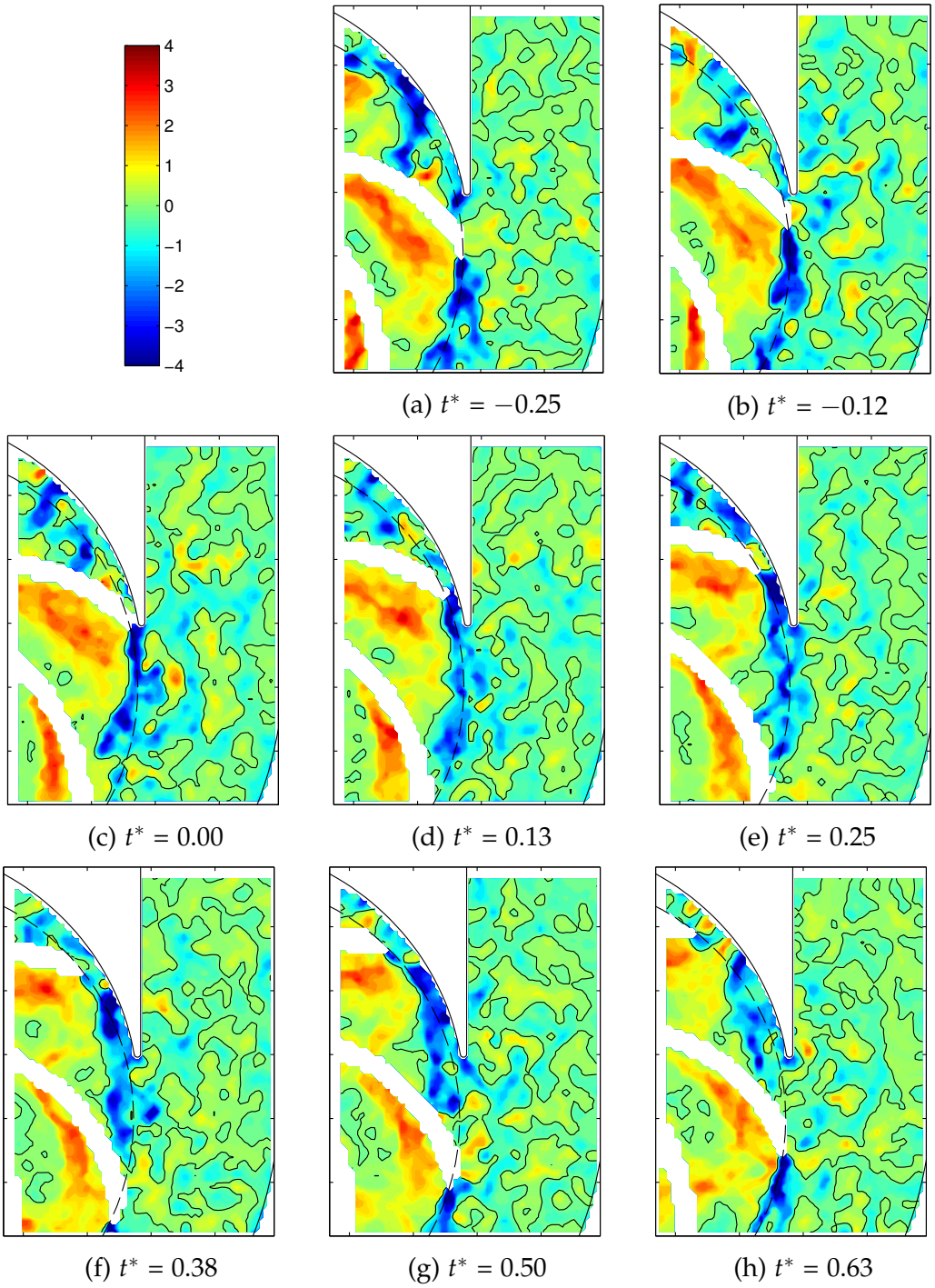

(a) $t^* = -0.25$ (b) $t^* = -0.12$

(c) $t^* = 0.00$ (d) $t^* = 0.13$ (e) $t^* = 0.25$

(f) $t^* = 0.38$ (g) $t^* = 0.50$ (h) $t^* = 0.63$

Figure B.2: Normalized instantaneous vorticity ω_z^* [-] at low M and 40 % Q_N

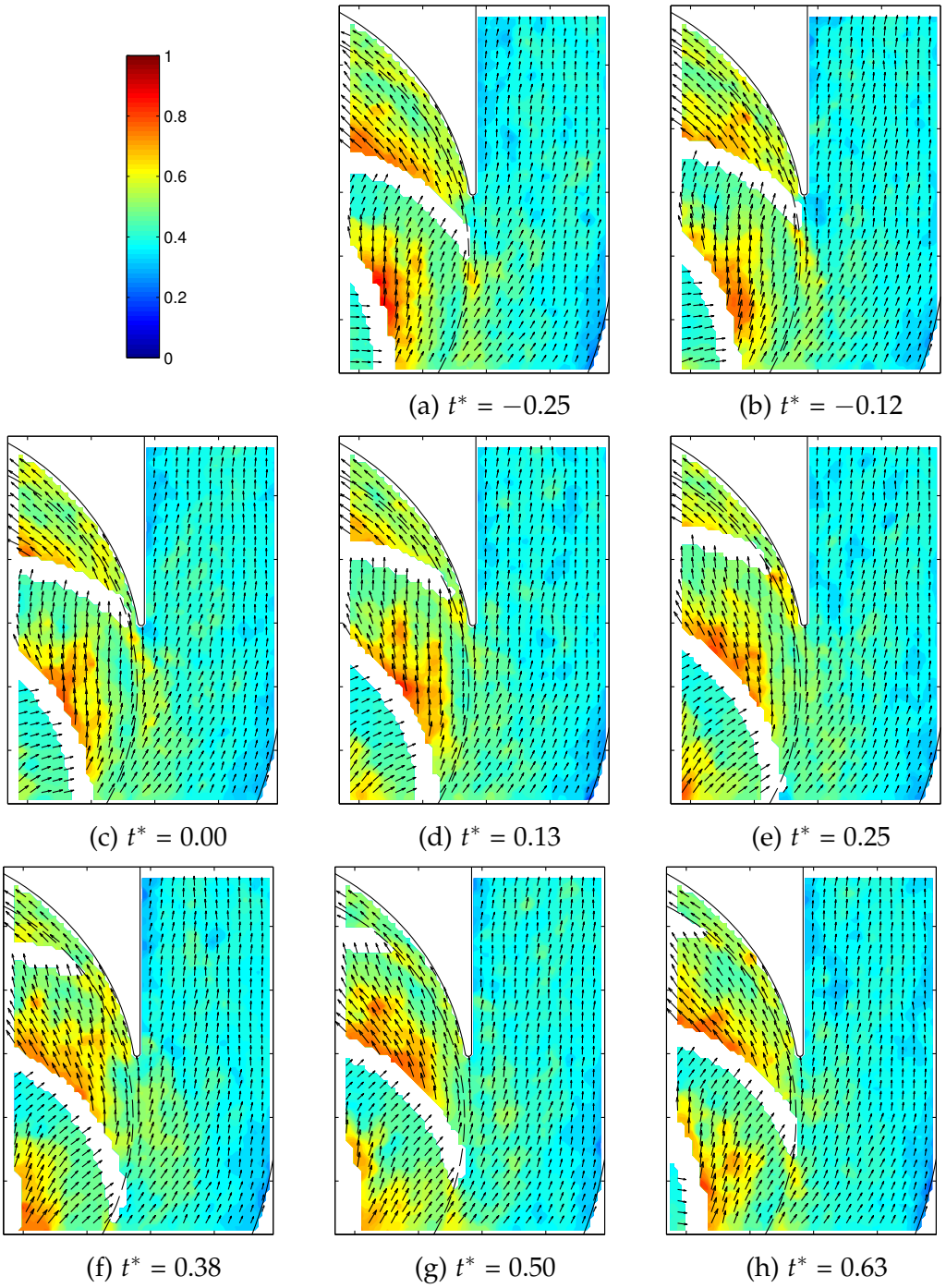

(a) $t^* = -0.25$ (b) $t^* = -0.12$

(c) $t^* = 0.00$ (d) $t^* = 0.13$ (e) $t^* = 0.25$

(f) $t^* = 0.38$ (g) $t^* = 0.50$ (h) $t^* = 0.63$

Figure B.3: Normalized instantaneous in-plane velocity magnitude u^* [-] at low M and Q_N. Every 3rd vector is represented

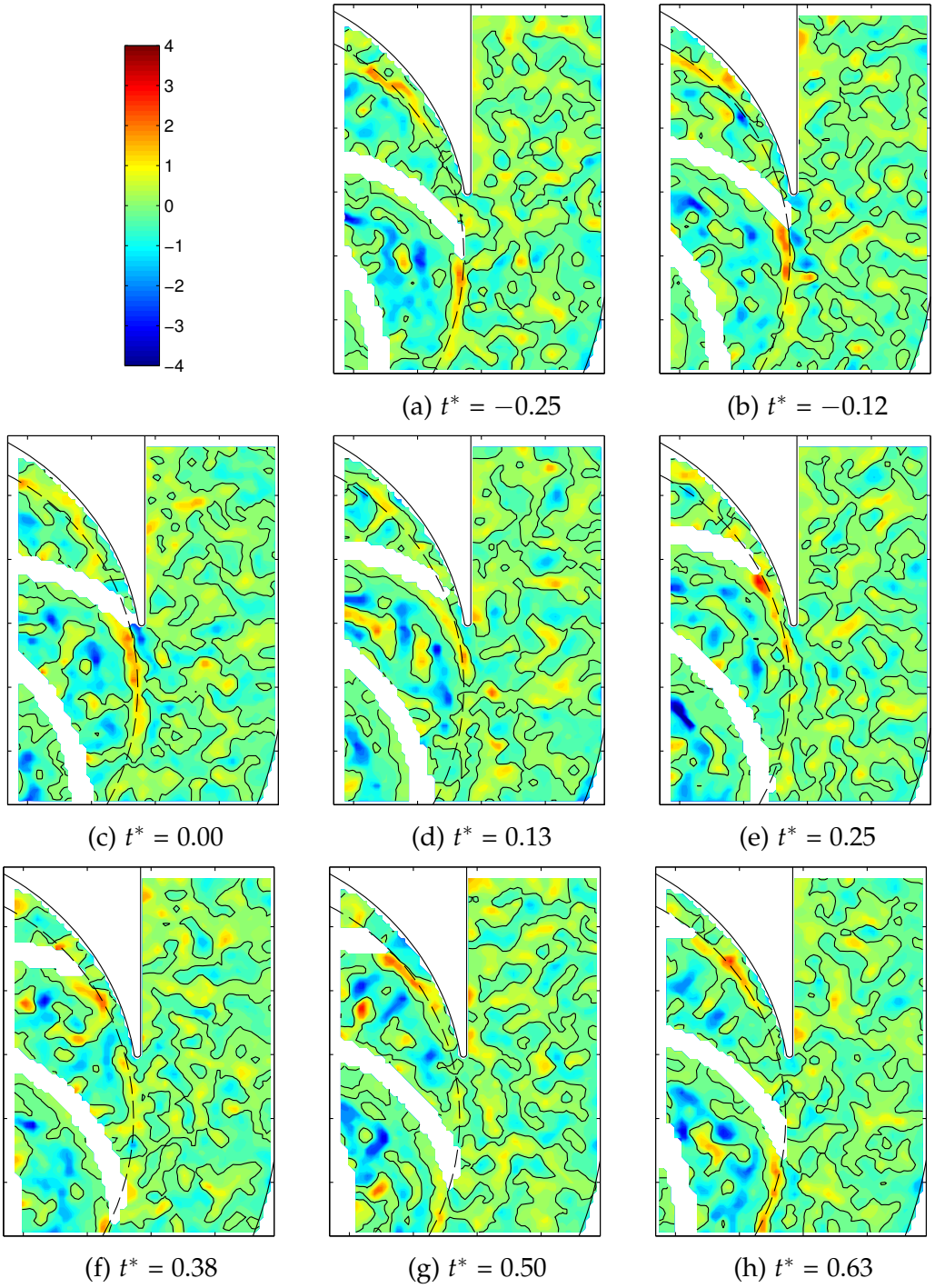

(a) $t^* = -0.25$ (b) $t^* = -0.12$

(c) $t^* = 0.00$ (d) $t^* = 0.13$ (e) $t^* = 0.25$

(f) $t^* = 0.38$ (g) $t^* = 0.50$ (h) $t^* = 0.63$

Figure B.4: Normalized instantaneous vorticity ω_z^* [-] at low M and Q_N

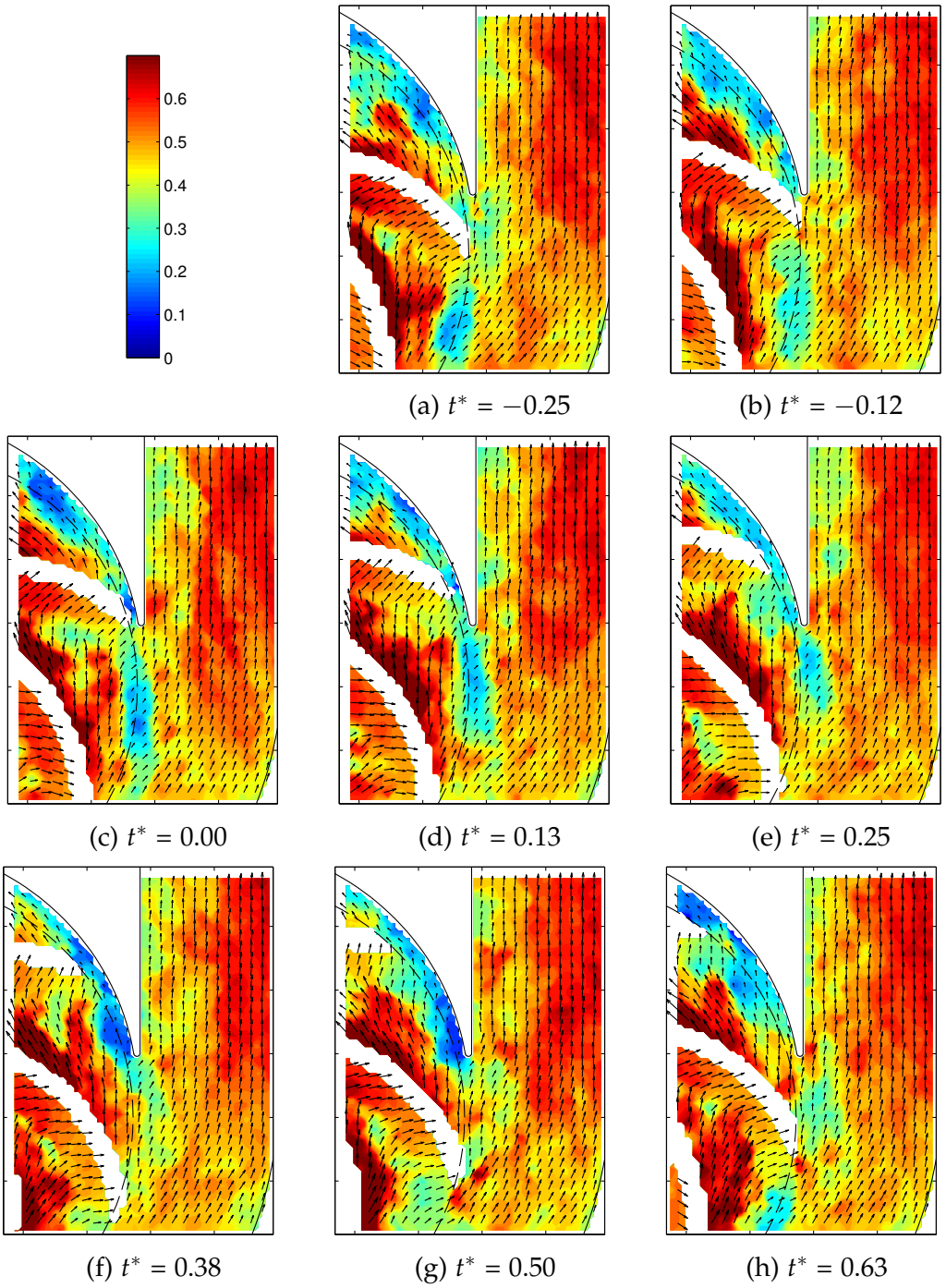

(a) $t^* = -0.25$ (b) $t^* = -0.12$

(c) $t^* = 0.00$ (d) $t^* = 0.13$ (e) $t^* = 0.25$

(f) $t^* = 0.38$ (g) $t^* = 0.50$ (h) $t^* = 0.63$

Figure B.5: Normalized instantaneous in-plane velocity magnitude u^* [-] at low M and 150 % Q_N. Every 3rd vector is represented

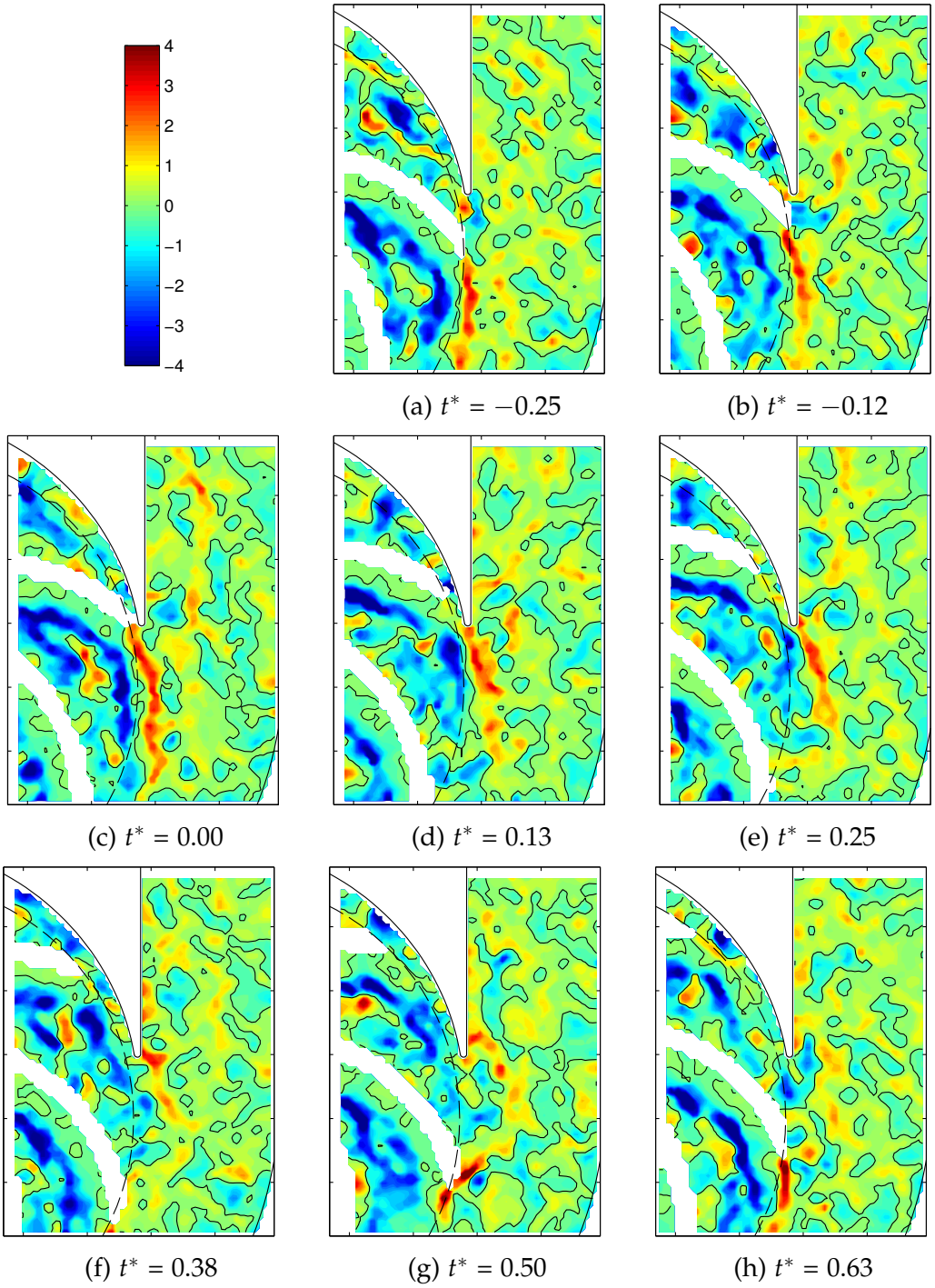

(a) $t^* = -0.25$ (b) $t^* = -0.12$

(c) $t^* = 0.00$ (d) $t^* = 0.13$ (e) $t^* = 0.25$

(f) $t^* = 0.38$ (g) $t^* = 0.50$ (h) $t^* = 0.63$

Figure B.6: Normalized instantaneous vorticity ω_z^* [-] at low M and 150 % Q_N

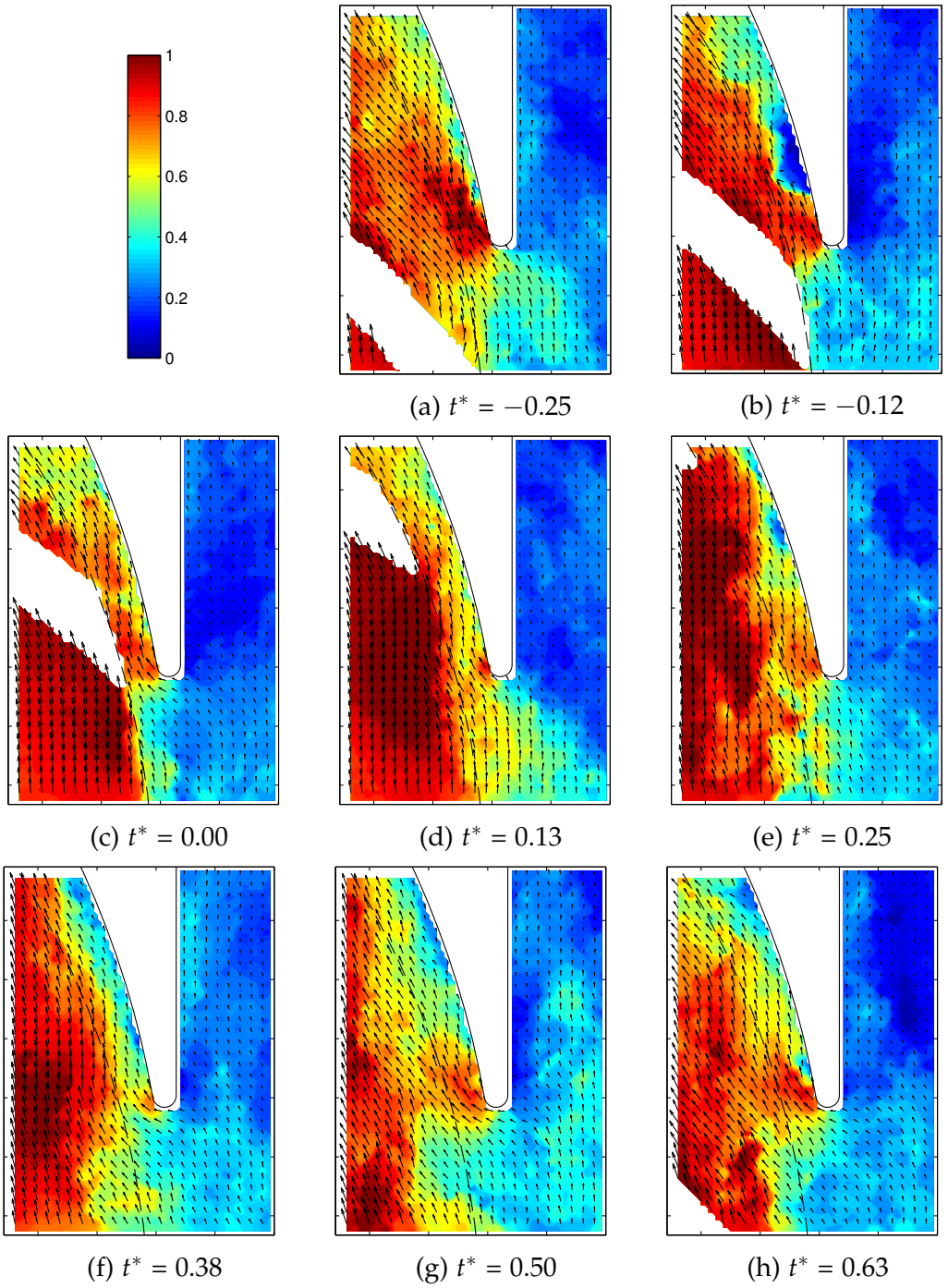

(a) $t^* = -0.25$ (b) $t^* = -0.12$

(c) $t^* = 0.00$ (d) $t^* = 0.13$ (e) $t^* = 0.25$

(f) $t^* = 0.38$ (g) $t^* = 0.50$ (h) $t^* = 0.63$

Figure B.7: Normalized instantaneous in-plane velocity magnitude u^* [-] at high M and 40 % Q_N. Every 3rd vector is represented

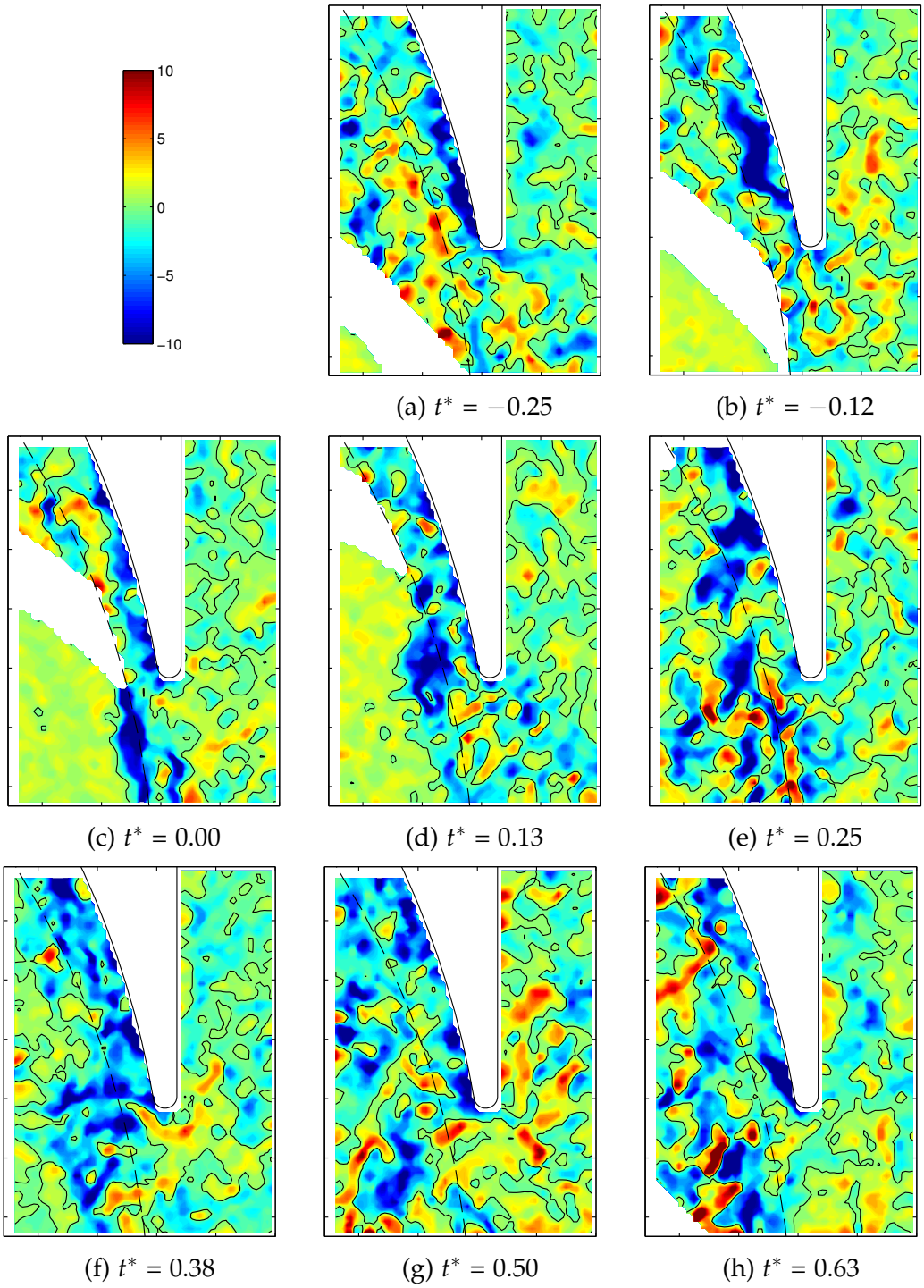

(a) $t^* = -0.25$ (b) $t^* = -0.12$

(c) $t^* = 0.00$ (d) $t^* = 0.13$ (e) $t^* = 0.25$

(f) $t^* = 0.38$ (g) $t^* = 0.50$ (h) $t^* = 0.63$

Figure B.8: Normalized instantaneous vorticity ω_z^* [-] at high M and 40 % Q_N

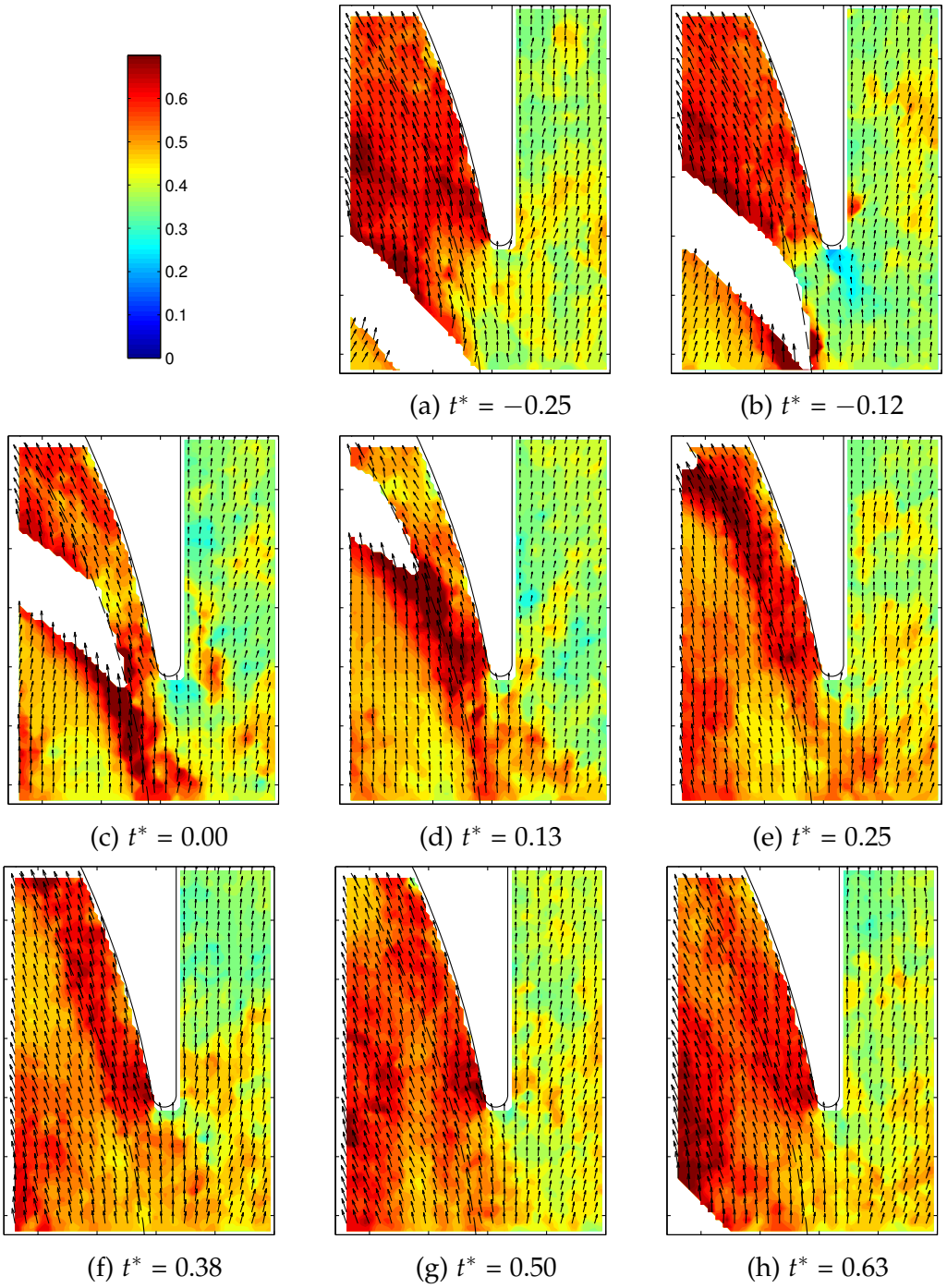

(a) $t^* = -0.25$ (b) $t^* = -0.12$

(c) $t^* = 0.00$ (d) $t^* = 0.13$ (e) $t^* = 0.25$

(f) $t^* = 0.38$ (g) $t^* = 0.50$ (h) $t^* = 0.63$

Figure B.9: Normalized instantaneous in-plane velocity magnitude u^* [-] at high M and Q_N. Every 3rd vector is represented

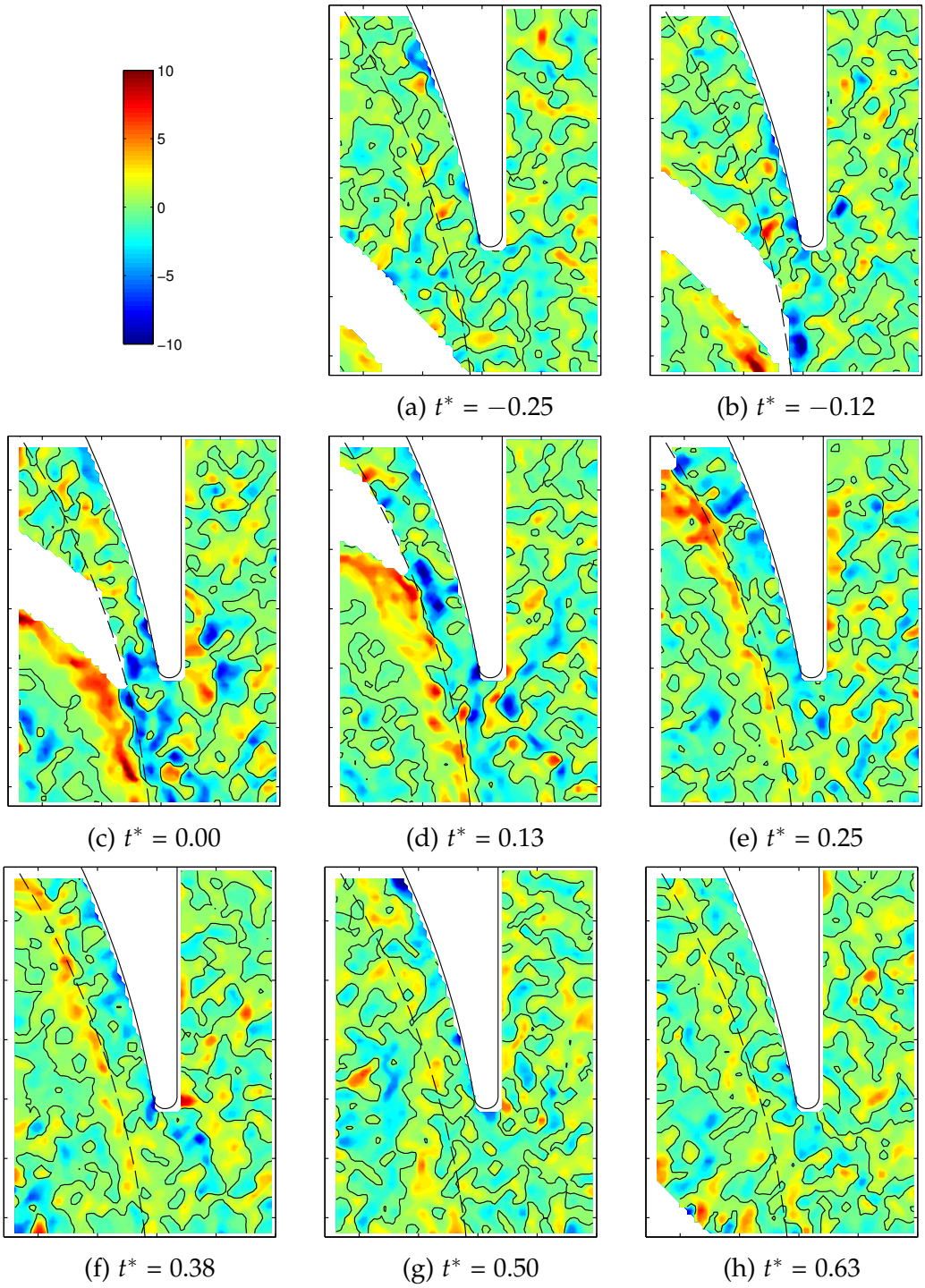

(a) $t^* = -0.25$ (b) $t^* = -0.12$

(c) $t^* = 0.00$ (d) $t^* = 0.13$ (e) $t^* = 0.25$

(f) $t^* = 0.38$ (g) $t^* = 0.50$ (h) $t^* = 0.63$

Figure B.10: Normalized instantaneous vorticity ω_z^* [-] at high M and Q_N

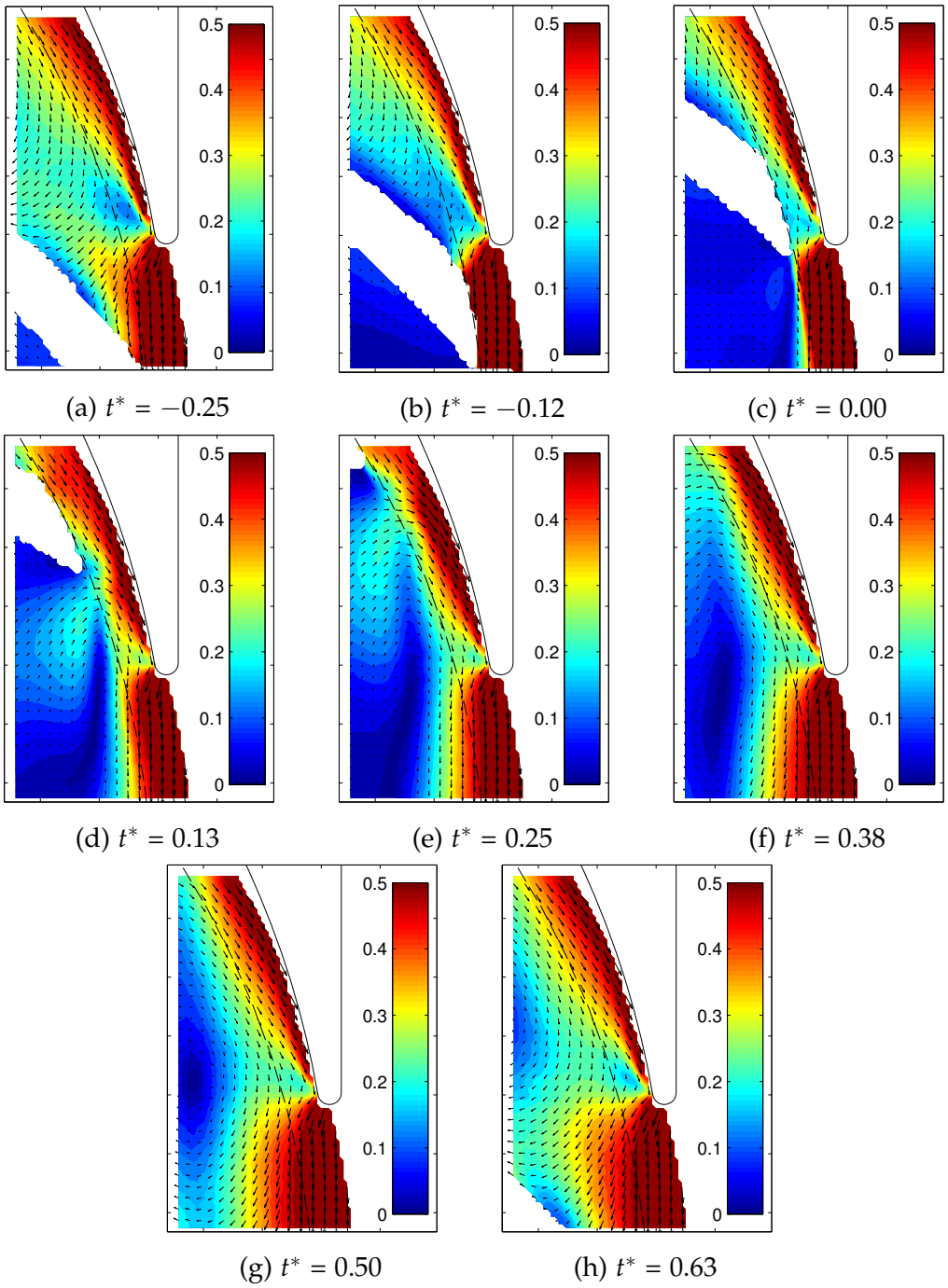

(a) $t^* = -0.25$ (b) $t^* = -0.12$ (c) $t^* = 0.00$

(d) $t^* = 0.13$ (e) $t^* = 0.25$ (f) $t^* = 0.38$

(g) $t^* = 0.50$ (h) $t^* = 0.63$

Figure B.11: Normalized phase-averaged in-plane relative velocity magnitude W^* [-] at high M and 40 % Q_N. Region shown up to 1.05·r_{tip}. Every 3rd vector is represented

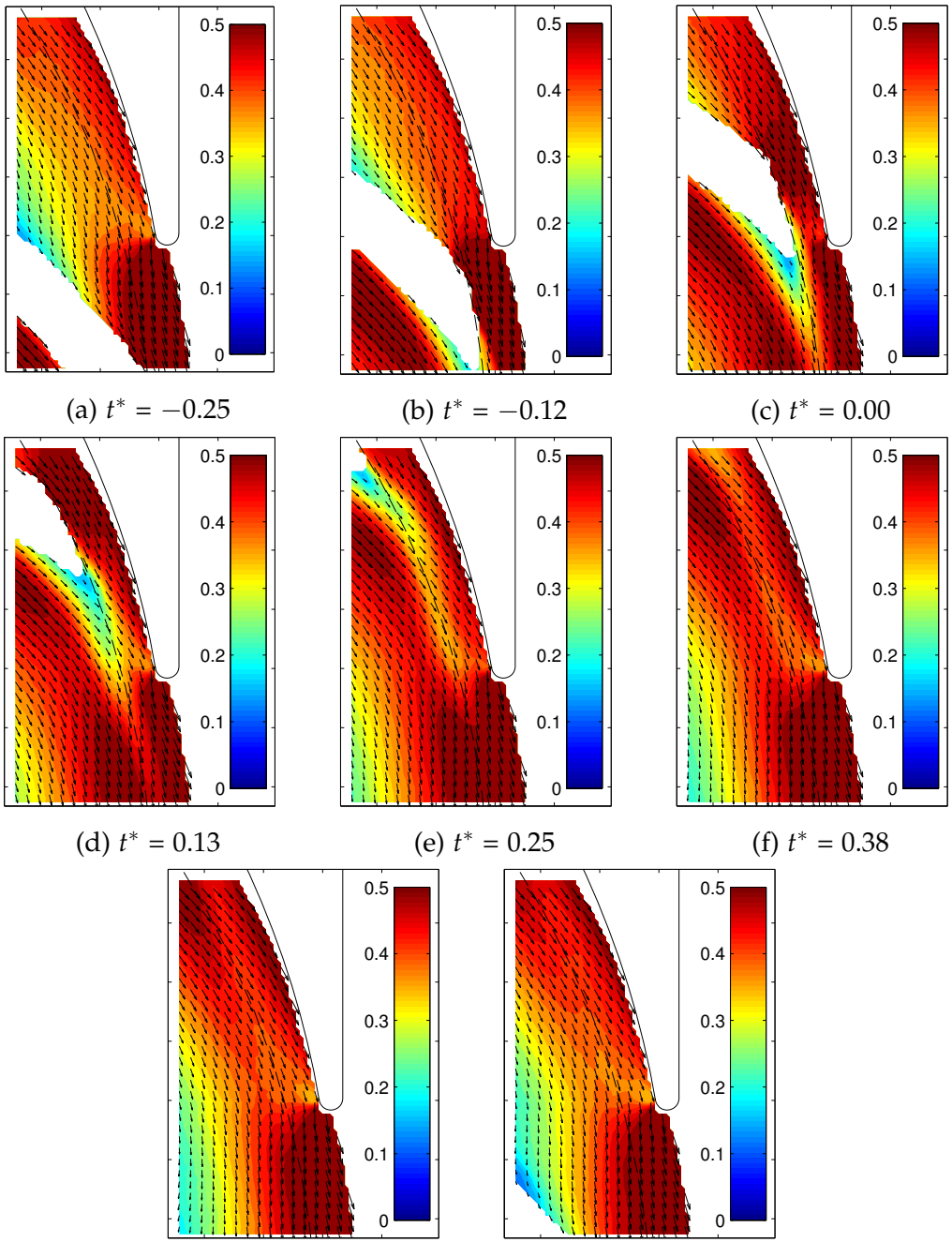

(a) $t^* = -0.25$ (b) $t^* = -0.12$ (c) $t^* = 0.00$

(d) $t^* = 0.13$ (e) $t^* = 0.25$ (f) $t^* = 0.38$

(g) $t^* = 0.50$ (h) $t^* = 0.63$

Figure B.12: Normalized phase-averaged in-plane relative velocity magnitude W^* [-] at high M and Q_N. Region shown up to $1.05 \cdot r_{tip}$. Every 3rd vector is represented

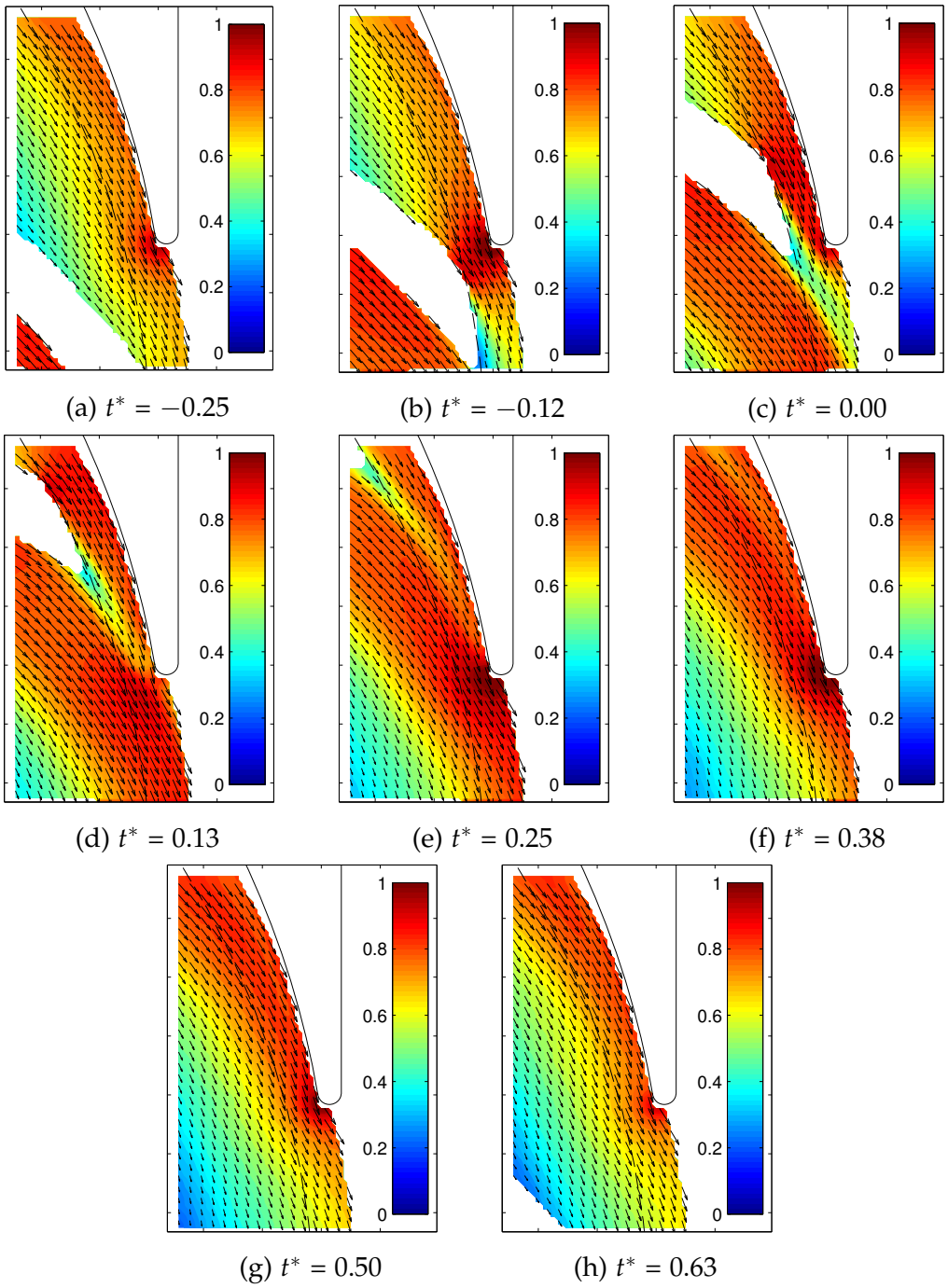

(a) $t^* = -0.25$ (b) $t^* = -0.12$ (c) $t^* = 0.00$

(d) $t^* = 0.13$ (e) $t^* = 0.25$ (f) $t^* = 0.38$

(g) $t^* = 0.50$ (h) $t^* = 0.63$

Figure B.13: Normalized phase-averaged in-plane relative velocity magnitude W^* [-] at high M and 150 % Q_N. Region shown up to 1.05·r_{tip}. Every 3rd vector is represented

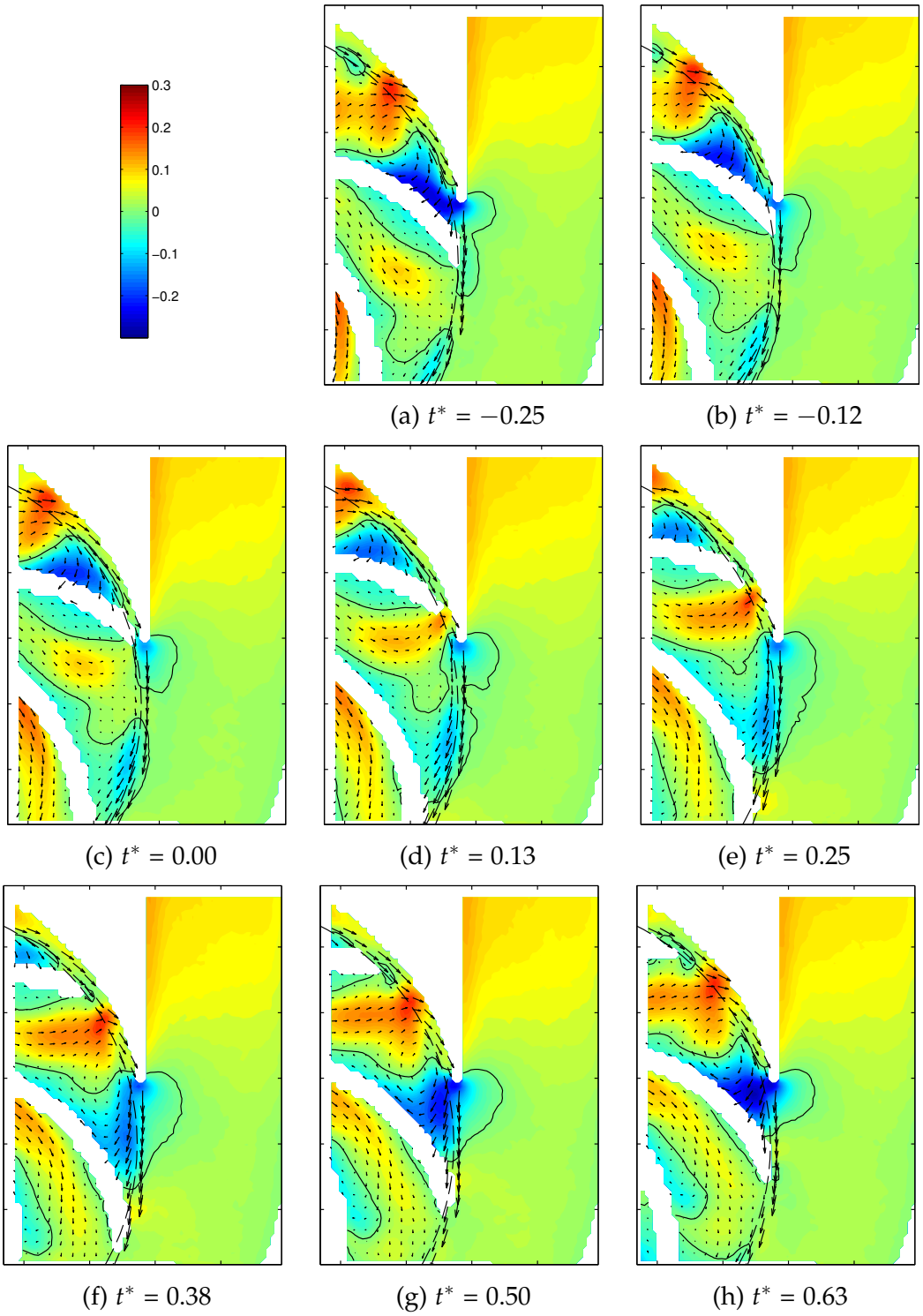

(a) $t^* = -0.25$ (b) $t^* = -0.12$

(c) $t^* = 0.00$ (d) $t^* = 0.13$ (e) $t^* = 0.25$

(f) $t^* = 0.38$ (g) $t^* = 0.50$ (h) $t^* = 0.63$

Figure B.14: Normalized radial velocity contour plot u_r^* [-] with relative velocity vectors W^* at low M and 40 % Q_N. Every 3rd vector is represented. Black contour at $u_r = 0$

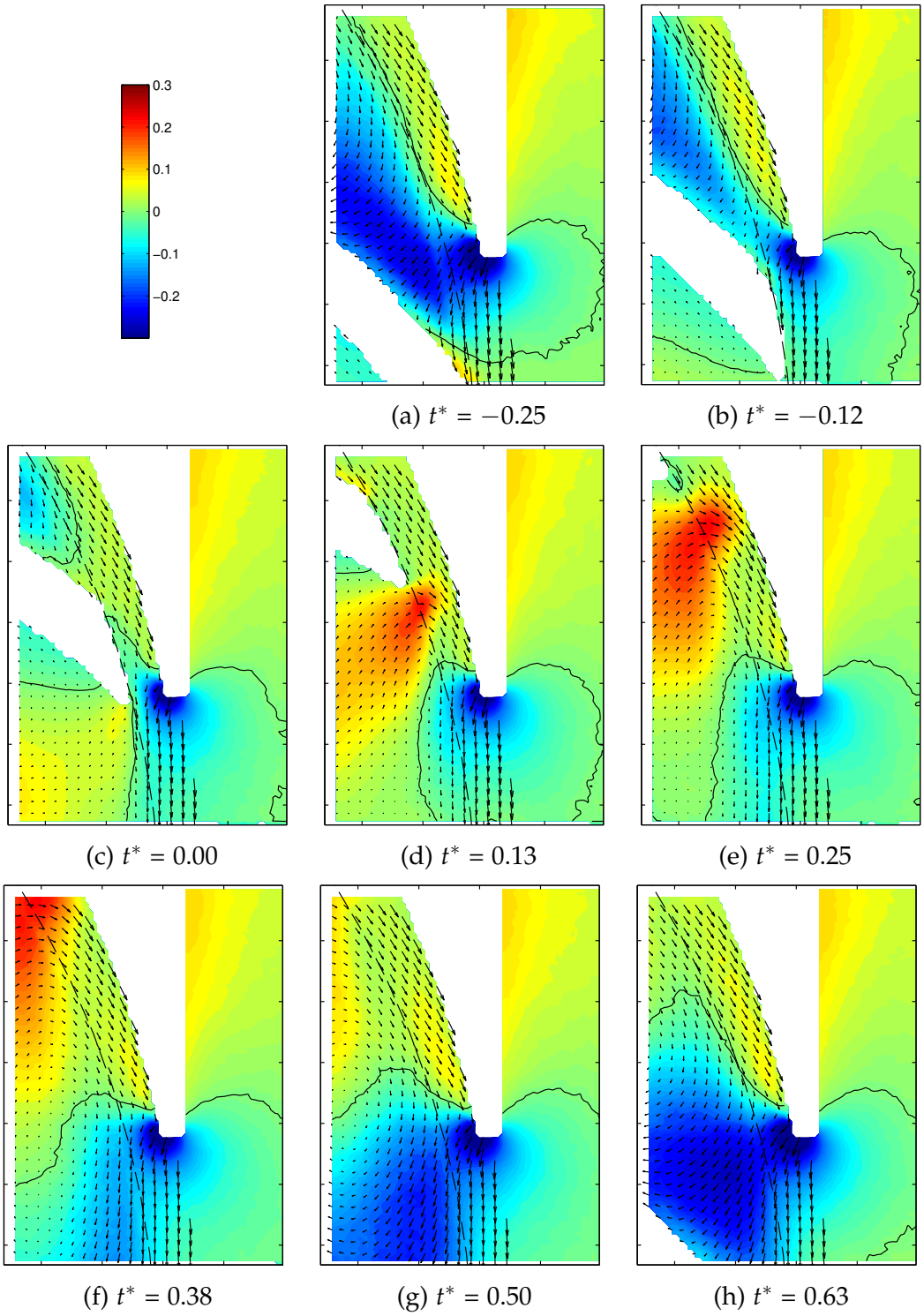

(a) $t^* = -0.25$ (b) $t^* = -0.12$

(c) $t^* = 0.00$ (d) $t^* = 0.13$ (e) $t^* = 0.25$

(f) $t^* = 0.38$ (g) $t^* = 0.50$ (h) $t^* = 0.63$

Figure B.15: Normalized radial velocity contour plot u_r^* [-] with relative velocity vectors W^* at high M and 40 % Q_N. Every 3rd vector is represented. Black contour at $u_r = 0$

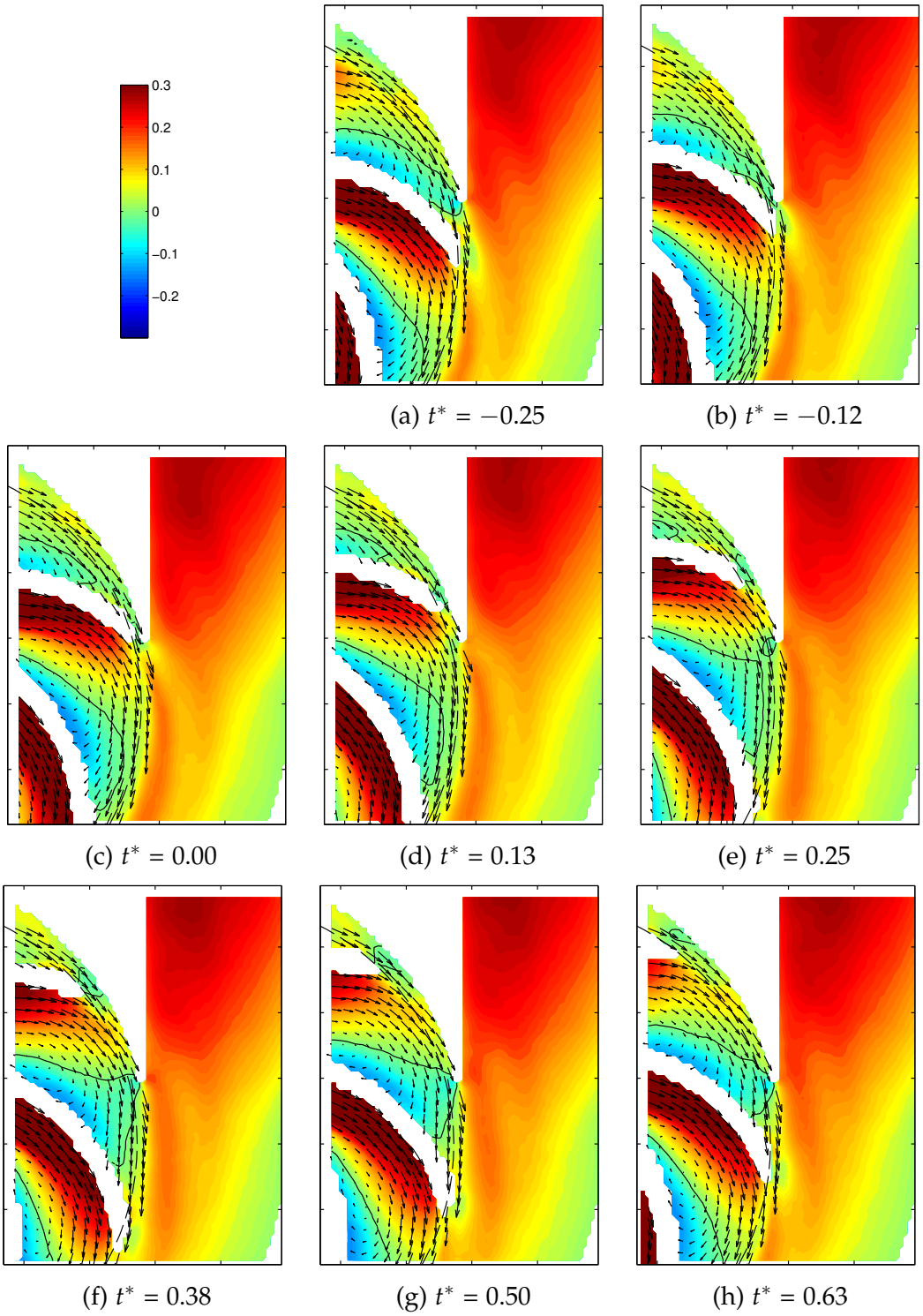

(a) $t^* = -0.25$ (b) $t^* = -0.12$

(c) $t^* = 0.00$ (d) $t^* = 0.13$ (e) $t^* = 0.25$

(f) $t^* = 0.38$ (g) $t^* = 0.50$ (h) $t^* = 0.63$

Figure B.16: Normalized radial velocity contour plot u_r^* [-] with relative velocity vectors W^* at low M and Q_N. Every 3rd vector is represented. Black contour at $u_r = 0$

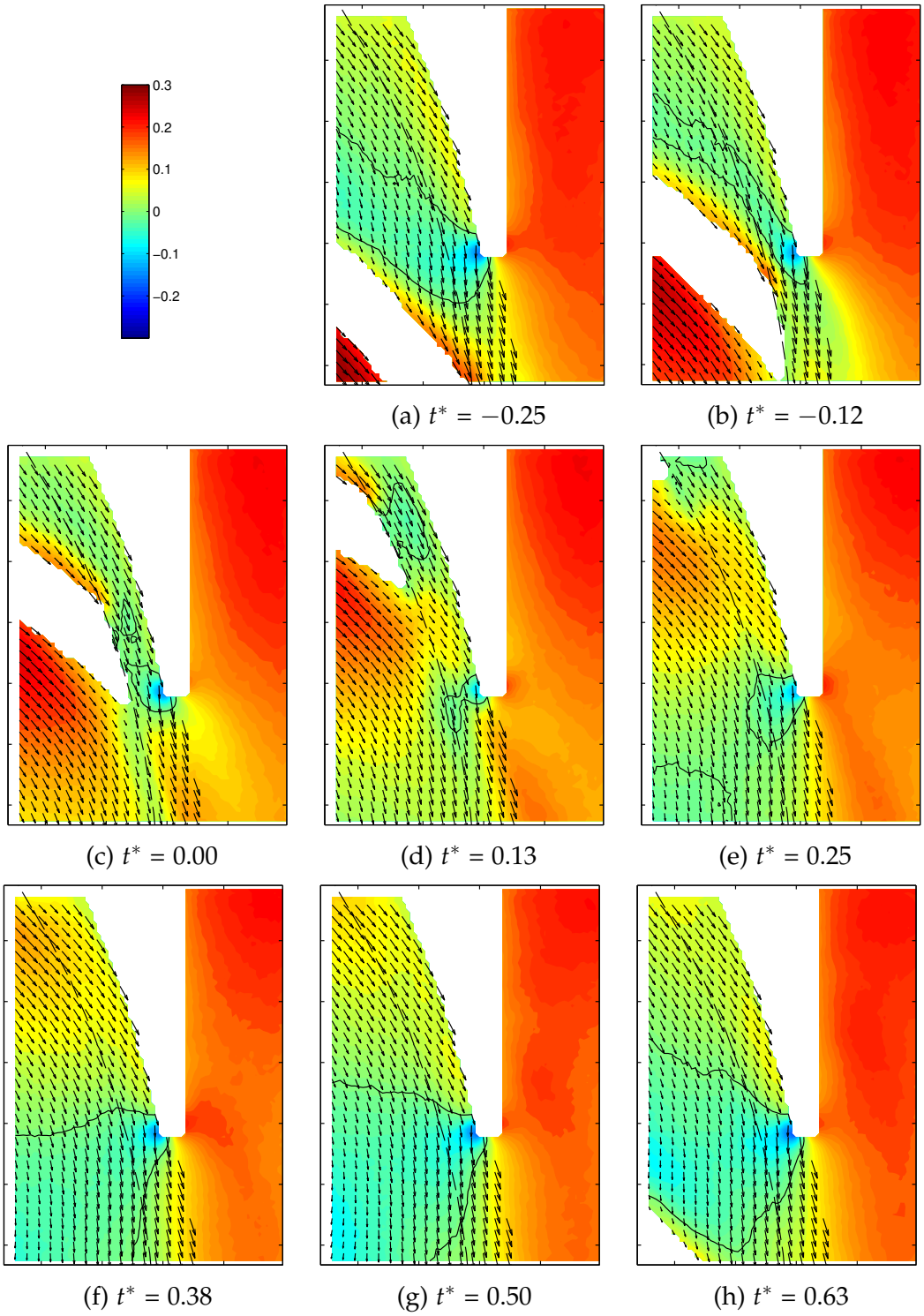

(a) $t^* = -0.25$ (b) $t^* = -0.12$

(c) $t^* = 0.00$ (d) $t^* = 0.13$ (e) $t^* = 0.25$

(f) $t^* = 0.38$ (g) $t^* = 0.50$ (h) $t^* = 0.63$

Figure B.17: Normalized radial velocity contour plot u_r^* [-] with relative velocity vectors W^* at high M and Q_N. Every 3rd vector is represented. Black contour at $u_r = 0$

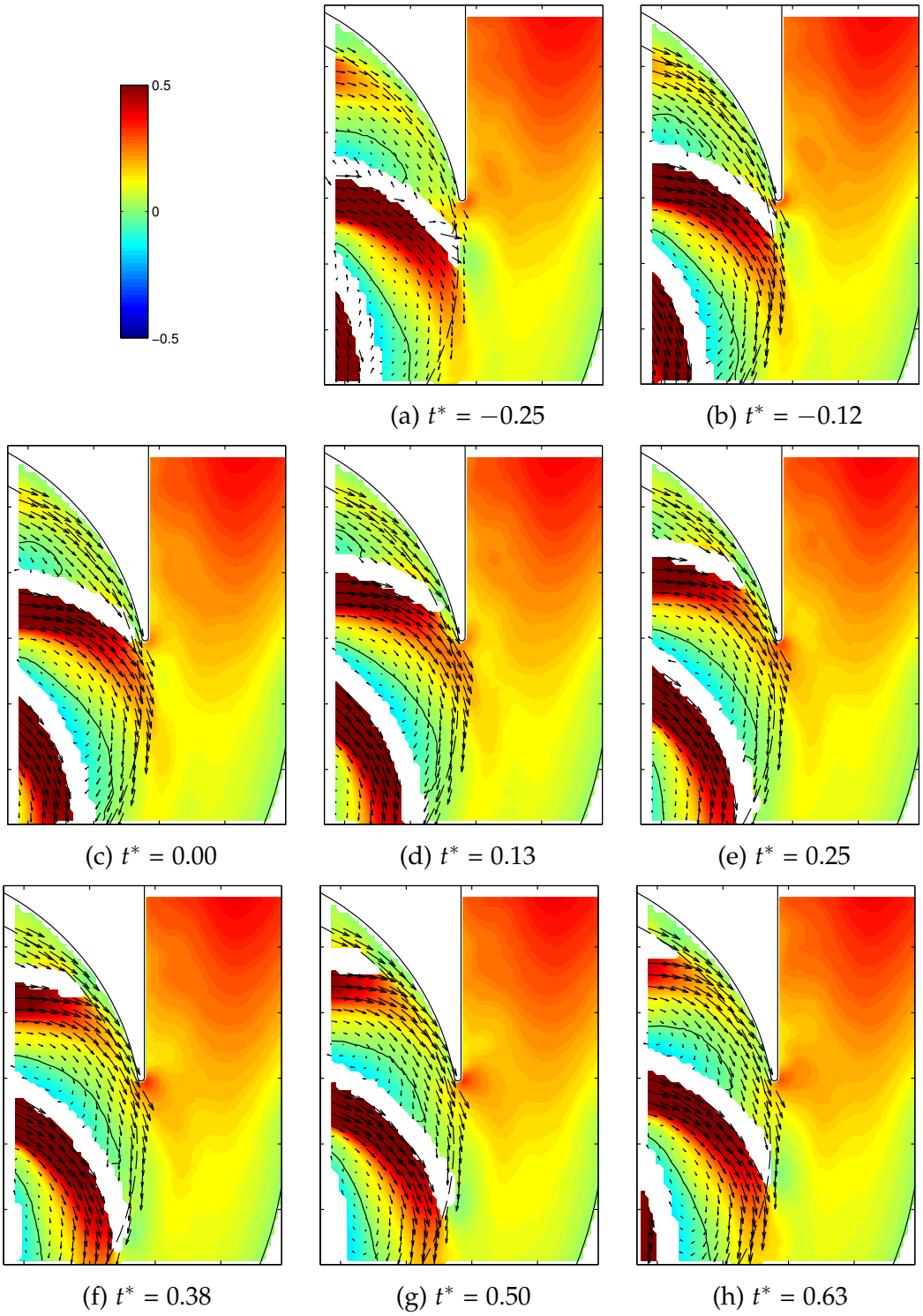

(a) $t^* = -0.25$ (b) $t^* = -0.12$

(c) $t^* = 0.00$ (d) $t^* = 0.13$ (e) $t^* = 0.25$

(f) $t^* = 0.38$ (g) $t^* = 0.50$ (h) $t^* = 0.63$

Figure B.18: Normalized radial velocity contour plot u_r^* [-] with relative velocity vectors W^* at low M and 150 % Q_N. Every 3rd vector is represented. Black contour at $u_r = 0$

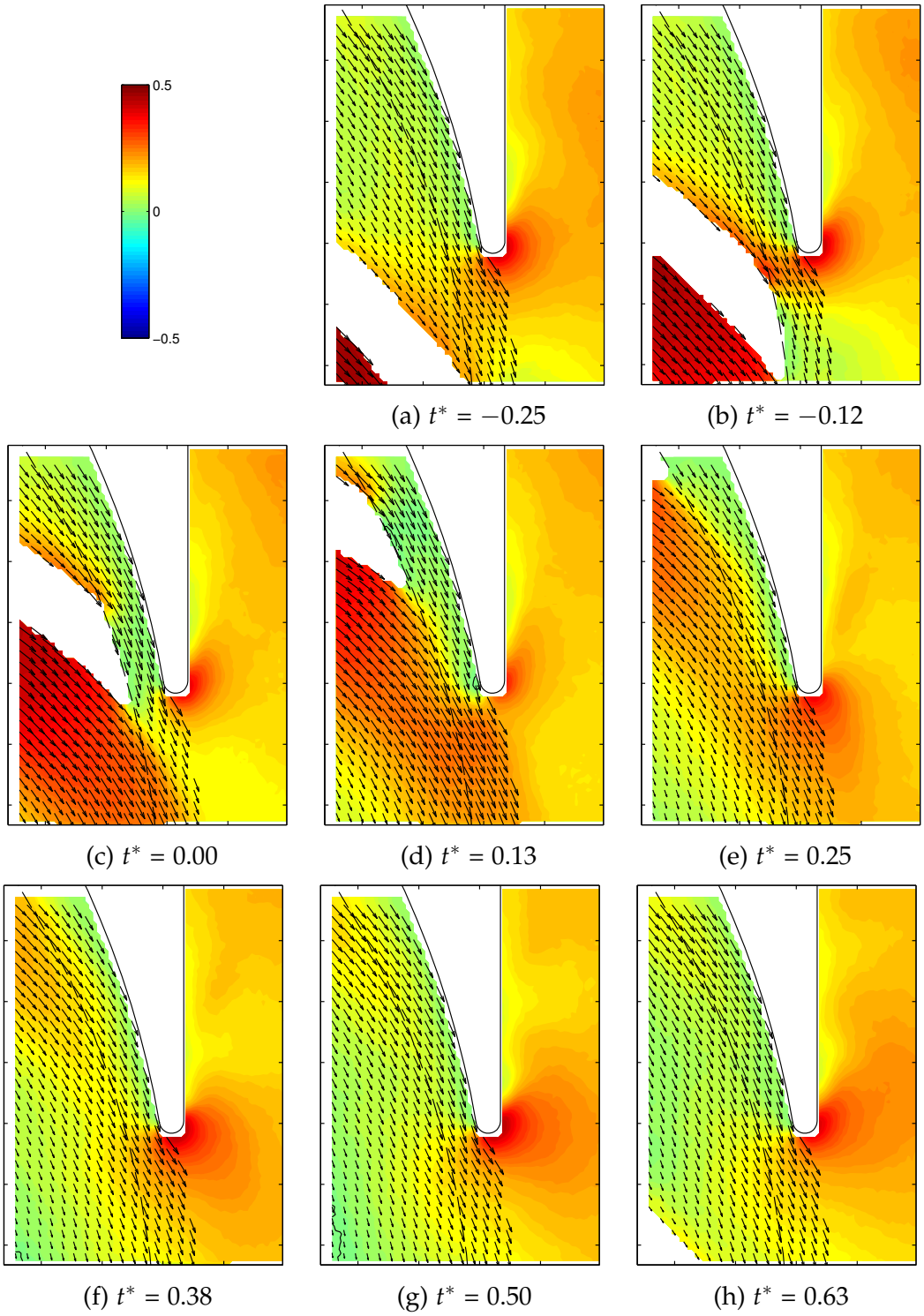

(a) $t^* = -0.25$ (b) $t^* = -0.12$

(c) $t^* = 0.00$ (d) $t^* = 0.13$ (e) $t^* = 0.25$

(f) $t^* = 0.38$ (g) $t^* = 0.50$ (h) $t^* = 0.63$

Figure B.19: Normalized radial velocity contour plot u_r^* [-] with relative velocity vectors W^* at high M and 150 % Q_N. Every 3rd vector is represented. Black contour at $u_r = 0$

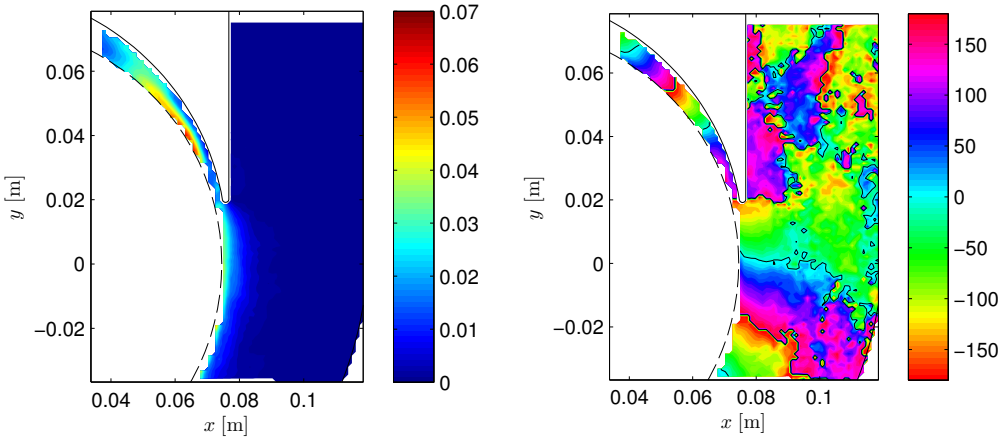

(a) Amplitude [-] at $2f_{BP}$ (b) Phase [°] at $2f_{BP}$

Figure B.20: Amplitude and phase distribution at $2f_{BP}$ of U^* [-] at low M and 40 % Q_N

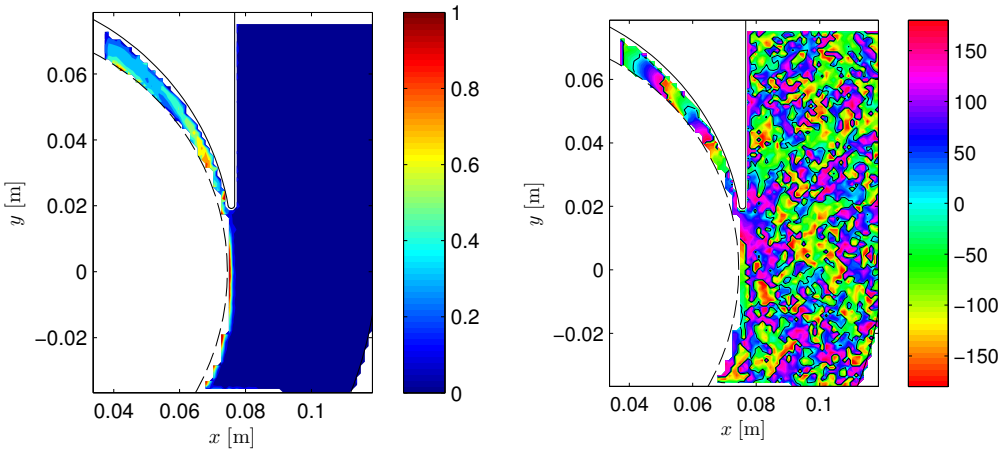

(a) Amplitude [-] at $2f_{BP}$ (b) Phase [°] at $2f_{BP}$

Figure B.21: Amplitude and phase distribution at $2f_{BP}$ of ω_z^* [-] at low M and 40 % Q_N

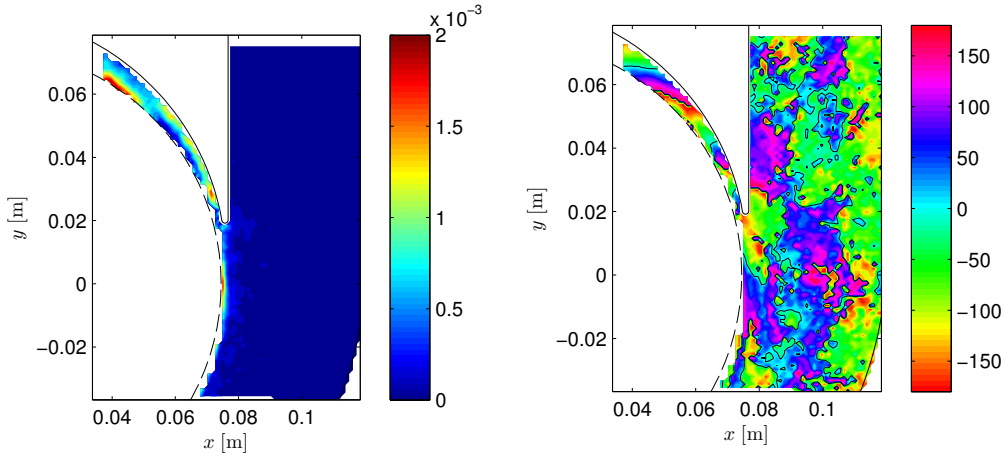

(a) Amplitude [-] at $2f_{BP}$

(b) Phase [°] at $2f_{BP}$

Figure B.22: Amplitude and phase distribution at $2f_{BP}$ of k^*_{2D} [-] at low M and 40 % Q_N

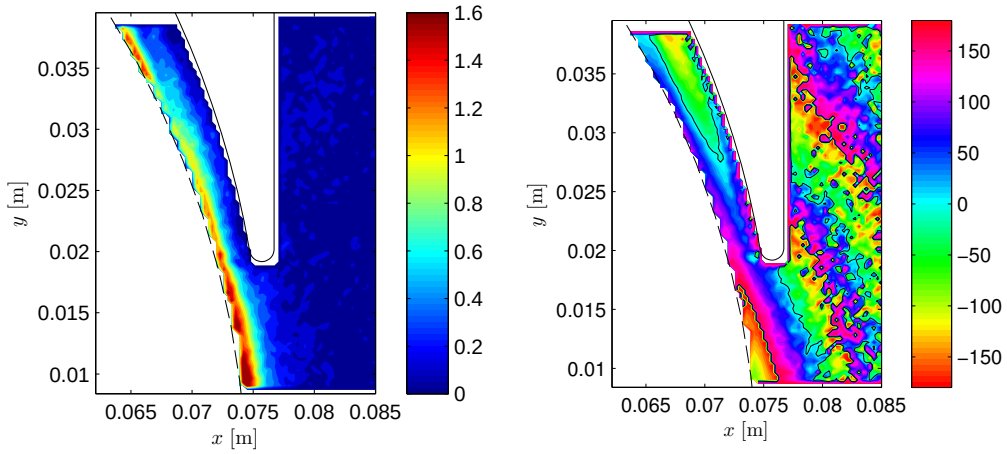

(a) Amplitude [-] at $2f_{BP}$

(b) Phase [°] at $2f_{BP}$

Figure B.23: Amplitude and phase distribution at $2f_{BP}$ of ω^*_z [-] at high M and Q_N

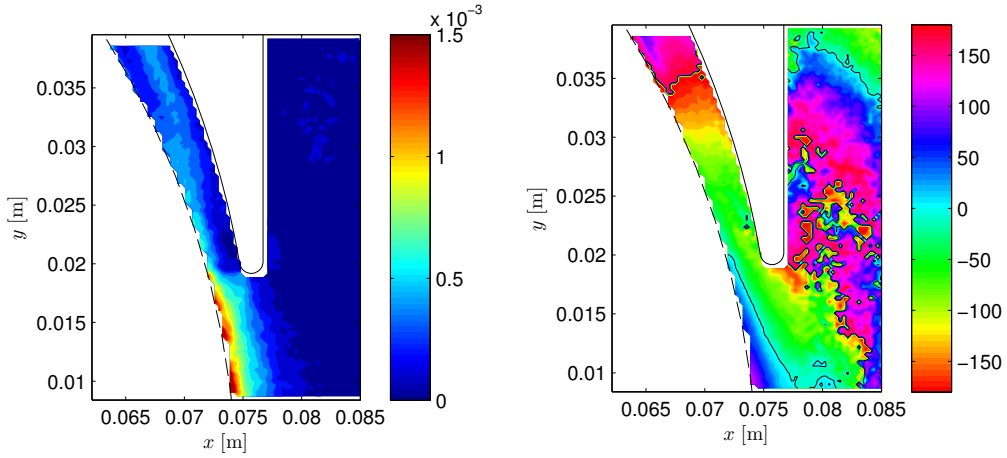

(a) Amplitude [-] at $2f_{BP}$ (b) Phase [°] at $2f_{BP}$

Figure B.24: Amplitude and phase distribution at $2f_{BP}$ of k^*_{2D} [-] at high M and Q_N

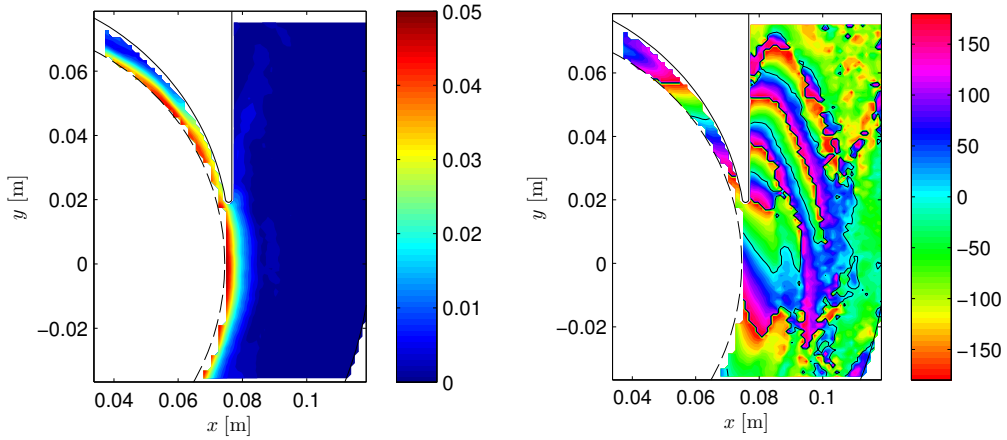

(a) Amplitude [-] at $2f_{BP}$ (b) Phase [°] at $2f_{BP}$

Figure B.25: Amplitude and phase distribution at $2f_{BP}$ of U^* [-] at low M and Q_N

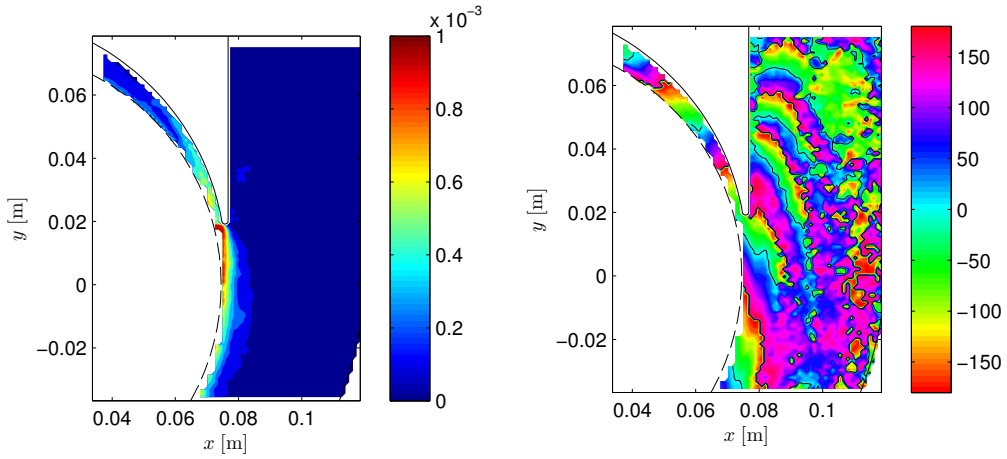

(a) Amplitude at $2f_{\mathrm{BP}}$

(b) Phase [°] at $2f_{\mathrm{BP}}$

Figure B.26: Amplitude and phase distribution at $2f_{\mathrm{BP}}$ of k^*_{2D} [-] at low M and Q_{N}

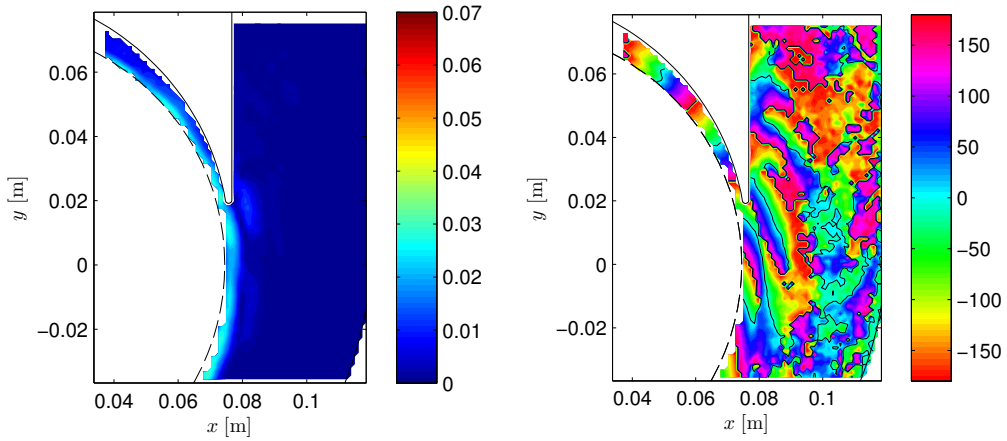

(a) Amplitude [-] at $3f_{\mathrm{BP}}$

(b) Phase [°] at $3f_{\mathrm{BP}}$

Figure B.27: Amplitude and phase distribution at $3f_{\mathrm{BP}}$ of U^* [-] at low M and 150 % Q_{N}

C Pressure results

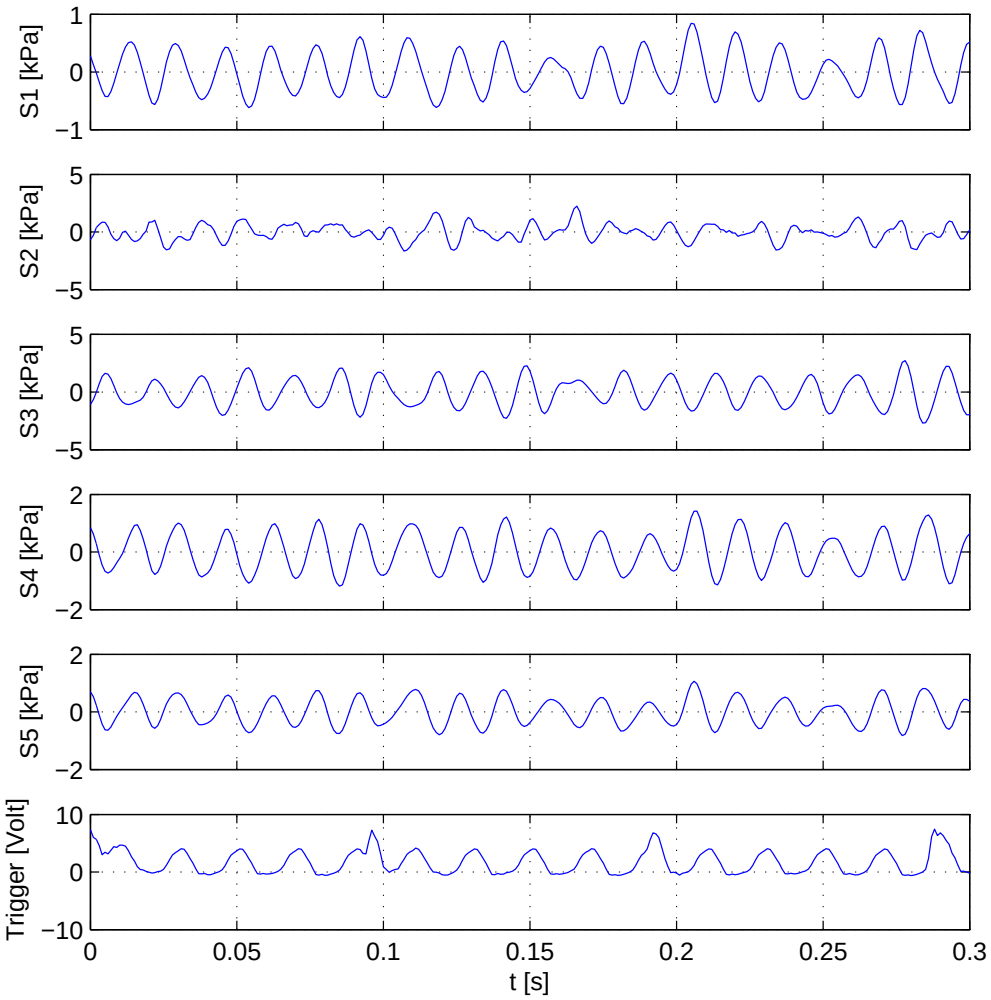

Figure C.1: Instantaneous pressure time signal at transparent pump volute at 40 % Q_N

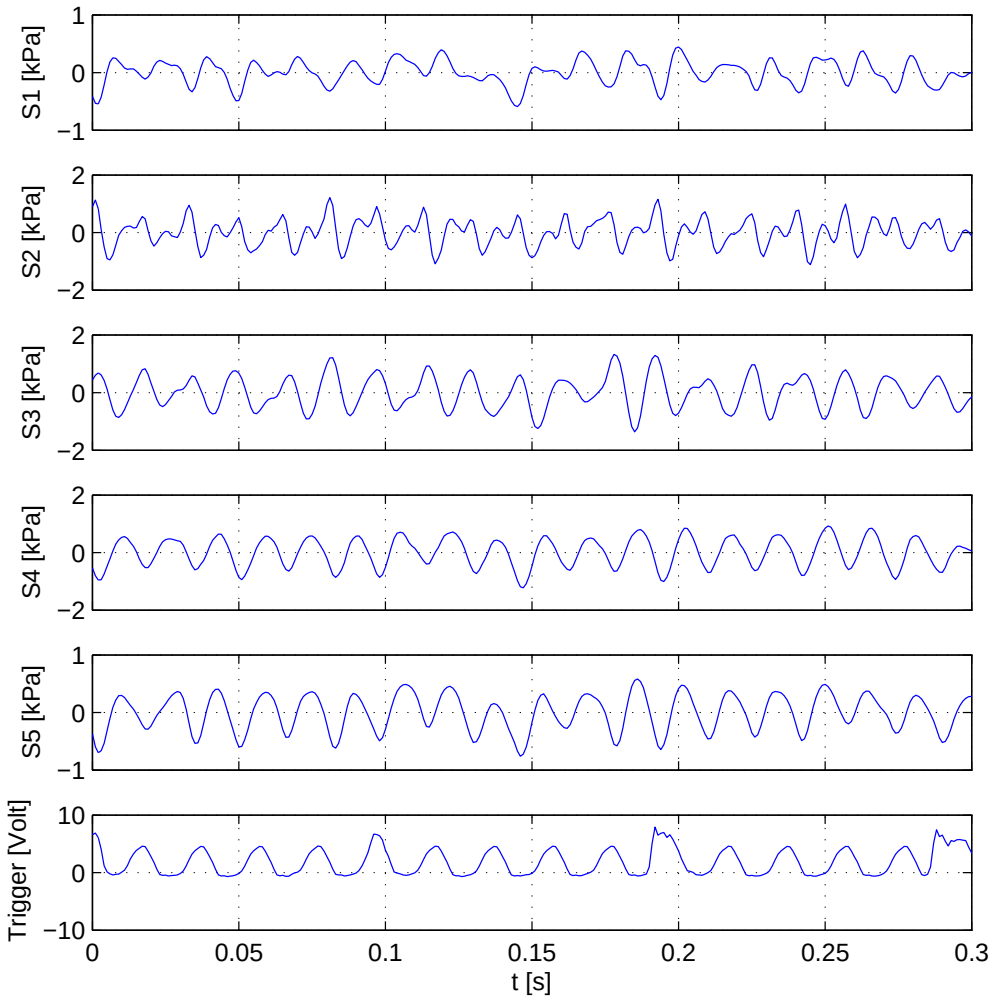

Figure C.2: Instantaneous pressure time signal at transparent pump volute at Q_N

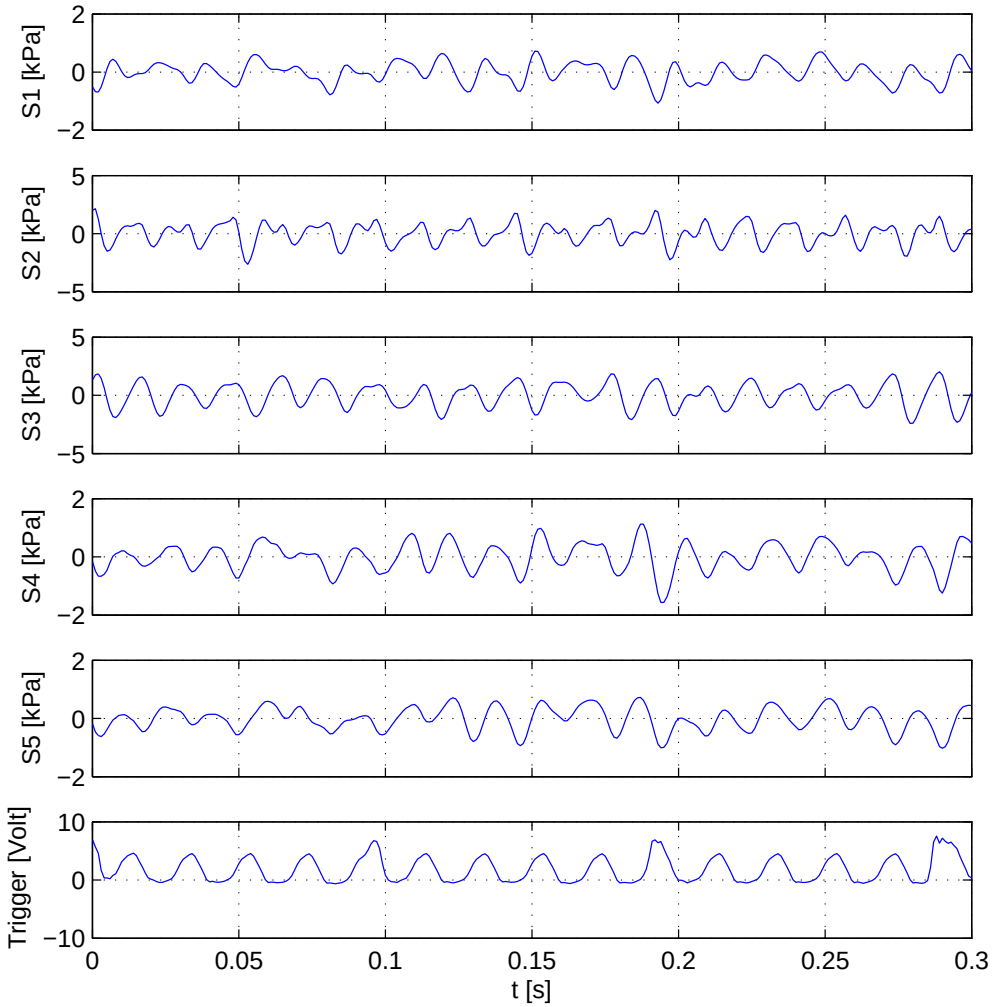

Figure C.3: Instantaneous pressure time signal at transparent pump volute at 150 % Q_N

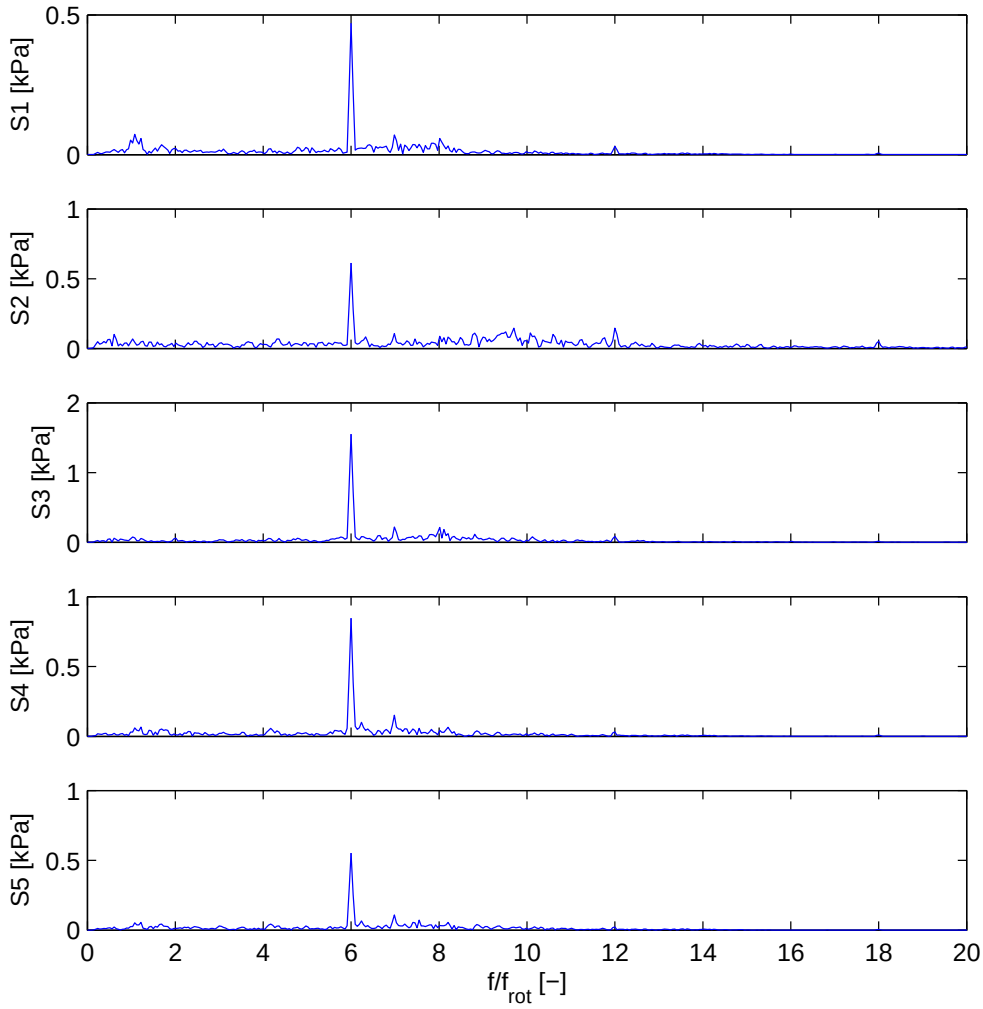

Figure C.4: Spectra of instantaneous time signal at transparent pump volute at 40 %Q_N

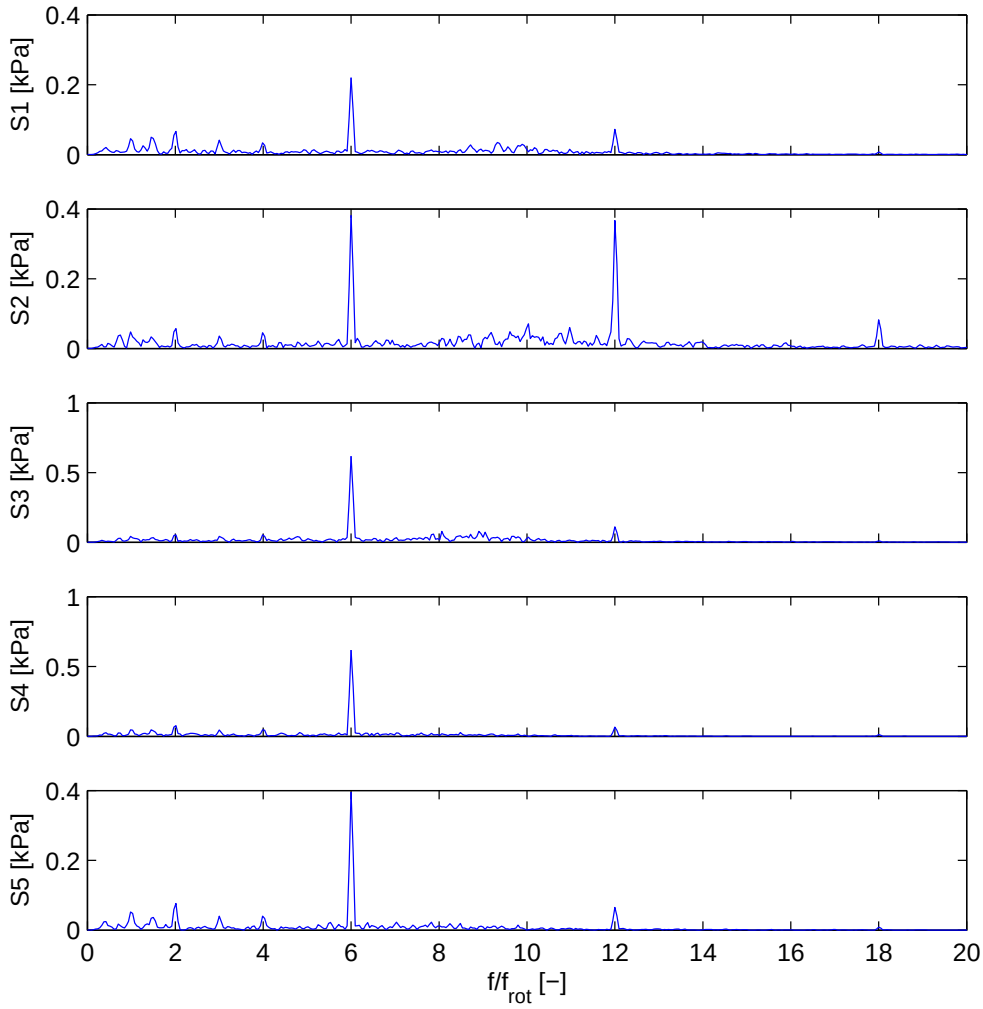

Figure C.5: Spectra of instantaneous time signal at transparent pump volute at Q_N

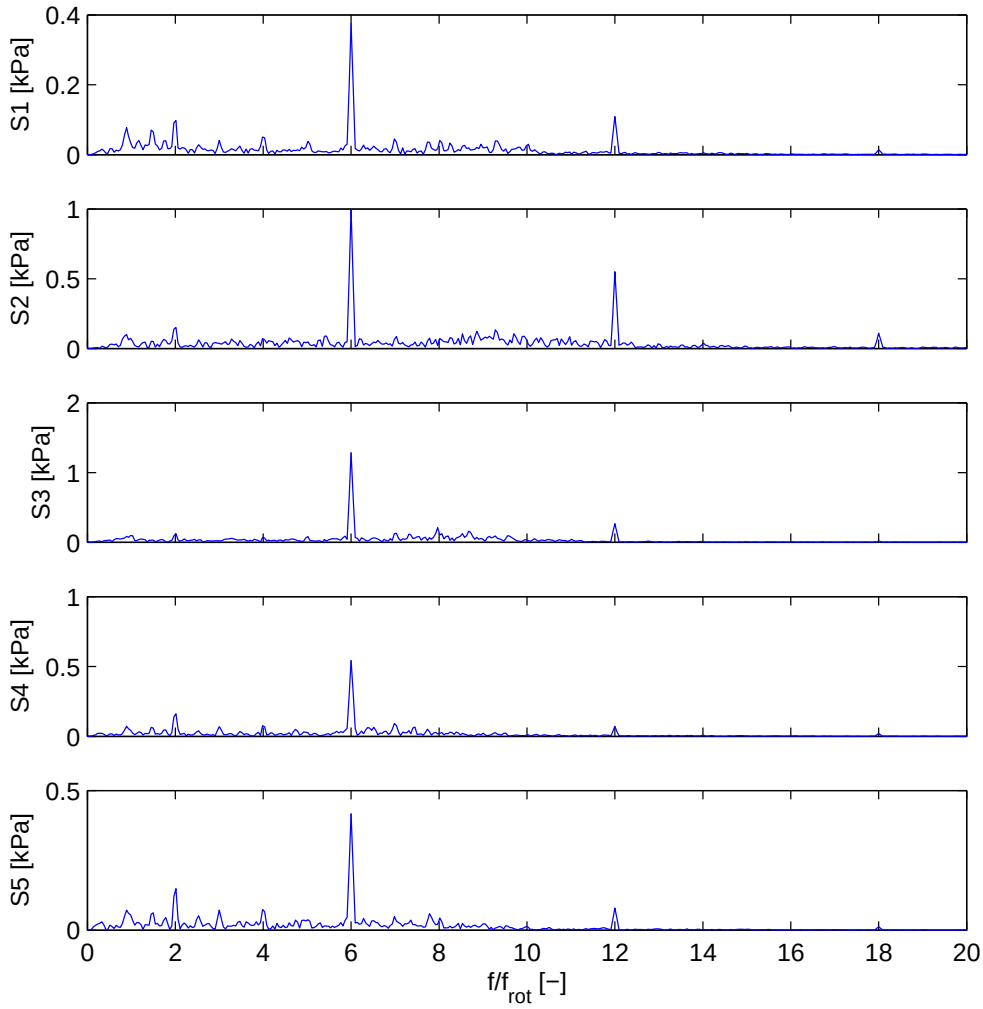

Figure C.6: Spectra of instantaneous time signal at transparent pump volute at 150 %Q_N

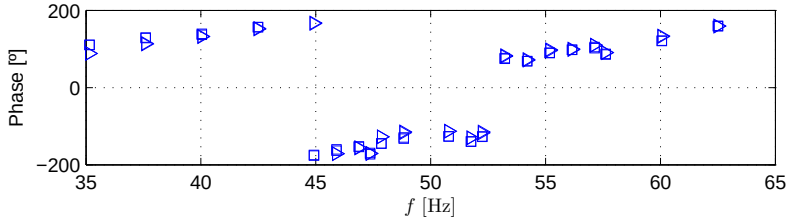

(a) Sensor 1

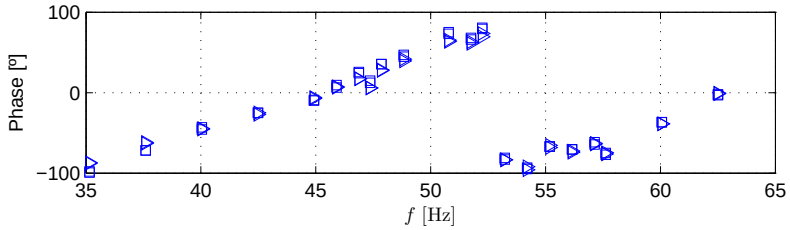

(b) Sensor 2

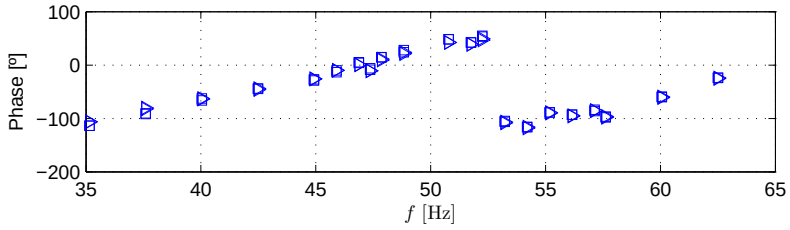

(c) Sensor 3

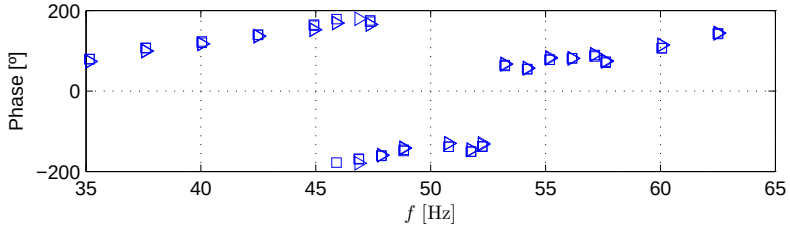

(d) Sensor 4

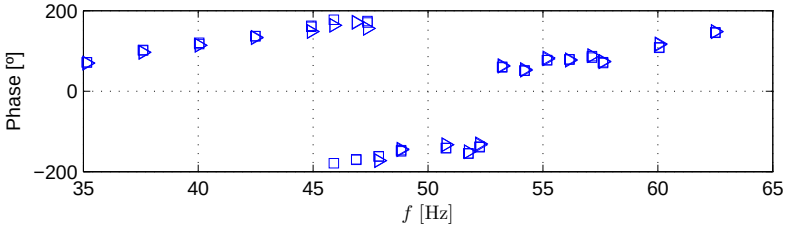

(e) Sensor 5

Figure C.7: Influence of valve open (▷) and closed (□) at 40 % Q_N on phase at f_{BP} of pressure sensors at pump volute for different pump rotational speeds

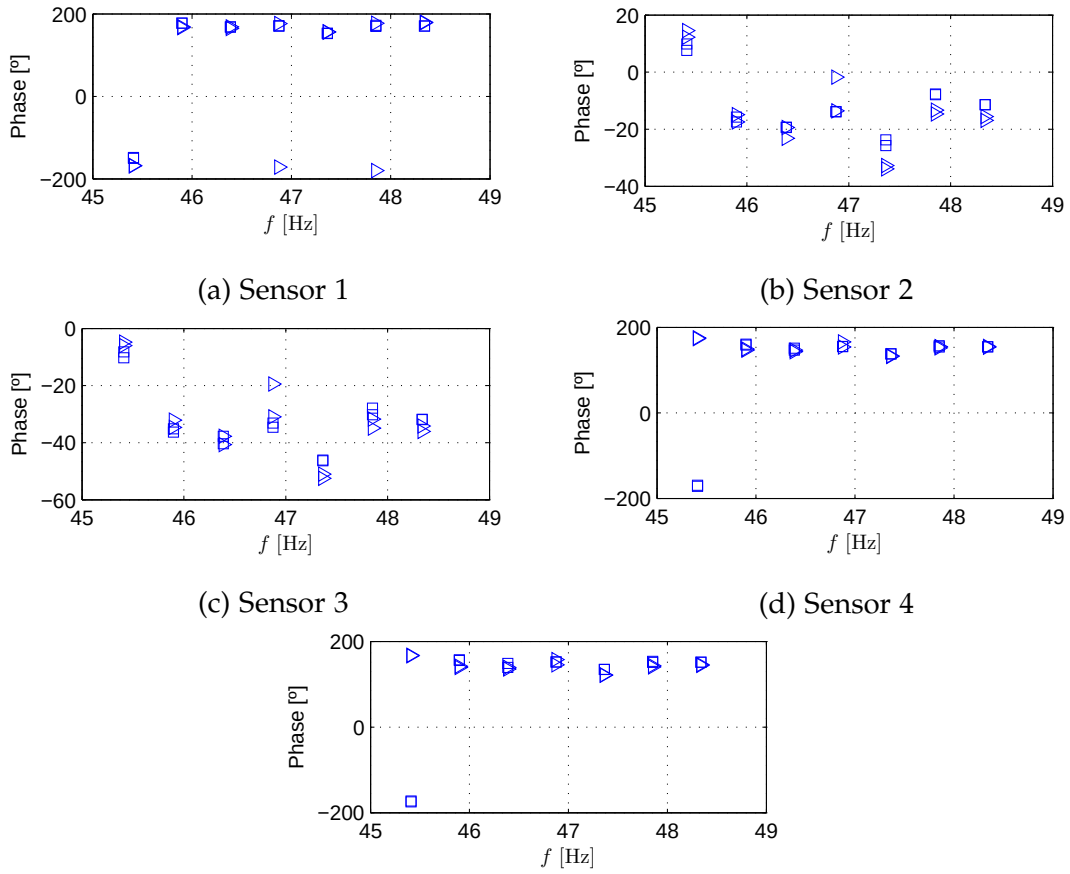

(a) Sensor 1

(b) Sensor 2

(c) Sensor 3

(d) Sensor 4

(e) Sensor 5

Figure C.8: Influence of valve open (▷) and closed (□) at 40 % Q_N on phase at f_{BP} of pressure sensors at pump volute for different pump rotational speeds between 45 and 48 Hz

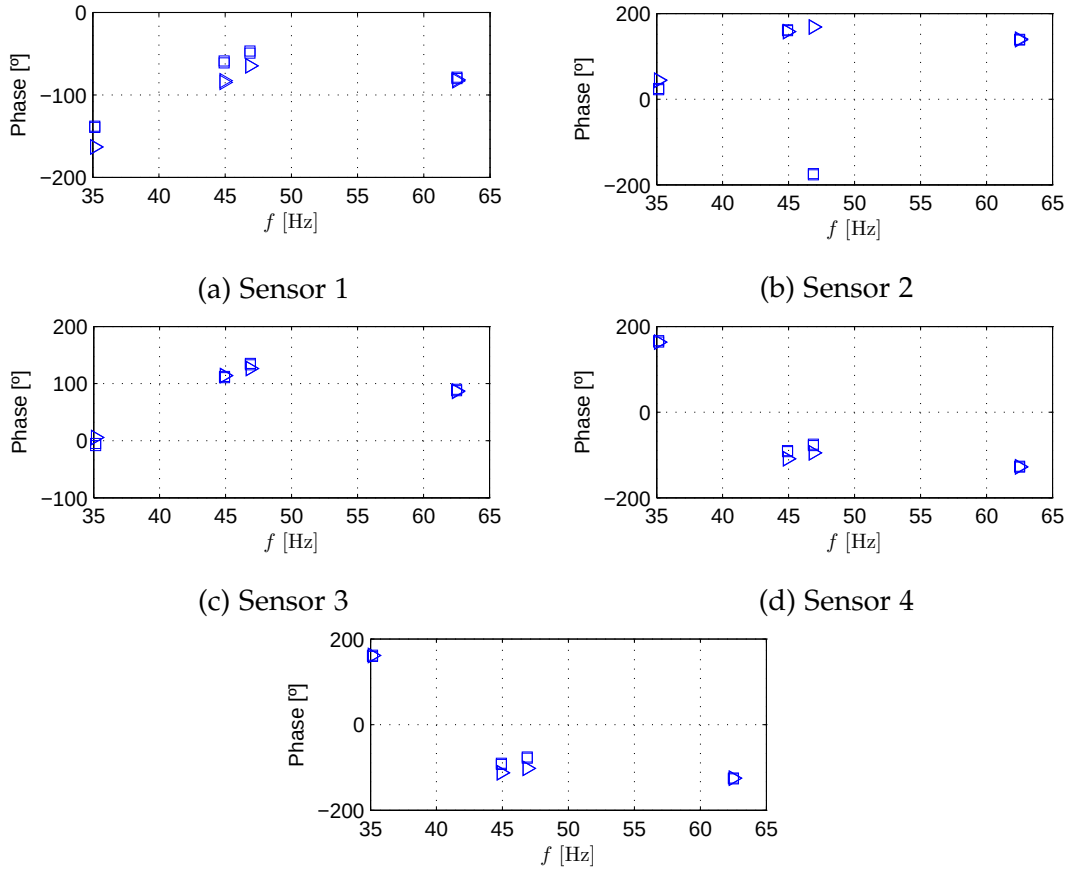

(a) Sensor 1

(b) Sensor 2

(c) Sensor 3

(d) Sensor 4

(e) Sensor 5

Figure C.9: Influence of valve open (▷) and closed (□) at Q_N on phase at f_{BP} of pressure sensors at pump volute for different pump rotational speeds